Reconstructing the southern Greenland Ice Sheet and deep ocean circulation during the Plio-Pleistocene intensification of Northern Hemisphere glaciation

Submitted by Keziah Rose Blake-Mizen, to the University of Exeter as a thesis for the degree of Doctor of Philosophy in Geology, March 2019

Declaration

The contents of this thesis are all my, the candidate's, own original work, except for where otherwise stated. The views and opinions expressed herein are my own, and not necessarily those of any other person or organisation unless so attributed.

One article included in this thesis has been published by the candidate pertaining to the research within. This publication forms the basis for Chapter 4 and was published in *Quaternary Science Reviews* in February 2019. The paper was authored by the candidate with supervisory comments from Ian Bailey, with improvements to the manuscript suggested by Robert Hatfield and Joseph Stoner (Oregon State University) and two anonymous reviewers. The full article can be found at https://doi.org/10.1016/j.quascirev.2019.01.015 and the accepted manuscript (including Supplementary) is reproduced in Appendix A. The chapter includes an additional assessment of physical grain-size distribution for selected samples over the study interval and its potential relationship to the strength of deep ocean currents.

Abstract

Reconstructing the southern Greenland Ice Sheet and deep ocean circulation during the Plio-Pleistocene intensification of Northern Hemisphere glaciation

Keziah Blake-Mizen

College of Engineering, Mathematics and Physical Sciences

University of Exeter, Penryn Campus

DPhil in Geology

2019

The Greenland Ice Sheet (GrIS) is thought to have reached modern-like extents during cold stages for the first time during the Plio-Pleistocene intensification of Northern Hemisphere glaciation (iNHG, ~3.6–2.4 million years ago, Ma). However, questions remain regarding the spatial maturation of the southern GrIS during this time – a region thought to be particularly sensitive to changes in climate – including its extent during the mid-Piacenzian warm period (mPWP; 3.264–3.025 Ma), considered an analogue to near-future climate with atmospheric CO_2 levels >400 ppmv and temperatures elevated by ~2–3 °C relative to today. Difficulties in obtaining long continuous sediment core records back to the late Pliocene in the subpolar North Atlantic, as well as chronological uncertainty in existing records, have previously hampered efforts to address these unknowns. In this thesis, I present high-resolution records of ice-rafted debris concentration and provenance, environmental magnetics and elemental X-ray fluorescence (XRF) spanning ~3.2–2.2 Ma from North Atlantic Integrated

Ocean Drilling Program Site U1307 on Eirik Drift, just offshore southern Greenland. The study benefits from a newly-resolved high-fidelity relative paleointensity-based age model, the first of its kind for high-latitude sediments deposited during this interval, which enables variability in the records to be accurately and precisely dated. This multi-proxy approach enables constraints to be placed on the spatio-temporal evolution of iceberg-calving margins on southern Greenland, as well as contemporaneous changes in surface water productivity and delivery of glaciofluvial silt via the deep Western Boundary Undercurrent (WBUC) to Eirik Drift during iNHG. Provenance analysis of ice-rafted debris pinpoints the evolution of important modern-day southern Greenland iceberg-calving sources, revealing that a modern-like GrIS with extensive southern iceberg-calving margins had developed by ~2.4 Ma. Elevated glaciofluvial erosion throughout the mPWP traced by XRF and magnetics refutes predictions for complete GrIS deglaciation during this time, and sedimentation rates and environmental magnetics provide the first direct evidence that the strength of the WBUC changed contemporaneously with increasing southern GrIS extents between 2.9 and 2.7 Ma.

Acknowledgements

I give my sincere thanks to my primary supervisor Ian Bailey and secondary supervisor Stephen Hesselbo, who granted me the opportunity to work on this exciting project almost five years ago and for which I am incredibly grateful. Their guidance, feedback and advice has helped me every step of the way in seeing the research aims through to success and gaining confidence in my abilities as an independent researcher. I have immensely enjoyed my time at Penryn Campus with the University of Exeter, whom I thank for providing the scholarship for my PhD that throughout the duration has helped me to collect data, collaborate, network, present my research and explore in many beautiful places including Oregon, New Orleans, Barcelona, Vienna and Bremen.

This research used marine core samples provided by the IODP, which was sponsored by the European Consortium for Ocean Research Drilling (ECORD) and participating countries under management of Joint Oceanographic Institutions, Inc. I thank Walter Hale and Alex Wülbers at MARUM Bremen for help with sampling, and Megan Spencer and Paul Wilson at the National Oceanography Centre Southampton for their assistance with sample processing. Gratitude is also given to Aurélie Aubry at Université du Québec à Montréal for discussions about our revised splice and age model. I thank my collaborators at Oregon State University, Rob Hatfield, Joe Stoner, Mo Walczak and Anders Carlson for invaluable discussions, feedback and advice when writing my very first publication. I also thank the PMag Lab staff at OSU, Brendan Reilly and Ann Morey-Ross, for their help with managing my slightly overwhelming PMag data.

I am indebted to the laboratory staff here at the Camborne School of Mines within CEMPS, especially Robert Fitzpatrick, Sharon Uren, Gavyn Rollinson,

fellow cake enthusiast Malcolm Spence and Joe Pickles for all their supervision and advice during my various stages of labwork. Special thanks to Steve Pendray for the absolutely flawless resin sample stubs. I also thank Andy Milton at NOCS who worked tirelessly to help us get the most out of our lead-isotope data on the Neptune.

Big love to all the PrettyHugeDucks I've had the honour of sharing the hysterics of this stage of our academic careers with, especially Robyn Pointer, Dóra Kavecsánszki, Ricardo Celestino, Chri Yeomans, Gnarlo Robiati, Jordan Lindsay, Matt Head, Charlotte Beasley, Bex Parker, Bobby Pell, Laurens Tijsseling, Milly Owens, Matty Tonkin, Tomasa Sbaffi, Luke Palmer, Safaa Hussein and Jane Galwey. Endless gratitude also to my best buds Danni Long, Chris Cock, Danny Davies, Sam Reece, Emma Winfield and Zoë Butters for being fountains of encouragement and believing in me when I really didn't.

This thesis is dedicated to my parents Barry and Lindsey, who throughout my life have always encouraged me to do my best and try new things, and supported me in everything I do even if my choices are sometimes a bit questionable. It means the whole Earth to make you proud.

Contents

List of Figures

Chapter 1

Chapter 2

Chapter 3

Chapter 4

Chapter 5

Chapter 6

List of Tables

Chapter 3

Chapter 4

Chapter 5

Chapter 6

Definitions

Key terms and abbreviations specific to this work are defined here in alphabetical order.

AB	Archaean Block
AMOC	Atlantic Meridional Overturning Circulation
ARM	Anhysteretic remanent magnetisation
EC	East Caledonides
EGC	East Greenland Current
GrIS	Greenland Ice Sheet
iNHG	Intensification of Northern Hemisphere glaciation, ~3.6 to 2.4 Ma
IRD	Ice-rafted debris
KMB	Ketilidian Mobile Belt
MIS	Marine Isotope Stage
mPWP	The mid-Piacenzian warm period, 3.264 to 3.025 Ma
NADW	North Atlantic Deep Water
NHG	Northern Hemisphere glaciation
NMB	Nagssugtoqidian Mobile Belt
NRM	Natural remanent magnetisation
***p*CO_2**	The partial pressure of carbon dioxide in the atmosphere (μatm)
PF	Polar Front
RPI	Relative palaeointensity, here defined as NRM/ARM
WBUC	Western Boundary Undercurrent
XRF	X-ray fluorescence

Definitions and Abbreviations

All terms specific to this work, as well as any abbreviations used in this thesis, are defined here in alphabetical order.

AF Alternating field, a magnetic current that alternates direction between positive and negative

AMOC Atlantic Meridional Overturning Circulation, a series of deep and intermediate interlinked Atlantic Ocean currents responsible for transporting and redistributing heat and salinity between the high and low latitudes (also known as the Thermohaline Circulation, THC)

ARM Anhysteretic remanent magnetisation, a type of residual magnetisation recorded by ferromagnetic minerals in rocks and sediments, measured by exposing the sample to a large alternating field (AF) current and small direct current (DC) field, which is then gradually reduced and DC bias removed to isolate the remanence

EGC East Greenland Current

GrIS Greenland ice sheet

iNHG The intensification of Northern Hemisphere glaciation, marking the growth of terrestrial ice on the majority of northern high-to-mid-latitude landmasses including Greenland, Scandinavia, North America, Northern Europe and Russia, which occurred between approximately 3.6 and 2.4 Ma

IRD	Ice-rafted debris; clay- to boulder-sized sediment subglacially-eroded on land and transported out to sea in icebergs, which melt and deposit their load on the seafloor
ka	Thousands of years ago
Ma	Millions of years ago
MIS	Marine Isotope Stage, alternating 'warm' (interglacial) and 'cold' (glacial) orbital periods in Earth's history as defined by the stable oxygen isotope record, with glacials (more positive $\delta^{18}O$) denoted by even numbers and interglacials (more negative $\delta^{18}O$) by odd numbers
mPWP	The mid-Piacenzian warm period, which occurred between 3.264 and 3.025 Ma
mT	Milli Tesla, a measure of magnetic field strength (or flux density)
NHG	Northern Hemisphere glaciation, referring to the presence of terrestrial ice on the majority of northern high-to-mid-latitude landmasses including Greenland, Scandinavia, North America, Northern Europe and Russia
NRM	Natural remanent magnetisation, a type of residual magnetisation recording the Earth's magnetic field at the time ferromagnetic minerals in a sediment/magma were deposited and/or lithified
***p*CO_2**	The partial pressure of carbon dioxide (CO_2) in the atmosphere, measured in micro-atmospheres (μatm)
PF	Polar Front
RPI	Relative palaeointensity, a measure of the relative strength of the Earth's magnetic field through time. In this work it is defined as the

	slope of the natural remanent magnetisation versus the anhysteretic remanent magnetisation, or NRM/ARM
XRF	X-ray fluorescence

Chapter 1

Introduction

This chapter outlines the motivation for undertaking the work presented in this thesis, defines the aims and research questions tackled, and provides an overview of the thesis structure.

1.1 Motivation for Studying Greenland Ice Sheet History

The Arctic is one of the fastest-warming regions on Earth today (Bindoff *et al*., 2013) and is home to the Greenland Ice Sheet (GrIS), which presently covers an area of approximately 1.7 million km^2. Greenland is considered the key nucleation site for Northern Hemisphere glaciation, leading the regional response to climate forcings since the first ephemeral growth of terrestrial ice in the middle Eocene, ~46 million years ago (Ma) (Larsen *et al*., 1994; St John, 2008). Multiple proxy records show the GrIS has consistently lost and gained mass in response to warming and cooling climates, respectively (e.g., Jansen *et al*., 2000; St John and Krissek, 2002; Thiede *et al*., 2011), with mass loss carried out primarily through low elevation glacier-melting and iceberg-calving (Alley *et al*., 2010). This has implications for global eustatic sea-level change; in its present state, the GrIS is estimated to hold the equivalent to ~7 m of eustatic sea-level rise (Meehl *et al*., 2007).

Mass loss from the GrIS has greatly accelerated in recent decades, almost quadrupling from 102 Gt yr^{-2} in 2003 to 393 Gt yr^{-2} in 2013 as a result of rising global temperatures, increasing the GrIS contribution to eustatic sea-level rise by ~1.1 mm per year (Chen *et al*., 2017). Marine-terminating glaciers in southeast and northwest Greenland have been in rapid retreat (Bjørk *et al*., 2012; Bevis *et al*., 2018), with dynamic thinning taking place across the whole ice-sheet (Pritchard *et al*., 2008). The greatest acceleration of ice-loss in recent years has taken place in southwest Greenland, however, where increasing air temperatures are starting to have a significant effect on mass balance (Bevis *et al*., 2018). This accelerating rate of melt is likely to substantially reduce Greenland ice volume and raise eustatic sea-level over the coming decades, and it is estimated that warming of just a few degrees Celsius above average 20th Century values could

result in total GrIS loss (Letréguilly *et al*., 1991; Alley *et al*., 2010). Indeed, the most recent Special Report published by the IPCC states with 'medium confidence' that irreversible GrIS loss could be triggered by just 1.5 to 2°C of global warming (IPCC, 2018).

Predictions for GrIS deglaciation and associated eustatic sea-level impact over the coming century depend heavily upon the capabilities of numerical climate models, which at present are unable to accurately reconstruct past ice-sheet configurations and are hampered by large uncertainties (e.g., Cuffey and Marshall, 2000; Otto-Bliesner *et al*., 2006; Lunt *et al*., 2008; Haywood *et al*., 2009; Fyke *et al*., 2011; Applegate *et al*., 2012; Stone *et al*., 2013). In order to reliably constrain thresholds for change, models must be able to simulate conditions for a range of past warmer- and colder-than-present climate states. Thus, ground-truthing of such models with sufficient palaeodata from regions sensitive to climatic variability is a critical endeavour in advancing our understanding of these systems and feedbacks (Thiede *et al*., 2011; Colville *et al*., 2011; Reyes *et al*., 2014; Raymo *et al*., 2018).

During the Last Interglacial, ~128–116 thousand years ago (ka), various lines of evidence including sea-level records, ice-core records, geochemical sediment analysis and modelling studies show that the GrIS was reduced in volume and made a substantial contribution to the estimated ~4–6 m higher LIG sea level compared to today (e.g., Cuffey and Marshall, 2000; Otto-Bleisner *et al*., 2006; Carlson *et al*., 2008; Colville *et al*., 2011; Grant *et al*., 2012; Stone *et al*., 2013; Rohling *et al*., 2017; Kopp *et al*., 2014). Despite around 30 years of marine core drilling in the high-latitude North Atlantic, however, our understanding of the spatial history of ice-sheet growth prior to the Late Quaternary remains uncertain; even less is known about the specific evolution of

the GrIS. This is particularly the case for the late Pliocene and earliest Pleistocene intensification of Northern Hemisphere glaciation (iNHG; ~3.6–2.4 Ma; Mudelsee and Raymo, 2005), the last great climate transition of the Cenozoic. This interval also encompasses the mid-Piacenzian warm period (mPWP, 3.264–3.025 Ma; Dolan *et al*., 2011), widely considered an analogue to future equilibrium climate (Burke *et al*., 2018) with a similar-to-modern atmospheric carbon dioxide concentration (pCO_2; ≥400 ppmv) and global temperatures elevated by 2–3°C relative to today (e.g., Raymo *et al*., 1996; Dowsett *et al*., 2010; Martínez-Botí *et al*., 2015; Bachem *et al*., 2017; Raymo *et al*., 2018).

Model simulations of the GrIS response to mPWP climate suggest significant retreat resulting from estimated ~4–10 °C higher Arctic temperatures than present (e.g., Haywood and Valdes, 2004; Lunt *et al*., 2010). In one modelled scenario, just ~7% of modern GrIS extent remained as small residual ice-caps in the coastal mountains of East Greenland (Solgaard *et al*., 2011). Others simulate less extreme retreat, with more extensive ice-caps persisting in eastern and southern high elevations (e.g., Lunt *et al*., 2010; Dolan *et al*., 2011). Proxy records for sea-level rise during this period are also highly variable; estimates range from ~10 to 30 m above present, assuming complete GrIS loss and a variable degree of ice-sheet retreat in Antarctica (Raymo *et al*., 2018). The uncertainty over the assumption of full GrIS loss, however, highlights the need for additional palaeodata to better constrain the likely GrIS contribution to eustatic sea-level rise under warmer-than-present climate conditions.

During glacial intensification following the mPWP, models simulate the development of a modern-sized GrIS around 2.7 Ma, with shelf-edge glaciation first achieved during cold stages in the northwest and finally in the southeast as

the climate cooled (e.g., Solgaard *et al*., 2011). This modelled history is yet to be confirmed or further constrained by sufficient palaeodata, however, since many of the available marine core records are incomplete and/or poorly-dated due to discontinuous coring, a lack of calcareous biostratigraphic markers and/or no reliable magnetostratigraphy. One important region where understanding lacks is for the southern GrIS, which a number of studies suggest has been particularly sensitive to climate change in the past (e.g., Letréguilly *et al*., 1991; Willerslev *et al*., 2007; Colville *et al*., 2011; Reyes *et al*., 2014).

Causes of iNHG are also still widely debated. While a long-term decline in atmospheric CO_2 due to continental weathering is generally accepted to have driven the Cenozoic cooling trend that pushed Northern Hemisphere climate over a threshold allowing widespread glaciation by ~2.5 Ma (e.g., Raymo and Ruddiman, 1992; Lunt *et al*., 2008b; DeConto *et al*., 2008; Koenig *et al*., 2011; Martínez-Botí *et al*., 2015), other tectonic mechanisms such as Iceland hotspot activity (e.g., Steinberger *et al*., 2015), mid-latitude mountain uplift (e.g., Birchfield and Weertman, 1983; Ruddiman and Kutzbach, 1989) and tectonic seaway closure (e.g., Bartoli *et al*., 2005; Sarnthein *et al*., 2009; McKay *et al*., 2012) have also been implicated in preconditioning the high northern latitudes for iNHG. The latter invokes a ‘spin-up’ in the strength of the Atlantic Meridional Overturning Circulation (AMOC), the ‘engine’ driving the distribution of heat and salinity between the low and high latitudes with significant implications for temperature and precipitation on Greenland (e.g., Klocker *et al*., 2005; Lunt *et al*., 2008a). Various studies contrastingly cite a ‘slow-down’ in AMOC vigour during iNHG due to reduced export of North Atlantic Deep Water (NADW; Bell *et al*., 2015; Horikawa *et al*., 2015) or northward migration of Southern Ocean fronts restricting the warm Agulhas leakage (e.g., McKay *et al*., 2012), or no significant change

(e.g., Lawrence *et al*., 2013). Currently, however, no records exist from sites well-situated to directly measure aspects of AMOC variability in the North Atlantic during iNHG in order to test these competing hypotheses.

1.2 Project Scope and Research Aims

Two things become clear from assessing the present state of records for GrIS evolution: 1) there is a lack of well-dated, high-resolution records that can be used to corroborate modelled predictions for GrIS extent during the mPWP and iNHG GrIS extent; and 2) a true southern Greenland perspective is missing for the entire iNHG interval. This is further accentuated by both palaeo and modern studies that have highlighted the southern GrIS as a region particularly sensitive to warming (e.g., Willerslev *et al*., 2007; Carlson *et a*l., 2008; Alley *et al*., 2010; Bevis *et al*., 2018). Modern iceberg-trajectory modelling (Bigg *et al*., 1998; Rignot and Kanagaratnam, 2006; Andrews *et al*., 2014a; Smith *et al*., 2018) demonstrates that records from the marine realm immediately south of Greenland are crucial in building a more complete GrIS history, since this region is fed icebergs calved from a wide range of eastern, southeastern and southern Greenland sources via the East Greenland Current (EGC; Fig. 1.1). Eirik Drift, a mounded contourite deposit just off the southern tip of Greenland (Fig. 1.1), presents an ideal opportunity for such studies since it lies beneath the path of the EGC and contains an expanded sedimentary sequence through the Plio-Pleistocene (Hunter *et al*., 2007). Studies on Late Pleistocene Eirik Drift records have already yielded a wealth of information on GrIS history using its long-term records of ice-rafted debris, radiogenic isotopes, environmental magnetism and elemental ratios (e.g. Stoner *et al*., 1995; Carlson *et al*., 2008; Colville *et al*., 2011; Mazaud *et al*., 2015; Hatfield *et al*., 2013, 2016, 2017). Eirik Drift is also

dynamically shaped by the Western Boundary Undercurrent (WBUC), a deep current comprising a combination of overflow waters originating in the Nordic Seas (Fig. 1.1), which transports fine sediment eroded from Greenland and elsewhere in the Arctic region (Pickart, 1992; Hunter *et al*., 2007). The WBUC continues into the North Atlantic where it contributes ~16–18 Sverdrup to the volume of NADW (Fig. 1.1), the main deep northern component of AMOC (Hunter *et al*., 2007).

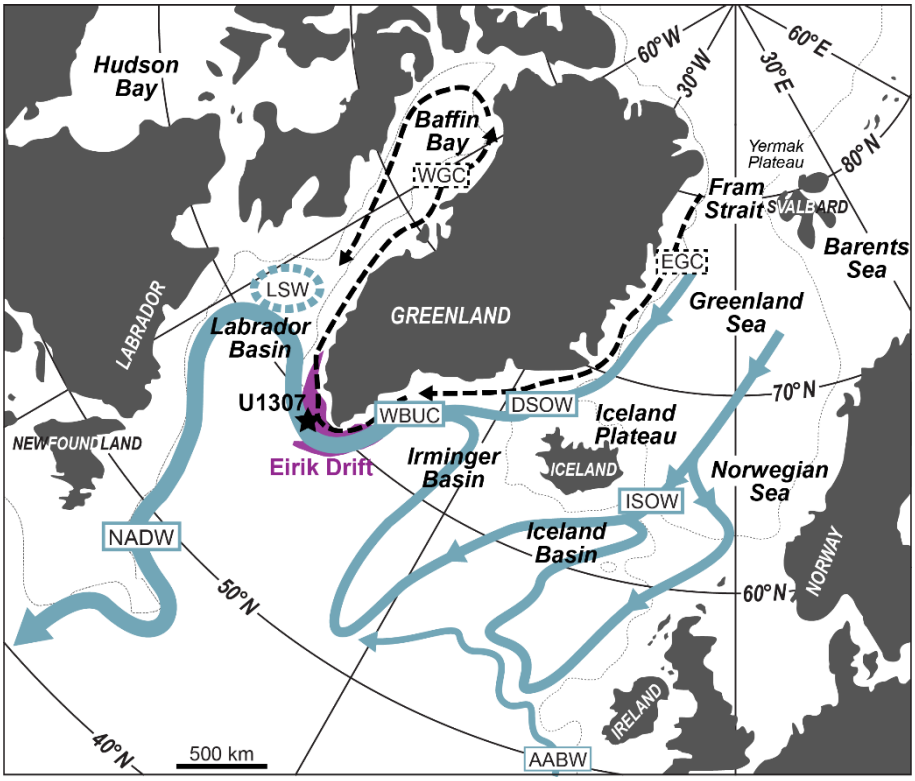

Figure 1.1 Map of Greenland and surrounding landmasses and ocean basins, showing the location of IODP Site U1307 on Eirik Drift and its relationship to the paths of key modern deep (solid blue) and surface (dashed black) ocean currents relevant to this study. EGC = East Greenland Current, WGC = West Greenland Current, ISOW = Iceland-Scotland Overflow Water, DSOW = Denmark-Scotland Overflow Water, AABW = Antarctic Bottom Water, WBUC = Western Boundary Undercurrent, LSW = Labrador Sea Water, NADW = North Atlantic Deep Water. The 1000 m isobath is given by thin dotted lines.

Integrated Ocean Drilling Program (IODP) Expedition 303 to Site U1307, situated on Eirik Drift (~59°N; Fig. 1.1), recovered a long sedimentary record back to the early Late Pliocene with a shipboard-estimated basal age of ~3.6 Ma. Sediments recovered from this site therefore represent a unique opportunity to study iNHG

and the mPWP in the context of GrIS extent and variability in WBUC transport. As a drift site with an average sedimentation rate of ~5 cm kyr^{-1} (Expedition 303 Scientists, 2006), U1307 has the potential to yield millennial-scale records throughout (Hunter *et al*., 2007) – making it ideal for studying orbital-scale variability over this crucial interval in Earth's climatic history.

The research reported in this thesis was designed to combine in a variety of ways a number of long-ranging high-resolution datasets across the interval(s) of interest, to address the following aims:

A1: To reconstruct southern Greenland Ice Sheet ice-rafting history and spatial extents during the intensification of Northern Hemisphere glaciation interval, including the mPWP;

A2: To measure the presence of internal, actively-eroding Greenland ice in the absence of abundant ice-rafted debris during the mPWP;

A3: To elucidate changes, if any, in deep-ocean circulation during the intensification of Northern Hemisphere glaciation.

A thorough literature review was carried out to assess the current state of understanding of Greenland glacial history and proposed drivers of iNHG, identifying where gaps in understanding persist and previously-employed methodologies that could be used to investigate them (Chapter 2). Data collection occurred in several phases using various sedimentological and geochemical methods to glean as complete a picture of variability over the study interval as possible, and these data are analysed and interpreted in context with other authors' previous work. The key questions framing the work in this thesis directly address the research aims:

Q1: Was a GrIS of modern size ever established during iNHG?

Q2: Is there evidence for ice on southern Greenland during the mPWP?

Q3: Did WBUC behaviour change during iNHG?

The key methodologies employed to meet the research aims and to address the research questions are as follows:

M1: Discrete measurements of ice-rafted debris concentrations, whole-sample mineralogical analysis and individual grain lead-isotope provenance analysis to reconstruct extents and locations of marine-calving margins;

M2: U-channel palaeomagnetic measurements to build a high-fidelity, orbital-resolution age-model, and assess both terrestrial and marine drivers of environmental magnetic parameters;

M3: U-channel X-ray fluorescence elemental measurements to elucidate changes in sediment source, internal ice-sheet erosion and marine productivity.

In summary, this research presents an unprecedented opportunity to combine multiple high-resolution records and proxies to fill the gaps in our knowledge of GrIS history, particularly its southern extents, and to link this variability with drivers and feedbacks associated with a changing Plio-Pleistocene climate. The findings of this work may prove to be of interest to Plio-Pleistocene ice-sheet modellers who wish to ground-truth simulations with invaluable palaeodata, and to policy-makers concerned with understanding the range of natural variability in GrIS extents under both warmer- and colder-than-present climate states.

1.3 Thesis Overview

Short summaries of each subsequent chapter comprising this PhD thesis are as follows:

Chapter 2: Background

An in-depth literature review summarising previous work undertaken to define the history of iNHG and Greenland glaciation, including an assessment of proposed associated drivers and/or feedback mechanisms, highlighting the gaps in knowledge that the work in this thesis aims to address.

Chapter 3: Materials and Methodologies

An overview of the main materials and methodologies employed in undertaking the research for this thesis, including study site context, sampling of the core material, and the main analytical methods used to investigate the research questions.

Chapter 4: Southern Greenland glaciation and Western Boundary Undercurrent evolution recorded on Eirik Drift during the late Pliocene intensification of Northern Hemisphere glaciation

Presentation and interpretation of new Site U1307 ice-rafted debris and environmental magnetic records, including revisions to the site splice and age model. Presented as a modified version of the paper published in *Quaternary Science Reviews*.

Chapter 5: Geochemical evidence that ice existed inland on southern Greenland during the mid-Piacenzian warm period

Presentation and interpretation of new Site U1307 XRF elemental records. Presented as a draft version of the paper in prep for *Geology*.

Chapter 6: Tracking the lead-isotope and petrographic provenance of Greenland-sourced ice-rafted debris deposited on Eirik Drift during the Plio-Pleistocene intensification of Northern Hemisphere glaciation

Presentation and interpretation of new Site U1307 Pb-isotope and QEMSCAN mineralogical provenance records. Presented as a draft version of the paper in prep for *Earth and Planetary Science Letters*.

Chapter 7: Key Findings and Data Outlook

Summary of all data chapter findings in context with the original literature review, an assessment of the extent to which the research questions have been answered and research aims met, and suggestions for future work to refine and build on the findings of this research.

Appendices

Extended datasets associated with each data chapter.

Chapter 2

Background

This chapter summarises the evidence for the evolution of Cenozoic bi-polar glaciation, and critically assesses the proposed long- and short-term drivers for the Plio-Pleistocene intensification of Northern Hemisphere glaciation.

2.1 History of Cenozoic Glacial Evolution

The Cenozoic Era (~66 Ma to present) is distinguished in Earth's history by a marked shift in global climate from a 'Greenhouse' world, characterised by high temperatures relative to the present day and an absence of continental-ice, to a cooler 'Icehouse' world with widespread glaciation in the high latitudes of both hemispheres (e.g., Moran *et al*., 2006; Zachos *et al*., 2008). This long-term cooling trend, punctuated by short, transient phases of climatic warming, is recorded in the stable oxygen isotope composition (the ratio of ^{18}O to ^{16}O, $\delta^{18}O$) of deep-sea benthic foraminifera (Fig. 2.1; Lisiecki and Raymo, 2005; Zachos *et al*., 2008). Cenozoic global temperatures initially peaked during the Paleocene-Eocene Thermal Maximum (PETM), ~55 Ma, and remained relatively high through the Early Eocene Climatic Optimum (EECO), ~52–50 Ma (Fig. 2.1a; Zachos *et al*., 2001a, 2008). Earth's climate then gradually cooled towards the present day, forced by a significant reduction in atmospheric CO_2 concentration (pCO_2) and thus radiative forcing to approximately modern levels (DeConto and Pollard, 2003; Pagani *et al*., 2005; Foster *et al*., 2017), only punctuated significantly by the Mid-Miocene Climatic Optimum (MMCO) between ~17 and 15 Ma (Fig. 2.1a; Zachos *et al*., 2008). Below is a summary of the evidence for the evolution of bi-polar glaciation as the Cenozoic cooling trend progressed.

2.1.1 Early continental- and sea-ice in the Eocene-Oligocene

The first evidence for the presence of ice in the Arctic may date back as early as the Paleocene-Eocene boundary, with intermittent sedimentological and geochemical sea-ice markers identified in Svalbard's Central Basin (Fig. 2.2) that at this time was connected to northeastern Greenland (Spielhagen and Tripati, 2009). High abundances of the sea-ice-dependent diatom genus *Synedropsis*

(Stickley *et al*., 2009) and weathering textures of quartz grains in the coarse sand fraction (St John, 2008) of Integrated Ocean Drilling Program (IODP) Expedition 302 cores drilled on Lomonosov Ridge indicate the presence of seasonal sea-ice in the central Arctic during the mid-Eocene (~46 Ma), as well as rafting of terrestrial sediment by both sea-ice and icebergs (ice-rafted debris; IRD) at this time (Stickley *et al*., 2009; St John, 2008). This evidence points to early partial freezing of the surface ocean and nucleation of small glaciers on circum-Arctic landmasses during the period of cooling following the EECO (St John, 2008; Zachos *et al*., 2001a; 2008). These discoveries support a hypothesis based on eustatic sea-level reconstructions that ephemeral (short-lived) glacial ice may have existed in the Arctic during short Eocene intervals of low insolation (Miller *et al*., 2005), and suggest that early stages of glaciation may have taken place on both poles almost contemporaneously; in fact, the very first appearance of ice in the Northern Hemisphere may even marginally pre-date that in the Southern Hemisphere (Thiede *et al*., 2011).

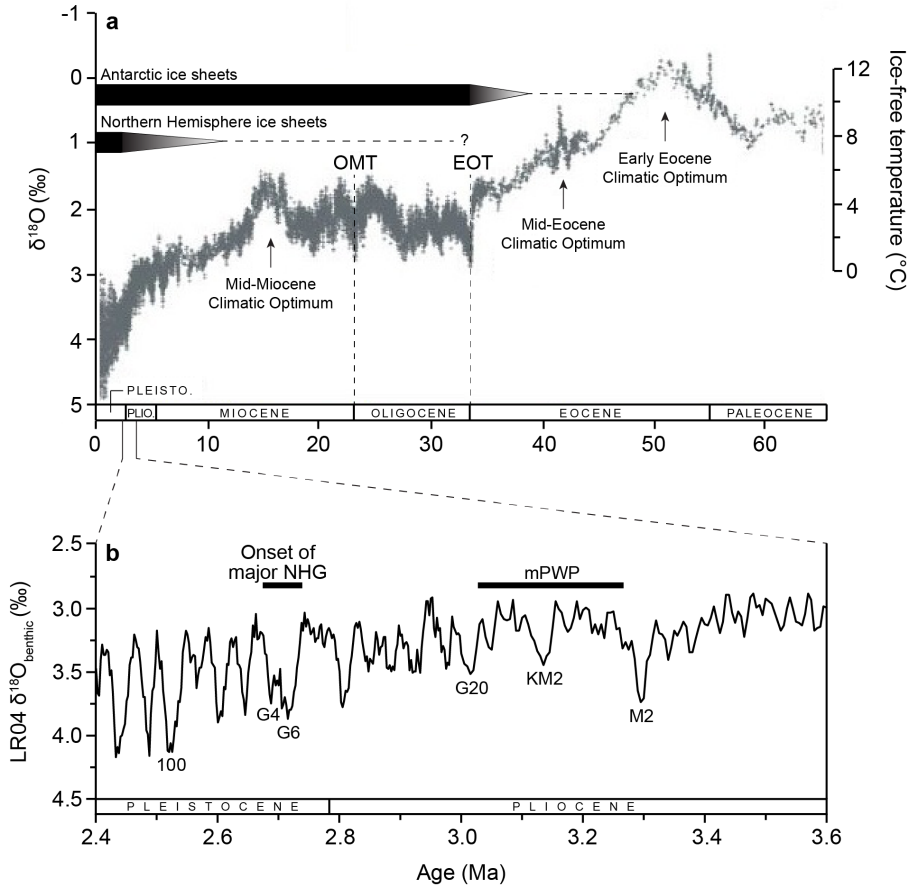

Figure 2.1 (**a**) Long-term Cenozoic climate change (past ~66 Myr), as tracked by the stable oxygen isotope composition of benthic foraminifera ($\delta^{18}O$), with timings of climatic optimums, epoch boundaries (EOT = Eocene-Oligocene Transition; OMT = Oligocene-Miocene Transition), and the episodic (dashed lines) and permanent expansion of Antarctic and Northern Hemisphere ice-sheets indicated (modified from Zachos *et al*., 2008); with (**b**) an expanded view of the intensification of Northern Hemisphere glaciation (iNHG, 3.6 to 2.4 Ma; Mudelsee and Raymo, 2005), with key marine isotope stages, the onset of major Northern Hemisphere glaciation (NHG) and the duration of the mid-Piacenzian warm period (mPWP) labelled (Lisiecki and Raymo, 2005; Dolan *et al*., 2011).

Records of IRD in the circum-Antarctic region indicate localised glaciation took place on East Antarctica from at least the mid-Eocene (Birkenmajer, 1988), becoming more widespread through the late Eocene (e.g., Carter *et al*., 2017). The general consensus is that significant (i.e., modern-like) permanent East and West Antarctic ice-sheets (EAIS and WAIS, respectively) were established rapidly at the Eocene-Oligocene transition (EOT) ~34 Ma (Fig. 2.1a), when a two-step increase in benthic foraminiferal $\delta^{18}O$ (Coxall *et al*., 2005), interpreted as two separate cooling events each lasting ~40 thousand years (kyr), occurred coeval with increases in Southern Ocean IRD and other glacial weathering

proxies (Kennett, 1977; Miller *et al*., 1991; Lear *et al*., 2000; Cooper and O'Brien, 2004; Coxall *et al*., 2005; Ivany *et al*., 2006; Zachos *et al*., 1992, 1996, 2001a, 2008; Scher *et al*., 2011). The occasional presence of coarse sand and dropstones in Norwegian Sea (Fig. 2.2) sediments ~44–30 Ma suggests iceberg-rafting may have also been an important process in the (sub)polar Arctic during times of low insolation in this interval (Eldrett *et al*., 2007; Tripati *et al*., 2008). Much of this IRD comprises basalt likely originating from the Paleogene volcanics of East Greenland (Tripati and Darby, 2018), indicating the presence of at least isolated glaciers calving at sea-level in this region at a time when temperatures and pCO_2 were higher than at present (Fig. 2.1a; Eldrett *et al*., 2007, Thiede *et al*., 2011). Estimates of polar surface and deep ocean temperature in the Southern Hemisphere during the EOT indicate, however, that the second benthic $\delta^{18}O$ step primarily reflects growth of the Antarctic ice-sheets (DeConto *et al*., 2007; Lear *et al*., 2008; Liu *et al*., 2009), which is thought to have been accompanied by a ~70 m fall in eustatic sea-level (Pekar *et al*., 2002).

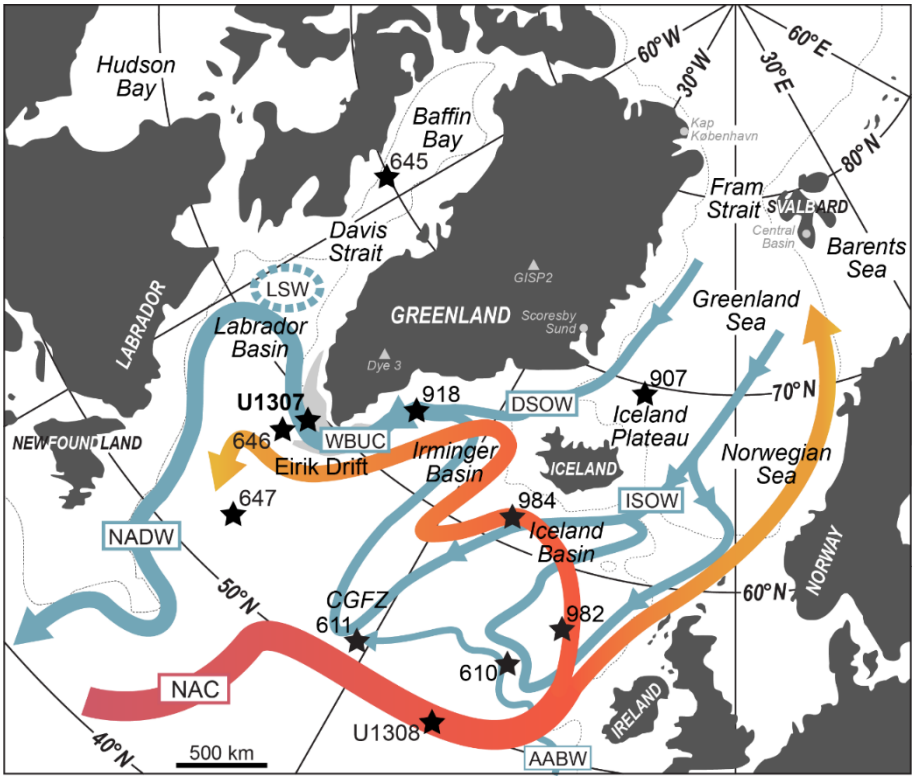

Figure 2.2 Map of Greenland and surrounding landmasses and ocean basins, showing the location of IODP Site U1307 (the focus of this thesis) on Eirik Drift, the position of North Atlantic ODP/DSDP/IODP drill sites mentioned in the text, and their relationships to the paths of key modern cold deep (blue) and warm surface (red-yellow gradient) ocean currents relevant to this study. NAC = North Atlantic Current, ISOW = Iceland-Scotland Overflow Water, DSOW = Denmark Strait Overflow Water, AABW = Antarctic Bottom Water, WBUC = Western Boundary Undercurrent, LSW = Labrador Sea Water, NADW = North Atlantic Deep Water. CGFZ = Charlie-Gibbs Fracture Zone. Also labelled are key localities and ice-core sites (GRIP2 and Dye 3) mentioned in the text. The 1000 m isobath is given by thin dotted lines.

Both observations and numerical model simulations of benthic $\delta^{18}O$ and atmospheric CO_2 across the EOT indicate pCO_2 decline, and thus a reduced greenhouse effect, was primarily responsible for initiating the scale of cooling observed at this time (e.g., DeConto and Pollard, 2003; Huber *et al*., 2004; Coxall *et al*., 2005; Pearson *et al*., 2009; Pagani *et al*., 2011; Ladant *et al*., 2014). Recent modelling efforts (e.g., Ladant *et al*., 2018) also appear to support the theory that the late Eocene opening of the Drake Passage was key to initiating the Antarctic Circumpolar Current (ACC), which is thought to have sustained Antarctic glaciation by thermally isolating the landmass from warm subtropical low-latitude waters (Kennett, 1977; Miller *et al*., 1991; Lear *et al*., 2000; Stickley *et al*., 2004; Sijp and England, 2004). Both pCO_2 decline and the development of a vigorous

ACC therefore likely acted in tandem to ensure widespread and permanent Antarctic glaciation by the early Oligocene (Fig. 2.1a; Lear and Lunt 2016), aided by enhanced northward heat transport via feedbacks with the thermohaline circulation from ~35 Ma (Coxall *et al*., 2018). Earth's orbit also favoured cool summers during the EOT due to a period of low-amplitude variability in the Earth's axial tilt (obliquity), known as a 'node' (e.g., Zachos *et al*., 2001b), which would have enabled a positive winter snow budget to persist through reducing summer ablation (e.g., Maslin *et al*., 1998; DeConto *et al*., 2003, 2008; Coxall *et al*., 2005). Since the earliest Oligocene, the benthic $\delta^{18}O$ record has therefore reflected a combination of changes in both deep-water temperature and continental-ice budgets (Fig. 2.1; Kennett, 1977; Lear *et al*., 2000; Lisiecki and Raymo, 2005; Zachos *et al*., 2008).

2.1.2 Bi-polar ice-sheet growth in the Miocene

Antarctic ice-sheets waxed and waned on ~110 kyr timescales into the early Miocene, ~30 to 17 Ma (Naish *et al*., 2001; Liebrand *et al*., 2016), driven by high-amplitude eccentricity-paced pCO_2 changes (Liebrand *et al*., 2017). Maximum Antarctic ice volume is thought to have been reached during the Oligocene-Miocene transition (OMT), ~23 Ma (Fig. 2.1a; Liebrand *et al*., 2017), driven by another period of low orbital variability lasting ~200 kyr (Zachos *et al*., 2001b) and continued pCO_2 decline (Beerling and Royer, 2011; Zhang *et al*., 2013). Subsequent long-term warming into the MMCO, ~17–15 Ma (Fig. 2.1a; Liebrand *et al*., 2017) led to a dynamic and variable EAIS (e.g., Zachos *et al*., 1992; Coxall *et al*., 2005), which is thought to have driven eustatic sea-level variations on the order of ~40 m (Miller *et al*., 2005). The ACC is thought to have occupied its deep modern-like path after the cessation of the MMCO, ~14 Ma, driving further

Antarctic cooling and ensuring the long-term stability of the EAIS (Lewis *et al*., 2007; Dalziel *et al*., 2013). Benthic $\delta^{18}O$ and Mg/Ca records demonstrate that continental ice-sheet growth and deep-sea cooling continued on and around Antarctica throughout the Miocene (e.g., Lear *et al*., 2000; Zachos *et al*., 2001a), with evidence for marine-grounding events in the Ross Sea off West Antarctica suggesting expansions of the marine-based WAIS continued to take place during cold periods of the late Miocene (Bart, 2003).

IRD from cores in the Fram Strait east of Greenland (Fig. 2.2) and off northeastern and southern Greenland indicate the potentially continuous existence of ice on the landmass, at least in the form of mountain glaciers, since the mid-Miocene (~18 Ma) or even earlier (Thiede *et al*., 2011). It is not until ~10 Myr later, however, that the true 'birth' of the GrIS is considered to have occurred; several Greenland-proximal ice-rafting records (site locations indicated in Fig. 2.2) suggest glaciation began to intensify on this landmass from ~8 Ma with occasionally marine-terminating glaciers. This suggestion is supported by the occurrence of dropstones and minor IRD in sediments from Baffin Bay Ocean Drilling Program (ODP) Site 645 and Labrador Basin ODP Site 646 with a mostly western Greenlandic origin (Korstgaard and Nielsen, 1989; Thiede *et al*., 2011), and a diamicton layer in Irminger Basin ODP Site 918 off the southeast coast of Greenland dated to ~7.3 Ma, which indicates advance of the ice-sheet to the proximal continental shelf-edge in this region (St John and Krissek, 2002). This event is contemporaneous with a significant fall in eustatic sea-level (Haq *et al*., 1988), cooling and increased ice volume in both hemispheres (Fronval and Jansen, 1996; Zachos *et al*., 2001a) and an increase in the equator-to-pole (meridional) SST gradient (Herbert *et al*., 2016).

2.1.3 Intensification of Northern Hemisphere glaciation in the Plio-Pleistocene

From the start of the Pliocene Epoch, 5.33 Ma, numerous records indicate several strong cold pulses lead to the establishment of widespread glaciation in the Northern Hemisphere. Another diamicton layer at Site 918 dated to ~4.8 Ma suggests significant GrIS expansion for the first time since the Miocene (Fig. 2.3c; St John and Krissek, 2002), and may correlate with both the first of a series of prograding offshore sedimentary wedges interpreted to represent past glaciogenic debris flows (GDFs; another indicator for shelf-edge glaciation) in the Davis Strait Drift Complex off southwest Greenland (Figs. 2.2 and 2.3e; Nielsen and Kuijpers, 2013), and a fall in eustatic sea-level (Haq *et al*., 1988). The age-models for the iNHG interval at Site 918 and Davis Strait are poorly-constrained, however, leading to uncertainty in the exact timing and correlation of these significant marine-terminating glaciations (St John and Krissek, 2002; Nielsen and Kuijpers, 2013).

Elevated pCO_2 (of ~400 ppmv) and temperatures 3–4 °C above present during the warmest intervals of the early to mid-Pliocene between ~4.5 and 3.3 Ma, as well as a weaker equator-to-pole temperature gradient (e.g., Raymo *et al*., 1996; Brierley *et al*., 2009; Haywood *et al*., 2009; Dowsett *et al*., 2010; Seki *et al*., 2010), resulted in reduced extents of both the WAIS (e.g., Pollard and DeConto, 2009; Naish *et al*., 2009) and continental ice in the Northern Hemisphere (e.g., Hill *et al*., 2010). This warmth was terminated ~3.3 Ma by a global cooling event known as Marine Isotope Stage (MIS) M2, represented by a significant positive excursion in the global benthic $\delta^{18}O$ record (Fig. 2.1b; Lisiecki and Raymo, 2005). A high-resolution sedimentary record from beneath the present-day Ross Ice Shelf recovered by the ANDRILL project indicates

significant WAIS and sea-ice expansion during MIS M2, followed by ongoing cooling and intensification of Antarctic glacial conditions through the late Pliocene (Naish *et al*., 2009; McKay *et al*., 2012; Riesselman and Dunbar, 2013). A number of studies evidence a coeval significant expansion of the GrIS at this time (Fig. 2.3), suggesting an early short-lived intensification of glacial conditions took place contemporaneously on both poles during MIS M2 (e.g., Thiede *et al*., 2011). At ODP Site 907 on the Iceland Plateau (Fig. 2.2), a major IRD pulse attributed to shelf-edge glaciation of (north)eastern Greenland is dated to ~3.3 Ma (Fig. 2.3b; Jansen *et al*., 2000). It is possible that the third-oldest IRD pulse recorded at Site 918 is also related to the same short-lived MIS M2 expansion (Fig. 2.3c; St John and Krissek, 2002). Contemporaneous IRD pulses to the Barents Sea appear in records from offshore Svalbard (Fig. 2.3d; Knies *et al*., 2014), along with intensified glacial inputs to Baffin Bay as evidenced by both IRD content (Srivastava *et al*., 1987) and clay mineral composition of marine sediments (Theibault *et al*., 1989), indicating simultaneous growth of continental-ice took place on other circum-Arctic landmasses at this time (Thiede *et al*., 2011).

MIS M2 was terminated by the mid-Piacenzian warm period (mPWP) 3.264–3.025 Ma (Dolan *et a*l., 2011), during which time subdued IRD deposition around Greenland is indicative of warmer conditions suppressing glaciation (e.g., Jansen and Sjøholm, 1991; Jansen *et al*., 2000; St John and Krissek, 2002; Larsen *et al*., 2006) (Fig. 2.3). Estimates of eustatic sea-level rise during the mPWP range widely from ~10–30 metres above present, with full GrIS loss implied (Raymo *et al*., 2018). Complete mPWP GrIS deglaciation remains to be confirmed by palaeodata, however, and some modelling studies suggest a relatively low sensitivity of GrIS volume to mPWP warmth (Hill *et al*., 2010) with substantial internal ice-sheet expansion still possible during its coldest intervals

(Dolan *et al*., 2011, 2015). Resumed cooling in the Northern Hemisphere from ~3 Ma is signalled by a kick-up in IRD both on the Iceland Plateau (Fig. 2.3b; Jansen *et al*., 2000) and in the Irminger Basin (Fig. 2.3c; St John and Krissek, 2002), as well as in the Labrador Basin (Wolf and Thiede, 1990) (Fig. 2.2). This reflects renewed glacial expansion to the coast in at least isolated areas, and corroborates the hypothesis that Greenland responded to climatic forcing earlier than other Northern Hemisphere landmasses (Jansen *et al*., 2000; Bailey *et al*., 2013).

In all available records from the Greenland-proximal marine realm spanning the iNHG interval (Fig. 2.3), the onset of major late Quaternary-style IRD peaks only occurs with a second significant cooling step at MIS G6 ~2.72 Ma (Jansen *et al*., 2000; Mudelsee and Raymo, 2005; Rohling *et al*., 2014) and a notable increase in the amplitude of benthic $\delta^{18}O$ cycles on orbital-obliquity timescales, signalling enhanced glacial cooling and continental-ice growth from this time (Maslin *et al*., 1998; Lisiecki and Raymo, 2005) (Fig. 2.1b). This major expansion again coincided with a significant fall in sea-level (Haq *et al*., 1988; Rohling *et al*., 2014), the deposition of a large diamicton package at Site 918 (Fig. 2.3c; St John and Krissek, 2002), a decline in sea-surface temperatures as measured by alkenones at North Atlantic ODP Site 982 (Fig. 2.2; Lawrence *et al*., 2009), and potentially the second-oldest GDF in Davis Strait (~2.5 Ma, Fig. 2.3e; Nielsen and Kuijpers, 2013). MIS G6 is therefore considered to signal the inception of a comparable-to-modern GrIS during cold stages, with frequently iceberg-calving margins along much of the coastline established by MIS 100, 2.52 Ma, as deduced by multiple Greenland-proximal and North Atlantic IRD records (Fig. 2.3; Korstgaard and Nielsen, 1989; Jansen and Sjøholm, 1991; Jansen *et al*., 2000; Knies *et al*., 2002, 2014; St John and Krissek, 2002; Thiede *et al*., 2011;

Bailey *et al*., 2012). A seismic transect crossing the central East Greenland margin, extending ~150 km southeast from Scoresby Sund (Fig. 2.2), also identifies a number of progradational glacimarine sequences indicating the central-eastern GrIS was frequently grounded below sea-level from ~2.6 Ma (Vanneste *et al*., 1995).

This evidence for a Greenland-led expansion of NHG has been corroborated by lead (Pb)-isotope provenance analysis of individual ice-rafted feldspars from central North Atlantic Deep Sea Drilling Project (DSDP) Site 611 (Fig. 2.2), which can be used to geochemically fingerprint IRD back to its distinct source region (e.g., Bailey *et al*., 2012, 2013; White *et al*., 2016). Areas of Earth's crust with distinct geologies, ages and tectonic/metamorphic histories, known as terranes, exhibit systematic differences in their range of Pb-isotope compositions, recorded by Pb-bearing minerals (in particular K-feldspar) that comprise the rocks in each region (e.g., Gwiazda *et al*., 1996; Connelly and Thrane, 2005; see also Chapter 3). These results, along with the temporal and spatial distribution of IRD deposition in ocean basins adjacent to the major Northern Hemisphere landmasses (e.g., Kleiven *et al*., 2002; Balco and Rovey, 2010), indicate a roughly contemporaneous onset of significant iceberg-calving ice-sheet margins on Greenland and Scandinavia at ~2.74–2.72 Ma, with the North American Laurentide Ice Sheet expanding to the coastline approximately 100 kyr later (Bailey *et al*., 2013). These reconstructions are corroborated by recent modelling efforts that simulate a modern-like GrIS during glacials from ~2.7 Ma, which persisted more continuously along with other Northern Hemisphere ice-sheets from MIS 100, ~2.5 Ma (Willeit *et al*., 2015). Despite the widespread expansion of continental-ice on the circum-Arctic landmasses at this time, the first true Pleistocene glacial sea-level lowstand may not have occurred until ~2.15 Ma

(Rohling *et al*., 2014). This indicates that Northern Hemisphere ice-sheets did not substantially build in thickness until ~0.5 Myr after extensive iceberg-calving margins were established (Rohling *et al*., 2014).

Following the onset of major iNHG, GrIS extents remained highly dynamic. In the Kap København Formation of northernmost Greenland (Fig. 2.2), a succession rich in fossil flora and fauna documents a temporary switch from Arctic to boreal conditions with estimated maximum interglacial summer temperatures of >10°C in North Greenland, tentatively dated to ~2.4 Ma (MIS 98–93; Fig. 2.3e), leads the argument for a reduced northern GrIS at this time (Letréguilly *et al*., 1991; Funder *et al*., 2001). A recent study of cosmogenic beryllium (^{10}Be) and aluminium (^{26}Al) radionuclide concentrations in bedrock recovered beneath the central GrIS during drilling of the GISP2 ice core (Fig. 2.2; Schaefer *et al*., 2016) may corroborate this likelihood, with the suggestion that Greenland was almost ice-free for extended periods during Pleistocene interglacials from ~2.6 Ma in one of its modelled scenarios (Fig. 2.3e). However, this is at odds with results of a similar study on ^{10}Be and ^{26}Al radionuclide contents of preglacial soils that concluded ice cover has been continuous on central Greenland since at least ~2.7 Ma (Fig. 2.3e; Bierman *et al*., 2014), and with records of sustained glacial outputs in the marine realm to the north (Thiede *et al*., 1998) and east (Jansen *et al*., 2000; Bierman *et al*., 2016) of Greenland throughout the NHG interval. Modelling studies for future equilibrium climate (e.g., Fyke *et al*., 2014) suggest local ice-caps may persist in highlands even if 95% of the GrIS were to disappear; more detailed studies into the timing and spatial extents of ice growth, even in the absence of marine-calving margins, are therefore required to test these deglaciation scenarios.

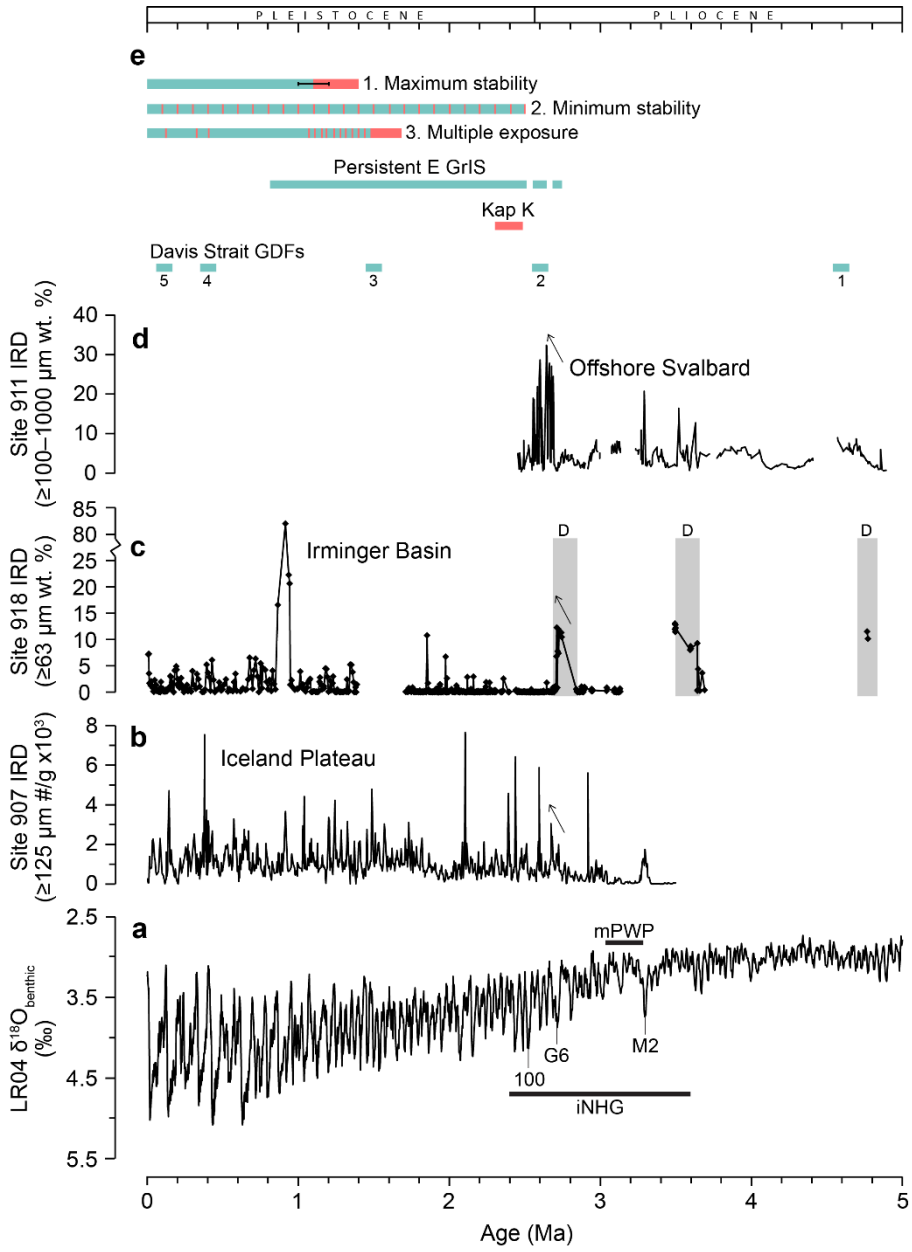

Figure 2.3 Synthesis of ice-rafting and other palaeoclimatic records (locations given in Fig. 2.2) relevant to the Plio-Pleistocene history of Greenland Ice Sheet (GrIS) evolution, alongside (**a**) the LR04 $\delta^{18}O_{benthic}$ stack for reference of climate state (Lisiecki and Raymo, 2005); (**b**) Iceland Basin ODP Site 907 IRD (Jansen *et al*., 2000); (**c**) Irminger Basin ODP Site 918 IRD (diamicton 'D' layers indicated by grey boxes; St John and Krissek, 2002); and (**d**) Yermak Plateau (offshore Svalbard) ODP Site 911 IRD (Knies *et al*., 2014). Panel (**e**) is a summary of other palaeoclimatic reconstructions for the GrIS (from bottom to top of panel): occurrences of glaciogenic debris flows (GDFs) identified in the Davis Strait Drift Complex off southwest Greenland reflecting shelf-edge glaciations (Nielsen and Kuijpers, 2013); approximate age of the Kap København warm-affinity faunal deposit in northernmost Greenland (Funder *et al*., 2001); periods of eastern GrIS growth and stability inferred from seismic profiles (Vanneste *et al*., 1995) and from cosmogenic beryllium (^{10}Be) and aluminium (^{26}Al) isotopes in marine cores (Bierman *et al*., 2016) offshore eastern Greenland, indicating frequent grounding of the eastern (E) GrIS below sea-level from ~2.6 Ma; and three scenarios for central (C) GrIS glaciation consistent with ^{10}Be and ^{26}Al isotopes in bedrock from the base of the GISP2 ice core (1. Maximum stability scenario = 280 ±30 kyr ice-free conditions followed by 1.1 Ma continuous ice cover, 2. Minimum stability scenario = ice-free for 8 kyr of each 100-kyr cycle, 3. Multiple exposure scenario = ice-free for several thousand years during numerous major Pleistocene interglacials; Schaefer *et al*., 2016). Labels in (a) are Marine Isotope Stages, and durations of the intensification of Northern Hemisphere glaciation (iNHG; Mudelsee and Raymo, 2005) and the mid-Piacenzian warm period (mPWP; Dolan *et al*., 2011) are also indicated.

2.1.4 GrIS history over the past ~1 million years

Northern Hemisphere ice-sheet volume has fluctuated substantially since the mid-Pleistocene transition (MPT) ~1.25–0.70 Ma, a major perturbation in Earth's climate system characterised by a switch in climate pacing from a 41-kyr obliquity cycle to a 100-kyr eccentricity-like cycle (Pisias and Moore, 1961; Lisiecki and Raymo, 2007). This most recent major climatic transition in Earth's history is thought to have been driven by global ice-volume crossing a critical threshold, initiating the more extreme glacial-interglacial cycles characteristic of the late Pleistocene, which the prevailing theories attribute either to extensive global ice-sheets responding to and internally amplifying insolation changes (e.g., Imbrie *et al*., 1993, Huybers, 2006; Lisiecki and Raymo, 2007), or to an increased threshold for deglaciation forcing glacial climates to 'skip over' some insolation peaks (Tzedakis *et al*., 2017). Relatively speaking, our knowledge of GrIS history over the past ~1 Myr is fragmentary and poorly-constrained prior to the Last Glacial Maximum (LGM, ~26.5 thousand years ago, ka), and what we do know is skewed towards our understanding of the behaviour of the southern GrIS during interglacials of the past ~400 kyr. MIS 11 (~400 ka) and MIS 5e (or the Eemian, ~125 ka) are the most widely-studied late Pleistocene interglacials in making inferences of ice-loss from Greenland because they were globally warmer than present (e.g., Otto-Bleisner *et al*., 2006), and are widely reconstructed to have been associated with sea-levels appreciably higher than present (e.g., Cuffey and Marshall, 2000).

A number of studies have taken advantage of the fact changes in the pollen content (recording changes in local vegetation) and geochemical, isotopic and magnetic properties of the terrigenous fraction (recording changes in the flux and/or source of subglacially-eroded sediment) of marine cores recovered from

Eirik Drift (Fig. 2.4a) and other southern Greenland-proximal locations can be used to track southern GrIS retreat during late Pleistocene interglacials. For example, increases in pollen abundance and changes in their assemblage recorded at ODP Sites 646 and 647 on/near Eirik Drift and in the base of the Dye-3 ice core (Fig. 2.2) indicate that significant reductions in southern GrIS extent enabled the growth of shrub-tundra-type vegetation in the region during MIS 11 and 5e (Willerslev *et al*., 2007; De Vernal and Hillaire-Marcel, 2008). Eirik Drift deposits also contain high abundances of terrigenous sediments glacially eroded on southern Greenland and transported to the adjacent marine realm, via both icebergs calved from outlet glaciers transported in the East Greenland Current (EGC) and the deep Western Boundary Undercurrent (WBUC) (Fig. 2.4a) (e.g., Bigg *et al*., 1996; Hunter *et al*., 2007; White *et al*., 2016). Recent efforts to classify the geochemical, isotopic and magnetic properties of glacially-eroded material from distinct Greenland source regions (summarised in Fig. 2.4) have made it possible to identify and discriminate spatial variations in fluxes of Precambrian southern Greenland-sourced material to surrounding ocean basins during intervals of the late Pleistocene. For example, the strontium-neodymium-lead (Sr-Nd-Pb) isotopic composition of the subglacially-eroded silt-size fraction of Eirik Drift sediments (Colville *et al*., 2011; Reyes *et al*., 2014) has been successfully used to interpret a reduction in terrigenous deposition from the southern Precambrian terranes during late Pleistocene interglacials. These studies demonstrate the potential collapse of the southern GrIS (and perhaps its minimum extent since the onset of major NHG) during MIS 11 (Reyes *et al*., 2014), and that mass loss from the southern GrIS contributed significantly to the ~4–6 m MIS 5e sea-level highstand relative to today (Otto-Bleisner *et al*., 2006; Carlson *et al*. 2008). By contrast, MIS 6 (~180–130 ka), a significantly cold ice

age represented by the youngest GDF in the Davis Strait seismic record (Nielsen and Kuijpers, 2013), may mark the time the GrIS reached its maximum extent; reconstructions based on both on- and offshore sedimentological evidence indicate the ice-sheet was over 1 km deep at this time in parts of East Greenland that are currently ice-free (Funder *et al*., 1998).

The geology of Greenland is summarised in Fig. 2.4a. The majority of the Greenland landmass comprises ancient Precambrian shield, a felsic crystalline basement of gneisses and granites, which acted as a stable block onto which younger sedimentary units continued to accrete throughout the Paleozoic (Escher and Watt, 1976). The Precambrian shield is subdivided into geochemical 'terranes' based on regional differences in geology, formation age and tectonic history (in approximate order of oldest to youngest): the Archaean Block (AB), the Nagssugtoqidian Mobile Belt (NMB) and the Ketilidian Mobile Belt (KMB) (Escher and Watt, 1976; Hansen and Friderichsen, 1989) (Fig. 2.4a). The youngest rocks are in East Greenland, where deformation associated with the Caledonian Orogeny (~390–490 Ma) created the East Caledonide (EC) terrane in the region of Scoresby Sund (Fig. 2.4a) (Escher and Watt, 1976; Gilotti *et al*., 2008; Kalsbeek *et al*., 2008). Immediately south of the EC and Scoresby Sund, and discontinuously across central Greenland to the west coast, are Palaeogene basalts resulting from magmatic activity associated with the opening of the North Atlantic Ocean (~60–50 Ma) (Escher and Watt, 1976; Storey *et al*., 2007) (Fig. 2.4a). Systematic differences in the magnetic character of sediments originating from different regions of Greenland and Iceland (Fig. 2.4b) (Hatfield *et al*., 2013; 2017) have been successfully used to demonstrate that, following maximum GrIS extents in MIS 6, an increase in the bulk magnetic grain-size of sediments deposited on Eirik Drift reflects destabilisation of the ice mass on southern

Greenland as Earth's climate warmed into the Eemian (MIS 5e, ~125 ka; Stoner *et al*., 1995). Magnetic properties of Eirik Drift sediments and their interpretation are discussed in more detail in Chapter 3 Section 3.3, and form the basis for data and interpretations presented in Chapter 4.

Elemental XRF analysis of sediments from Eirik Drift (Carlson *et al*., 2008), as well as the Gardar (Grützner and Higgins, 2010) and Faeroe (Hodell *et al*., 2010) drifts also formed by Nordic Seas overflow waters, have also proven useful in tracking the delivery and provenance of glaciofluvial sediment to the subpolar North Atlantic in the late Pleistocene. Increased concentrations of the terrestrial elements Ti and Fe in Eirik Drift sediments, tracking overall terrigenous delivery, are interpreted to reflect enhanced sediment outflow and iceberg discharge from the proximal southern GrIS in MIS 5e (Carlson *et al*., 2008). XRF and its applications in these settings are discussed in more depth in Chapter 3 Section 3.4, and form the basis for the data and interpretations presented in Chapter 5.

Recent isotopic characterisation and dating of sand-sized mineral grains from Greenland glaciofluvial sediments at source, along with those from core-top (Holocene to modern) sediments in adjacent marine cores, has also shown that the Pb-isotope composition of individual feldspars and the argon-argon ($^{40}Ar/^{39}Ar$) ages of hornblendes can be used to track iceberg-calving sources from Greenland to the proximal marine realm, due to systematic differences in the ages and metamorphic histories of distinct regions (Fig. 2.4c; White *et al*., 2016). Feldspars eroded within glacier catchments occupying each Greenlandic terrane have distinct Pb-isotope values (Fig. 2.4c), which has enabled the identification of iceberg-calving sources to Eirik Drift, as well as Sites 907 and 918, during the modern to Holocene (White *et al*., 2016). The Pb-isotope provenance of individual feldspars deposited at North Atlantic Site 611 (Fig. 2.2) also indicates renewed

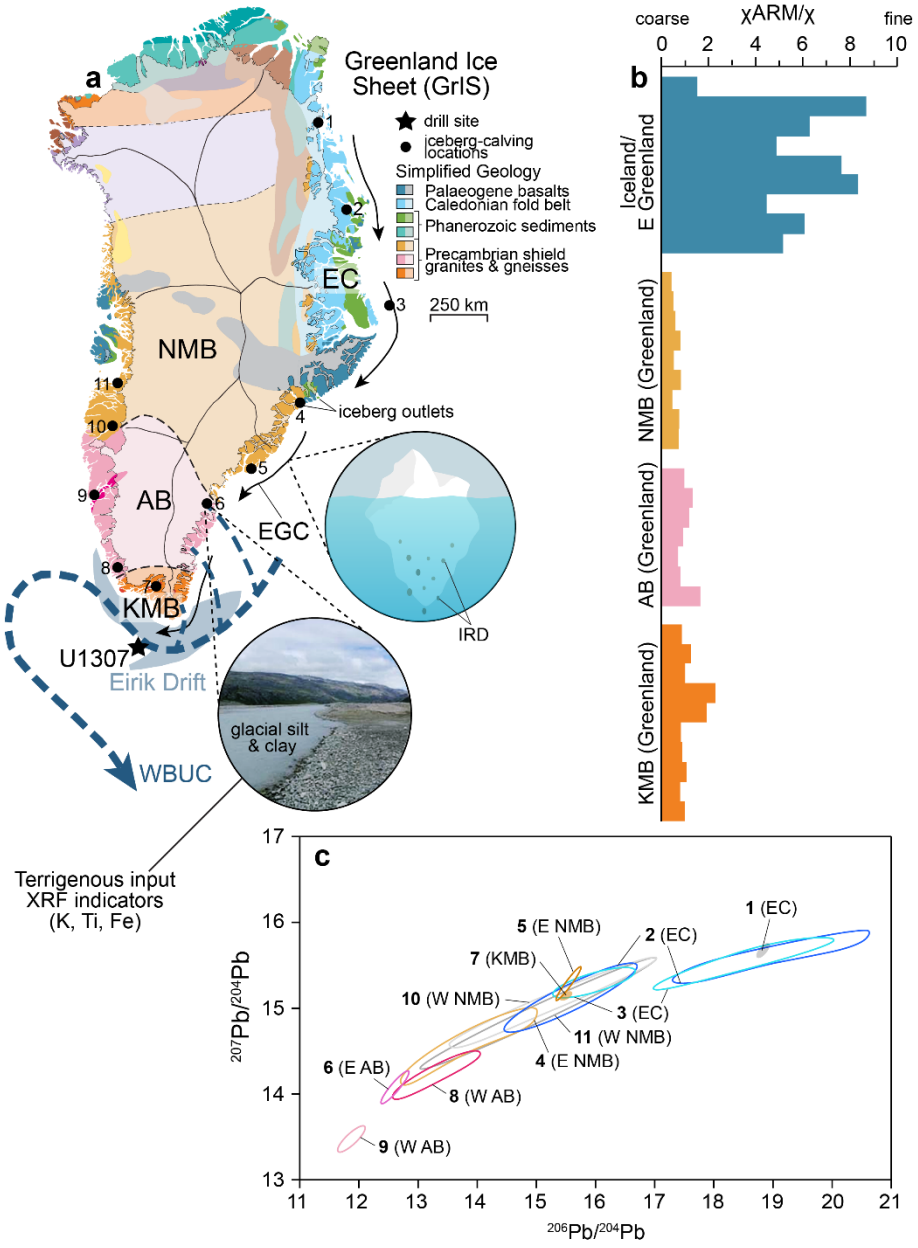

Figure 2.4 Summary of Greenland geochemical terranes and their magnetic and isotopic properties: (**a**) Geological map of Greenland with geochemical terranes labelled (NMB = Nagssugtoqidian Mobile Belt, AB = Archaean Block, KMB = Ketilidian Mobile Belt, EC = East Caledonides), and modern-day paths of the East Greenland Current (EGC) transporting ice-rafted debris (IRD)-laden icebergs and the Western Boundary Undercurrent (WBUC) transporting subglacially-eroded silt and clay, and the location of IODP Site U1307 (the focus of this thesis) on Eirik Drift, also indicated (modified from White *et al*., 2016); (**b**) histograms of bulk magnetic grain size (χARM/χ; higher/lower values = finer/coarser magnetic grains) of terrestrial sediment samples from Iceland and the three southern Greenland terranes (modified from Hatfield *et al*., 2013); and (**c**) the Pb-isotope composition ($^{206}Pb/^{204}Pb$ vs. $^{207}Pb/^{204}Pb$) of individual sand-sized (>150 μm) feldspars in glaciofluvial and fjord sediments from localities around the Greenland coastline as indicated by matching numbers in (a) (modified from White *et al*., 2016).

ice-rafting to the sub-polar North Atlantic from Greenland and other landmasses during the LGM, (Bailey *et al*., 2012), thought to represent the last time substantial ice-sheets occupied much of the Northern Hemisphere terrestrial realm. This

technique is discussed in more detail in Chapter 3 Section 3.6, and forms the basis for data and interpretations presented in Chapter 6.

During the early Holocene (MIS 1), ~12 ka, elevated boreal summer insolation relative to the present gave rise to the warm global temperatures of the Holocene thermal maximum, the timing of which varied across the Northern Hemisphere (e.g., Kaufman *et al*., 2004; Carlson *et al*., 2008; Marcott *et al*., 2013). Radiocarbon dating of biological material and relative sea-level histories from currently ice-free regions (e.g., Bennike and Björck, 2002; Tarasov and Peltier, 2002) reveal that this most recent extended period of Northern Hemisphere warmth led to dramatic reductions in GrIS extent. Recent ^{10}Be radionuclide analysis of surface exposures from around the western and southern GrIS margins (Carlson *et al*., 2014) indicate that this early Holocene retreat occurred much earlier in southern Greenland (~11.1–10.6 ka) relative to in west and southwest regions (~7.9–6.8 ka). Fining of the magnetic grain-size of sediments deposited on the Rockall Trough south of Iceland between ~12–8 ka has also been used to infer the reduced influence of terrestrial detrital sources at this time due to rising eustatic sea-levels, as well as the reorganisation of bottom-water circulation (Channell *et al*., 2016).

Renewed boreal summer cooling drove GrIS margin advance to its late Holocene maximum extents (Carlson *et al*., 2014). Since then, both natural and anthropogenic-enhanced warming following the Industrial Revolution (1760–1840 AD) has resulted in the ongoing reduction of NHG (Alley *et al*., 2010), leaving Greenland home to the only remaining ice-sheet in the Northern Hemisphere today. Summer warming of at least ~1°C in southern and western Greenland over the last century (Hanna *et al*., 2009) has seen GrIS margins retreat significantly from their late Holocene maximum extents (e.g., van den

Broeke *et al*., 2009; Kelley *et al*., 2012; Bjørk *et al*., 2012), with their current position suggesting southern Greenland may have now warmed to, or even above, summer temperatures typical of the early Holocene (Carlson *et al*., 2014).

In summary, a wide range of sedimentological and geochemical techniques have been applied in Greenland-proximal marine settings, particularly Eirik Drift, to elucidate past extents and behaviour of the southern GrIS under changing global climates. Yet, despite their success reconstructing relatively recent GrIS history in detail, these methods have yet to be widely applied to deeper time.

2.2 Proposed Causes of Northern Hemisphere Glaciation

The causes of iNHG are hotly debated, but most studies agree that high-latitude cooling and an increase in the meridional SST gradient from prior to the late Pliocene were both critical factors in establishing widespread Northern Hemisphere continental ice-sheets (e.g., Lunt *et al*., 2008a; De Schepper *et al*., 2009; Brierley and Fedorov, 2010; Naafs *et al*., 2010). Outlined below is a review of the factors, acting on various timescales, relevant to this thesis, that have been implicated as a forcing agent of, or positive feedback in, widespread glaciation of Greenland and other Northern Hemisphere landmasses during the late Cenozoic.

2.2.1 Long-term preconditioning factors

The long-term Cenozoic cooling trend is generally implicated in driving the growth of continental-ice in both hemispheres (e.g., Zachos *et al*., 2001, 2008; DeConto et al., 2008; Alley *et al*., 2010). A number of specific long-term tectonic factors have nevertheless also been cited as important in preconditioning Greenland and the wider Northern Hemisphere for glaciation. Three acting over the past ~60 Ma

relate to the latitudinal position and elevation of the Greenland landmass itself: 1) northward motion of Greenland relative to the mantle (equivalent to a ~6° latitude increase); 2) poleward rotation of the mantle and crust (equivalent to a ~12° latitude increase); and 3) a series of mantle plume pulses, beginning with the emplacement of the NAIP and continuing with transient Iceland plume activity up to ~5 Ma, accelerating regional uplift and elevating parts of East Greenland to over 3 km above sea-level (Steinberger *et al*., 2015). These factors would have helped precondition Greenland for glaciation by bringing the landmass to more northerly, colder latitudes and creating higher elevations in eastern and southern regions, where the GrIS was able to nucleate during times of low insolation (Steinberger *et al*., 2015). Periodic temporary uplift associated with Iceland plume activity since the early Cenozoic may be implicated in this way for helping to drive the inferred short-lived glaciations of Greenland in the Eocene, and later during the Miocene and Pliocene (e.g., Japsen and Chalmers, 2000; Storey *et al*., 2007).

At the broadest level, it is widely accepted that evidence for a secular decline in pCO_2 is coupled to the long-term Cenozoic cooling trend (e.g., Zachos *et al*., 2008), since a direct relationship between global temperature and atmospheric CO_2 concentrations is well-known from studies of the 140 kyr-long high-resolution Vostok ice core record (e.g., Petit *et al*., 1999; Shakun *et al*., 2012). There is also a generally good correspondence between pCO_2 and the occurrence of icehouse/greenhouse states over the past ~420 Myr of Earth's history (Foster *et al*., 2017). Over multi-million-year timescales, pCO_2 is primarily controlled by the balance between inputs from volcanic activity, metamorphism and weathering of organic carbon, and outputs from chemical weathering of silicate rocks exposed at Earth's surface and burial of organic carbon (e.g., Walker *et al*., 1981; Raymo and Ruddiman, 1992; Foster *et al*., 2017). Studies

modelling the sensitivity of ice-sheet budgets to pCO_2 indicate that minimum thresholds of ~280 ppmv in the Northern Hemisphere and ~750 ppmv in the Southern Hemisphere must be crossed to enable significant growth of continental ice-sheets under favourable cold orbital conditions (DeConto *et al*., 2008; Lunt *et al*., 2008a). The boron isotopic composition of glassy planktic foraminifera from the mid-Eocene record an approximate halving of pCO_2 following the EECO, from ~1400 parts per million by volume (ppmv) to ~650 ppmv by ~40 Ma (Anagnostou *et al*., 2016). Reorganised Siberian drainage patterns following the collision of the India subcontinent into the Eurasian plate are thought to have led to the creation of a 'brackish water lid' over the Arctic Ocean at this time, favouring seasonal sea-ice formation (Clementz *et al*., 2011; Thiede *et al*., 2011).

Since the mid-Cenozoic, mid-latitude tectonic uplift and plateau formation in Central Asia (the Himalaya and Tibetan Plateau) and North America (the Rocky Mountains) are implicated in helping to precondition the high northern latitudes for glaciation via continued pCO_2 drawdown and other mechanisms (e.g., Ruddiman and Raymo, 1988; Ruddiman and Kutzbach, 1989; Raymo and Ruddiman, 1992; Garzione, 2008; Foster *et al*., 2010). The proposed cooling mechanisms are as follows: 1) increased elevations promoting ice-growth in these temperate regions, giving rise to longer winters and enhanced albedo effect (Birchfield and Weertman, 1983); 2) perturbation of atmospheric masses by elevated regions leading to different circulation patterns (Kutzbach *et al*., 1989; Ruddiman and Kutzbach, 1989); and 3) enhanced chemical weathering due to increased exposure of silicate minerals at the Earth's surface, a process by which CO_2 is removed from the atmosphere (Raymo *et al*., 1988). The formation of the Tibetan Plateau at ~40 Myr (Wang *et al*., 2008) is particularly implicated in driving pCO_2 drawdown since the mid-Eocene (Raymo and Ruddiman, 1992). During the

present day this broad, high region of elevation is known to enhance the regional monsoon circulation, so could perturb circulation patterns on a hemispheric level (Garzione, 2008). Experiments run using general circulation models (GCMs) to isolate the effect of Tibetan Plateau uplift on climate simulate the basic direction of many observed changes in the Cenozoic geological record on shorter timescales, particularly winter cooling of the Arctic and Northern Hemisphere continents, due to plateau-ocean temperature gradients driving increased orographic diversion of westerly winds and intensified vertical atmospheric circulation (Ruddiman and Kutzbach, 1989; Kutzbach *et al*., 1989). Long-term chemical weathering of exposed silicate rocks is the main mechanism cited to explain the role of Tibetan Plateau uplift in forcing late Cenozoic climate on longer timescales, however (Raymo and Ruddiman, 1992). Late Miocene uplift of the Rocky Mountains is also specifically implicated in the glaciation of North America (Foster *et al*., 2010); in the present day, this extensive region of high orography along the western North American coast forms a barrier to westerly atmospheric circulation, deflecting warm and moisturous (Banks, 2018) jet-stream air masses to maintain a cool polar winter climate over northeastern North America (e.g., Seager *et al*., 2002). Sensitivity modelling indicates a significant response of North American glaciation to Rocky Mountain uplift in the late Miocene, argued to have helped enhance NHG through ice-albedo feedbacks (Foster *et al*., 2010). Previous simulations using a fully-coupled atmosphere-ocean GCM together with an ice-sheet model corroborate this proposed local cooling effect on North America during the winter, and also found that in summer this signal is deflected over much of Canada and Greenland; however, this results in a generally drier climate over Greenland (Lunt *et al*., 2008a).

It must be noted that some evidence used to infer enhanced uplift in these regions over the past ~10–2 Ma – including incised stream beds, changes to colder-affinity flora and enhanced sedimentation around mountain ranges and their offshore drainage areas – may actually themselves be a mere product of late Cenozoic cooling and increased associated storminess, implying that inferred recent uplift in some areas, and thus its role in forcing Northern Hemisphere glaciation, may be exaggerated (Molnar and England, 1990). Even assuming the inferred amount of uplift, however, experiments modelling the effects of elevated regions on Northern Hemisphere climate as a whole only simulate a modest cooling and ice-growth response (Ruddiman and Kutzbach, 1989; Lunt *et al*., 2008a).

Additional factors acting on shorter timescales in the lead-up to iNHG hence require investigation to explain a decrease in summer ablation substantial enough to enable the build-up of large continental Northern Hemisphere ice-sheets in the Plio-Pleistocene (Raymo and Ruddiman, 1992).

2.2.2 Cessation of ‘permanent El Niño conditions’

Several authors have put forward the hypothesis that ‘permanent El Niño conditions’ – also known as ‘El Padre’ – prevailed in the early Pliocene equatorial Pacific Ocean between ~5–3 Ma (Fig. 2.6a), and that this may not only provide an explanation for sustained global warmth and muted glacial-interglacial cycle amplitude through this period, but also the onset of widespread glaciation upon the termination of this climate state (e.g., Philander and Fedorov, 2003; Ravelo *et al*., 2004; Wara *et al*., 2005; Lawrence *et al*., 2006; Fedorov *et al*., 2006). During the present day, the low-latitude Pacific Ocean is a key driver of global climate as it provides a large portion of atmospheric latent heat (Cane, 1998). An

average temperature gradient of ~6°C between the western equatorial Pacific (WEP; ~29°C) and eastern equatorial Pacific (EEP; ~23°C) (Levitus and Boyer, 1994) drives Walker cell circulation, with warm air rising in the west and sinking in the east (Wara *et al*., 2005). The trade winds associated with this circulation are in turn responsible for driving surface ocean currents westward and enabling colder, nutrient-rich waters originating at higher latitudes to upwell in the EEP (Philander and Fedorov, 2003; Sarmiento *et al*., 2004). This results in the presence of a thick warm mixed layer in the WEP and much thinner equivalent in the EEP, and thus an asymmetrical vertical thermocline across the equatorial Pacific (Wara *et al*., 2005; Lawrence *et al*., 2006). This 'usual' state of a ventilated thermocline and strong W–E temperature gradient is disrupted every ~2–7 years when the EEP upwelling region warms, significantly reducing this gradient and weakening the Walker circulation, which in turn alters global heat distribution and the intensity and position of high/low pressure centres in the subtropics (Wara *et al*., 2005). These short-term collapses of the equatorial Pacific W–E gradient, resulting in a more symmetrical thermocline, are known as El Niño events (Wara *et al*., 2005). El Niño events can have a significant effect on climate patterns around the globe, with a strong correlation observed between modern tropical Pacific SSTs, heat transport to the subtropics and regional hydrological impacts (Fedorov *et al*., 2006; McPhadden *et al*., 2006). Indeed, the global expression of Pliocene warmth as deduced from geological proxy records appears to resemble the teleconnection pattern that occurs during El Niño events (Molnar and Cane, 2002).

During the warm early to mid-Pliocene, Mg/Ca-, alkenone- and $\delta^{18}O$-based SST reconstructions between sites in the WEP and EEP indicate a much-reduced temperature gradient of ~1.5 (±0.9)°C prevailed across the equatorial

Pacific (Ravelo *et al*., 2004; Ravelo and Wara, 2004; Wara *et al*., 2005; Haywood *et al*., 2005; Lawrence *et al*., 2006). This state is very similar to during modern El Niño events, with minimal latitudinal heat transfer and a deep, more symmetrical thermocline, but persisted for around 2 Myr between ~5 and 3 Ma (Wara *et al*., 2005; Fedorov *et al*., 2006). Model simulations suggest this 'El Padre' climate state could have contributed to overall Pliocene warmth by reducing the coverage of stratus clouds and thus the albedo effect, as well as increasing the partial pressure of water vapour in the atmosphere (pH_2O) and hence the natural greenhouse effect (Berreiro *et al*., 2006). A positive feedback between more frequent, stronger hurricanes and their ability to heat and vigorously mix the upper central Pacific Ocean may also have been key to maintaining warm conditions, reducing poleward heat transport and in turn causing more hurricanes (Fedorov *et al*., 2010). The warmer, deeper thermocline may also have reduced glacial-interglacial variability by dampening the ocean-atmosphere feedbacks required to amplify small changes in orbital forcing via atmospheric circulation (Wara *et al*., 2005).

From ~3.5 Ma, the thermocline began to shoal and cool (Wara *et al*., 2005) and the amplitude of glacial-interglacial cycles with clear 41-kyr frequency began to increase as reflected in the global benthic foraminiferal $\delta^{18}O$ stack (Fig. 2.6c; Lisiecki and Raymo, 2005; Ravelo *et al*., 2006). This onset of intensified glacial conditions marked the end of 'El Padre' (Philander and Fedorov, 2003; Fedorov *et al*., 2006), as the thermocline shoaled with cooling of the surface and deep ocean and ventilated connections between the high and low latitudes were re-established, with a similar-to-modern W-E temperature gradient of ~4°C established by ~1.6 Ma (Lear *et al*., 2000; Ravelo et al., 2004; Wara *et al*., 2005). This gradual shoaling of the global thermocline must have involved changes in

the oceanic heat budget and transport, indicating a threshold was crossed at this time that enabled trade winds to bring cold water to upwelling zones (Philander and Fedorov, 2003; Fedorov *et al*., 2006). This in turn is hypothesised to have introduced ocean-atmosphere feedbacks, which amplified 41-kyr obliquity cycles and in turn ice-albedo effects at high-latitudes via enhanced northward moisture transport (Fedorov *et al*., 2006). As SSTs declined in the EEP at the cessation of 'El Padre', productivity increased, with clear modulation of these tightly-coupled records by high-latitude changes in obliquity (Philander and Fedorov, 2003; Lawrence *et al*., 2006). The extent of this increase in productivity suggests an additional control by nutrient availability of the source waters (Lawrence *et al*., 2006). In the modern ocean, cold nutrient-rich waters upwelling in the EEP are originally derived from sinking water masses in the high latitudes of the North Pacific and Southern Ocean (Philander and Fedorov, 2003; Sarmiento *et al*., 2004), with a greater contribution from the latter (Toggweiler *et al*., 1991). Evidence for polar stratification driving productivity crashes in both the Southern Ocean and North Pacific is synchronous with the abrupt increase in EEP productivity and the start of iNHG (Haug *et al*., 1999; Sigman *et al*., 2004). This suggests that an excess of nutrients in waters sourced from these regions, due to intensifying glacial conditions at high latitudes, drove greater productivity where they upwelled at lower latitudes (Lawrence *et al*., 2006). A strong 41-kyr orbital pacing in the sea-surface salinity (SSS) gradient at EEP ODP Site 849 between ~2.75 and 2.4 Ma, not present in the SST record, may reflect glacial southward and interglacial northward oscillations in the position of the Intertropical Convergence Zone (ITCZ), caused by altered Hadley circulation driven by waxing and waning Northern Hemisphere ice-sheets (Chiang and Bitz, 2005; Jakob *et al*. 2017).

In summary, the termination of 'El Padre' itself may not have been a driver of iNHG, but rather a knock-on effect of already intensifying glacial conditions at high latitudes, so may only have helped to amplify orbital insolation changes via ocean-atmosphere feedbacks from ~3 Ma. Sensitivity tests using a coupled atmosphere-ocean model indicate that the 'El Padre' state would only have increased mid-Pliocene average global mean surface temperatures by ~0.6 °C (Haywood *et al*., 2007), and subsequent modelling has suggested summer temperatures over Greenland were relatively unchanged despite a slight precipitation increase in southeastern regions (Lunt *et al*., 2008a). The contribution of 'El Padre' to iNHG upon its termination is therefore unlikely to have been significant (Haywood *et al*., 2007).

2.2.3 Tectonic seaway closure

The role of seaway closure in the onset of Quaternary-style climates has been hotly debated in recent decades. Tectonic closure of the Indonesian Seaway ~5–3 Ma is argued to have played a role in iNHG by switching the source of waters flowing through Indonesia from the warm South Pacific to the relatively cold North Pacific, reducing atmospheric heat transport from the tropics to high latitudes via restricting the warm Agulhas leakage into the Atlantic Ocean (Fig. 2.5) (Cane and Molnar, 2001; McKay *et al*., 2012). However, this may have merely exacerbated already-dampened interhemispheric heat transport associated with expanding Antarctic ice-sheets (McKay *et al*., 2012).

Several authors have argued for linkages between the stepwise inception of NHG and the closure state of the Central American Seaway (CAS), implicating alterations to ocean circulation and precipitation patterns (e.g., Keigwin, 1982; Haug and Tiedemann, 1998; Driscoll and Haug, 1998; Bartoli *et al*., 2005;

Sarnthein *et al*., 2009; De Schepper *et al*., 2013). This theory is also known as the 'Panama Hypothesis', due to the resultant emergence of the Isthmus of Panama that today connects the North and South American continents (Fig. 2.5). Regional collision between the Cocos and Caribbean tectonic plates is thought to have driven the formation of the Isthmus of Panama and limited deepwater exchange between the Pacific and Caribbean since at least the late Miocene (Montes *et al*., 2012, 2015), which was restricted further by falling eustatic sea-level since the early Pliocene, ~3.6 Ma (Haug and Tiedemann, 1998). It is hence difficult to establish a clear chronology for CAS closure (e.g., Molnar, 2008). Evidence for multi-phase closure of the CAS during the Plio-Pleistocene comes mainly from reconstructions of SST and SSS differences between the Caribbean and North Pacific basins either side of the Isthmus of Panama, which are inferred to indicate 'reversible' shoaling events occurred ~3.75 and ~3.5–3.3 Ma with a more significant event at ~3.16 Ma, and a proposed 'final closure' in two steps between ~2.95 and 2.5 Ma (Fig. 2.6e; Sarnthein *et al*., 2009). Modelling studies have linked an open CAS to weakened Atlantic Meridional Overturning Circulation (AMOC) and hence northward heat and moisture transport to high latitudes, and vice versa when the seaway is closed (Lunt *et al*., 2008a; Klocker *et al*., 2005). However, authors interpret the link of CAS closure to iNHG differently depending upon the feedback mechanisms invoked to explain the build-up of large Northern Hemisphere ice-sheets.

Around 3.6 Ma, throughflow from the East Pacific to the Caribbean Basin appears to have been minimal, which is hypothesised to have resulted in maximum AMOC strength at this time and elevated temperatures in the high-latitude North Atlantic (De Schepper *et al*., 2013). This was followed by a rise in eustatic sea-level (Miller *et al*., 2005) enabling the re-entry of cold nutrient-rich

Pacific water into the Caribbean, as inferred from records of SST and SSS (De Schepper et al., 2013) and evidence for poor ventilation and carbonate dissolution (Haug and Tiedemann, 1998). Coeval ~3–4 °C cooling of North Atlantic surface waters measured at DSDP Sites 603 and 610 and IODP Sites U1308 and U1313 (Fig. 2.5) suggest a major weakening and southward shift of the warm North Atlantic Current (NAC; Figs. 2.2, 2.5), the northern arm of the Gulf Stream, which is thought to have established a steep latitudinal SST gradient in the North Atlantic immediately prior to MIS M2 at ~3.32 Ma (De Schepper *et al*., 2013). This is hypothesised to have reduced air temperature and increased snowfall over the northern landmasses, both key factors favouring large-scale glacial inception (Brierley and Fedorov, 2010). This unique series of events, along with favourable orbital conditions and perhaps a short-lived reduction in pCO_2 (Tan *et al*., 2017) is thought to have thermally isolated the Greenland landmass, enabling the first major GrIS expansion during MIS M2 (~3.3 Ma) despite the overall relative warmth and high pCO_2 of the mid-Pliocene (De Schepper *et al*., 2013).

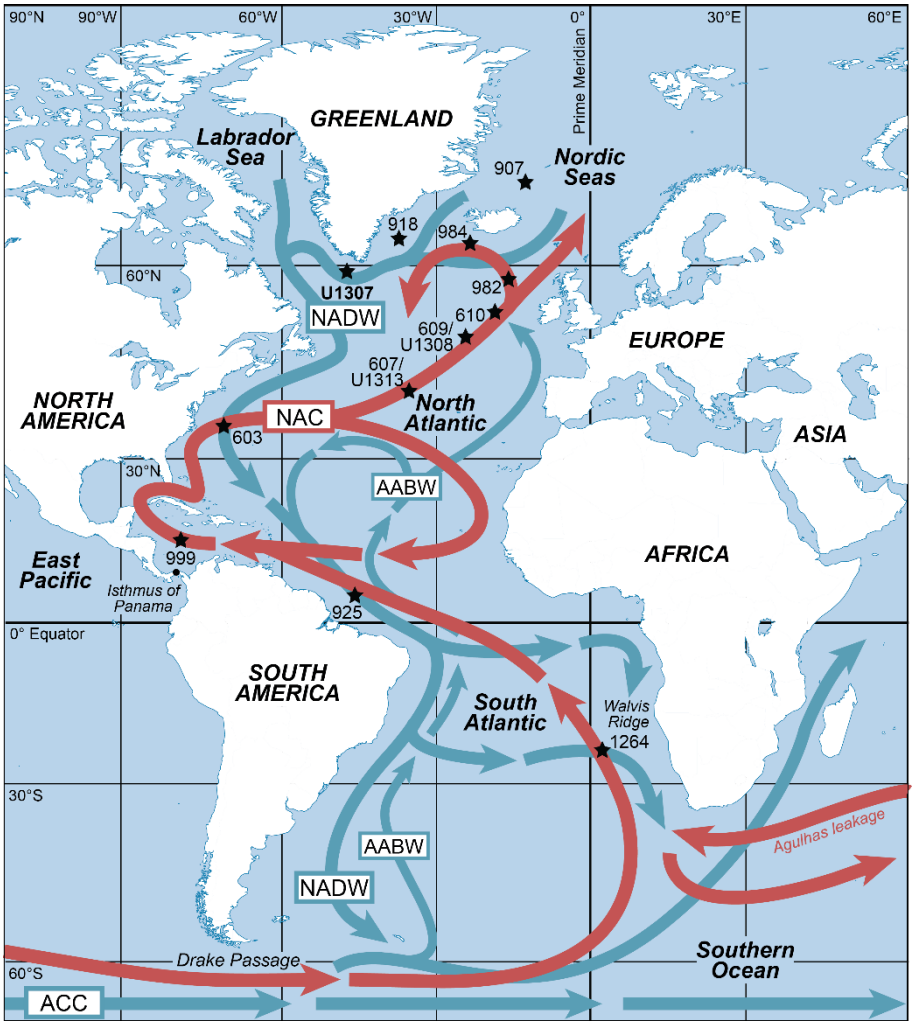

Figure 2.5 Map of the Atlantic Ocean and surrounding continents showing the location of IODP Site U1307 (the focus of this thesis), the position of Atlantic ODP/DSDP/IODP drill sites mentioned in the text, and their relationships to the paths of key modern cold deep (blue) and warm surface (red) ocean currents relevant to this study (adapted from Langton *et al*., 2016 and Praetorius, 2018). NAC = North Atlantic Current, NADW = North Atlantic Deep Water, ACC = Antarctic Circumpolar Current, AABW = Antarctic Bottom Water. Also labelled are key localities mentioned in the text. Base map courtesy of comersis.com.

The short-lived nature of MIS M2 has been proposed to be the result of a consequent negative-feedback loop; as eustatic sea-level fell following continental-ice expansion (Miller *et al*., 2005), the CAS shoaled once more, halting Pacific-Atlantic throughflow (De Schepper *et al*., 2013). This is hypothesised to have accumulated heat in the Caribbean Warm Pool (CWP), which is a mechanism known from the Last Deglacial to be crucial in re-establishing AMOC and the northward flow of heat transport via the NAC once the CWP reached a critical size (Carlson *et al*., 2008). Alkenone-based SST

reconstructions from Site 982 may support the predicted enhanced heat transport to the North Atlantic at this time (Lawrence *et al*. 2009). As a result, it is thought MIS M2 effectively terminated itself via eustatic feedbacks through the CAS, with a reinvigorated NAC back in operation on its modern path by ~3.29 Ma as mPWP climate and modern-like AMOC were established (Raymo *et al*., 1996; Zhang *et al*., 2013). It is hypothesised that this would have warmed waters around the Northern Hemisphere landmasses and reduced the GrIS to isolated mountain glaciers at this time (De Schepper *et al*., 2013, Thiede *et al*., 2011). Recent modelling efforts have called the importance of this mechanism into question, however, and suggest instead that a lack of substantially cold summers due to low-amplitude obliquity during ~4.5–3.1 Ma (Haug and Tiedemann, 1998) prevented the persistence of large, long-term glaciation during this interval (Tan *et al*., 2017).

This mechanism to explain Northern Hemisphere cooling during MIS M2 appears to be at odds with others that propose CAS closure, rather than enhanced throughflow, preconditioned or forced Northern Hemisphere ice-sheet expansion at ~2.7 Ma (e.g., Haug and Tiedemann, 1998; Driscoll and Haug, 1998; Bartoli *et al*., 2005; Sarnthein *et al*., 2009). Records of SSS and SST from North Atlantic Sites 984, 609 and 610 along the path of the modern NAC (Fig. 2.5) indicate a 2–3 °C warming following each CAS shoaling event, and cooling events appear to occur coeval with re-openings (Sarnthein *et al*., 2009). This undisputed warming effect of CAS closure on the North Atlantic is hypothesised by some authors to have preconditioned ice-sheet growth by increasing atmospheric moisture content via evaporative cooling of the surface ocean, along with invigorating the NAC and enhancing NADW formation (Keigwin *et al*., 1982; Haug and Tiedemann, 1998). Stable isotope records from ODP Site 1264 on

Walvis Ridge, directly in one of the major export pathways of NADW (Fig. 2.5), refute the latter, however, by suggesting no apparent change in NADW formation and thus deep Atlantic Ocean structure in response to CAS shoaling (Bell *et al*., 2015). Additionally, intensification of the Gulf Stream and associated NADW formation should be evidenced by step-wise increases in deep-water ventilation coeval with proposed progressive CAS closure (Maslin *et al*., 1998); however, North Atlantic benthic foraminiferal $\delta^{13}C$ records, which track changes in deep water mass structure (e.g., Tiedemann, 1991; Raymo *et al*., 1992, 1996; Dwyer *et al*., 1995; Shackleton *et al*., 1995), all demonstrate a long-term decrease between ~3.5 and 2.0 Ma, indicating NADW formation actually reduced at this time.

Increased rainfall over Eurasia as a result of CAS closure is hypothesised to have enhanced freshwater delivery to the Arctic via Siberian rivers, promoting sea-ice formation and ice-sheet growth via ice-albedo feedbacks (Driscoll and Haug, 1998; Bartoli *et al*., 2005; Sarnthein *et al*., 2009). This is in turn thought to have isolated the heat capacity of the ocean from the atmosphere, acting as a negative feedback on the efficiency of AMOC (Driscoll and Haug, 1998). Indeed, modelling simulates a slight rise in northward moisture transport to northwest Eurasia in response to CAS closure (Lunt *et al*., 2008b). Pliocene climates were generally wetter than the present day (Salzmann *et al*., 2008), however, so the moisture available for substantial snowfall and ice expansion during favourable orbital conditions may have already been present (De Schepper *et al*., 2013). In addition, there is little wider spatial context for AMOC change during this period outside of the Caribbean Basin, hence evidence for ocean-scale circulation change and related moisture transport is unclear (Bell *et al*., 2015).

Simulations carried out using a fully coupled ocean-atmosphere GCM (Lunt *et al*., 2008a) confirm that CAS closure would have increased snowfall over Greenland, particularly in southeast mountainous elevations. However, none of the simulations produced a larger expansion of the GrIS than predicted by orbital forcing alone when run through a high-resolution ice-sheet model, hence these modelled changes in ice volume may be too small to invoke CAS closure as a main driver of iNHG (Lunt *et al*., 2008a, 2008b). It is also important to note that the proposed final phase of CAS closure dated to between ~2.95–2.5 Ma (Sarnthein *et al*., 2009) occurred after the onset of major Greenland glaciation (e.g., Wolf and Thiede, 1991; Jansen *et al*., 2000; St John and Krissek, 2002; Thiede *et al*., 2011) (Fig. 2.6e). Considering that the final emergence of the Isthmus of Panama was itself likely a result of gradually falling global eustatic sea-level (e.g., Miller *et al*., 2005; Groeneveld *et al*., 2014), and that the exact timing of shoaling events and deep circulation changes are difficult to link (e.g., Maslin *et al*., 1998; Molnar, 2008; Bartoli *et al*., 2011; Montes *et al*., 2012, 2015; Bell *et al*., 2015), the role of CAS closure in iNHG may be merely a positive precipitation feedback (e.g., Haug and Tiedemann, 1998) following an initial delay of glacial conditions.

Owing to a lack of well-dated studies directly linking the onset of significant ice-rafting to the North Atlantic with changes in AMOC and heat transport hypothesised as a result of tectonic gateway closure, it remains a challenge to interpret the relationship between these processes during iNHG. This highlights the importance of studying, at high resolution and with high fidelity age control, sediments from sites well-placed to measure these aspects of the climate system.

2.2.4 pCO_2 and orbital forcing

The role of uplift-related CO_2 drawdown in driving long-term Cenozoic cooling has already been established, along with its ability to force short-lived glaciation when orbital conditions favour cool summers (Raymo and Ruddiman, 1992; DeConto *et al*., 2008). Estimates of pCO_2 for shorter timescales have improved in recent decades (e.g., Foster *et al*., 2017), and several studies have linked periodic Northern Hemisphere cooling and glaciation to intervals of falling pCO_2 since the Miocene. Model simulations suggest the threshold of ~280 ppmv required for significant ice growth on Greenland may have been initially crossed during glacials as early as ~25 Ma (DeConto *et al*., 2008), with some alkenone- and boron-based estimates suggesting this threshold was periodically crossed with further reductions in pCO_2 throughout the mid- and late Miocene (Foster *et al*., 2012; Badger *et al*., 2013a; Greenop *et al*., 2014). IRD in the Fram Strait dating to ~18 Ma (Thiede *et al*., 2011) may therefore reflect the early expansion of an ice mass on northern Greenland at this time. Early to mid-Pliocene temperatures 3–4 °C warmer than present (e.g., Haywood *et al*., 2009) are thought to have been primarily driven by glacial-interglacial pCO_2 in the region of ~290 to 460 ppmv based on alkenone and boron estimates (Pagani *et al*., 2009; Seki *et al*., 2010; Bartoli *et al*., 2011; Zhang *et al*., 2013), reflected in the sporadic IRD evidence for the very occasional presence of iceberg-calving margins during this time (Thiede *et al*., 2011). A transient decline in boron-based pCO_2 ~3.4–3.3 Ma (Bartoli *et al*., 2011; Zhang *et al*., 2013) occurred coeval with the increase in global ice volume associated with MIS M2 (e.g., Jansen *et al*., 2000; Bartoli *et al*., 2011; Knies *et al*., 2014). Relative warmth of ~2–3 °C warmer than present re-established during the mPWP, 3.26–3.025 Ma (e.g., Raymo *et al*., 1996), is thought to be likely associated with a return to interglacial pCO_2 levels of between

~350 and 450 ppmv (Fig. 2.6c) according to separate estimates (Bartoli *et al*., 2011; Martínez-Botí *et al*., 2015). Cooling following the mPWP and up to ~2.8 Ma, associated with minimum glacial pCO_2 values of ~250 ppmv (Fig. 2.6c), is thought to be responsible for the increase in glacial IRD in the North Atlantic during this time (Bartoli *et al*., 2011; Martínez-Botí *et al*., 2015). However, SSTs 2–3°C warmer than present recorded between 3.05–2.8 Ma off southern Iceland suggest that continued warming over the North Atlantic, associated with relatively high interglacial pCO_2 and low obliquity, jointly prevented further GrIS growth during this time (Bartoli *et al*., 2011). A further fall in glacial pCO_2 to consistently below the ~280 ppmv threshold followed at ~2.7 Ma (Fig. 2.6c; Bartoli *et al*., 2011; Martínez-Botí *et al*., 2015), enabling the build-up of large persistent Northern Hemisphere ice-sheets at this time as summer ablation rates low enough to allow a positive ice budget to persist (Lunt *et al*., 2008a; Willeit *et al*., 2015). Recent modelling efforts, in good agreement with available IRD records, have highlighted how Plio-Pleistocene GrIS extents remained dynamic after ~2.7 Ma under pCO_2 levels between 320 and 280 ppmv (Tan *et al*., 2018).

As touched on previously in this Chapter, a reduction in pCO_2 is not enough on its own to build large ice-sheets; favourable orbital conditions must also be implicated in modulating Northern Hemisphere and global climate on these timescales (e.g., Zachos *et al*., 2001b; Medina-Elizalde and Lea, 2005; DeConto *et al*., 2008; Lunt *et al*., 2008a). If a positive annual snow budget persists over many consecutive years due to cooler summers, ice-sheets are able to nucleate and further advance their margins through positive albedo feedbacks with the climate system (e.g., Maslin *et al*., 1998; De Schepper *et al*., 2009). Earth's climate system in the Plio-Pleistocene was regulated by a 41-kyr periodicity (Fig. 2.6d; Lisiecki and Raymo, 2005), as clearly evidenced from

geological records the globe over. These records include, but are by no means limited to: polar ice-volume inferred from the global benthic $\delta^{18}O$ record covarying with IRD deposition in circum-polar regions (e.g., Shackleton *et al*., 1984; Lisiecki and Raymo, 2005; Naish *et al*., 2009; Thiede *et al*., 2011); patterns in ocean circulation as inferred from water-mass mixing, temperature, upwelling and productivity proxies (e.g., Dwyer *et al*., 1995; Lawrence *et al*., 2006; Hodell and Venz-Curtis, 2006; Crundwell *et al*., 2008; Bell *et al*., 2015; Lunt *et al*., 2016; Jakob *et al*., 2017); atmospheric circulation as inferred from continental-sourced dust records (Ding *et al*., 2002; Bailey *et al*., 2011; Lang *et al*., 2014); global sea-level fluctuations recorded on continental margins (e.g., Miller *et al*., 2005; Naish *et al*., 2007); and Asian monsoon intensity reflected in erosion proxies (e.g., Clemens *et al*., 1996; Zhang *et al*., 2009). These records are linked by the propagation of various feedbacks between Earth's atmospheric, oceanic and terrestrial realms, most importantly the distribution of heat and moisture between high and low latitudes and the sequestration and release of CO_2 (Lunt *et al*., 2008a; De Schepper *et al*., 2009; Naafs *et al*., 2010; Bell *et al*., 2015). The primary driver for the observed pacing of variability in Plio-Pleistocene records is thus changes in the amount of summer insolation received from the Sun due to the obliquity of the Earth's orbit, i.e. its axial tilt, which varies between 22° and 24.5° over a 41-kyr cycle (e.g., Milankovitch, 1941, 1949; Berger, 1988; Laskar *et al*., 1993; Loutre and Berger, 1993) (Fig. 2.6a–b). Precession, i.e. the Earth's 'wobble' on the tilt of its axis, varies on a 23-kyr cycle and also controls the intensity of this summer insolation (e.g., Milankovitch *et al*., 1949; Loutre and Berger, 1993; Huybers *et al*., 2006) (Fig. 2.6a–b). Plio-Pleistocene glacial cycles are more sensitive to the insolation integrated over the length of the Northern Hemisphere summer, however, primarily controlled by obliquity (Raymo *et al*.,

2006; Huybers *et al.*, 2006). Indeed, modern observations support average amount and duration of summer insolation – rather than its intensity – as the best indicator of glacial variability, as it most strongly corresponds to ablation rates (Wunsch, 2003).

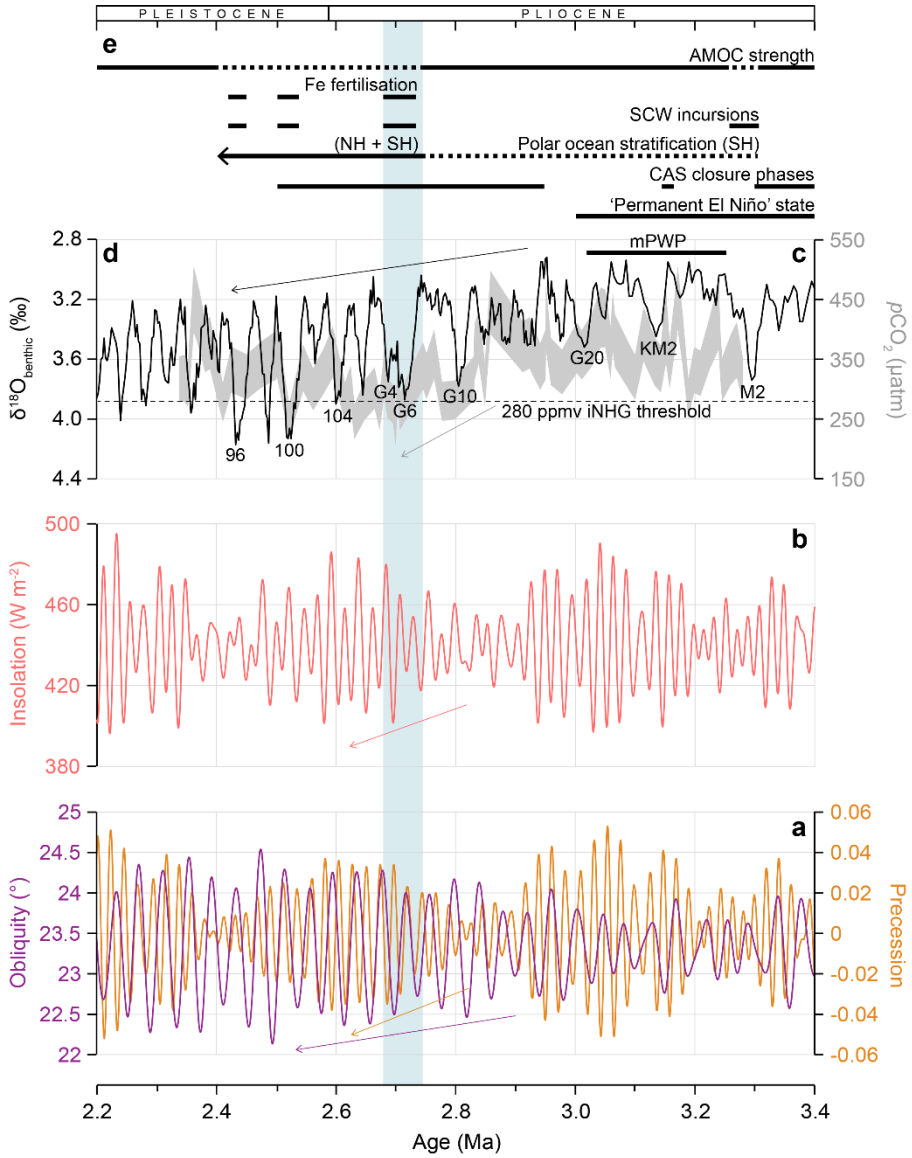

Figure 2.6 Comparison between (**a**) the key orbital parameters of the Pliocene, obliquity and precession, and (**b**) the resultant insolation at 65°N as calculated by Loutre and Berger (1993), alongside (**c**) the atmospheric carbon dioxide concentration (pCO_2) estimated from planktic foraminiferal boron isotopic composition ($\delta^{11}B$; Martínez-Botí *et al.*, 2015) and (**d**) the benthic foraminiferal $\delta^{18}O$ stack (Lisiecki and Raymo, 2005). Black bars in (**e**) indicate timescales of key proposed contributing factors to iNHG, as discussed in the text: 'Permanent El Niño' ('El Padre') state; phases of Central American Seaway (CAS) closure; onset of Southern Hemisphere (SH) and later both Northern Hemisphere (NH) and SH polar ocean stratification; incursions of southern-component water (SCW) into the deep Atlantic; iron (Fe) fertilisation of the high-latitude surface ocean; and relative strength (solid = strong, dashed = weak) of Atlantic Meridional Overturning Circulation (AMOC). Arrows indicate general tends in the data; labels in panel (d) are Marine Isotope Stages, and the duration of the mid-Piacenzian warm period (mPWP) is indicated (Dolan *et al.*, 2011). Light blue shaded interval indicates the rapid intensification of Northern Hemisphere glaciation during MIS G6–G4 (2.72–2.68 Ma; Maslin *et al.*, 1998; Bailey *et al.*, 2013).

It is this average summer insolation integrated over long timescales that is modelled to control surface melting of Northern Hemisphere ice-sheets at the obliquity period (Huybers *et al*., 2006). Between ~3.2 and 2.75 Ma, the gradual enrichment of ^{18}O in the deep ocean reveals global ice volume was already increasing (Maslin *et al*., 1998; Lisiecki and Raymo, 2005), with significantly reduced radiative forcing acting upon Northern Hemisphere climate associated with rapid pCO_2 decline from mPWP levels of ~400 ppmv to just ~280 ppmv (DeConto *et al*., 2008; Pagani *et al*., 2009; Lunt *et al*., 2008a; Bartoli *et al*., 2011; Willeit *et al*., 2015; Martínez-Botí *et al*., 2015) (Fig. 2.6b–d). Reconstructions of late Pliocene orbital forcing (Fig. 2.6a) indicate that an extended node in obliquity ~3.3–2.9 Ma, combined with two low-amplitude precession intervals ~3.3–3.2 Ma and 2.9–2.8 Ma (Loutre and Berger, 1993), may have aided the persistence of winter ice expansion during MIS M2 and following the mPWP via reducing seasonality, as is thought to have been the case during the EOT and OMT (Zachos *et al*., 2001b).

High insolation amplitude with high summer insolation occurred during the mPWP (Fig. 2.6b; Loutre and Berger, 1993), likely closely linked to the relative warmth and reduced NHG during this time. From ~2.8–2.6 Ma, lower summer insolation occurred during a period of large insolation amplitude (Fig. 2.6b; Loutre and Berger, 1993), which would have favoured the observed rapid expansion of Northern Hemisphere ice-sheets at this time via minimising summer ablation (Song *et al*., 2017). During this time both $\delta^{18}O$ and IRD variations also increased in amplitude (Fig. 2.3), mirroring the transition to more extreme glacial-interglacial cycles at the obliquity level (e.g., Lisiecki and Raymo, 2005, 2007; Thiede *et al*., 2011) and indicating increased seasonality in the Northern Hemisphere (Maslin *et al*., 1998). The progressively stronger response to obliquity forcing during this

interval is reflected in many other climate proxy records, suggesting a strong link between the initiation and persistence of NHG and the overall climate response to obliquity-paced insolation variability at this time (Song *et al*., 2017). Three intervals with relatively heavy $\delta^{18}O$ values followed the initial increase in ice-volume between 2.72 and 2.68 Ma (MIS G6, G5 and G4), with minimal recovery between them (Fig. 2.6d; Lisiecki and Raymo, 2005); the absence of an intervening warm interglacial to ablate much of the glacial volume likely encouraged further ice-sheet growth and stability (Tiedemann *et al*., 1994; Shackleton *et al*., 1995; Maslin *et al*., 1998).

From ~2.5 Ma, the response of $\delta^{18}O$ and glacial cycles to 23-kyr precession forcing began a long-term exponential increase, indicating the climate system started to become more sensitive to changes in summer insolation intensity (Huybers *et al*., 2006) as well as still being primarily modulated by obliquity variations (Lisiecki and Raymo, 2007). During the early Pleistocene, 70% of variance in ice-volume is in the obliquity band, which itself is in phase and 80% consistent with the summer energy forcing (Huybers *et al*., 2006). Various studies propose that Northern Hemisphere ice volume responds in different ways to obliquity and precession, depending on the specific effects each exerts on both the latitudinal and seasonal distribution of insolation (e.g., Philander and Fedorov, 2003; Raymo *et al*., 2006; Huybers, 2006). The global benthic $\delta^{18}O$ stack doesn't obviously reveal this increased precession sensitivity during iNHG, however, as obliquity was in-phase across the hemispheres (e.g., Naish *et al*., 2009) – so dominates the global signal (Fig. 2.6) – whereas precession was out-of-phase as it only affects the seasonal distribution of insolation rather than the global average (Lisiecki and Raymo, 2007). Modelling has revealed that ice-volume in each hemisphere responds to local insolation forcing, so out-of-phase precession

responses almost balanced out between the North and South poles prior to the appearance of large Northern Hemisphere ice-sheets (Raymo *et al*., 2006). As NHG progressed, however, its strengthened response to precession forcing is modelled to have begun to outweigh the Southern Hemisphere response, thus increasing precessional power in the global climate signal (Raymo *et al*., 2006; Lisiecki and Raymo, 2007).

The development of an asymmetric shape to glacial cycles through the Plio-Pleistocene (also beginning from ~2.5 Ma; Fig. 2.6d) is indicative of internal Northern Hemisphere ice-sheet feedbacks influencing the system (e.g., Paillard, 1998; Clark *et al*., 1999), as glacial dynamics can act in a non-linear way to propagate a symmetrical forcing (e.g., Huybers and Wunsch, 2004; Huybers, 2007; Lisiecki and Raymo, 2007). These internal dynamics act against rapid long-term glaciation via a negative feedback between ice-sheet elevation and accumulation and lead to rapid deglaciation via basal sliding, calving, non-linear temperature sensitivity and positive sea-level feedback (Clark *et al*., 1999; Tarasov and Peltier, 2004), effects which are thought to have caused Pleistocene glacial cycles to exhibit a relatively slow, shallow ‘glaciation’ limb and faster, steeper ‘deglaciation’ limb (MacAyeal, 1993; Marshall *et al*., 2000; Lisiecki and Raymo, 2007). In addition, a cooling climate increases the threshold at which melting can occur, which in turn leads to more variable summer energy that is more sensitive to precession variations (Huybers, 2006). Hence, the onset of iNHG coincided with the start of a gradual change in glacial cycle shape and sensitivity to precession, which was either a direct result of Northern Hemisphere ice-sheet dynamics, or of the same forcing that determines glacial maxima in high northern latitude ice volume (Lisiecki and Raymo, 2007).

Modelling efforts have been made to delineate the effects of orbital forcing and other proposed drivers on iNHG. In a simple model assuming linearly decreasing pCO_2, low-amplitude periods of ice growth are simulated from ~2.9 Ma, driven by variations in insolation forcing, and become much higher-amplitude from 2.75 to 2.45 Ma (Maslin *et al*., 1998) in strong agreement with North Atlantic and Nordic Seas IRD records (e.g., Jansen *et al*., 2000; Kleiven *et al*., 2002; Thiede *et al*., 2011). A similar study also found that linear pCO_2 decrease only triggered large Northern Hemisphere ice-sheets after 2.9–2.7 Ma when obliquity was lowest (Li *et al*., 1998; Fig. 2.6).

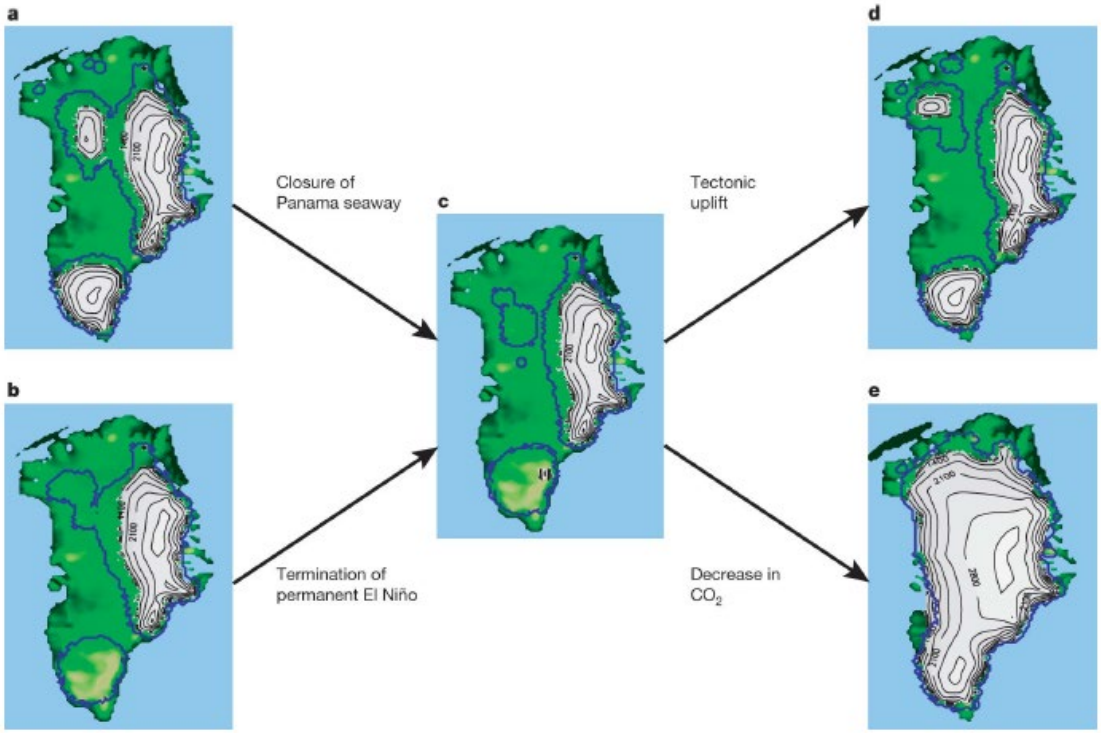

Figure 2.7 Modelled Pliocene GrIS configurations for different scenarios: (**a**) open Panama seaway, (**b**) permanent El Niño, (**c**) closed seaway, no El Niño, low orography and high CO_2 ('warm Pliocene' control), (**d**) high orography, and (**e**) low CO_2. The blue line represents the extent of the ice-sheet under orbital conditions favourable for inception. Arrows represent the direction of geological time with proposed forcing events. From Lunt *et al*. (2008a).

Subsequent more sophisticated modelling using a fully-coupled atmosphere-ocean GCM simulated and assessed the impacts of each proposed mechanism for iNHG discussed so far in this Chapter, and the impact of pCO_2 and orbital

state on the GrIS in particular (Fig. 2.7; Lunt *et al*., 2008a, 2008b). In these simulations, both the Panama and 'El Padre' hypotheses resulted in increased precipitation over Greenland, and the effects of regional uplift and declining pCO_2 together reduced temperatures over Greenland (Lunt *et al*., 2008a, 2008b). These modelled anomalies associated with each scenario were run through an ice-sheet model, which revealed that only global cooling of 1.3°C predicted from declining Plio-Pleistocene pCO_2 could force a significant increase in GrIS volume (~6.3 m SLE) with extensive marine-calving margins; while the Panama and 'El Padre' scenarios resulted in net GrIS reduction (Fig. 2.7; Lunt *et al*., 2008a). Each scenario was then repeated with favourable 'cold orbit' conditions, and found that the GrIS only gained further volume in the decreased pCO_2 simulation (Fig. 2.7; Lunt *et al*., 2008a). A recent 'inverse' approach to the problem used transient simulations to generate virtual pCO_2, benthic $\delta^{18}O$ and SST records under different scenarios using an intermediate-complexity Earth system model, and compared these to existing equivalent palaeodata (Willeit *et al*., 2015). The best fit of simulated datasets to palaeodata required pronounced pCO_2 variability in the 41-kyr obliquity band, and this accurately replicated a relatively abrupt iNHG at ~2.7 Ma, consistent with a threshold response to gradual pCO_2 decline combined with orbital forcing (Willeit *et al*., 2015).

In summary, all of these modelling studies suggest that while long-term forcings of uplift and gateway closure may have brought the Northern Hemisphere to critical conditions favouring glaciation by ~3 Ma, the rapid transition to a high-amplitude glacial-interglacial climate regime with extensive marine-calving GrIS margins was only possible when induced by the combination of decreasing pCO_2 from high mPWP concentrations and favourable 'cold' orbital conditions (Fig. 2.7) (Maslin *et al*., 1998; Lunt *et al*., 2008a; Willeit *et al*., 2015). It

must be noted, however, that the ~280 ppmv pCO_2 threshold for iNHG was reached at a relatively rapid rate of ~400 ppmv Myr^{-1} following deterioration of mPWP climate at ~3 Ma (Bartoli *et al*., 2011; Martínez-Botí *et al*., 2015), almost thirty times faster than the long-term average Cenozoic pCO_2 drawdown associated with continental weathering (Ruddiman and Raymo, 1992; Zhang *et al*., 2013; Anagnostou *et al*., 2016; Foster *et al*., 2017). One question therefore still remains: what drove this rapid late Pliocene drawdown of CO_2 that ultimately enabled widespread NHG under favourable orbital conditions?

2.2.5 AMOC and the polar oceans

The global ocean is the largest reservoir of CO_2 on Earth, with the Southern Ocean a particularly important region equilibrating with the atmosphere on glacial-interglacial timescales (e.g., Sarmiento and Toggweiler, 1984; Sigman *et al*., 2010). It is therefore highly likely that changes in the oceanic realm and its connection with the atmosphere drove the observed short-term orbitally-paced pCO_2 changes over the Plio-Pleistocene (e.g., Broecker, 1982). Processes taking place in the polar surface-ocean and feedbacks propagated via AMOC may therefore provide the answer to why and how NHG was able to become so widespread at MIS G6, ~2.72 Ma.

2.2.5.1 The modern polar oceans and global climate

Surface waters in polar regions are a key connection point between the atmosphere and deep ocean via the global overturning thermohaline circulation (e.g., Broecker, 1982; Sigman *et al*., 2004, 2010; Song *et al*., 2017). Deep Atlantic circulation is known to influence climate through a) the meridional redistribution of heat, and b) changes to pCO_2 via stratification and the efficiency of biological

productivity (e.g., Bell *et al*., 2015). Polar surface water processes including mixing, cooling, sea-ice formation, surface stratification and biological productivity all control the characteristics of new water masses sinking to the ocean interior, thus regulating deepwater ventilation rates for a large fraction of the world's oceans, and ultimately pCO_2 (Hodell and Venz-Curtis, 2006). Biological productivity in the ocean lowers pCO_2 via the 'biological pump'; biologically-produced carbon-based organic matter sinks out of surface waters where it is created and into the deep oceanic interior, lowering the concentration of CO_2 in the surface ocean and drawing it out of the atmosphere (Sigman *et al*., 2010). Stratification of the polar ocean due to sea-ice expansion and surface cooling prevents mixing between deep and shallow water masses, limiting reventilation of sequestered CO_2 (Toggweiler, 1999; Sigman *et al*., 2004, 2010). During late Pleistocene glacial cycles, Southern Ocean CO_2 leakage decreased due to increased stratification and a more efficient biological pump, storing more CO_2 in the deep ocean and so further cooling glacial climate (Keeling and Visbeck, 2001; Martinez-Garcia *et al*., 2009; Sigman *et al*., 2010). The opposite is true for deglacials; during the Last Deglaciation, boron isotopes from the Southern Ocean indicate reduced stratification along with a less efficient biological pump enabled reventilation and upwelling of carbon-rich sequestered water, releasing CO_2 back into the atmosphere and enhancing climatic warming (Sigman *et al*., 2010; Martínez-Botí *et al*., 2015).

In the northern North Atlantic, continuous increases in surface water density due to cooling and sea-ice formation eventually lead to deep convection and formation of deep water masses in the Nordic Sea abyss; these (as Iceland-Scotland Overflow Water, ISOW, and Denmark Strait Overflow Water, DSOW) then escape southward over the Greenland-Scotland Ridge and are transported

around the southern tip of Greenland in the deep WBUC before becoming NADW (Hunter *et al*., 2007; Bell *et al*., 2015) (Fig. 2.2). In the modern Arctic, ISOW more directly influences NADW formation on short timescales, and so ISOW variability is closely correlated with changes in NADW properties on short (decadal) timescales (Eldevik *et al*., 2009; Bell *et al*., 2015). NADW is fully-formed once it reaches the western North Atlantic, after entraining additional Labrador Sea Water (LSW) in the Labrador Basin (Hunter *et al*., 2007; Bell *et al*., 2015) (Fig. 2.2). NADW is then exported southwards at depth and is compensated for by the net northward flow of warm upper-ocean water via the NAC (Bell *et al*., 2015) (Fig. 2.5). Since the NAC serves as a transitional boundary between warm oligotrophic subtropical surface waters and the cold productive polar water masses of the Polar Front, its position and strength controls the transport of heat to high northern latitudes and thus surface conditions in the North Atlantic (Lawrence *et al*., 2009; Friedrich *et al*., 2013), with high SSTs generally reflecting an intense NAC and vice versa (Naafs *et al*., 2010). The amount and temperature of southward-exported NADW upwelling around Antarctica influences the mass balance of the marine-based Antarctic ice-sheets, and therefore the salinity of AABW and deep-ocean stratification (Adkins, 2013). Each component of AMOC (NAC, ISOW, NADW and AABW) is thus intimately linked, and represents a crucial teleconnection propagating heat and salinity changes between the poles (e.g., Hunter *et al*., 2007).

During the LGM, nutrient- and carbon-poor NADW (also referred to in this context as northern-component water, NCW) was replaced at depth in the western North Atlantic by nutrient- and carbon-rich southern-component water (SCW), although the relationship between this glacial alteration in ocean structure and AMOC remains unclear (Böhm *et al*., 2015; Lang *et al*., 2016). Millennial-

scale changes in climate reflected in Greenland ice core isotopic records over the last glacial period reveal a general contemporaneousness of warm ('interstadial') episodes with stronger thermohaline convection in the Nordic Seas, and vice versa for cold ('stadial') episodes (e.g., Rasmussen *et al*., 1997), indicating a close relationship between climate state, ice-sheet growth/decay and the vigour of heat transport via ocean circulation in the high northern latitudes.

2.2.5.2 Mid- to late Pliocene

Prior to ~3.6 Ma, reduced intra- and interbasinal temperature and salinity gradients meant North and South Atlantic conditions were relatively similar (Hodell and Venz-Curtis, 2006), with tropical Atlantic benthic $\delta^{13}C$ records suggesting only minor northward AABW advection even during glacials (Billups *et al*., 1997). The North Atlantic was under the influence of an intense NAC transporting warm oligotrophic waters poleward at this time, as inferred from Site 982 (Lawrence *et al*., 2009) and Site U1313 (Fig. 2.5) SST and productivity records (Naafs *et al*., 2010). An increase in North Atlantic carbonate preservation ~3.6 Ma suggests this was an 'optimal period' for NADW production with a well-ventilated deep ocean (Haug and Tiedemann, 1998; Hodell and Venz-Curtis, 2006; Bell *et al*., 2015), and a coeval $\delta^{13}C$ increase in both the Southern Ocean and Caribbean to more North Atlantic-like values at this time is thought to indicate a well-ventilated Southern Ocean due to reduced sea-ice, enhanced gas exchange and more complete nutrient utilisation (Hodell and Venz-Curtis, 2006). These records suggest AMOC was strong during the warm Late Pliocene (Fig. 2.6e), with diminished Antarctic ice-sheet extents inferred from limited AABW and Lower Circumpolar Deep Water (LCDW) formation (McKay *et al*., 2012).

A marked negative $\delta^{13}C$ excursion at equatorial Atlantic ODP Site 925 (Fig. 2.5) at ~3.4 Ma (MIS MG4) is thought to mark the first Late Pliocene northward expansion of AABW/LCDW into the Atlantic (Billups *et al*., 1997). The record of ε_{Nd} (a water mass tracer not influenced by the biological pump) from DSDP Site 607/IODP Site U1313 (reoccupation; Fig. 2.5) also indicates a greater influence of SCW in bottom-waters bathing the deep North Atlantic on glacial timescales from MIS M2, ~3.3 Ma (Lang *et al*., 2016). Coeval major ice-shelf and sea-ice expansion in the Ross Sea and other circum-Antarctic regions is hypothesised to have driven enhanced deep-water production (McKay *et al*., 2012), potentially leading to the observed incursions of SCW to the deep central North Atlantic at this time (Lang *et al*., 2016). The lead-up to MIS M2 was also accompanied by a southward shift and slowdown of the NAC (previously discussed in context of CAS closure; Naafs *et al*., 2010; Friedrich *et al*., 2013). This weakened northward heat transport is likely to have thermally isolated the Greenland landmass, enabling short-lived glaciation during MIS M2 and the development of more glacial-like surface circulation in the North Atlantic at this time (De Schepper *et al*., 2009, 2013; Naafs *et al*., 2010; Friedrich *et al*., 2013). In addition, greater SCW influence in the North Atlantic on orbital timescales from ~3.3 Ma is thought to have helped precondition the Northern Hemisphere for glaciation and further intensified glacial conditions via low-latitude cooling and high-latitude ice-albedo and oceani-atmosphere feedbacks (McKay *et al*., 2012; Lang *et al*., 2016).

At the onset of the mPWP, AMOC is thought to have been reinvigorated to an enhanced state relative to modern (Raymo *et al*., 1996; Zhang *et al*., 2013) (Fig. 2.6e), causing the high-latitude Northern Hemisphere to remain relatively warm and the deep ocean well-ventilated with reduced continental-ice volume

(Dowsett *et al*., 1992; Haywood and Valdez, 2004; Robinson, 2009; Naafs *et al*., 2010; Salzmann *et al*., 2011). Dinoflagellate assemblages from Sites 610 and U1313 have been used to infer that NADW influence remained high with vigorous AMOC up to MIS G6, ~2.72 Ma (Hennissen *et al*., 2014) (Fig. 2.6e).

2.2.5.3 Plio-Pleistocene transition

The intensification of Northern Hemisphere glaciation ~2.7 Ma is exactly coincident with the timing of increased high-latitude ocean stratification, as evidenced by a decline in opal accumulation and increased nitrate utilisation in the subpolar North Pacific (Sigman *et al*., 2004; Bartoli *et al*., 2011) and Southern Ocean (Sigman *et al*., 2004; Hodell and Venz-Curtis, 2006; Waddell *et al*., 2009), and extended sea-ice presence over the Yermak Plateau and south of Iceland (Clotten *et al*., 2019). Expanding sea-ice shortens the productive diatom season, leading to reduced opal burial, and a decrease in the rate of exposure of nutrient-bearing deep water (reflected in nitrogen isotopes) enables those nutrients to be more completely utilised by primary producers (Sigman *et al*., 2004). The respective effects of temperature and salinity on seawater density compete to control the stratification state of the polar oceans: in the 'usual' state, the vertical temperature gradient promotes overturning, with warmer water masses over colder; the salinity distribution, however, promotes fresher over saltier (Sigman *et al*., 2004). The sensitivity of seawater density to temperature reduces as water approaches its freezing point, allowing the salinity effect to take over in determining its density; ~2.75 Ma thus marks the crossing of a cooling threshold that drove polar ocean stratification (Fig. 2.6e; Sigman *et al*., 2004). In addition, the development of a sea-ice cap on the surface ocean would have physically trapped the direct respiration of CO_2 back into the atmosphere (Stephens and

Keeling, 2000; Sigman *et al*., 2010). Expanding sea-ice, increased stratification, decreased Ekman-induced upwelling and reduced vertical mixing thus together limited the ventilation of respired CO_2 as NHG progressed, causing relatively light carbon (low $\delta^{13}C$) to accumulate in the abyss (Raymo *et al*., 1990; Mix *et al*., 1995; Hodell and Venz-Curtis, 2006; McKay *et al*., 2012). Together with the ocean's attendant carbonate alkalinity response (Toggweiler, 1999), this process is thought to have sequestered pCO_2 from the atmosphere and amplified global cooling and glacials from this time (Sigman *et al*., 2004; Hodell and Venz-Curtis, 2006; Waddell *et al*., 2009; Bartoli *et al*., 2011).

The expansion of continental- and sea-ice is also thought to influence AMOC via various feedbacks. Recent modelling has shown that prevention of sea-air heat exchange by expanded sea-ice at high northern latitudes in the Plio-Pleistocene may have reduced heat loss to the atmosphere, dampening deep oceanic convection in these regions and driving further cooling and ice-growth in the North Atlantic (Song *et al*., 2017). Increased Arctic sea-ice could also have exerted a freshwater forcing, further weakening AMOC (Knies *et al*. 2014). Wind feedbacks resulting from glacial expansion can also have a significant impact on oceanic circulation, as inferred for late Pleistocene glacials (Bard and Rickaby, 2009; Sijp and England, 2009) and the LGM (Murati *et al*., 2010). These wind feedbacks can also amplify the Hadley circulation response to obliquity forcing via an increase in topographic height (Song *et al*., 2017), which may help to explain the link between southward shifts of the ITCZ and resultant orbitally-paced productivity in the EEP on glacial timescales with the onset of iNHG (Chiang and Bitz, 2005; Lawrence *et al*., 2006; Jakob *et al*., 2017).

From an Antarctic perspective, wind feedbacks are thought to have driven the northward migration of ocean fronts, reducing the warming effect of Southern

Hemisphere subtropical gyres on the high latitudes and restricting the warm Agulhas leakage from the Indian Ocean (McKay *et al*., 2012; Fig. 2.5). This process is also hypothesised to have reduced the influence of upwelling NADW along the Antarctic margin, instead favouring local deepwater formation near the southern Polar Front – all of which would have driven increased upwelling of cooler water in lower latitudes, thus impacting global heat transport (McKay *et al*., 2012).There is also evidence for increased iron (Fe) fertilisation by aeolian dust during glacials from ~2.75 Ma in the Southern Ocean (Martinez-Garcia *et al*., 2011) and North Pacific (Bailey *et al*., 2011; Lang *et al*., 2014) (Fig. 2.6e) due to enhanced atmospheric circulation and/or expansion of cold arid conditions in continental interiors (Cane and Molnar, 2001; Martinez-Garcia *et al*., 2011; Naafs *et al*., 2012). This would have increased export productivity and nutrient utilisation in the surface ocean, leading to even greater pCO_2 drawdown in these regions (Hillenbrand and Cortese, 2006; Bartoli *et al*., 2011). Cold, nutrient-rich waters thus instead upwelled in the EEP and eastern South Atlantic, driving high productivity at this time (Marlow *et al*., 2000; Lawrence *et al*., 2006; Bolton *et al*., 2011); indeed, models simulate a potential 44% reduction in heat flux to the EEP under increased Southern Hemisphere sea-ice scenarios (Lee and Poulsen, 2006).

MIS G6 therefore signifies a crossed threshold, with the initiation of a glacial-interglacial pattern in oceanic ventilation and intensification of a chemical divide in the Atlantic between well-ventilated intermediate water and poorly-ventilated deep water (Hodell and Ciesielski, 1990; Hodell and Venz-Curtis, 2006) driven by the onset of polar stratification and Fe fertilisation responsible for glacial pCO_2 decrease (Bartoli *et al*., 2011) (Fig. 2.6e). Prominent glacials from this time were characterised by LGM-magnitude expansions of cold SCW into the

deep North Atlantic at the expense of NADW (Raymo *et al*., 1992; Sosdian and Rosenthal, 2009; Hennissen *et al*., 2014; Kostov *et al*., 2014; Lang *et al*., 2016) (Fig. 2.6e), alongside significant cooling of mid- and high-latitude SSTs (Naafs *et al*., 2012; Brigham-Grette *et al*., 2013) and major Northern Hemisphere ice-rafting events (Kleiven *et al*., 2002; Thiede *et al*., 2011; Bailey *et al*., 2012). These SCW incursions likely further enhanced NHG by increasing CO_2 sequestration in the deep North Atlantic (Woodard *et al*., 2014; Lang *et al*., 2016). This, possibly via reduced NCW formation (Böhm *et al*., 2015), led to observed tighter coupling of interhemispheric climate on orbital timescales from this time (McKay *et al*., 2012).

2.2.5.4 Early to mid-Pleistocene

By ~2.4 Ma, long-term Northern Hemisphere ice-volume increase was slowing as high-latitude cooling reached a plateau (Bell *et al*., 2015). A significant increase in interglacial $\delta^{18}O$ and an enhanced vertical temperature gradient over Walvis Ridge at this time indicates greater ocean stratification and enhanced export of dense ISOW into the deep eastern North Atlantic during warm intervals from ~2.4 Ma (Bell *et al*., 2015). This may have been compensated for by an increased return inflow of warm salty surface water via the NAC (supported by a cease in surface-water cooling at Site 982; Lawrence *et al*., 2010), suggesting enhanced AMOC may have acted as a negative feedback to long-term global cooling and thus limited the size of Northern Hemisphere ice-sheets from this time (Bell *et al*., 2015) (Fig. 2.6e). This mechanism could explain inferred northern GrIS retreat and warming associated with the Kap København formation (Funder *et al*., 2001), and support models suggesting the GrIS retreated significantly during Pleistocene interglacials from this time (e.g., Schaefer *et al*., 2016; Fig. 2.3e). Increased opal accumulation in the Southern Ocean from ~2 Ma marks renewed

ventilation and nutrient utilisation, linked to productivity decline in the EEP, but NHG remained intensified due to ongoing ice-albedo feedbacks (Lawrence *et al*., 2006). In addition, interglacial pCO_2 remained fairly high until ~2 Ma, suggesting another mechanism was responsible for continuing to lower interglacial pCO_2 after the iNHG interval (Bartoli *et al*., 2011). One possible explanation is that intensified upwelling in Benguela ~2.1–1.9 Ma (Marlow *et al*., 2000) or off Namibia ~2.4–2.0 Ma (Etourneau *et al*., 2010) would have released deep CO_2 to the surface ocean until ~2 Ma, thus counteracting the effects of CO_2 sequestration in the polar oceans and delaying further ice-volume increase until this time (Bartoli *et al*., 2011).

2.2.5.5 Northern or Southern Hemisphere driver?

The extent to which proposed ocean circulation change forced iNHG remains debated. Site U1313 ε_{Nd} changes lag benthic $\delta^{18}O$ by a few kyr from ~2.9 Ma, similar to during the late Pleistocene, suggesting circulation change was a response to, rather than a secular forcer of, glaciation (Lang *et al*., 2016). SST and productivity records from this site and Site 610 (Fig. 2.5) also indicate southward shifts and/or slowdowns of the NAC during prominent glacials from ~2.75 Ma (Naafs *et al*., 2010; Friedrich *et al*., 2013; Hennissen *et al*., 2014), thought to represent weakened NAC influence similar to during mid- and late Pleistocene glacials. Resultant changes in productivity and stratification are thought to have provided additional positive feedbacks via enhancing storage of CO_2 on orbital timescales (Naafs *et al*., 2010; Sigman *et al*., 2010; Woodard *et al*., 2014; Lang *et al*., 2016) and further thermally isolating the high northern latitudes (Haywood *et al*., 2000; Lawrence *et al*., 2009). Weakened glacial southward export of deep water would have in turn reduced the amount of NADW

upwelling around Antarctica, driving southern polar ocean stratification and pCO_2 drawdown and further reducing northward heat transport (Hodell and Venz-Curtis, 2006; Bartoli *et al*., 2011; McKay *et al*., 2012).

These inferred changes in NAC vigour may be linked to equatorward advection of the Southern Ocean nutrient pool (Bolton *et al*., 2011), implicating deep-water circulation changes as a primary driver of northward heat transport (e.g., Dowsett *et al*., 1992; Robinson *et al*., 2009). Other authors argue, however, that changes in deep-water formation and ice-volume could only have acted as a positive feedback mechanism for NAC intensity, as they lag records of surface-water variability by a few kyr throughout the late Pliocene and early Pleistocene (Versteegh *et al*., 1996; De Schepper *et al*., 2009; Lawrence *et al*., 2009; Naafs *et al*., 2010), which in turn slightly leads the deep-water response (e.g., Imbrie *et al*., 1992).

Changes in solar insolation, amplified by sea-ice extent changes, are thought to have altered the strength and latitudinal position of the strongest westerlies during iNHG, thus influencing the position and strength of the NAC and subsequent northward heat transport on glacial-interglacial timescales (Versteegh *et al*., 1996; Lawrence *et al*., 2009; Hennissen *et al*., 2014; Davini *et al*., 2015). This is corroborated by the link found between the strength of the North Atlantic pressure system and the northward extent of the NAC on decadal (Flatau *et al*., 2003) and millennial timescales (Giraudeau *et al*., 2010) during the modern and Holocene, respectively. The modelled magnitude of North Atlantic SST cooling for iNHG (Song *et al*., 2017) is only half of that actually observed at Sites 982 and 607 (Lawrence *et al*., 2009; Hill *et al*., 2017), however, highlighting the need for additional drivers to explain the full extent of surface ocean cooling during the onset of NHG (Song *et al*., 2017).

The eustatic closure of the Bering and Canadian Archipelago Straits from ~3.3 Ma is linked to a long-term ~1.3 °C SST decline (Otto-Bleisner *et al*., 2007) due to increased inflow of cold low-salinity water into the Arctic Ocean, which may have further disrupted NADW formation and/or enhanced Arctic sea-ice formation from this time (Horikawa *et al*., 2015). Increased Antarctic sea-ice expansion also from ~3.3 Ma may have aided the post-mPWP CO_2 drawdown (e.g., McKay *et al*., 2012); once Arctic stratification began to take place shortly afterwards, however, CO_2 sequestration was likely modulated by oceanic processes at both poles on glacial-interglacial timescales (e.g., Naafs *et al*., 2010; Lang *et al*., 2016).

2.3 Summary

The glacial history of Greenland, and of the Northern Hemisphere as a whole, is relatively loosely-constrained prior to the Late Quaternary. Numerous different proxies have been used successfully to gain insight into changing Greenland Ice Sheet (GrIS) extents during interglacials of the late Pleistocene, but rarely has this detail been attempted or achieved for orbital- and longer-scale climate changes in deeper time. There also remains a great deal of debate over to what extent proposed tectonic, oceanic and orbital changes during the late Pliocene and earliest Pleistocene forced or preconditioned the intensification of Northern Hemisphere glaciation between ~3.6 and 2.4 Ma.

As highlighted by several of the authors who carried out much of the research presented in this chapter (e.g., Lunt *et al*., 2008a; Naish *et al*., 2009; Bartoli *et al*., 2011; Bell *et al*., 2015), new studies from sites well-situated to monitor climate-related processes – particularly glacial ice-rafting and changes in Atlantic Meridional Overturning Circulation strength – within a well-dated

framework are needed to improve our knowledge of the exact spatio-temporal evolution of the GrIS during iNHG, and its relationship to proposed forcings and feedbacks in the climate system.

Chapter 3

Materials and Proxies

This chapter provides an overview of the main materials and proxies employed in undertaking the research for this thesis. The study site is introduced in context with its tectonic and oceanographic setting, and the strategy for sampling the core material is described. The main analytical methods employed to investigate the research questions (described in detail in each respective data chapter) are then outlined, along with examples of their application and limitations.

3.1 Study Site

3.1.1 Expedition aims and drilling recovery overview

Integrated Ocean Drilling Program (IODP) Expedition 303 to the North Atlantic Ocean onboard the JOIDES Resolution in 2004 aimed to investigate Quaternary millennial-scale climatic and hydrographic variability, and obtain new palaeomagnetic records for the region (Expedition 303 Scientists, 2006a). Site U1307 (58°30.3'N, 46°24.0'W) of this expedition is located at 2575 m below sea-level on the northern flank of Eirik Drift (Fig. 3.1), an elongate mounded contourite drift situated on the continental slope and rise just offshore southern Greenland (Fig. 3.2; Hunter *et al.*, 2007). A 175-metre Plio-Pleistocene section was recovered across two holes, U1307A and U1307B, with a shipboard-estimated basal age of ~3.58 million years (Ma) and an average sedimentation rate of ~5 cm kyr^{-1} (Expedition 303 Scientists, 2006a).

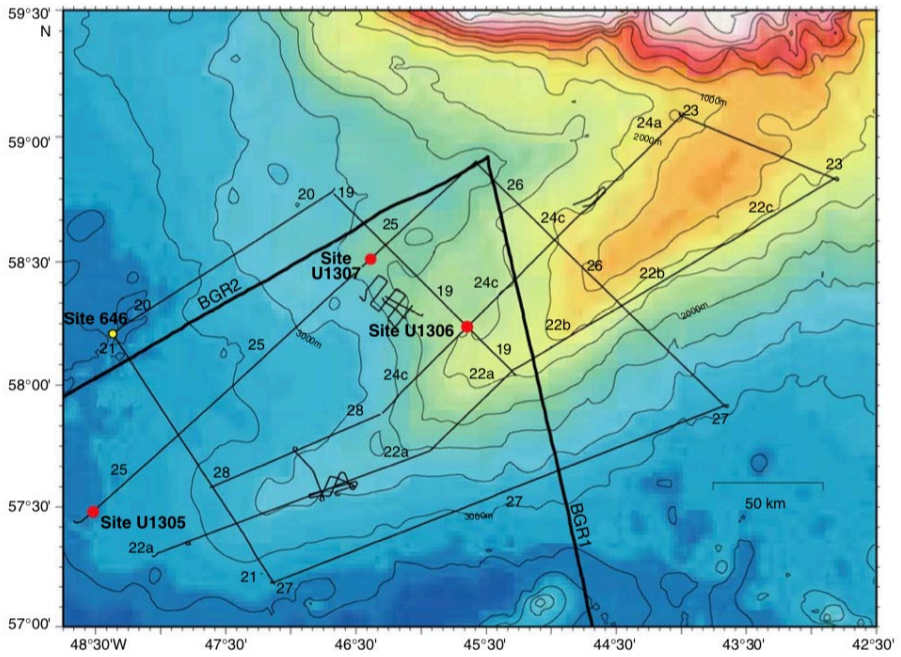

Figure 3.1 Seafloor topographic map of Eirik Drift in the northern North Atlantic, showing the location of IODP Site U1307 on its northern flank in relation to Sites U1305 and U1306 drilled during Expedition 303, and deepwater ODP Site 646. Straight black lines are seismic transects taken during previous expeditions to the area. From Expedition 303 Scientists (2006a).

3.1.2 Tectonic setting

Eirik Drift sits at the junction between the Labrador Basin and northern North Atlantic Ocean (Fig. 3.2), with the region's tectonic evolution closely tied to the opening of these two basins. Rifting between Greenland and Labrador in the early Late Cretaceous occurred contemporaneously with the start of seafloor spreading in the North Atlantic, and continued until the late Eocene–early Oligocene (Srivastava and Tapscott, 1986). The Farewell Fracture Zone, related to the opening of the Labrador Basin, is associated with a WSW-trending basement high, which underlies Eirik Drift and is thought to have influenced its original formation (Srivastava and Arthur, 1989).

Norwegian-Greenland Sea tectonics have also played a crucial role in modulating the accumulation of Eirik Drift sediments, which only began in the early Miocene (Parnell-Turner *et al*., 2015). The mantle plume presently underlying Iceland is responsible for the formation of the North Atlantic Ocean and North Atlantic Igneous Province outcrops on Iceland and Greenland during the Tertiary (e.g., Storey *et al*., 2007), and for the creation of the Greenland-Scotland Ridge (GSR; Fig. 3.2), a large swelling in the oceanic crust between Greenland and Scotland that exerts a regional control on the flow of Norwegian Sea-sourced waters into the deep North Atlantic (Wright, 1998). Recent seismic studies have shown sediment accumulation on Eirik Drift increased significantly at ~5.5 Ma as the plume cooled and the GSR subsided, allowing sediment-laden water to overflow and build up the drift throughout the Plio-Pleistocene, alongside others in the region (e.g., the Bjørn and Gardar Drifts situated in the Iceland Basin; Fig. 3.2) (Parnell-Turner *et al*., 2015).

3.1.3 Oceanographic setting

Greenland is thermally isolated from warm northward-flowing Atlantic surface currents by cold Arctic waters, which travel in a predominantly clockwise direction through the Fram Strait and around the landmass into Baffin Bay (e.g., Thiede *et al*., 2011). This surface current is termed the East Greenland Current (EGC) where it flows past the eastern coast, and the West Greenland Current (WGC) where it passes the western coast (e.g., Andrews, 2000) (Fig. 3.2). This pattern of circulation has likely persisted for a substantial duration of the Cenozoic (Thiede *et al*., 2011; De Schepper *et al*., 2015), although the Fram Strait is only thought to have fully opened in the middle Miocene (Jakobsson *et al*., 2007). Like most marine settings in the subpolar North Atlantic, Site U1307 receives eroded detrital material from Greenland as a result of glacial advance and retreat. Detritus-laden icebergs calved from outlet glaciers on eastern and southeastern Greenland are transported to surface waters overlying Site U1307 via the EGC (Fig. 3.2), where they shed clay- to boulder-sized ice-rafted debris (IRD) on the seabed (Bigg *et al*., 1996; Andrews, 2000; White *et al*., 2016). Site U1307 is therefore well-placed to record changing fluxes of material over the Plio-Pleistocene from a range of important modern-day iceberg-calving sources, particularly from Greenland's southernmost terranes (Bigg *et al*., 1998; White *et al*., 2016; Smith *et al*., 2018).

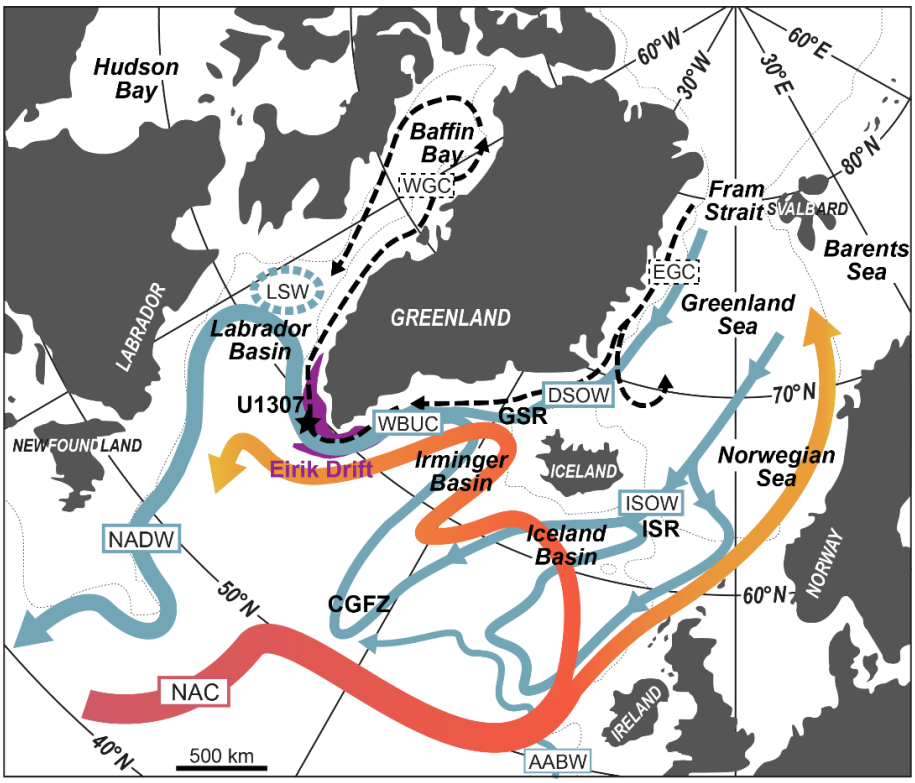

Figure 3.2 Map of Greenland and surrounding landmasses and ocean basins, showing the location of IODP Site U1307 (the focus of this thesis) on Eirik Drift and its relationship to the paths of key modern cold deep (blue) and warm surface (red-yellow gradient) ocean currents relevant to this study. NAC = North Atlantic Current, ISOW = Iceland-Scotland Overflow Water, DSOW = Denmark Strait Overflow Water, AABW = Antarctic Bottom Water, WBUC = Western Boundary Undercurrent, LSW = Labrador Sea Water, NADW = North Atlantic Deep Water. GSR = Greenland-Scotland Ridge, ISR = Iceland-Scotland Ridge, CGFZ = Charlie-Gibbs Fracture Zone. The position of the modern-day Arctic Front is also indicated. The 1000 m isobath is given by thin dotted lines.

At 2575 m water depth, the bottom-waters bathing Site U1307 also lie within the present-day range of the main flow axis of the Western Boundary Undercurrent (WBUC; 1900–3000 m; Fig. 3.2), which transports subglacially-eroded southern Greenland Precambrian terrane bedrock clay- and silt-sized sediment, as well as Paleogene and Neogene volcanic detritus from East Greenland and Iceland, to Eirik Drift (Colville *et al.*, 2011; Reyes *et al.*, 2014; Hatfield *et al.*, 2016). In the vicinity of Eirik Drift, four main water masses comprise the WBUC (Dickson and Brown, 1994; Hoogakker *et al.*, 2011): Denmark Strait Overflow Water (DSOW), Iceland Scotland Overflow Water (ISOW), Labrador Sea Water (LSW) and modified Antarctic Bottom Water (AABW) (Fig. 3.2). DSOW and ISOW both form from intermediate Nordic Sea waters, but follow very different paths before joining

together in the WBUC. DSOW flows between East Greenland and Iceland over the shallow (~550 m) GSR in this region, before rapidly descending and forming the lower, denser layer of the WBUC (up to 3000 m depth) as it flows over Eirik Drift (Fig. 3.2). ISOW, on the other hand, crosses the Iceland-Scotland Ridge (ISR) east of Iceland and flows around Reykjanes Ridge, through the Charlie Gibbs Fracture Zone (CGFZ) where it entrains minor AABW and into the Irminger Basin, forming the upper layer of the WBUC at ~2000 m depth in the vicinity of Eirik Drift (Fig. 3.2).

The present-day transport of the WBUC at Eirik Drift is estimated at ~13–14 Sverdrup (Sv) (e.g., Dickson and Brown, 1994), and relative contributions of each constituent current to this bulk flow are estimated at DSOW ~3–10 Sv, ISOW 2–3 Sv, LSW 4–8 Sv, and AABW 1–2 Sv (Dickson and Brown, 1994; Schmitz, 1996; Alvarez *et al*., 2004). After flowing over Eirik Drift, the WBUC swings around southern Greenland into the Labrador Basin where it entrains further minor LSW, AABW and ISOW to become fully-fledged North Atlantic Deep Water (NADW), the deep lower limb of AMOC in the North Atlantic (Fig. 3.2). Eirik Drift sediments thus potentially contain a 'long-term barometer' of deepwater flux on glacial-interglacial timescales, which also may be linked to variability in the broader ocean-wide thermohaline circulation (Hunter *et al*., 2007; Stanford *et al*., 2011).

3.1.4 Lithostratigraphy

Site U1307 sediments are dominated by terrigenous quartz (2–95%), clay minerals (0–75%) and detrital carbonate (0–35%), with minor but significant heavy minerals (particularly hornblende; 0–10%) and occasional dropstones of a range of lithologies from acidic/metamorphic (granites and granitoids), to basic

igneous/metamorphic (basalts and metabasalts) and (meta)sedimentary (sandstones and quartzites) rocks. Biogenic components such as nannofossils, foraminifera, diatoms and sponge spicules are also common; in the lower Pliocene-age sediments nannofossil ooze is a minor but significant lithology (Fig. 3.3), whereas the majority of the planktic foraminifera are found in the upper late Pleistocene part of the succession. Pyrite burrows and iron-oxide grain coatings are minor authigenic components. Bioturbation is moderate to abundant with mottling on the centimetre scale between lithological changes. The most common lithology is dark greenish grey silty clay (Fig. 3.3; Expedition 303 Scientists, 2006a).

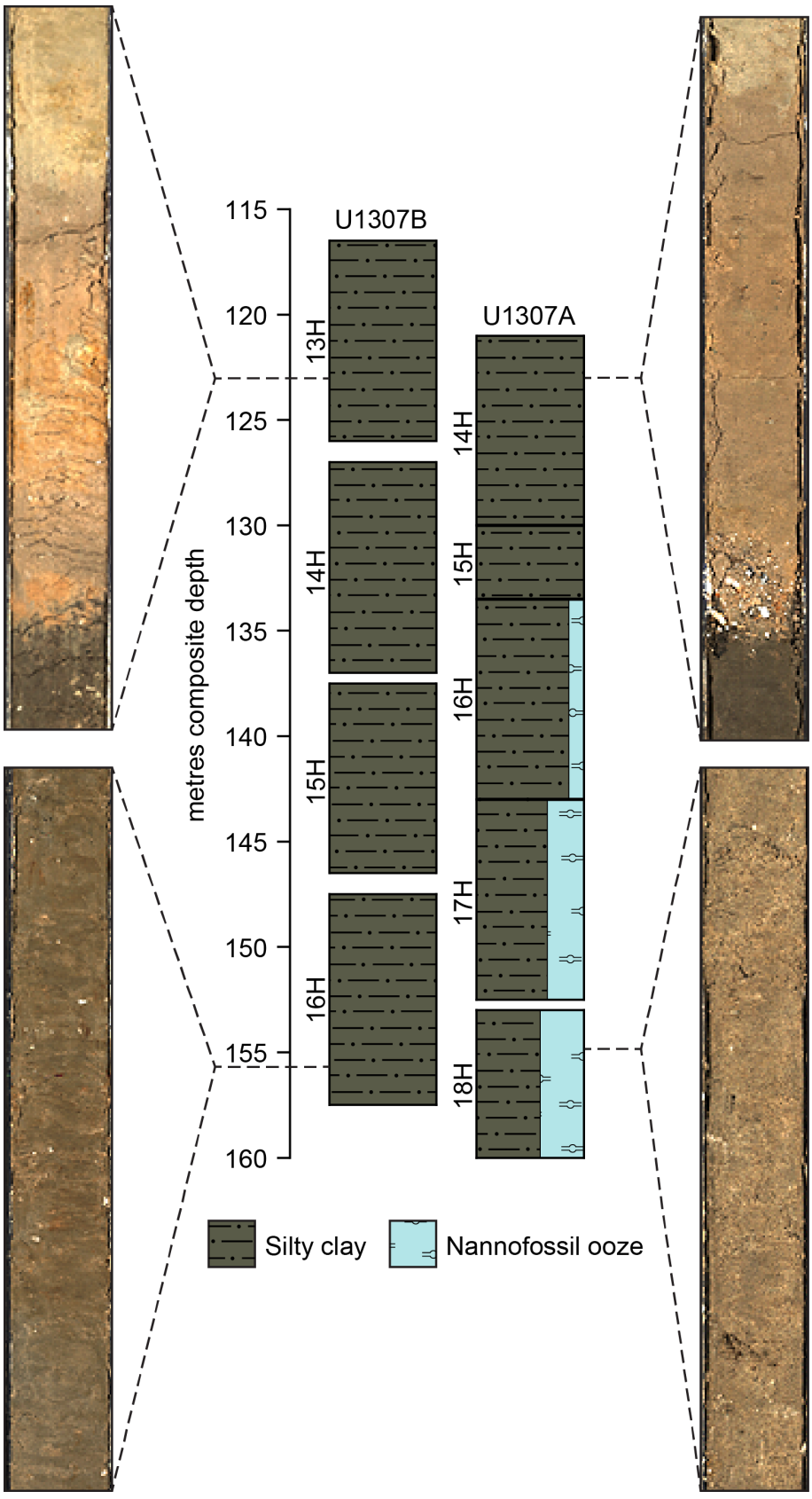

Figure 3.3 IODP Site U1307 Hole A and B simplified graphic log (modified from shipboard report; Expedition 303 Scientists, 2006a) for approximately the iNHG interval, on the original shipboard metres composite depth (Expedition 303 Scientists, 2006a). Photographs of select u-channelled core sections (taken on the ITRAX X-ray fluorescence scanner at Oregon State University prior to the elemental XRF analysis presented in Chapter 5) illustrate the variability in sediment colour and texture present within the broad 'silty clay' description of much of the material.

3.2 Sampling Method

To examine the evolution of the southern GrIS and WBUC during iNHG, I sampled the Site U1307 Plio-Pleistocene composite section at the MARUM IODP Core Repository in Bremen, Germany, over a week in September 2014. Sampling was guided by the shipboard-derived palaeomagnetochron stratigraphy and primary splice (Expedition 303 Scientists., 2006a). To facilitate the construction of both continuous high-resolution and spaced discrete records (for palaeomagnetic and X-ray fluorescence analysis, and IRD abundance and provenance analysis, respectively), I sampled the selected cores with a total of 38 u-channels – continuous 2 × 2 × 150 (unless stated otherwise) cm^3 samples encased in plastic with a clip-on lid constituting one of the sides (Weeks *et al*., 1993) – and 351 discrete ~10 cm-spaced 20 cm^3 samples scoops between ~113–148 mbsf in U1307A, and ~110–136 mbsf in U1307B (see Table 3.1). Sections in cores A-16H and -17H, although outside the primary shipboard splice (Expedition 303 Scientists, 2006a), were included in sampling to achieve a more continuous splice with iNHG-age cores B-14H, -15H and -16H, as shipboard recovery suggests substantial gaps of ~0.2–0.9 m between them (Fig. 3.4). See Chapter 4 for how the new splice was constructed.

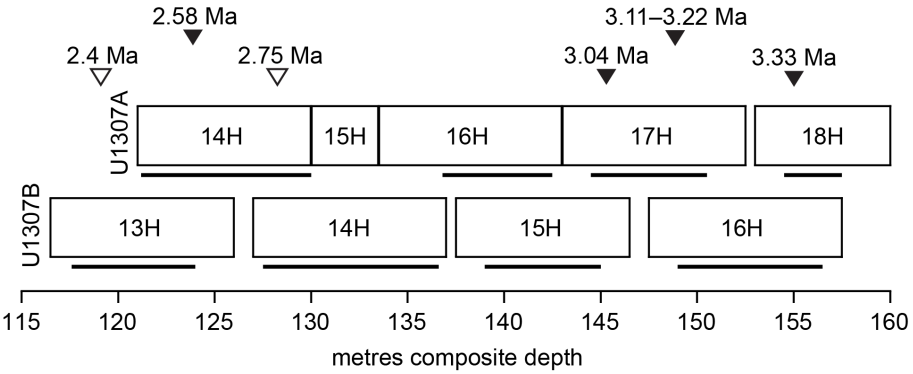

Figure 3.4 IODP Site U1307 Hole A and B shipboard recovery for approximately the iNHG interval on the original shipboard metres composite depth (Expedition 303 Scientists, 2006a). Black bars denote where u-channel samples were taken in order to build a more continuous splice between the two holes (see Table 3.1 for further sampling detail). Clear/filled triangles indicate the position of initial shipboard-derived biostratigraphic/palaeomagnetic datums, respectively (Expedition 303 Scientists, 2006a).

Table 3.1 List of IODP Site U1307 core sections and depths (metres below seafloor; mbsf) sampled with u-channels and discrete scoops for the work presented in this thesis.

Exp.	Site	Hole	Core	Type	Section	Top (cm)	Bottom (cm)	mbsf (top)
303	1307	B	13	H	1	112	149	110.42
303	1307	B	13	H	2	0	150	110.80
303	1307	B	13	H	3	0	150	112.30
303	1307	B	13	H	4	0	150	113.80
303	1307	B	13	H	5	0	150	115.30
303	1307	A	14	H	1	20	149	112.60
303	1307	A	14	H	2	0	150	113.90
303	1307	A	14	H	3	0	150	115.40
303	1307	A	14	H	4	0	150	116.90
303	1307	A	14	H	5	0	150	118.40
303	1307	A	14	H	6	0	150	119.90
303	1307	A	14	H	7	0	70	121.40
303	1307	B	14	H	1	50	150	119.30
303	1307	B	14	H	2	0	150	120.30
303	1307	B	14	H	3	0	150	121.80
303	1307	B	14	H	4	0	150	123.30
303	1307	B	14	H	5	0	150	124.80
303	1307	B	14	H	6	0	150	126.30
303	1307	B	14	H	7	0	63	127.80
303	1307	B	15	H	2	0	150	129.80
303	1307	B	15	H	3	0	150	131.30
303	1307	B	15	H	4	0	150	132.80
303	1307	B	15	H	5	0	150	134.30
303	1307	A	16	H	3	30	145	129.00
303	1307	A	16	H	4	0	150	130.20
303	1307	A	16	H	5	0	150	131.70
303	1307	A	16	H	6	0	150	133.20
303	1307	B	16	H	2	4	150	139.34
303	1307	B	16	H	3	0	150	140.80
303	1307	B	16	H	4	0	150	142.30
303	1307	B	16	H	5	0	150	143.80
303	1307	B	16	H	6	0	150	145.30
303	1307	A	17	H	2	0	150	136.70
303	1307	A	17	H	3	0	150	138.20
303	1307	A	17	H	4	0	150	139.70
303	1307	A	17	H	5	0	150	141.20
303	1307	A	18	H	2	0	150	146.23
303	1307	A	18	H	3	0	150	147.73

3.3 Palaeomagnetism

3.3.1 Overview and measurement of marine core palaeomagnetism

Palaeomagnetism is a commonly-employed non-destructive tool for age-model generation and palaeoenvironmental studies of marine cores (Ogg, 2012; Liu *et al*., 2012; Channell *et al*., 2014). Marine sediments contain iron-bearing ferrimagnetic minerals – most commonly (titano)magnetite – that record various types of magnetic remanence imparted by the Earth's magnetic field at or just following deposition (e.g., King *et al*., 1983; Channel and Guyodo, 2004). The alignment of these magnetic minerals records the palaeodirection (or polarity) of the magnetic dipole field, which has undergone multiple 'flips' between a 'normal' and 'reversed' state over Earth's history (e.g., Ogg, 2012). They also contain a record of the intensity of the magnetic field, or relative palaeointensity (RPI), which has fluctuated over time; typically reaching minima during field reversals when the magnetosphere briefly shrinks, then growing again once the field direction has stabilised (e.g., Valet *et al*., 2012).

One such type of magnetic remanence is natural remanent magnetisation (NRM). NRM intensity is sensitive to the strength of Earth's magnetic field recorded by aligned ferrimagnetic grains upon, or just following, deposition, and the concentration of ferrimagnetic grains in a sediment sample (King *et al*., 1983). NRM is most responsive to coarse pseudo-single domain (PSD) grains (Banerjee *et al*., 1981). NRM also records component magnetisation directions, inclination and declination, which provide information about the normal or reversed palaeodirection of the magnetic field (Kirschvink, 1980). NRM is typically measured by passing a u-channeled sample through a magnetometer with an alternating field (AF) and 3-axis system to record the various directional components of its magnetisation at 1 cm resolution, and this is commonly done

at progressively greater AF field strengths as the sample is demagnetised (e.g., Mazaud *et al*., 2015; Channell *et al*., 2016). Anhysteretic remanent magnetisation, or ARM, is another measure of magnetic remanence sensitive to the concentration of ferrimagnetic grains in a sample, and is most sensitive to single domain (SD) and smaller PSD grains (Banerjee *et al*., 1981). ARM is first acquired by passing the u-channelled sample through the magnetometer (after NRM measurement) under a direct current (DC) bias field, then its response to stepwise AF demagnetisation is recorded every 1 cm (e.g., Mazaud *et al*., 2015). Since ARM is sensitive to NRM-carrying ferrimagnetic grains, and should vary close to unity, the NRM-ARM regression (or slope) is a useful proxy for RPI (King *et al*, 1983; Channell and Guyodo, 2004; Yamazaki and Oda, 2005; Mazaud *et al*., 2015).

Since variations in magnetic field direction and strength are recorded synchronously in sediments and volcanic sequences the globe over, the palaeomagnetic record at any one site can be used as a geochronological tool to build a high-resolution magnetostratigraphy-based age model (e.g., Chen *et al*., 2017). Ferrimagnetic minerals are also sensitive to a variety of environmental processes, including (but not limited to) climate- and deep ocean current-driven changes in sediment source and transport, and bottom-water conditions affecting sediment deposition and diagenesis (e.g., Stoner *et al*., 1995; Liu *et al*., 2012, Hatfield *et al*., 2013; Roberts, 2015). Analyses of marine core magnetic properties therefore also have the potential to yield a wealth of information on these processes.

3.3.2 Palaeomagnetism in age model generation

The diversity and abundances of foraminifera tests at sites like U1307 usually employed to generate oxygen isotope stratigraphies and age-models via correlation to the global benthic stack (Lisiecki and Raymo, 2005) can fluctuate substantially with seasonal and longer-term shifts of the Arctic Front (e.g., Bashirova *et al*., 2014; Friedrich *et al*., 2013). The relatively high Plio-Pleistocene sedimentation rates over Eirik Drift also result in a low abundance of benthic foraminifera (Hillaire-Marcel and Bilodeau, 2000). It is therefore difficult to generate a benthic $\delta^{18}O$-based age-model for drift sites like U1307. While the abundance of planktic foraminifera tests in drift sediments is often higher, it is also challenging to use planktic $\delta^{18}O$ stratigraphies for age control at Site U1307 because basin-wide signals can be overprinted at this site by local freshwater inputs from the GrIS (e.g., Rohling and Bigg, 1998; Bilodeau *et al*., 1998; Andrews *et al*., 1999).

When $\delta^{18}O$ stratigraphies cannot be employed for age control, RPI data underpinned by a palaeomagnetochron stratigraphy can be correlated to palaeomagnetic records from another site where age-depth control is also tightly constrained by a robust orbital-resolution $\delta^{18}O$ stratigraphy. This is achieved through a nested approach of identifying corresponding peaks and troughs in intensity between two RPI records, guided by the positions of known field reversals (see Chapter 4 for the application of this method in constructing a new, high fidelity, RPI-based age model for Site U1307). While RPI records between sites can vary due to regional and/or local factors such as effects of the non-dipole magnetic field, deposition rates, sediment source and diagenesis (e.g., Tauxe, 1993; Channel and Guyodo, 2004; Roberts, 2015; Valet *et al*., 2016; Chen

et al., 2017), the same relative trends are commonly evident in two records separated by large geographic distances.

3.3.3 Principles and measurement of environmental palaeomagnetism

A wide range of geological and environmental processes can be responsible for concentrating (ferri)magnetic minerals in deep ocean sedimentary records. Continuous u-channel sample magnetic measurements can thus provide a wealth of information on how and when these processes operated in the geological past (Liu *et al*., 2012). One of the most commonly-utilised properties of marine sediments in environmental magnetism is bulk low-field magnetic susceptibility, which can be quantified as either mass-specific (χ) or volume-specific (κ). The latter, κ, is the measurement resulting from continuous u-channel sample measurements at 1 cm resolution, and takes into account the density of the sediment (e.g., Xuan *et al*., 2016). Volume-specific κ is measured by running the u-channel sample on a purpose-built track through a coil magnet, recording the its response (or induced magnetisation, M) to the applied magnetic field (H), such that $\kappa = dM/dH$ (Liu *et al*., 2012). Magnetic susceptibility is also controlled by the concentration of ferrimagnetic grains in a sample, and is sensitive to coarser PSD and multidomain (MD) grains (Banerjee *et al*., 1981). Unlike magnetic remanence, however, all constituents of the sediment – including strongly, weakly and non-magnetic grains – contribute to the bulk susceptibility, which can make it a challenging parameter to interpret in terms of individual constituents (Liu *et al*., 2012). Magnetic susceptibility measurements have nevertheless proven useful in a wide variety of marine core studies for tracking a range of climatically-influenced processes, including but not limited to: aeolian dust deposition, ice-sheet extents, monsoon strength and diagenesis (e.g.,

Bloemendal *et al*., 1992; Stoner *et al*., 1995; Hounslow and Maher, 1999; Zhisheng *et al*., 2001; Richter *et al*., 2001).

The grain-size of magnetic particles carrying the bulk κ signal can be indirectly estimated with the proxy κ_{ARM}/κ (e.g., Banerjee *et al*., 1981). ARM is proportional to the DC bias field applied during acquisition, and the susceptibility of ARM, or κ_{ARM}, is calculated by normalising the ARM by the DC bias field value (Liu *et al*., 2012). Since κ and κ_{ARM} are sensitive to different magnetic grain-sizes, a plot of κ vs. κ_{ARM} can be interpreted as a distribution of magnetic grain-size; greater slopes (higher κ_{ARM}/κ values) represent a smaller average magnetite grain-size assemblage, and vice versa (Fig. 3.5a; Banerjee *et al*., 1981; King *et al*., 1983; Bloemendal *et al*., 1992). This parameter has been utilised in multiple Pleistocene North Atlantic studies to monitor variations in deep-water circulation strength and trace influxes of Greenland-sourced detritus (e.g., Robinson *et al*., 1995; Stoner *et al*., 1995; Kissel *et al*., 1999; Snowball and Moros, 2003; Stanford *et al*., 2006; Kissel *et al*., 2009; Mazaud *et al*., 2012; Channell *et al*., 2014).

Eirik Drift is sensitive to detrital inputs from multiple sources, including glaciofluvial silt-size sediments subglacially eroded from felsic crystalline bedrock by the GrIS, and from Paleogene–Neogene volcanics in Iceland and East Greenland that form part of the North Atlantic Igneous Province (e.g., Colville *et al*., 2011). Hatfield *et al*., (2013; 2017) developed a method to discriminate magnetically between these two main terrestrial sources based on their silt-size magnetic and mineralogical properties. They demonstrate that silts derived from Iceland and East Greenland volcanic sources are characterized by a magnetically-fine grain assemblage (high κ_{ARM}/κ ratios), whereas southern Greenland-derived silt-sized sediments contain coarser ferrimagnetic grains (low κ_{ARM}/κ values) (Fig. 3.5b). These differences result from how ferrimagnetic grains

are hosted within the parent material; magnetite grains from Greenland dominantly (though not entirely) exist as discrete entities, while those from Iceland exist as fine-grained titanomagnetite inclusions within larger polycrystalline host grains (Hatfield *et al.*, 2017). Thus, in the absence of diagenetic alteration, variations in ferrimagnetic grain-size in marine sediments on Eirik Drift can be sensitive to sediment provenance (Hatfield *et al.*, 2013), which in turn may be linked to climatic and oceanic changes responsible for concentrating material from a specific source. I employ volume-specific κ and κ_{ARM}/κ in Chapter 4 to investigate changes in the supply of southern Greenland-sourced glaciofluvial silt to Site U1307 over the iNHG interval.

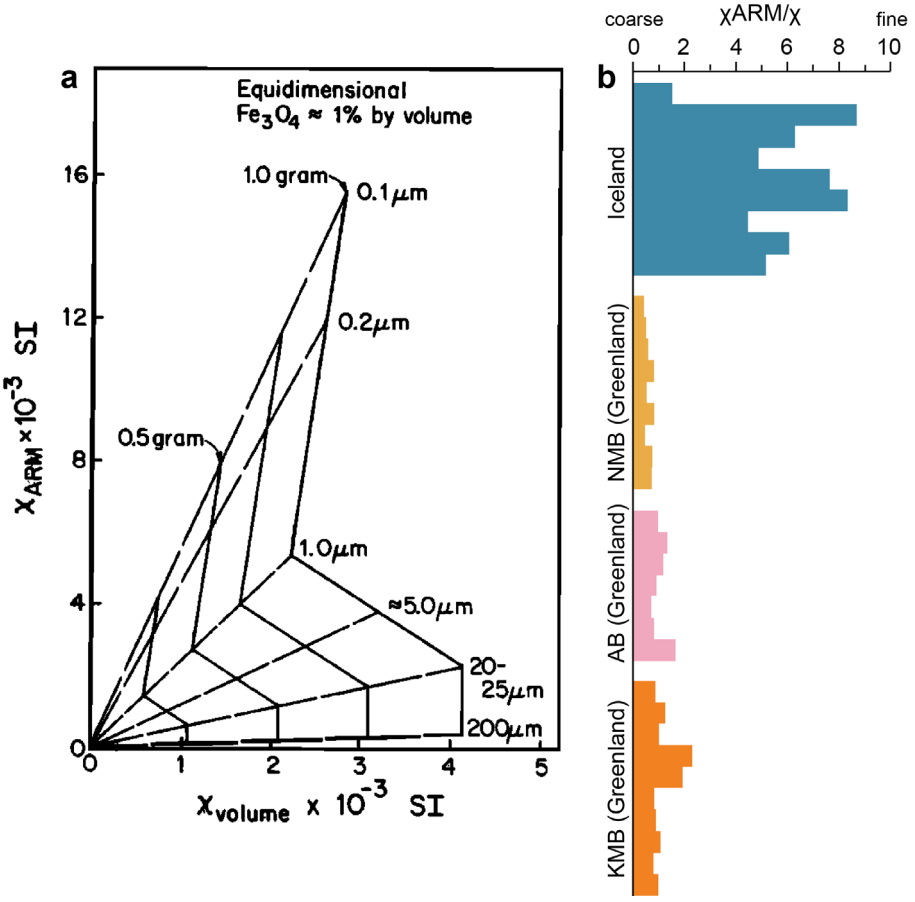

Figure 3.5 How the bulk magnetic properties of a sediment can be used to infer average magnetic grain-size. (**a**) A simple phenomenological model of the χARM vs. χ method for detecting magnetite particle size variation of natural materials (from King *et al.*, 1983); (**b**) histograms of bulk magnetic grain size (χARM/χ; higher/lower values = finer/coarser magnetic grains) of terrestrial sediment samples from Iceland and the three southern Greenland terranes (adapted from Hatfield *et al.*, 2013; for terrane map see Fig. 3.9).

3.3.4 Limitations of marine core palaeomagnetism

The interpretation of marine core magnetic records requires a few points of consideration. Reversals of the dipole magnetic field take place in three phases: 1) a precursory phase, 2) a 180° field flip, and 3) a rebound phase (Valet *et al*., 2012). All three phases are usually recorded in the thermal remanence preserved by rapidly-lithified lava flows, and the main reversal phase can take up to ~20 kyr in some cases (e.g., during the Bruhnes-Matuyama transition, ~790 ka; Valet *et al*., 2014). Depending upon the sedimentation rate at any given marine core site, however, the three phases may be integrated over typically ~2 to 12 kyr, and the time taken for a reversal to take place increases with latitude (Clement, 2004). Hence, medium- to low-sedimentation-rate sites may not preserve all features of a polarity reversal event (Valet *et al*., 2016). In general, however, the reversal is captured within a few cm of sediment (Valet *et al*., 2012), so is adequate for constraining the age of sediments at this resolution.

Bioturbation, current action and diagenesis during early burial can also affect how quickly and reliably marine sediment records the magnetic signal at the time of deposition (Valet *et al*., 2012; Roberts, 2015). However, there is evidence to suggest magnetisation is rapidly locked-in within 10 cm of the decimetre-scale mixed surface layer of the sediment (Channel and Guyodo, 2004). In addition, early studies into how magnetic mineralogy and grain-size affect a sediment's capacity to record a reliable record of palaeointensity demonstrated that both should be fairly uniform throughout a specific sedimentary record, with magnetic parameters such as susceptibility and ARM varying within an order of magnitude of each other (King *et al*., 1983; Tauxe, 1993).

3.4 Scanning X-Ray Fluorescence

3.4.1 Overview of marine core XRF

X-ray fluorescence (XRF) scanning is another commonly-used technique in palaeoenvironmental studies of marine cores. XRF scanning is a rapid, non-destructive method for constructing a high-resolution (up to 1 mm), quasi-continuous record of relative variations in elemental composition down-core (Richter *et al*., 2006). These valuable data have many applications, including (but not limited to): down-core correlation (for construction of composite sections), recognition of sedimentological features (e.g., turbidites, ice-rafted debris, facies interpretation, ash layers), and astronomically-tuned climatic and oceanic processes (e.g., terrigenous sediment delivery, biogenic productivity, diagenesis, anoxia, aeolian dust flux, sediment provenance) (Pälike *et al*., 2001; Richter *et al*., 2006; Rothwell and Croudace, 2015).

3.4.2 Common marine core XRF palaeoenvironmental applications

The most commonly-studied elements in marine core XRF analyses are Ca, a proxy for biogenic productivity (e.g., Solignac *et al*., 2011), and Fe and Ti, which generally reflect terrigenous input (e.g., Haug *et al*., 2003; Carlson *et al*., 2008). The use of Ti is often preferable, as it is insensitive to diagenetic redox changes (Rothwell and Croudace, 2015). The calcium carbonate ($CaCO_3$) contents of Atlantic Ocean sediments are well-known to vary on glacial-interglacial timescales, with a greater flux to the deep sea due to high productivity commonly during warmer interglacials, and vice versa (e.g., Balsam and McCoy, 1987). As a result, the ratio Ca/Ti (or Ca/Fe), representing the relative abundance of biogenic carbonate to detrital terrigenous sediment (Rothwell *et al*., 2006), is commonly used as a first-order stratigraphic tool to recognise and correlate

glacial-interglacial cycles (e.g., Richter *et al*., 2006; Hepp *et al*., 2006; Rincón-Martínez *et al*., 2010). Care should be taken when interpreting these sorts of records, however, as this ratio can be skewed by terrigenous dilution and/or calcite dissolution (Rothwell and Croudace, 2015). The Ca/Fe ratio is also useful in Atlantic Ocean textural studies, with coarser intervals characterised by high Ca related to the presence of foraminifera (e.g., Rothwell *et al*., 2006). Peaks in general terrigenous elements Fe, Ti, K and Si can also be indicative of ice-rafting episodes to the deep sea that result in concentrated intervals of coarse IRD (e.g., Hepp *et al*., 2006; Itambi *et al*., 2009). I employ these key elements and their interpretations in my XRF-scanning analysis of Site U1307 sediment, presented in Chapter 5.

A number of XRF studies have been carried out on marine cores from the North Atlantic and Greenland-proximal realm, the majority of which trace climatically-driven changes in flux and composition of terrigenous material. Since the chemistry of sediment eroded from any given source area is governed by that of its parent geology, ratios of certain elements in marine sediments can also be employed to elucidate variations in the relative balance of material from chemically-distinct continental source regions. XRF-scanning-derived ratios of Ti/K and Zr/K have been utilised to trace Svalbard-sourced IRD to the Vøring Plateau during iNHG, since the geology of Svalbard is a unique source for zirconium (Knies *et al*., 2014). On Gardar Drift, southeast of Iceland, the K/Ti ratio has been employed to trace orbitally-paced changes in acidic (higher K/Ti) vs. basaltic (lower K/Ti) sources of sediment and IRD for the past ~1.8 Ma (Grützner and Higgins, 2010) and last glacial cycle (Hodell *et al*., 2010). The K/Ti ratio of sediments deposited on the Faeroe Margin in the Late Pleistocene has also been used in conjunction with magnetic susceptibility data to track greater current-

derived input of basaltic material eroded from the North Atlantic Igneous Province during warm interstadials, with higher K/Ti ratios reflecting greater contributions of ice-rafted continental material during cold stadials (Richter *et al*., 2006). I use the K/Ti ratio in a similar way in Chapter 5 to measure relative changes in the contribution of felsic southern Greenland-sourced material to Site U1307 over the iNHG interval.

The ratios Ca/Sr and Si/Sr have also been used as tracers of Laurentide ice-sheet (LIS) IRD input – sourced from carbonate and silicate parent geologies, respectively – from Hudson Bay to the mid-North Atlantic within the past ~1.4 Ma (Hodell *et al*., 2008). For the Late Quaternary on the southeast Greenland margin, Fe/K ratios have also been used to distinguish basaltic material in IRD (Kuijpers *et al*., 2003). Abundances of Ti and Fe in Eirik Drift sediments have been interpreted to reflect southern Greenland ice-sheet response to the penultimate and last deglaciations (Carlson *et al*., 2008). The release of LIS meltwater from Lake Agassiz ~8.4 ka has also been recognised in Eirik Drift sediments using slightly different XRF methods: one study identified the flood event with the dilution of calcium carbonate (Ca) by terrigenous input (K and Si) (Kleiven *et al*., 2008), whereas another employed Ca/Sr ratios as a tracer of detrital carbonate eroded by the LIS (Nicholl *et al*., 2012).

3.4.3 XRF measurement and limitations

XRF-scanning measurements are performed on split sediment cores or u-channel samples, typically using an Avaatech or Itrax Core Scanner, whereby at each measurement position an incoming X-ray beam hits the surface of the sediment at a 45° angle (Fig. 3.6). Atoms of different elements emit characteristic wavelengths of electromagnetic radiation when excited by X-rays, with intensities

proportional to their concentration in the sediment, and these are recorded by a detector at an opposing 45° angle to the sediment surface (Fig. 3.6) (Richter *et al*., 2006). Each element also has a unique response depth in the sediment depending upon its atomic mass, wavelength of emitted radiation, and chemical composition of the surrounding sediment matrix (Jenkins and De Vries, 1970), and this response depth is smaller the lighter the element; e.g., 1–2 mm for Sr, 1 mm for Fe and 0.5 mm for Ca (Fig. 3.6). The detection limit is therefore highest for the lightest detectable elements (e.g., Al), to ensure a statistically significant signal-to-noise ratio (Richter *et al*., 2006).

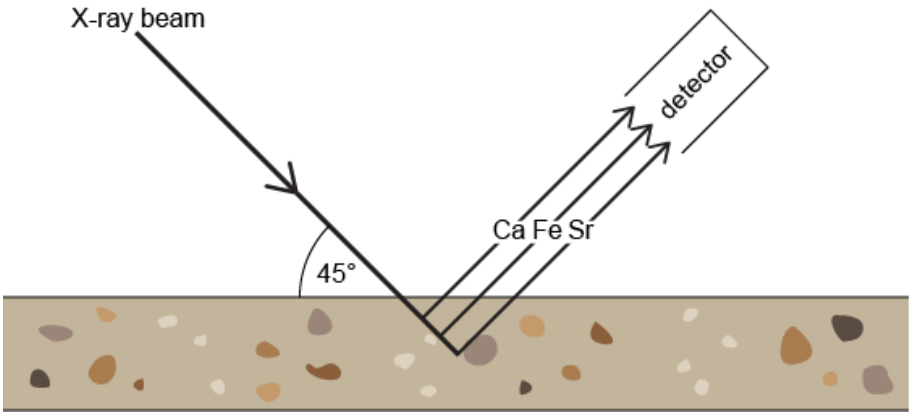

Figure 3.6 Simplified diagram demonstrating XRF analysis on a sediment core sample, with relative response depths (not to scale) of selected elements to incoming X-ray radiation.

Measurement parameters, especially tube voltage and measurement time, can be varied to optimise XRF settings for specific elements, or sets of elements, of interest. The resolution is also important to attain a sufficient analytical volume of sediment to give reliable counts; for fine-grained clayey marine sediments, this is generally accepted as 1 mm (Richter *et al*., 2006). While XRF scanning benefits from many advantages, including minimal sample preparation, non-destructive measurement and rapid acquisition of large elemental datasets, it is important to remember that this data is only semi-quantitative due to the 'rough' nature of split-core and u-channel samples. Unlike high-quality homogenised samples prepared

for discrete XRF analysis, absolute element counts resulting from XRF scanning can be affected by sample heterogeneity, surface roughness and interstitial water content (e.g., Chen *et al*., 2016). Nevertheless, since all detected elements are assumed to be affected similarly by these features, the relative variations in elements downcore are faithfully represented (Richter *et al*., 2006).

3.5 Ice-Rafted Debris Estimates

3.5.1 Overview of IRD

IRD is composed of clay- through boulder-sized terrigenous material that has been glacially eroded and entrained into the basal ice on land via abrasion or plucking, then transported out to sea in icebergs calved from outlet glaciers (e.g., Grobe, 1987; Andrews, 2000) (Fig. 3.7). This definition of IRD is distinct from the generally finer clay- to silt-sized terrigenous material mainly incorporated into, and rafted by, sea-ice in polar regions (sea-ice-rafted debris, SIRD; Darby, 2003), although grain-size cannot be used straightforwardly to distinguish between these two modes of transport in marine sediments (St John *et al*., 2015). Terrigenous clasts that have been subject to iceberg transport typically exhibit an angular shape and textures indicative of mechanical weathering, such as striations and conchoidal fracture (e.g., Eldrett *et al*., 2007; Tripati *et al*., 2008). Debris transported in sea-ice, on the other hand, tends to be (sub)rounded and show textural evidence of chemical weathering, such as silica dissolution pits (e.g., Stickley *et al*., 2009; St John *et al*., 2015). The occurrence of coarse, angular terrigenous sand grains (63–2000 μm) and larger clasts (dropstones) in open subpolar ocean cores is thus interpreted as indirect evidence of terrestrial glaciation, since iceberg transport is the only method for transporting clasts of this nature to the deep ocean (Grobe *et al*., 1987; Bond *et al*., 1992; Andrews, 2000).

Since the presence of coarse IRD in deep marine settings is unaffected by dilution with additional bottom-current derived sedimentation, or winnowing of finer sediment by current action, its contents in a marine core are representative of iceberg activity (Grobe *et al*., 1987).

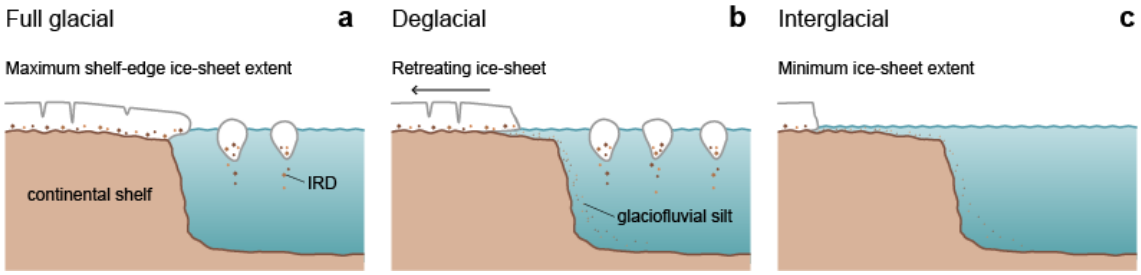

Figure 3.7 Simplified diagram of glacially-eroded sediment output from a high-latitude ice-sheet during different climate states: (**a**) full glacial, with marine-terminating ice-sheet margins and IRD export in calved icebergs; (**b**) deglacial, with retreating ice-sheet margins and export of both IRD via icebergs and glaciofluvial silt via subglacial rivers; and (**c**) interglacial, with minimal/no iceberg-calving and continued (but less) export of glaciofluvial silt.

Generally, the appearance of high abundances of coarse IRD from a given source is evidence for an active iceberg-calving margin in that region, either inland feeding a fjord to the open ocean, at the coast or grounded on the marine shelf, where it is able to calve icebergs at sea-level (e.g., Bailey *et al*., 2012, 2013) (Fig. 3.7). High iceberg flux is also associated with the deglaciation period immediately following these times of glacial maxima (e.g., Stein, 2008) (Fig. 3.7). The 1–3 m-thick layer of sediment entrained in the base of glaciers (Dowdeswell, 1986) is melted out relatively quickly – within a month to a year – from calved icebergs, thus the majority of IRD is deposited within a few 10s to 100s of kilometres from the ice margin (Andrews, 2000). As a result, very little coarse IRD reaches the mid-shelf environment offshore Greenland today, and only during glacial maxima when the GrIS is grounded at the shelf-break is IRD deposited in significant quantities in the deep North Atlantic (e.g., Dowdeswell *et al*., 1995; Andrews, 2000). Studies of Late Pleistocene to modern IRD deposition offshore

East Greenland demonstrate that, even during glacial maxima, the majority of coarse IRD is sourced from the adjacent proximal landmass (e.g., Linthout *et al*., 2000; Andrews *et al*., 2010).

3.5.2 Estimation techniques and limitations

Studies of marine-core IRD over recent decades have not utilised a standard quantification method, choosing various grain-size ranges to take as representative of the terrigenous ice-rafted fraction. These include, but are not limited to: 100–1000 μm (Knies *et al*., 2014), >125 μm (Jansen *et al*., 2000), >150 μm (Bolton *et al*., 2010), 250–2000 μm (St John and Krissek, 2002), and 180–3000 μm (Heinrich, 1988). The majority of these IRD records are presented as weight percent (wt.%) of the bulk sediment (e.g., Heinrich, 1988; St John and Krissek, 2002; Knies *et al*., 2014); however, others choose to employ the grains per gram of sediment (IRD/g) measurement (e.g., Jansen *et al*., 2000). Most methods involve isolating the chosen size fraction through washing the disaggregated bulk discrete sample over a sieve, then studying the dry sediment under binocular light microscope to estimate the amount of terrigenous ice-rafted material, excluding any biogenic and volcanoclastic components (e.g., St John and Krissek, 2002; Bailey *et al*., 2012, 2013). The wt.% IRD for each discrete sample is calculated by dividing the product of the proportion of IRD (a decimal) and the mass of the size fraction (in grams) by the sample dry bulk weight (DBW), which is then expressed as a percentage of the entire sample, such that:

$$wt.\% = \left(\frac{proportion\ IRD \times mass\ of\ fraction}{DBW}\right) \times 100$$

It is generally accepted that the fine sand (>125 μm) to gravel (>2000 μm) grain-size range is most suitable for IRD characterisation; grain-sizes smaller than this range may be transported by other means such as vigorous deep currents, and larger grains tend to be too sporadic in content to use as a realistic measure of iceberg discharge (e.g., Ruddiman, 1977; Bond *et al*., 1992; Andrews, 2000). Some studies also convert these estimates into IRD flux (mass accumulation rate, MAR) in order to represent IRD deposition rates during times of high or low sedimentation more accurately (e.g., Ruddiman, 1977; St John and Krissek, 2002). To do so reliably, however, the rate of sediment accumulation, particularly during peaks in IRD deposition, must be well-constrained (e.g., Andrews, 2000). In Chapter 4, I use the wt.% measure of IRD in the >212 μm fraction of Site U1307 sediments to measure the changing proportion of unequivocally iceberg-rafted material during the iNHG interval.

The interpretation of IRD peaks in ocean core records is not always straightforward (e.g., Andrews, 2000). Changes in IRD flux to the deep ocean can be a result of one or a combination of three different scenarios: 1) increased iceberg discharge, 2) a change in sediment concentration in the source glacier, and 3) a change in the region with the highest iceberg discharge rates (Fronval and Jansen, 1996; Andrews, 2000). Other methods, such as IRD provenance (via simple petrography or more complex geochemical means; e.g., Hemming *et al*., 1998; Linthout *et al*., 2000; Bailey *et al*., 2012, 2013; White *et al*., 2016), are recommended to more clearly interpret their origin (Andrews, 2000). In addition, the expression of ice-rafting recorded at any given site in the North Atlantic is limited by iceberg survivability and melt rates (e.g., Bailey *et al*., 2013); during the Last Glacial Maximum (LGM), IRD was deposited in high abundances in a southwest-northeast-trending zone between ~55–40°N (Ruddiman, 1977).

Surface currents and hence drift paths of icebergs calved from any particular source are also thought to have changed over time depending on climate (e.g., Bailey *et al*., 2013), and so iceberg-trajectory modelling for the present day (e.g., Bigg *et al*., 1998) may not predict the full range of iceberg sources to any given North Atlantic site.

3.6 Pb-Isotope IRD Provenance

3.6.1 Overview of Pb-isotope provenance

As outlined briefly in Chapter 2, the lead (Pb)-isotope composition of individual ice-rafted feldspars is a useful tool for assessing IRD provenance in the North Atlantic region (e.g. Gwiazda *et al*., 1996; Hemming *et al*., 1998; Connelly and Thrane, 2005; Bailey *et al*, 2012, 2013; White *et al*., 2016). Two stable radiogenic isotopes of lead, ^{206}Pb and ^{207}Pb, are created from the decay of two unstable uranium isotopes, ^{238}U and ^{235}U, with respective half-lives of 4.468 Gyr and 704 Myr. Both isotopes were created at similar rates in the time just after the Earth formed, ~4.5 Ga; but after ~2 Ga the production of ^{207}Pb slowed as the inventory of ^{235}U was more quickly depleted. By normalising the two radiogenic isotopes by the stable isotope ^{204}Pb and plotting these ratios versus each other, the isotopic evolution of lead over time can be visualised (Fig. 3.8; Gwiazda *et al*., 1996).

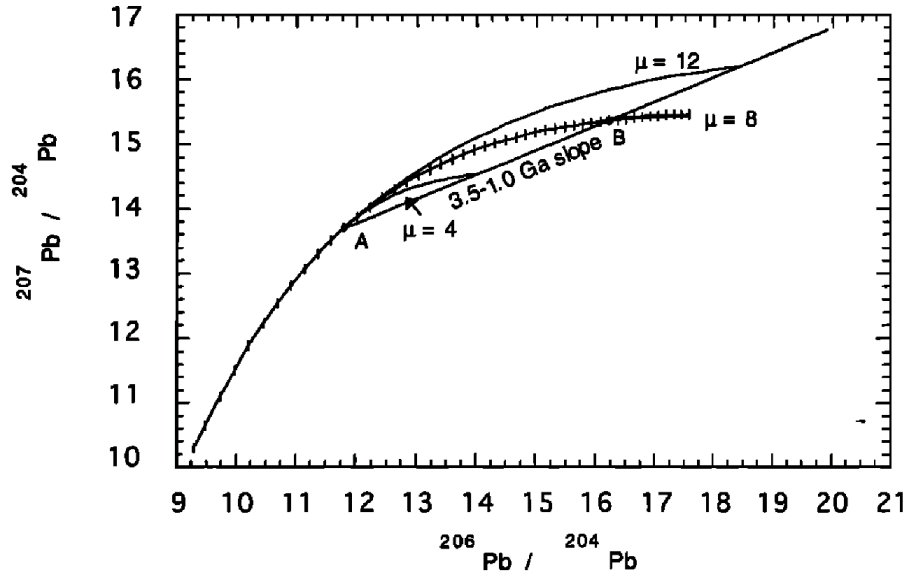

Figure 3.8 Evolution of lead (Pb) in $^{206}Pb/^{204}Pb$ vs. $^{207}Pb/^{204}Pb$ space. Tick lines mark 100 Myr intervals in Pb evolution. Point A is the Pb-isotopic composition of a feldspar grain that crystallized at 3.5 Ga from a reservoir with a $^{238}U/^{204}Pb$ ratio (μ) of 8. During a metamorphic event at 1 Ga the feldspars incorporated different amounts of radiogenic lead produced in the interval 3.5 to 1.0 Ga, represented by the mixing line, which intersects the lead evolution curve of the hypothetical μ = 8 mantle source at the times of initial crystallisation (point A) and metamorphism (point B). From Gwiazda *et al*. (1996).

Different areas of Earth's crust have a distinct Pb-isotopic signature inherited from the equally-distinct mantle reservoirs from which they formed – with additional complexity arising from the degree, extent, number and relative timing of metamorphic and tectonic events during their history – which is also recorded in the rock-forming minerals of each region (Connelly and Thrane, 2005). Adjacent crustal terranes with distinct Pb-isotope signatures that have accreted to each other, such as in Greenland, therefore also tend to have distinct lithologies and pre-orogenic histories (Connelly and Thrane, 2005; White *et al*., 2016). The radiogenic parent-daughter ratio $^{238}U/^{204}Pb$ (μ) is affected by metamorphism due to the higher mobility of U relative to Pb; thus higher-grade rocks have a lower μ (Connelly and Thrane, 2005). Feldspar minerals, especially potassium (K)-feldspar, have a tendency to sequester Pb in their mineral structure (>40 ppm); this makes their Pb-isotope composition a good measure of their initial composition at the time of crystallisation (Hemming *et al*., 1998; Tyrell *et al*.,

2006). K-feldspar is the most common low-μ mineral phase, so its composition is also taken to reflect the most recent phase of metamorphism (Connelly and Thrane, 2005). As such, the measured Pb-isotope composition of a feldspar grain is considered an excellent tracer of its origin (Hemming *et al*., 1998; Tyrell *et al*., 2006).

3.6.2 Pb-isotope provenance applications

The Pb-isotopic fingerprinting of individual sand-sized ice-rafted feldspars has proven useful in tracing sources of IRD to the subpolar North Atlantic during the LGM (Gwiazda *et al*., 1996; Hemming *et al*., 1998; Bailey *et al*., 2012), with single-grain analyses proving more effective at isolating specific sources than multiple-grain composite measurements (Gwiazda *et al*., 1996). The method has also been applied to NHG in order to constrain the relative timing of major glaciation on each Northern Hemisphere continent (Bailey *et al*., 2012, 2013). Changes in IRD provenance to a given site as a glacial cycle progresses are taken to reflect dilution by other sources becoming active iceberg-calving sites (Gwiazda *et al*., 1996; Bailey *et al*., 2012).

Until recently, however, the Pb-isotopic compositions of specific Greenlandic sources were poorly-constrained and based mainly on isolated bedrock samples (Gwiazda *et al*., 1996; Bailey *et al*., 2012). A number of important present-day Greenlandic IRD sources have now been characterised by analyses of individual sand-sized feldspars in samples taken from a range of sandurs (outwash plains formed by detritus-laden glacial meltwater) and Greenland fjord sediments close to iceberg-calving locations (Fig. 3.9a), enabling the designation of distinct individual source fields in Pb-isotope space (Fig. 3.9b) (White *et al*., 2016). The range of Pb-isotope values recorded by sandur and fjord

samples reflects the composition of grains eroded by the whole catchment area of the glacier system, which in some instances crosses terrane boundaries (White *et al*., 2016). Given the distinct ages and tectonic histories of each Greenlandic terrane – the Tertiary volcanic and metasedimentary East Caledonides (EC), and the Nagssugtoqidian Mobile Belt (NMB), Archaean Block (AB) and Ketilidian Mobile Belt (KMB) comprising the felsic Precambrian of southern Greenland (Fig. 3.9a; Escher and Watt, 1979; White *et al*., 2016) – sources from the same terrane tend to group closely in Pb-isotope space and show evolution from the oldest source rocks (lowest Pb-isotope ratios) to the youngest (highest Pb-isotope ratios; Fig. 3.9b).

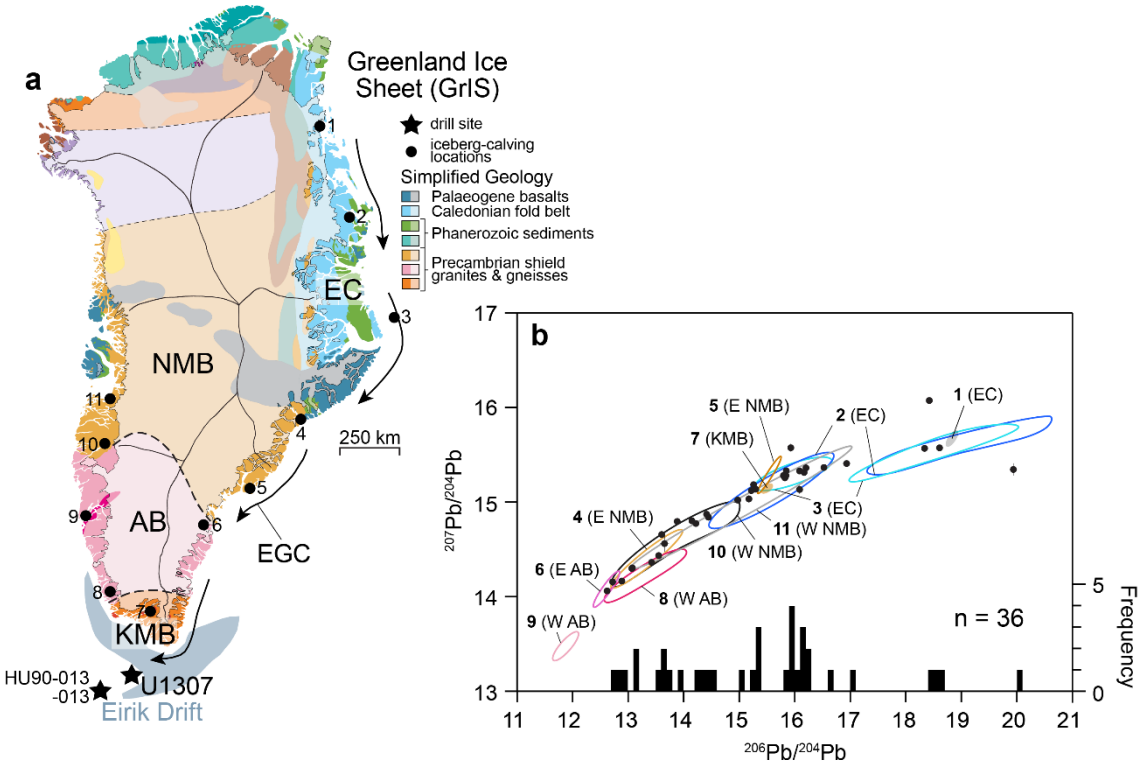

Figure 3.9 Summary of Greenland geochemical terranes and their lead (Pb)-isotopic signatures: (**a**) Geological map of Greenland with geochemical terranes labelled (NMB = Nagssugtoqidian Mobile Belt, AB = Archaean Block, KMB = Ketilidian Mobile Belt, EC = East Caledonides), and the modern-day path of the East Greenland Current (EGC) transporting ice-rafted debris (IRD)-laden icebergs to IODP Site U1307 (the focus of this thesis) on Eirik Drift also indicated; and (**b**) the Pb-isotope fields ($^{206}Pb/^{204}Pb$ vs. $^{207}Pb/^{204}Pb$) for key iceberg-calving locations around the Greenland coastline indicated by matching numbers in (a), defined by analysis of individual sand-sized (>150 μm) feldspars in glaciofluvial and fjord sediments at each locality, with the composition of individual sand-sized (>150 μm), ice-rafted feldspars from Eirik Drift Site HU90-013-013 deposited during the modern (core-top sediment). Histograms of $^{206}Pb/^{204}Pb$ are also shown for reference (modified from White *et al*., 2016).

Analysis of ice-rafted feldspars from core-top (recent) sediments on Eirik Drift plot within a wide range of southeastern Greenland source fields for all four terranes (Fig. 3.9; White *et al*., 2016), similar to those predicted by modern-day iceberg-trajectory modelling (e.g., Bigg *et al*., 1998). This technique therefore enables a level of source-specific detail not previously possible for studies of Greenland-sourced IRD, and can be readily applied to records of IRD deposited during iNHG. In Chapter 6, I use the Pb-isotope ratios of individual ice-rafted feldspars deposited during key glacial cycles throughout the iNHG study interval to investigate the evolution of key iceberg-calving sources, and hence the extent of iceberg-calving margins in southern Greenland, during this time.

3.6.3 Pb-isotope measurement and limitations

In order to ensure individual feldspar grains selected for analysis are unambiguously ice-rafted in origin, most studies utilise the >150 μm size-fraction of sediment (e.g., Gwiazda *et al*., 1996; Bailey *et al*., 2012, 2013); but others may be used as long as they are within the generally-accepted size range for IRD (e.g., >250 μm; Hemming *et al*., 1998). Once isolated, individual feldspars are set in a clear Pb-free epoxy resin block, polished to expose grain centres for analysis, and analysed for their Pb-isotopic composition typically using laser-ablation inductively-coupled-plasma mass-spectrometry (LA-ICP-MS) (e.g., Bailey *et al*., 2012, 2013; White *et al*., 2016). Ablation is performed in a 100% helium environment, and the ablated material and He are mixed with argon (+ N_2) gas downstream of the ablation chamber. Since each isotope of lead has a slightly different atomic mass, the instrument's magnet deflects them by a marginally different degree, and the relative abundance of each isotope is measured. Isobaric interference of ^{204}Hg on ^{204}Pb is corrected for using natural ratios of ^{204}Hg

with ^{202}Hg or ^{200}Hg (Platzner, 1997), and sample isotopic ratios are systematically compared to those of carefully-controlled internal standards to ensure reliablilty of measurements and correct for instrumental bias (Tyrell *et al*., 2006).

Despite the relatively good characterisation of IRD sources to the North Atlantic, there are a number of limitations to consider with this provenance method. A large degree of overlap exists between some Pb-isotope source fields (Fig. 3.8b), so unambiguous provenance identification is not always possible (Gwiazda *et al*., 1996; Bailey *et al*., 2012). In some cases the number of feldspars practically available in a sample for analysis may not meet the statistical minimum to capture and quantify the full range of provenance, especially minor rare sources (Gwiazda *et al*., 1996; Hemming *et al*., 1998). In addition, there may be important sources of IRD to the North Atlantic that are not yet characterised (e.g., from the Ketilidian Mobile Belt, KMB, to Eirik Drift; Fig. 3.8a) (White *et al*., 2016). Hence, a multi-proxy approach (e.g., composite multiple-grain/bulk sediment Pb-isotope analyses, other mineralogical analysis) is preferable to reduce ambiguity and provide additional evidence when attempting to tie IRD to specific sources (Gwiazda *et al*., 1996; Hemming *et al*., 1998).

3.7 SEM-Based IRD Mineralogical Provenance

3.7.1 Overview of QEMSCAN® and its applications

QEMSCAN® – Quantitative Evaluation of Minerals by SCANning Electron Microscopy – is an automated mineralogical analysis consisting of both hardware and software modules that control a scanning electron microscope (SEM) to rapidly gather and process high-resolution, quantitative mineral data from solid inorganic samples (e.g., Gottlieb *et al*., 2000; Pirrie *et al*., 2004; Pirrie and Rollinson, 2011). It was originally designed for use in the mining and mineral

processing industries to evaluate the grade of ore bodies and the effectiveness of mineral concentrate processing (Pirrie *et al*., 2004; Gu *et al*., 2003; Andersen *et al*., 2009; Pirrie and Rollinson, 2011). Due to its ability to rapidly quantify and produce false-colour images of whole-rock and particulate mineralogy, as well as other parameters such as shape, texture and density, it has since found many other uses in forensic geoscience (e.g., linking a suspect to a crime scene with soil provenance; Pirrie *et al*., 2004, 2013; Pirrie and Rollinson, 2011), archaeology (e.g., mineralogy and provenance of ancient ceramics; Knappett *et al*., 2011), sedimentology (e.g., sandstone mineralogy and provenance; Zhang *et al*., 2015) and environmental monitoring (e.g., soil contamination from local mining operations; Camm *et al*., 2004).

With an upper particle size limit of 1 mm and a minimum feature detection limit of 1 µm (Gottlieb *et al*., 2000; Pirrie *et al*., 2004; Pirrie and Rollinson, 2011), QEMSCAN® may prove to be an extremely useful, cost- and time-effective tool in rapidly quantifying the mineralogy, textures and shapes of IRD. This sort of information is typically collected through time-consuming manual point-counts under light microscope, with potential for human error. Automated SEM-based analysis of particle samples removes operator bias, produces statistically valid data (up to ~1000 grains per sample), ensures rare minerals (potentially important for determining provenance) are not overlooked, and allows direct comparison between samples due to the application of set operator-defined rules in the processing stages (Gottlieb *et al*., 2000; Pirrie *et al*., 2004; Pirrie and Rollinson, 2011).

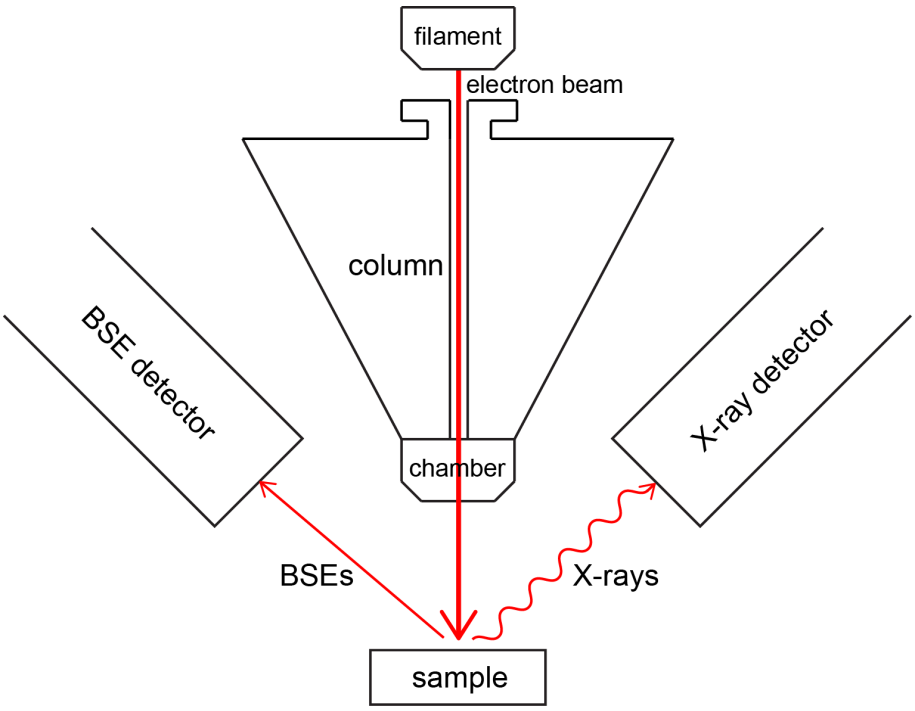

Figure 3.10 Simplified schematic of the SEM system configuration, illustrating how the electron beam generated in the tungsten filament and fired down the column (containing electromagnetic coils) interacts with the sample to produce back-scattered electrons (BSEs) and X-rays characteristic of each element excited, which are detected by separate detectors.

3.7.2 SEM measurement and limitations

Representative particle subsamples of ~1000 grains are typically set in a 30 mm-diameter clear epoxy resin block, ensuring random grain orientation and separation, and polished to expose grain centres for analysis (Gottlieb *et al*., 2000; Pirrie *et al*., 2004). The block is then coated with an extremely thin layer of carbon to create a conductive surface that inhibits the build-up of electric charge, reduces thermal damage to the sample and improves the secondary electron signal during analysis (Reed, 2005). Once mounted in the SEM analysis chamber under high vacuum, the mode of measurement, grain-size detection limits, pixel spacing, beam stepping interval, and other job-dependent parameters are defined based on the sample type, resolution required, and time limits (Pirrie *et al*., 2004; Pirrie and Rollinson, 2011). An electron beam is then fired at the sample surface, causing the production of 1) secondary electrons in the surface, 2) back-scatter electrons (BSE) in the subsurface, and 3) X-rays characteristic of the

element excited in the sample (energy-dispersive spectra, EDS), all of which are recorded by separate detectors above the sample surface (see Fig. 3.10 for a simplified schematic; Gottlieb *et al*., 2000; Pirrie *et al*., 2004; Reed, 2005). The sample is scanned on a micron grid basis, depending on the chosen pixel spacing, and both BSE and X-ray EDS data are collected for each analysis point at a rate of ~10 milliseconds per pixel (Pirrie *et al*., 2004). The BSE information is primarily used to build a high-resolution image of the sample surface, differentiating particles from the surrounding resin (Gottlieb *et al*., 2000; Pirrie *et al*., 2004). The X-ray EDS information produces spectra with peaks of varying heights resulting from the relative intensities of each element present, and so systematically maps the near-surface chemical composition of each particle (Pirrie *et al*., 2004). These acquired spectra are automatically compared to an in-built database that identifies the minerals (and mineral phases) present using the intensity of each element peak and their ratio to each other, based upon set definitions of which elements should and may be present (Gottlieb *et al*., 2000; Pirrie and Rollinson, 2011). This creates a false-colour mineralogical map of the sample (Pirrie and Rollinson, 2011).

Once the measurement is complete, the data is user-processed using the QEMSCAN® software based upon the level of detail required, extracting statistics and condensing the identified mineral species into groupings suitable for interpretation (Gottlieb *et al*., 2000). This exercise is dependent upon a good knowledge of relevant mineral species/phases needed to address the research aims (Pirrie and Rollinson, 2011). Care must be taken when assigning boundary phase minerals (commonly identified by the database where two different mineral phases meet) to one or another mineral grouping when cleaning up the data (Pirrie *et al*., 2004). Minerals that are very close to one another in chemical

composition – or polymorphs of minerals – may be differentiated based on the BSE information (Gottlieb *et al*., 2000; Pirrie and Rollinson, 2011). Aside from the skill and job-specific knowledge required in both running and processing QEMSCAN® sample data (Pirrie and Rollinson, 2011), using this information to glean an estimate of IRD provenance comes with its own limitations in that it requires good characterisation of source geologies, and that their compositions are accurately reflected by the associations of minerals in composite IRD grains (Pirrie *et al*., 2013). I employ this technique in Chapter 6 in order to investigate changes in Site U1307 bulk sand mineralogy, relating to the relative contribution of sediment originating from eastern mafic and southern felsic Greenland terranes.

3.8 Summary

I have a wide variety of sedimentological and geochemical tools and proxies at my disposal to investigate the history of the Greenland Ice Sheet (GrIS) during the intensification of Northern Hemisphere glaciation, many of which have already proven effective in measuring variability in ice-rafted debris (IRD) and glaciofluvial sediment delivery, as well as the provenance of IRD, in similar settings and more recent time periods. Generation of a new relative palaeointensity-based age model will enable variability in all records gleaned from Site U1307 sediments to be precisely dated, fulfilling the research aims by: 1) establishing when a modern-like GrIS was established during iNHG (Chapters 4 and 6); 2) elucidating changes (if any) in the delivery of sediment supplied by the deep Western Boundary Undercurrent (Chapter 4); 3) identifying the presence of inland ice in the absence of abundant IRD via glaciofluvial sediment

output (Chapters 4 and 5); and 4) reconstructing the specific evolution of key iceberg-calving sources (Chapter 6).

Chapter 4

Southern Greenland glaciation and Western Boundary Undercurrent evolution recorded on Eirik Drift during the late Pliocene intensification of Northern Hemisphere glaciation

This chapter is modified from **Blake-Mizen**, K., Hatfield, R.G., Stoner, J.S., Carlson, A.E., Xuan, C., Walczak, M., Lawrence, K.T., Channell, J.E.T., Bailey, I., 2019. Southern Greenland glaciation and Western Boundary Undercurrent evolution recorded on Eirik Drift during the late Pliocene intensification of Northern Hemisphere glaciation. *Quaternary Science Reviews 209 (2019), 40–51.* I performed the sample processing, ice-rafted debris analysis, grain-size analysis, palaeomagnetic data collection, splice revision and age-model generation, and the majority of the interpretations. Robert Hatfield and Chuang Xuan assisted with the palaeomagnetic data processing and interpretation. Rob Fitzpatrick assisted with physical grain-size data collection.

4.1 Introduction

While glaciers have existed intermittently on Greenland since at least the late Eocene, with its first ice-shelf glaciations occurring possibly as early as the Miocene (Larsen *et al*., 1994), multiple lines of evidence (e.g., Larsen *et al*., 1994; Jansen *et al*., 2000; Thiede *et al*., 2011; Bierman *et al*., 2016) suggest that a major ice-sheet was not a persistent feature on Greenland until the late Pliocene to earliest Pleistocene intensification of Northern Hemisphere glaciation (iNHG), ~3.6–2.4 Ma (Mudelsee and Raymo, 2005). Our understanding of the spatial history of ice-sheet expansion on Greenland at this time, however, remains uncertain.

Since terrestrial evidence of Greenland glaciation during iNHG is rare (and its temporal interpretation non-unique, e.g., Schaefer *et al*., 2016) due to its removal by subsequent glacial advances, our understanding of Greenland Ice Sheet (GrIS) evolution during the Plio-Pleistocene mainly relies on Greenland-proximal marine sediment records of ice-rafted debris (IRD; e.g., Jansen *et al*., 2000; Thiede *et al*., 2011). Greenland-proximal IRD deposition is dominated by terrigenous sediment transported mainly by the East Greenland Current (EGC) in icebergs derived from multiple GrIS iceberg-calving sources (Fig. 4.1; Bigg *et al*., 1998; White *et al*., 2016). Spatial comparisons of orbitally-resolved palaeo-records of marine IRD deposition near Greenland can therefore provide important insights into where and when the GrIS extended to the coast during iNHG. For this time period, IRD records are available from sites where ice-rafted sediments were sourced from northeastern (Ocean Drilling Project (ODP) Site 907; Jansen *et al*., 2000), eastern (ODP Site 907; Jansen *et al*., 2000; ODP Sites 914–918; Larsen *et al*., 1994; St John and Krissek, 2002) and southern (ODP Site 646; Wolf and Thiede, 1991) Greenland (Figs. 4.1 and 4.2). However, due to low

benthic foraminifera abundances, it is not possible to generate independent orbital-resolution benthic $\delta^{18}O$ stratigraphies for any of these Greenland-proximal records spanning iNHG. Poor core recovery has also prevented the construction of detailed palaeomagnetic stratigraphies for most of these sites.

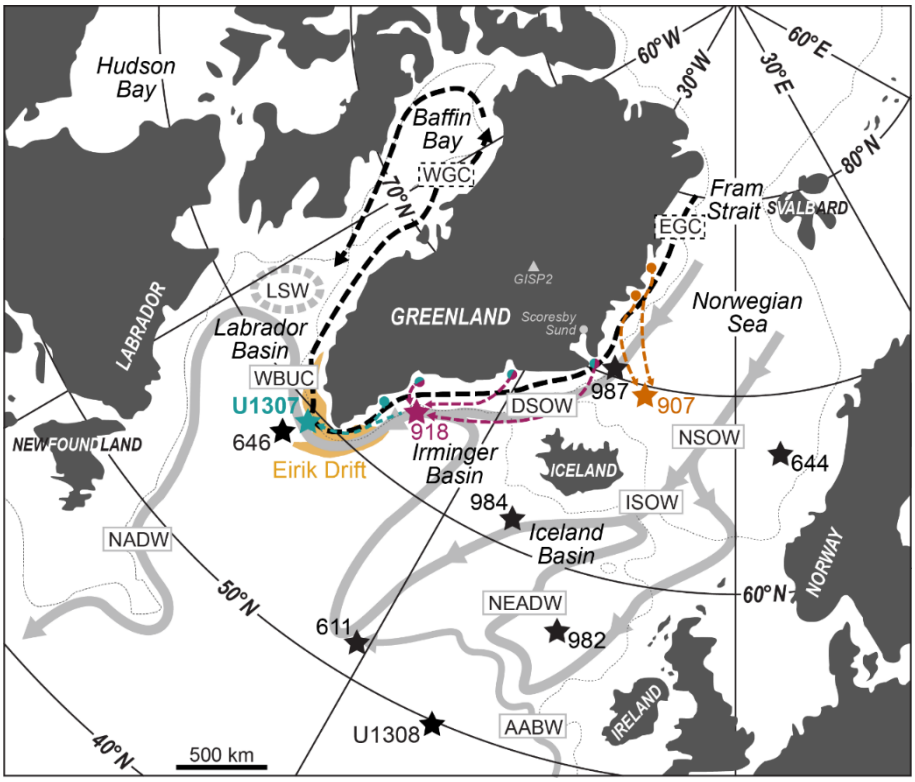

Figure 4.1 Map of Greenland and surrounding landmasses and ocean basins, showing the location of IODP Site U1307 on Eirik Drift, the position of sites mentioned in this text, and their relationships to the paths of key modern deep (solid grey) and surface (dashed black) ocean currents relevant to this study. ODP Sites 907 and 918, whose ice-rafting records are discussed in the text, are also highlighted, and main sources of ice-rafted debris to these sites and to U1307 are schematically represented by colour-coded arrows (based on iceberg trajectory simulations for the Last Glacial Maximum by Bigg *et al*., 1998). EGC = East Greenland Current, WGC = West Greenland Current, NSOW = Norwegian Sea Water, ISOW = Iceland-Scotland Overflow Water, DSOW = Denmark-Scotland Overflow Water, NEADW = Northeast Atlantic Deep Water, AABW = Antarctic Bottom Water, WBUC = Western Boundary Undercurrent, LSW = Labrador Sea Water, NADW = North Atlantic Deep Water. The 1000 m isobath is given by thin dotted lines.

The only continuous orbital-resolution Greenland-proximal IRD record with a complete palaeomagnetic reversal stratigraphy for iNHG comes from Site 907 on the Iceland Plateau (Figs. 4.1 and 4.2c; Jansen *et al*., 2000). Based on elevated IRD deposition at this site from ~3 Ma (Fig. 4.2c and d), it can be inferred that at least isolated iceberg-calving glaciers occupied coastal northeastern and eastern

Greenland on orbital timescales following the end of the mid-Piacenzian warm period (mPWP, 3.264–3.025 Ma; Dolan *et al*., 2011) (see iceberg trajectories shown in Fig. 4.1; Bigg *et al.*, 1998). A further and significant increase in IRD deposition at Site 907 from ~2.7 Ma indicates, however, that extensive iceberg-calving margins may not have been established in this region of Greenland until Marine Isotope Stage (MIS) G6, 2.72 Ma (Lisiecki and Raymo, 2005) (Fig. 4.2c and d). This suggestion is broadly supported by seismic evidence offshore Scoresby Sund that confirms the central-eastern GrIS was only frequently grounded below sea-level from ~2.6 Ma (Vanneste *et al*., 1995), and by a recent study of the cosmogenic radionuclide (^{10}Be and ^{26}Al) isotope composition of quartz sands from ODP Sites 918 and 987 (Figs. 4.1 and 4.2b; Bierman *et al*., 2016) that infers the existence of a large ice-cap on at least eastern Greenland since the onset of the Quaternary. Our ability to improve our understanding of the wider regional history of GrIS growth during this time is hampered, however, by a lack of a well-dated, orbital-resolution continuous IRD record that is well-placed to receive detritus from southeastern and southern Greenland during iNHG.

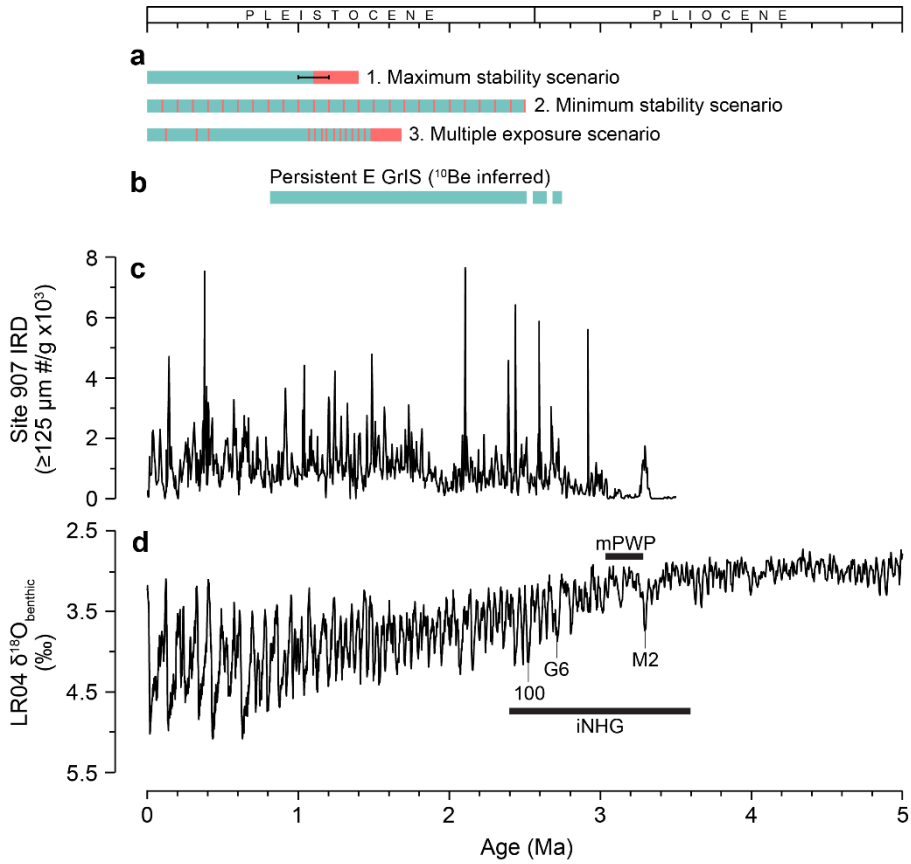

Figure 4.2 Synthesis of palaeoclimatic records relevant to the Plio-Pleistocene history of the Greenland Ice Sheet (GrIS): (**a**) three scenarios for GrIS glaciation consistent with cosmogenic beryllium (^{10}Be) and aluminium (^{26}Al) isotopes in bedrock from the base of the GISP2 ice core (see Fig. 4.1 for location) (1. Maximum stability scenario = 280 ±30 kyr ice-free conditions followed by 1.1 Ma continuous ice cover; 2. Minimum stability scenario = ice-free for 8 kyr of each 100-kyr cycle; 3. Multiple exposure scenario = ice-free for several thousand years during numerous major Pleistocene interglacials; Schaefer *et al*., 2016); (**b**) periods of eastern GrIS growth and stability inferred from seismic profiles offshore Scoresby Sund indicating East GrIS frequently grounded below sea-level (Vanneste *et al*., 1995) and from cosmogenic ^{10}Be and ^{26}Al isotopes in marine cores offshore eastern Greenland (Bierman *et al*., 2016); alongside (**c**) Iceland Basin ODP Site 907 IRD flux (Jansen *et al*., 2000); and (**d**) the LR04 $\delta^{18}O_{benthic}$ stack for reference (Lisiecki and Raymo, 2005). Labels in (d) are Marine Isotope Stages, and durations of the intensification of Northern Hemisphere glaciation (iNHG) and the mid-Piacenzian warm period (mPWP; Dolan *et al*., 2011) are also indicated.

Eirik Drift off southern Greenland is ideally located to monitor the history of the southern GrIS because it lies in the path of the EGC, and in the present day receives IRD from a range of eastern and southern Greenland iceberg-calving sources (Bigg *et al*., 1996; White *et al*., 2016). It is also well-positioned to monitor the strength of the Western Boundary Undercurrent (WBUC; Hunter *et al*., 2007), the behaviour of which during iNHG is not fully understood (Hunter *et al*., 2007; Müller-Michaelis and Uenzelmann-Neben, 2014; Parnell-Turner *et al*., 2015). Studies that combine analysis of both the sedimentological character and

environmental magnetic signature of Pleistocene sediments from Eirik Drift have proved particularly useful in this regard, because they can be utilised to reconstruct relative changes in bottom-current strength and the provenance of glacially-derived terrigenous sediments from southern Greenland that they entrain (e.g., Evans *et al.*, 2007; Stoner *et al*., 1995; Hatfield *et al*., 2016; 2017; Channell *et al.*, 2014). However, these techniques have yet to be applied to records spanning the iNHG interval.

To further our understanding of GrIS and WBUC behaviour during iNHG, this chapter presents high-resolution IRD, palaeomagnetic and environmental magnetic records spanning ~3.2 to 2.2 Ma from Integrated Ocean Drilling Program (IODP) Site U1307, situated on Eirik Drift in the northern North Atlantic Ocean (Fig. 4.1). This study benefits from updated chronological control through the generation of a new relative palaeointensity (RPI)-based age model – the first of its kind for high-latitude sediments deposited during iNHG. On this high-fidelity age model, the new high-resolution multi-proxy records demonstrate for the first time that glacial maturation of southern Greenland ~2.7 Ma occurred in concert with a change in WBUC behaviour.

4.2 Study Site and Methods

4.2.1 Study site and sampling

Eirik Drift is an extensive, elongate contourite drift located just south of Greenland (Fig. 4.1) that began to form in the Miocene (Hunter *et al*., 2007; Müller-Michaelis and Uenzelmann-Neben, 2014). It lies underneath the path of the EGC, a southward-flowing surface current that transports icebergs calved from outlet glaciers along Greenland's eastern coast. Eirik Drift is also sculpted directly by the vigorous and dynamic deep WBUC, the main axis of which shoals during late

Pleistocene glacials (Hillaire-Marcel *et al.*, 1994; Hillaire-Marcel and Bilodeau, 2000; Mazaud *et al*., 2015). The EGC and WBUC constitute major transport pathways for delivering detrital sediments glacially eroded on Greenland to the adjacent marine margins, and ultimately to Eirik Drift (Hunter *et al*., 2007). Icebergs transported along the EGC can contain clay- to boulder-sized IRD from a range of marine-terminating eastern and southern Greenland iceberg-calving sources, which rains out to the seabed as they melt (Fig. 4.1; White *et al*., 2016). The WBUC can entrain these sediments and mix them with subglacially-eroded southern Greenland Precambrian terrane bedrock clay- and silt-sized grains, as well as volcanic detritus from East Greenland and Iceland (Stoner *et al*., 1995; Carlson *et al*., 2008; Colville *et al*., 2011; Hatfield *et al*., 2016).

IODP Site U1307 is located on the northern flank of Eirik Drift (Fig 1; 58°30.3'N, 46°24.0'W, 2575 m water depth). Two holes were drilled at Site U1307 (U1307A and U1307B) during IODP Expedition 303 in 2004, which together recovered a ~175 m composite Plio-Pleistocene section (Expedition 303 Scientists, 2006a). To examine the evolution of the southern GrIS and WBUC during iNHG, I sampled the Site U1307 cores with u-channels (typically 2 × 2 × 150 cm continuous samples; Weeks *et al*., 1993) for palaeomagnetic analysis and discrete 20 cc scoops for IRD analysis at 10 cm intervals at the MARUM IODP Core Repository in Bremen, Germany, in September 2014. Sampling was guided by the shipboard-derived palaeomagnetic record and the primary splice (Expedition 303 Scientists, 2006a) between ~113 and 148 metres below seafloor (mbsf) in U1307A, and ~110 and 136 mbsf in U1307B.

4.2.2 Methods

4.2.2.1 Palaeo- and environmental magnetism

I measured the natural remanent magnetisation (NRM) and anhysteretic remanent magnetisation (ARM) of each u-channel sample at 1-cm intervals using a 2G Enterprises™ model 755-1.65UC superconducting rock magnetometer at the Palaeo- and Environmental Magnetism Laboratory at Oregon State University (OSU), in September–October 2015. The response function of this particular instrument has circular axial (z) coils with a diameter of ~85 mm, with saddle coil pairs of ~68 mm length formed on the same cylindrical tube with an axial-coil pair separation of ~24 mm; a setup optimised for both discrete sample measurements and high-resolution u-channel measurements (Oda and Xuan, 2014). NRM was measured following inline stepwise alternating field (AF) demagnetisation at peak AF from 20 to 80 mT. I applied additional steps up to peak AF of 100 mT to nine u-channels known from shipboard palaeomagnetic measurements to contain a polarity reversal (Expedition 303 Scientists, 2006a), in order to more fully capture the reversal. Component palaeomagnetic directions used to define the characteristic remanent magnetisation (ChRM) directions, and maximum angular deviation (MAD) used to assess the quality of the component magnetisation estimates, were calculated by my colleague Chuang Xuan from principal component analysis of 7 equally-spaced demagnetisation steps over 20–50 mT following Kirschvink (1980), using the UPmag software of Xuan and Channell (2009). Guided by the inclination data, I rotated declination values to a mean of 0° (180°) for periods of normal (reversed) polarity on a core-by-core basis.

ARM was acquired inline using a 100 mT peak AF and a 0.05 mT direct current (DC) bias field along each u-channel's long-axis. I remeasured the ARM after each 5–10 mT increment of AF demagnetisation in the 10–60 mT peak field

range. I also measured low-field volume-normalised (bulk) magnetic susceptibility (κ) every 1 cm for each u-channel at OSU's Marine Geology Repository, using a Bartington MS2C 36 mm diameter loop sensor mounted on a software motion-controlled track. ARM and κ both reflect the concentration of ferrimagnetic (titanomagnetite, magnetite) grains in a sample, although ARM is more sensitive to the fine ferrimagnetic fraction (King *et al*., 1983).

I determined the susceptibility of ARM (κ_{ARM}) by normalising ARM by the DC field applied during ARM acquisition. The ratio of κ_{ARM} over the low-field bulk magnetic susceptibility, κ_{ARM}/κ, is commonly used to track variations in ferrimagnetic grain-size. Low (high) κ_{ARM}/κ values imply a coarser (finer) average ferrimagnetic grain-size (King *et al*., 1983; Bloemendal *et al*. 1992), and this parameter has been used in Pleistocene North Atlantic studies to monitor variations in deep-water circulation and inputs of Greenlandic detritus (e.g., Stoner *et al*., 1995; Evans *et al*., 2007; Mazaud *et al*., 2012; Channell *et al*., 2014).

The magnetic signature of Eirik Drift is sensitive to deposition of glaciofluvial silt-size sediments subglacially eroded from Archean and Palaeoproterozoic felsic crystalline bedrock by the GrIS, and Cenozoic volcanics from Iceland and eastern Greenland (e.g., Colville *et al*., 2011). These distinct sources can be discriminated using radiogenic (Colville *et al.*, 2011) and magnetic (Hatfield *et al.*, 2013; 2017) properties measured on a particle-size specific basis. Clay-sized terrestrial fractions (defined here as <3 μm) from both Greenland and Iceland are characterised by low concentrations of ferrimagnetic minerals (low κ) and relatively fine ferrimagnetic grain-sizes (high κ_{ARM}/κ). In contrast, silt (and sand) size fractions from both sources have up to an order of magnitude higher magnetic susceptibility (Hatfield *et al.*, 2017), indicating higher concentrations of ferrimagnetic minerals in the larger size fractions. Silts and sands from Iceland

are dominated by magnetically fine-grained titanomagnetite inclusions (yielding higher κ_{ARM}/κ values), which can be discriminated from Greenland-derived silts and sands that are dominated by coarser discrete magnetites (yielding lower κ_{ARM}/κ values) (Hatfield *et al.*, 2013; 2017). While Eirik Drift bulk sediments are an aggregate of magnetically-fine silts and sands from Iceland and magnetically-fine clays that can originate from multiple sources, significant source-driven coarsening of the bulk magnetic grain-size record can only be driven by accumulation of Greenland-derived silt and sand, which can be linked to changes in GrIS dynamics (Colville *et al*., 2011; Hatfield *et al*., 2016).

4.2.2.2 Shipboard splice revision

To improve the continuity of the iNHG record from Site U1307, I used the new high-resolution u-channel κ data to revise the shipboard splice for the target interval. The revised splice for ~117–176 revised metres composite depth, rmcd (Fig. 4.3 and Table 4.1; see also Appendix A Table S1 for the complete Site U1307 revised splice) uses, but refines, tie points utilised in the shipboard splice (Expedition 303 Scientists, 2006a). By including cores A-16H and A-17H, existing gaps of ~0.2 m (between cores B-14H and B-15H) and ~0.9 m (between B-15H and B-16H) in the shipboard splice are almost fully resolved, with a negligible gap persisting between B-15H and B-17H (see also Appendix A Fig. S2).

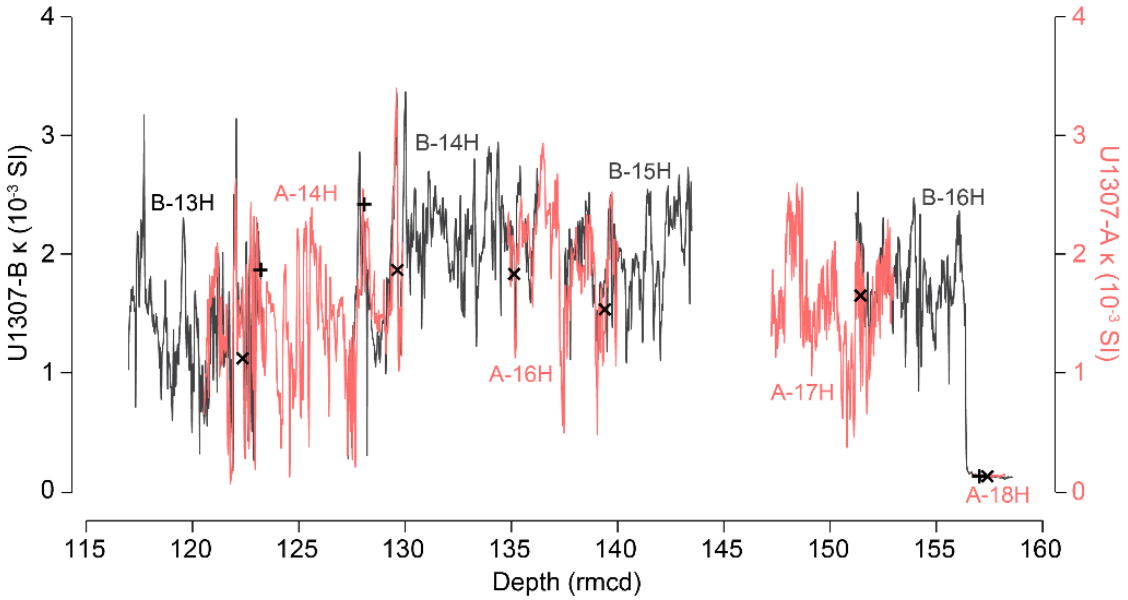

Figure 4.3 Plot of new high (1 cm)-resolution u-channel-derived magnetic susceptibility (κ) data for IODP Site U1307 Hole A (red) and Hole B (black) between ~117 and 158 revised metres composite depth (rmcd; see Table 4.1). Newly-determined splice-points are denoted by black crosses (×) with original shipboard splice points indicated by black plus (+) symbols. The data gap between B-15H and A-17H reflects the absence of u-channel κ data for the bottom 223 cm of B-15H and the top 150 cm of A-17H.

Table 4.1 Site U1307 stratigraphy: comparison of shipboard-derived and revised splice (this study). See Appendix A Table S1 for complete revised splice.

Hole-Core	Shipboard splice[a]		Revised splice			Hole-Core	Shipboard splice[a]		Revised splice	
	mbsf	mcd	mbsf	rmcd			mbsf	mcd	mbsf	rmcd
U1307B-13H	116.62	123.15	115.82	122.35	tie	U1307A-14H	115.24	123.15	114.44	122.35
U1307A-14H	120.13	128.04	121.73	129.64	tie	U1307B-14H	120.06	128.04	121.74	129.64
U1307B-14H	-	-	127.22	135.13	tie	U1307A-16H	-	-	129.34	135.13
U1307B-14H	128.40	136.38	-	-	append	U1307B-15H	128.30	136.55	-	-
U1307A-16H	-	-	133.62	139.40	tie	U1307B-15H	-	-	131.70	139.40
U1307B-15H	138.00	146.25	-	-	append	U1307B-16H	137.80	147.12	-	-
U1307B-15H	-	-	138.00	145.70	append*	U1307A-17H	-	-	135.20	145.70
U1307A-17H	-	-	140.93	151.43	tie	U1307B-16H	-	-	139.65	151.43
U1307B-16H	145.25	154.57	145.63	157.41	tie	U1307A-18H	146.18	154.47	146.89	157.41
U1307A-18H	152.93	161.32	152.93	163.44	append	U1307A-19H	153.10	163.71	153.10	165.83
						U1307A-19H	162.81	173.42	162.81	175.54

mbsf = metres below seafloor; (r)mcd = (revised) metres composite depth.
[a]Expedition 303 Scientists (2006a).
*See Appendix A Fig. S2.

4.2.2.3 Relative palaeointensity (RPI)-based age model

Benthic foraminifera abundances are low in Pliocene-aged Eirik Drift sediments (Expedition 303 Scientists, 2006a). It is therefore difficult to generate a benthic $\delta^{18}O$-based age model for Site U1307, and planktic $\delta^{18}O$-derived records from this region can be influenced by freshwater inputs from ice melt (Hillaire-Marcel *et al.*, 1994). To circumvent these problems, I generated a reversal- and a relative palaeointensity (RPI)-based magnetostratigraphy using the u-channel NRM and ARM data. To generate reliable RPI estimates, it is generally accepted that variations in magnetic grain size and magnetic concentration should be minimal (less than an order of magnitude in concentration), and that the magnetic mineralogy remains uniform throughout the interval of interest (e.g., Evans *et al*., 2007). For the study interval at Site U1307, κ and ARM vary within an order of magnitude (Fig. 4.4a).

Previous palaeomagnetic studies of Eirik Drift sediments (Stoner *et al*., 1995; Evans *et al*., 2007; Mazaud *et al*., 2012; Channell *et al*., 2014) and of Site U1307 cores in particular (Kawamura *et al*., 2012; Mazaud *et al*., 2015) have demonstrated that the magnetic assemblage is dominated by (titano)magnetite with relatively uniform grain-sizes, which aids the recording of a reliable magnetic signal (King *et al*., 1983). A Day plot (Day *et al*., 1977) of Site U1307 hysteresis ratios (Fig. 4.4b; Kawamura *et al*., 2012) shows that, for the study interval, ferrimagnetic grain sizes are fairly well-constrained in the coarse PSD range, and are similar to, and overlap with, hysteresis ratios from shallower depths at U1307 (Mazaud *et al*., 2015). This suggests that Site U1307 (titano)magnetites generally fall within the size range considered to be most suitable for RPI determination (King *et al*., 1983). The lack of a clear relationship between NRM/ARM vs. ARM data (Fig. 4.4c) indicates that NRM/ARM (RPI estimate) is not dependant on

environmental variations in ferrimagnetic concentration (e.g., King *et al*., 1983), and is thus sensitive to variations in past field intensity.

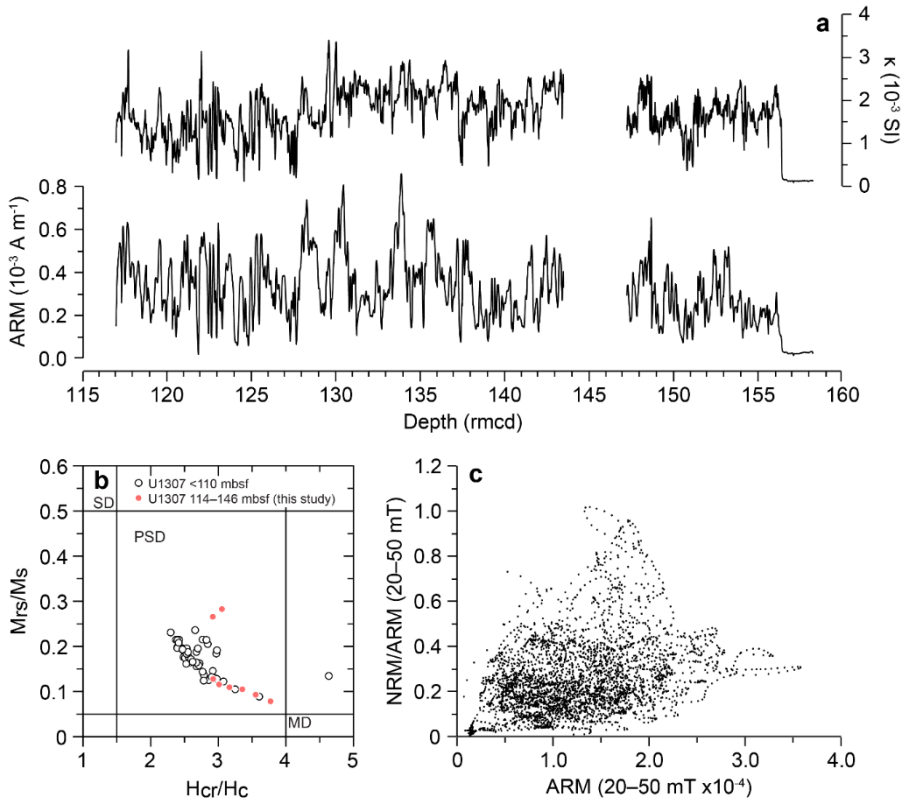

Figure 4.4 Plot of Site U1307 (**a**) low-field bulk volume magnetic susceptibility (κ) and u-channel-derived anhysteretic remanent magnetisation (ARM before AF demagnetisation) against revised metres composite depth (rmcd); (**b**) hysteresis parameters (Mrs/Ms, ratio of remanent saturation moment Mrs, to saturation moment Ms; against Hcr/Hc, ratio of remanent coercive force, Hcr, to coercive force, Hc) for single U1307 samples showing (titano)magnetite grain size distribution, plotted on a Day *et al*. (1977) diagram (MD = multi-domain grains, PSD = pseudo-single domain, SD = single domain), with samples in the study interval indicated by red points (modified from Kawamura *et al*., 2012); and (**c**) bivariate plot of natural remanent magnetisation (NRM)/ARM vs ARM for the 20–50 mT peak field interval.

Component u-channel inclination and declination data for ~117–158 rmcd are given in Figure 4.5a–b, alongside the MAD values in Figure 4.5c. MAD values are generally low (<5°), reflecting a well-defined ChRM magnetisation. However, higher (up to ~45°) values are a feature of polarity reversals and other low intensity intervals, indicating complex or poorly constrained ChRM directions at these times (Fig. 4.5c). Inclination values for both polarities vary close to the expected value (±72.5°) assuming a geocentric axial dipole field (Fig. 4.5b). The

declination record reveals reversal horizons coeval with the inclination data (Fig. 4.5a), which can then be correlated to the geomagnetic polarity time scale. Based on these data, I identify the Gauss-Matuyama (G/M) boundary (C2An.1n top) at 125.10 rmcd (~2.581 Ma; Ogg, 2012), the top of the Kaena (C2An.1r) at 147.97 rmcd (~3.032 Ma; Ogg, 2012), and short excursions to normal polarity within the Matuyama chron at ~117 rmcd and within the Kaena subchron at ~151 rmcd (see Table 4.2).

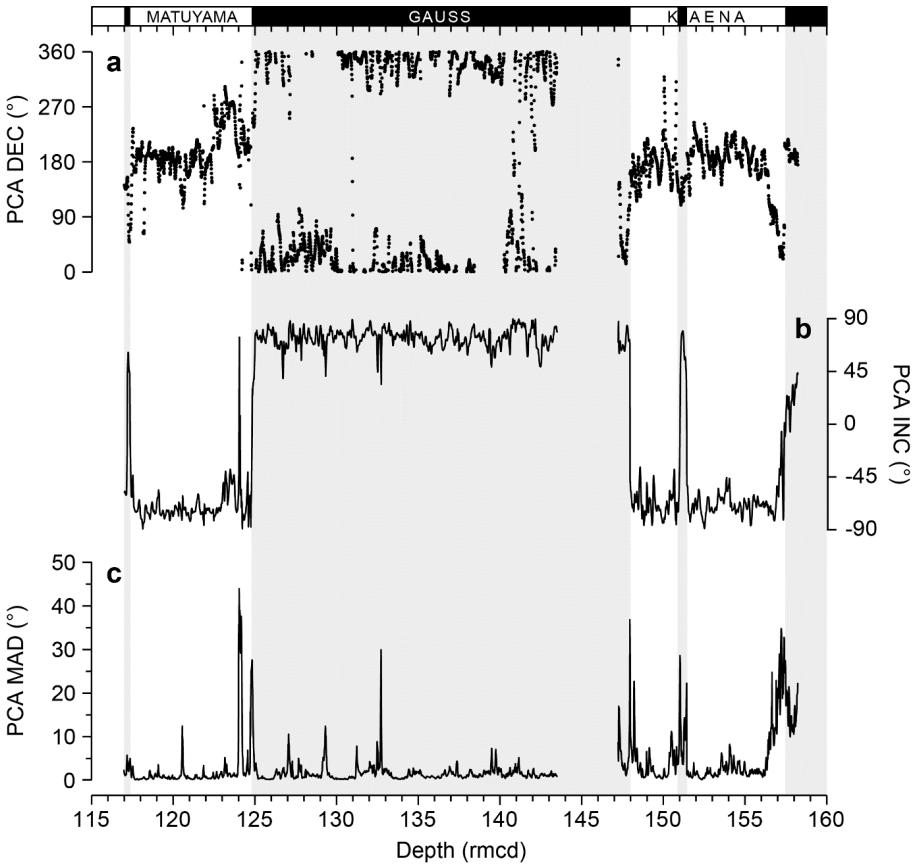

Figure 4.5 Site U1307 natural remanent magnetisation (NRM) component (**a**) declination, (**b**) inclination and (c) maximum angular deviation (MAD) values, calculated from principle component analysis of the 20–50 mT peak interval, against revised metres composite depth (rmcd). The absence of data between ~143.5–147.2 rmcd is the result of a sampling gap (the bottom 223 cm of U1307B-15H and the top 150 cm of U1307A-17H could not be u-channelled. Shipboard data do not suggest a reversal occurs during this interval; see Fig. 4.6). Polarity (normal/reversed) chrons are denoted at the top by black/white horizontal bars/grey vertical bars and labels.

I estimated RPI using the slope of NRM and ARM values over the 20–50 mT peak AF demagnetisation interval (Channell *et al*., 2002). To generate a U1307 RPI-based age model, I initially anchored the stratigraphy at the polarity reversal

boundaries, then tuned the RPI record within periods of stable polarity to the RPI record from IODP Site U1308 (Channell *et al*., 2016). The Site U1308 RPI record was chosen as a tuning target because it spans the past ~3.15 Ma, has a high-quality magnetic record and orbital-resolution benthic $\delta^{18}O$-based chronology tied to the LR04 stack, and serves as the anchor record for the PISO stack (Channell *et al*., 2009; 2016).

To provide a magnetic stratigraphy beyond the u-channelled interval and thus improve age control for the oldest sampled sediments, I constructed inclination and RPI proxy records using lower-resolution shipboard-acquired data for both U1307 and U1308, deriving a RPI estimate from NRM intensity (demagnetised in peak AF of 20 mT) normalised by bulk magnetic susceptibility, κ (e.g., Gorgoza *et al*., 2006). I achieved this by appending 5-cm resolution shipboard INC, NRM (10 mT) and κ data from cores U1308C 25H–29H to the base of the Site U1308 splice in Hole C (extending it from 248 to 266.5 mcd; Hole A data extends further, but the magnetic signal is not well-recorded in the deeper portion; Expedition 303 Scientists, 2006b), and cores U1307A 18H–19H to the base of the revised Site U1307 splice (to extend it from 158 to 175.5 rmcd, the maximum drilled depth). Where both types of data were available for a given depth, I normalised NRM by κ to give a 'rough and ready' measure of RPI, which compares favourably with u-channel-derived RPI data from both sites (Fig. 4.6). This estimate of RPI is not as robust as other u-channel-based estimates, partly due to imperfect normalisation of NRM by κ, but its use here is justified by the similarity of this record to the u-channel-derived RPI estimates where overlap exists (Fig. 4.6). Importantly, it allows the observations to be extended through the top of the Mammoth subchron (3.207 Ma), which improves the validity of the age model.

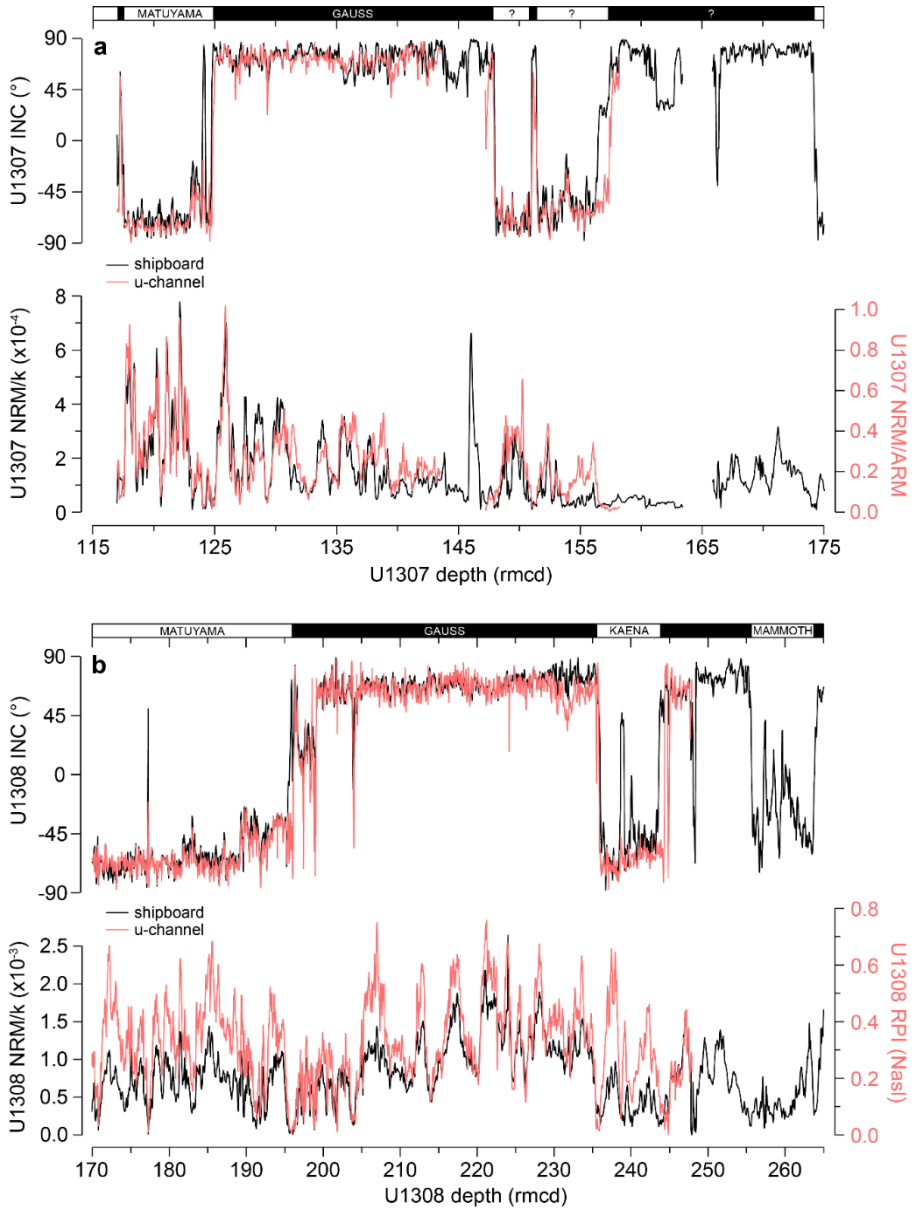

Figure 4.6 Shipboard- (black lines) and u-channel- (red lines) derived records of inclination (INC) and RPI for IODP Sites (**a**) U1307 and (**b**) U1308. The relationships shown demonstrate that shipboard-derived NRM/κ data >3.15 Ma can be used as a 'rough and ready' RPI record for these sites to help validate the new age model presented in this study for Site U1307.

4.2.2.4 Ice-rafted debris estimates

To examine the history of iceberg-rafting to Site U1307 during iNHG, I generated a record of weight percent (wt.%) IRD for the ≥212 μm size fraction. I dried each discrete sample in an oven over a number of days until its mass stabilised to determine its dry bulk weight, then each sample was disaggregated in a Calgon solution and washed over a 63 μm sieve to isolate the sand-sized fraction. I estimated the percentage of ice-rafted terrigenous material in the ≥212 μm

fraction of each sample (following further sieving) using a standard area percentage method (e.g., St. John and Krissek, 2002). Sand-sized constituents excluded from the definition of 'ice-rafted debris' were volcanic tephra, pyrite, biogenics (mostly diatoms and foraminifers) and burrow casts. I then estimated weight percent (wt.%) IRD for each sample using the ≥212 μm fraction weight as a percentage of the dry bulk sediment weight. To compare the history of terrigenous sand inputs at Site U1307 to those previously published from Eirik Drift at Ocean Drilling Program (ODP) Site 646 (Fig. 4.1; Wolf and Thiede, 1991), I also estimated the wt.% of sand-sized terrigenous constituents in the bulk ≥63 μm sand fraction of each of the samples.

The Iceland Plateau Site 907 IRD record is reported in ≥125 μm lithic grains per gram of dry sediment (Jansen *et al*., 2000), whereas this new IRD record from Site U1307 is reported as wt.% ≥212 μm IRD. To help compare my data to those available from Site 907, I generated twenty-eight additional IRD data for Site U1307 for the study interval, expressed as lithic grains (minus fresh volcanic glass and pyrite) ≥125 μm per gram of dry sediment, following Bailey *et al.* (2013). To investigate whether changes in the size fraction used to perform IRD counts have the potential to modify inferences made on the magnitude of iceberg rafting to the study site, I recounted the same samples after sieving for the ≥150 μm size-fraction.

4.2.2.5 Grain-size distribution

To evaluate the potential influence of changes in the relative abundance of clay, silt and sand deposited at Site U1307 during iNHG on the bulk magnetic records, I estimated physical grain-size distributions for the terrigenous fraction using discrete 1–2 cm^3 samples for 18 selected points between 136.9 and 118.3 rmcd

– an interval containing the largest-amplitude κ and ARM variations in the magnetic records (see Fig. 4.4a) – using a Malvern Mastersizer 3000 laser diffraction particle size analyser at the University of Exeter's Penryn Campus.

Prior to analysis, I removed organics and biogenics from each sample (see Appendix A Section E). I made ten repeat grain-size measurements on a well-mixed aliquot of each sample, and repeated this procedure on a separate subsample. The values reported for each sample are an average of all measurements made. Following Hatfield *et al*. (2013; 2017), size fractions are defined here as: clay <3 μm, very fine silt 3–10 μm, fine– medium silt 10–32 μm, medium–coarse silt 32–63 μm, and sand >63 μm.

4.3 Results and Discussion

4.3.1 New RPI-based age model for Eirik Drift sediments deposited during iNHG

The results of the nested magnetostratigraphic and RPI-based tuning exercise between Sites U1307 and U1308 are shown in Figure 4.7. Using the Gauss-Matuyama (G/M) boundary and the top of the Kaena as initial tie-points, the majority of the peaks and troughs in the U1307 and U1308 RPI estimates can be correlated between 3.22 and 2.24 Ma. The mismatch in RPI between U1307–U1308 during ~3.15–3.10 Ma (Fig. 4.7b) occurs at the same depth as part of the magnetic susceptibility low in this site's stratigraphy between 163.4 and 156.4 rmcd (Fig. 4.4a; Expedition 303 Scientists, 2006a), which indicates a low concentration of ferrimagnetic minerals in the sediments deposited during this interval. This cannot necessarily explain the low RPI values, however, since both NRM and ARM should be equally affected by magnetic concentration, and so the NRM/ARM ratio is independent of this. The match between the two RPI records

is achieved using thirty-three tie-points (Table 4.3) and an assumption of constant sedimentation rate between adjacent tie-points. The regionally-coherent nature of the RPI high captured at U1307 immediately prior to the G/M boundary, and of the trends in the U1307 record in general, are confirmed by the strong correspondence between the U1307 RPI and that from nearby Gardar Drift Site U1314 in the interval ~2.7 to 2.2 Ma (Appendix A Fig. S6; Ohno *et al*., 2012). Key similarities also exist between the U1307 RPI record and those derived from other globally-distributed sites, including ODP Leg 138 (Valet and Meynadier, 1993) and the equatorial Pacific EPAPIS-3000 stack (Yamazaki and Oda, 2005) (Appendix A Fig. S6). The limited planktic $\delta^{18}O$ data available for U1307 for this interval (Sarnthein *et al*., 2009) correlate well with the U1308 benthic $\delta^{18}O$ stratigraphy (and with the LR04 stack where U1308 data are absent) on this new age model (Fig. 4.7c), which acted as a double-check on the correlation between the two sites to provide independent confirmation for the RPI tuning.

Table 4.2 Polarity reversals and excursions at Site U1307 determined in this study compared to previously published interpretations.

Hole, core, section, interval (cm)	Depth (rmcd)	Transition interval	Reversal/excursion	Age (ka)	MIS[b]	Shipboard interpretation, age (ka)[d]	Alternative interpretation, age (ka)[e]
U1307B-13H-1 128	117.11	Upper	Unnamed excursion	2236[a]	86	-	-
U1307B-13H-2 11	117.44	Lower					
U1307A-14H-3 143	124.74	Upper	Gauss/Matuyama C2An.1n (t)	2595[b] (2581[c])	103	Gauss/Matuyama C2An.1n (t), 2581	Gauss/Matuyama C2An.1n (t), 2581
U1307A-14H-4 25	125.06	Lower					
U1307A-17H-2 61	147.81	Upper	Kaena top C2An.1n (b)	3029[b] (3032[c])	G21	Kaena top C2An.1n (b), 3040	Kaena top C2An.1n (b), 3040
U1307A-17H-2 97	148.17	Lower					
U1307A-17H-4 70	150.90	Upper	Unnamed excursion (?)	3060	G22	Kaena bottom C2An.2n (t), 3110	-
U1307A-17H-4 147	151.67	Lower				Mammoth top C2An.2n (b), 3220	-
U1307A-18H-2 31	157.06	Upper	Kaena bottom C2An.2n (t)	3116[b] (3110[c])	KM2	Mammoth bottom C2An.3n (t), 3330	Kaena bottom C2An.2n (t), 3110
U1307A-18H-2 82	157.57	Lower					
U1307A-19H-6 60	173.93	Upper	Mammoth top C2An.2n (b)	3207[c]	KM6	Gilbert/Gauss C2An.3n (b), 3580	Gilbert/Gauss C2An.3n (b), 3580
U1307A-19H-6 120	174.53	Lower					

[a]Channell and Guyodo (2004); [b]Channell *et al*. (2016); [c]Ogg *et al*. (2012); [d]Expedition 303 Scientists (2006a); [e]Sarnthein *et al*. (2009).

Table 4.3 List of revised depth-age tie-points for Site U1307 between 117.63–174.48 rmcd based on the new correlation to the Site U1308 RPI.

Depth (rmcd)	Age (ka)	Type	Chronology	Depth (rmcd)	Age (ka)	Type	Chronology
117.63	2253.84	RPI	IODP U1308[a]	136.86	2846.71	RPI	IODP U1308[a]
118.51	2268.70	RPI	IODP U1308[a]	137.47	2880.09	RPI	IODP U1308[a]
120.52	2319.38	RPI	IODP U1308[a]	138.13	2894.64	RPI	IODP U1308[a]
121.30	2340.27	RPI	IODP U1308[a]	138.56	2908.58	RPI	IODP U1308[a]
121.86	2364.20	RPI	IODP U1308[a]	138.80	2930.08	RPI	IODP U1308[a]
122.05	2370.48	RPI	IODP U1308[a]	139.31	2940.14	RPI	IODP U1308[a]
122.40	2380.28	RPI	IODP U1308[a]	141.12	2966.67	RPI	IODP U1308[a]
123.11	2429.18	RPI	IODP U1308[a]	143.76	3000.41	RPI	IODP U1308[a]
123.53	2464.37	RPI	IODP U1308[a]	147.97	3029	Reversal	Kaena (t)[a]
123.96	2521.41	RPI	IODP U1308[a]	151.01	3059.42	RPI	IODP U1308[a]
124.88	2595	Reversal	Gauss-Matuyama[a]	155.41	3093.99	RPI	IODP U1308[a]
127.32	2664.45	RPI	IODP U1308[a]	157.33	3116	Reversal	Kaena (b)[a]
129.10	2730.77	RPI	IODP U1308[a]	166.48	3149.18	RPI	IODP U1308[a]
129.73	2747.82	RPI	IODP U1308[a]	168.96	3167.34	RPI	IODP U1308[a]
132.00	2776.11	RPI	IODP U1308	170.70	3187.76	RPI	IODP U1308[a]
135.00	2804.08	RPI	IODP U1308[a]	174.48	3207	Reversal	Mammoth (t)[a]
136.03	2829.58	RPI	IODP U1308[a]				

[a]Channell *et al*. (2016)

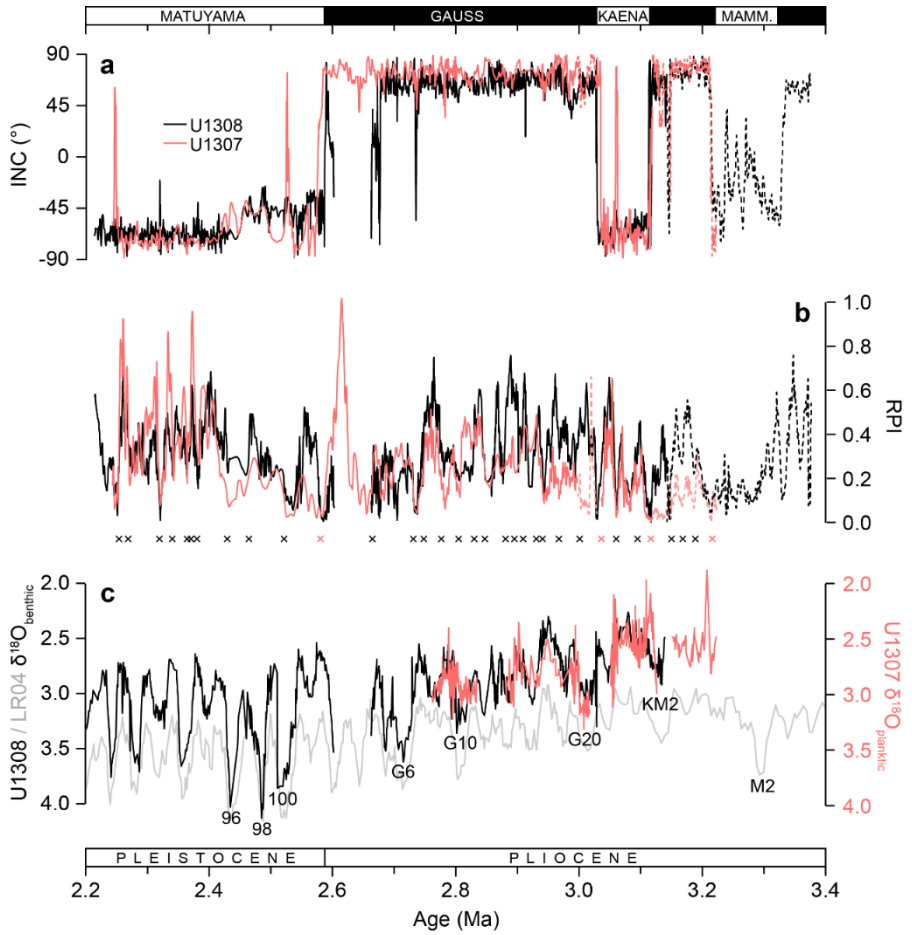

Figure 4.7 Site U1307 and U1308 records of (**a**) inclination (INC; red = this study; black = Channell *et al*., 2016), (**b**) relative palaeointensity (RPI; red = this study; black = Channell *et al*., 2016) and (**c**) $\delta^{18}O$ (red = Sarnthein *et al*., 2009; black = Channell *et al*., 2016; grey = Lisiecki and Raymo, 2005). Solid lines in (a) and (b) show u-channel-derived data. Dashed lines show shipboard-derived split core data (see Fig. 4.6). Red/black crosses indicate reversal-/RPI based tie-points, also given in Table 4.3. Labels in (c) are Marine Isotope Stages. The U1308 reference RPI stratigraphy was 'unhooked' at 197.40 mcd because a hiatus has been identified at this depth spanning MIS G2–104 (~2.65–2.60 Ma; Channell *et al*., 2016).

Based on the new age model, the oldest sediments recovered at Site U1307 are ~3.22 Ma and the oldest observed palaeomagnetic reversal is the top of the Mammoth (Fig. 4.7a; C2An.2r, 3.207 Ma; Ogg, 2012), significantly revising the shipboard-designated age of ~3.58 Ma. This new chronology suggests that the Site U1307 stratigraphy contains a near-complete record of the mPWP between ~175.5 and 146.7 rmcd. I tentatively propose that the short normal polarity excursion captured near the top of the record (Fig. 4.7a) is equivalent to an unnamed event recorded at ODP Site 982 at ~2.24 Ma (Channell and Guyodo, 2004). Other short normal polarity excursions occur at ~2.52 and ~3.06 Ma in the

U1307 record (Fig. 4.7a), but to my knowledge excursion events at these times have not been identified elsewhere.

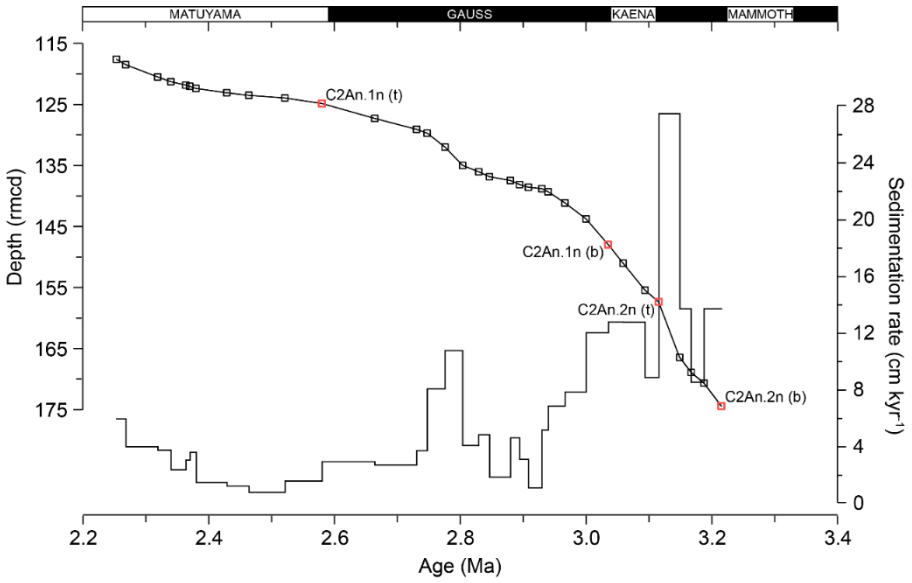

Figure 4.8 Age-depth relationship for Site U1307 based on tie-points between U1307 and U1308 shown in Fig. 4.7 (see Table 4.3), and linear sedimentation rates calculated between each tie-point. Black/red squares indicate relative palaeointensity-/reversal-based tie-points used.

The new age model reveals that between ~3.2 and 2.2 Ma, the average sedimentation rate at Site U1307 was ~6 cm kyr^{-1} (Fig. 4.8), similar to the average Pleistocene rate of ~5.5 cm kyr^{-1} reported by Mazaud *et al.* (2015). The early part of the record, however, is characterised by much higher and more variable sedimentation rates than this average, which decreased from values of ~10–12 cm kyr^{-1} to ~2–4 cm kyr^{-1} between ~3.0 and 2.7 Ma, reaching a minimum of just ~1 cm kyr^{-1} at ~2.5 Ma before quadrupling between ~2.4 and ~2.2 Ma (Fig. 4.8). The lowest sedimentation rates between ~2.6 and 2.4 Ma correspond to a stretching of the U1307 RPI record relative to U1308 during this interval (Fig. 4.7). Sedimentation rates estimated for the deeper-water Eirik Drift Site 646 (~3450 m), although highly averaged over the study interval due to limited age control, are broadly consistent with the new highly-resolved U1307 record and also hint

that sedimentation rates likely decreased over a wide range of water depths on Eirik Drift around 2.7 Ma (Appendix A Fig. S7b; Wolf and Thiede, 1991).

This new, high-fidelity RPI-based age model for Site U1307 highlights how previous attempts to assign ages to the site stratigraphy, based on lower resolution shipboard-acquired palaeomagnetochron and biostratigraphic datums, are inaccurate in the deeper Pliocene portion of the record. Two alternative age models for the late Pliocene and early Pleistocene portion of the shipboard-derived Site U1307 stratigraphy have previously been proposed by Sarnthein *et al*. (2009), which are based on their interpretation of the shipboard palaeomagnetochron stratigraphy and a discontinuous planktic foraminiferal *Neoglobigerina atlantica* (s) stable oxygen isotope record. The preferred U1307 age model of Sarnthein *et al*. (2009) – 'Age Model 2' – assumes that the lowermost palaeomagnetochron reversal preserved in the U1307 shipboard INC record is the Gilbert/Gauss reversal ~3.58 Ma, and that the Mammoth reversed subchron (C2An.2r) lies somewhere in the base of A-18H (within a magnetic susceptibility low) and the recovery gap with A-19H. Retuning of the U1307 RPI record to the U1308 stratigraphy guided by Sarnthein *et al*. (2009)'s 'Age Model 2' (Fig. 4.9) highlights the following deficiencies: 1) U1307-U1308 RPI match is poor below the Kaena (bottom); 2) the alignment of U1307 *N. atlantica* (s) $\delta^{18}O$ and U1308 benthic $\delta^{18}O$ (and the LR04 stack where U1308 $\delta^{18}O$ data are not available) below the Kaena (bottom) is unconvincing; and 3) there is no evidence in the inclination record that the reversed Mammoth subchron lies where assumed by Sarnthein *et al*. (2009). The new RPI correlation to U1308 presented in this chapter illustrates that the basal reversal in U1307 is instead the Mammoth top (~3.22 Ma), reducing the proposed maximum age of sediment recovered at

U1307 by ~330 kyr and ensuring subsequent records gleaned from sediments from this portion of the U1307 stratigraphy are accurately-dated.

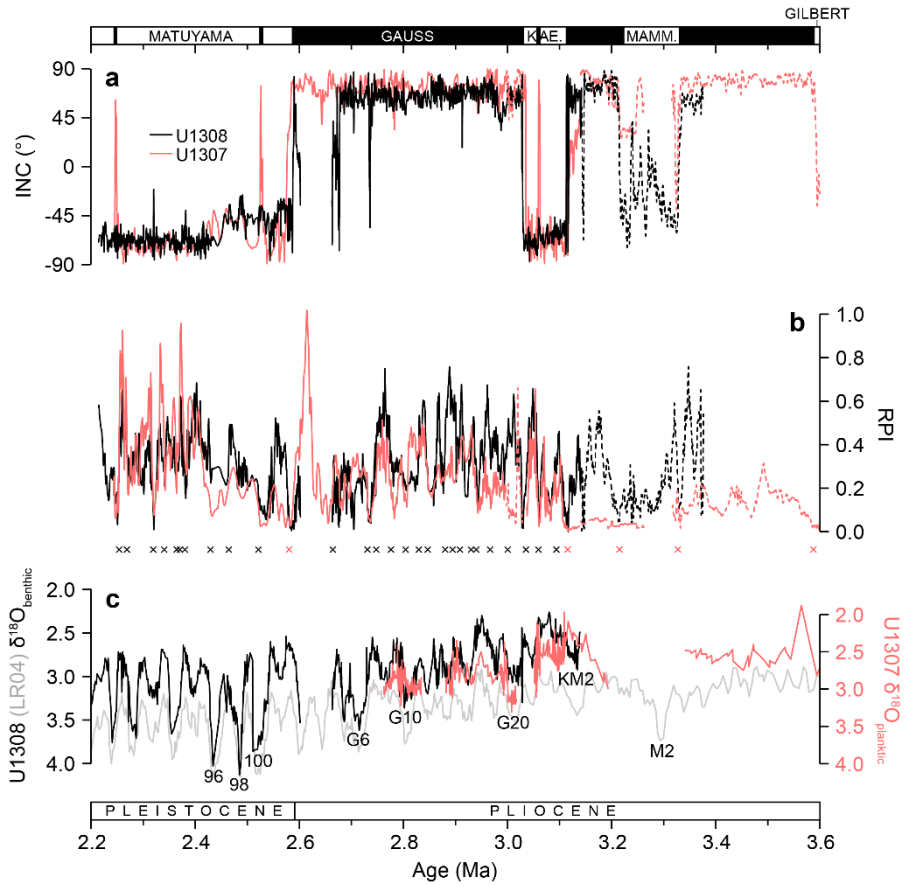

Figure 4.9 Records of (**a**) inclination (INC; red - this study; black – Channell *et al*., 2016), (**b**) relative paleointensity (RPI; red – this study; black – Channell *et al*., 2016) and (**c**) $\delta^{18}O$ (red – Sarnthein *et al*., 2009; black – Channell *et al*., 2016; grey – Lisiecki and Raymo, 2005). The relationship between the U1307 and U1308 $\delta^{18}O$ datasets shown in (c) is the product of tuning RPIs between U1307 and U1308 based on the 'Age Model 2' scenario for the U1307 stratigraphy proposed by Sarnthein *et al*. (2009). Application of this age model results in a poor fit between the two records prior to 3.1 Ma. Solid lines show u-channel-derived data. Dashed lines show shipboard-derived split core data. Labels in (c) are Marine Isotope Stages. Red/black crosses indicate reversal-/RPI based tie-points.

The last occurrence (LO) of the dinocyst *Operculodinium eirikianum* identified shipboard in the base of U1307A (Expedition 303 Scientists, 2006a) is dated at ~3.3 Ma, but I argue that it should not be used as an initial tie point in constructing the RPI-based age model for this site: (1) its LO is based on a core catcher sample, so its true LO could be up to ~10 m higher in the U1307A stratigraphy than reported; and (2) the ~3.3 Ma age assigned to this dinocyst LO is based on

unspliced, poorly-dated stratigraphy from Ocean Drilling Program (ODP) Labrador Sea Site 646 (this site lacks benthic $\delta^{18}O$ stratigraphy, dated only by palaeomagnetic reversals with the Kaena and Mammoth subchrons unresolved; Shipboard Scientific Party, 1987).

4.3.2 New records of IRD deposition and environmental magnetism on Eirik Drift during iNHG

The new late Pliocene to earliest Pleistocene records of coarse (wt.% ≥212 μm and grains ≥150 μm g^{-1}) IRD abundance, wt.% ≥63 μm terrigenous sand, bulk volume-specific magnetic susceptibility (κ) and magnetic grain-size (κ_{ARM}/κ) of Site U1307 sediments deposited between ~3.2 and 2.2 Ma are presented in Figure 4.10. The coarse IRD deposited at U1307 during the target interval is mainly composed of quartz, feldspar, mica and lithic clasts of granite, gneiss, basalt and troctolite/gabbro, with minor accessory hornblende and epidote. Variability in its abundance follows the same general pattern as that seen in early Pleistocene and other late Pliocene records (IRD elevated periodically on ~41-kyr timescales during cold stages and/or glacial terminations; Fig. 4.10b). Coarse IRD deposition was mainly absent at U1307 during the mPWP, and IRD is only present in small abundances (~1–2 wt.% ≥212 μm; ~200–1000 grains ≥150 μm g^{-1}) during (de)glacials between ~3 and 2.75 Ma. From MIS G8 onwards, however, coarse IRD inputs were persistently elevated on orbital timescales (with peak abundances during glacials of ~10–14 wt.% ≥212 μm; ~1800–3800 grains ≥150 μm g^{-1}).

The abundance of ≥63 μm sand in U1307 sediments deposited during the study interval also varies most strongly on ~41-kyr timescales, ranging from 0–40 wt.% throughout the study interval (Fig. 4.10a). In contrast to the coarse wt.%

≥212 μm IRD record, however, ≥63 μm terrigenous sand concentration at Site U1307 is strongly elevated during interglacials prior to ~2.7 Ma that in the vast majority of cases are not associated with coarse IRD (Fig. 4.10a and b). Sand deposited during these intervals is composed of mostly well-sorted, fine, rounded quartz sand grains, and contains a significant but variable (~10–70%) biogenic component of both foraminifera and diatom tests. Following the onset of persistently elevated coarse IRD deposition ~2.7 Ma, however, the ≥63 μm terrigenous sand fraction is composed of mostly (sub)angular grains that are heterogeneous in composition with at most a ~20% diatom component, and variations in its abundance closely follow changes in wt.% ≥212 μm IRD.

The U1307 environmental magnetic records (κ and κ_{ARM}/κ) exhibit orbital-scale variability throughout most of the study interval, with higher magnetic susceptibility and coarser magnetic grain-size generally characterising (de)glacial intervals containing coarse IRD (compare Fig. 4.10b to 10c and e). Site U1307 magnetic susceptibility increased dramatically from near-zero values during the termination of MIS KM2, ~3.1 Ma, and is associated with relatively low κ_{ARM}/κ values. Following the cessation of the mPWP, ~3 Ma, magnetic susceptibility remained high and κ_{ARM}/κ values relatively low, but glacial-interglacial variability in these parameters increased between 2.9 and 2.5 Ma, particularly in the κ_{ARM}/κ record. Both records show a marked shift between 2.9 and 2.7 Ma, coincident with the onset of persistently elevated coarse IRD inputs to U1307 – κ decreased and the average magnetic grain-size assemblage fined (higher κ_{ARM}/κ values).

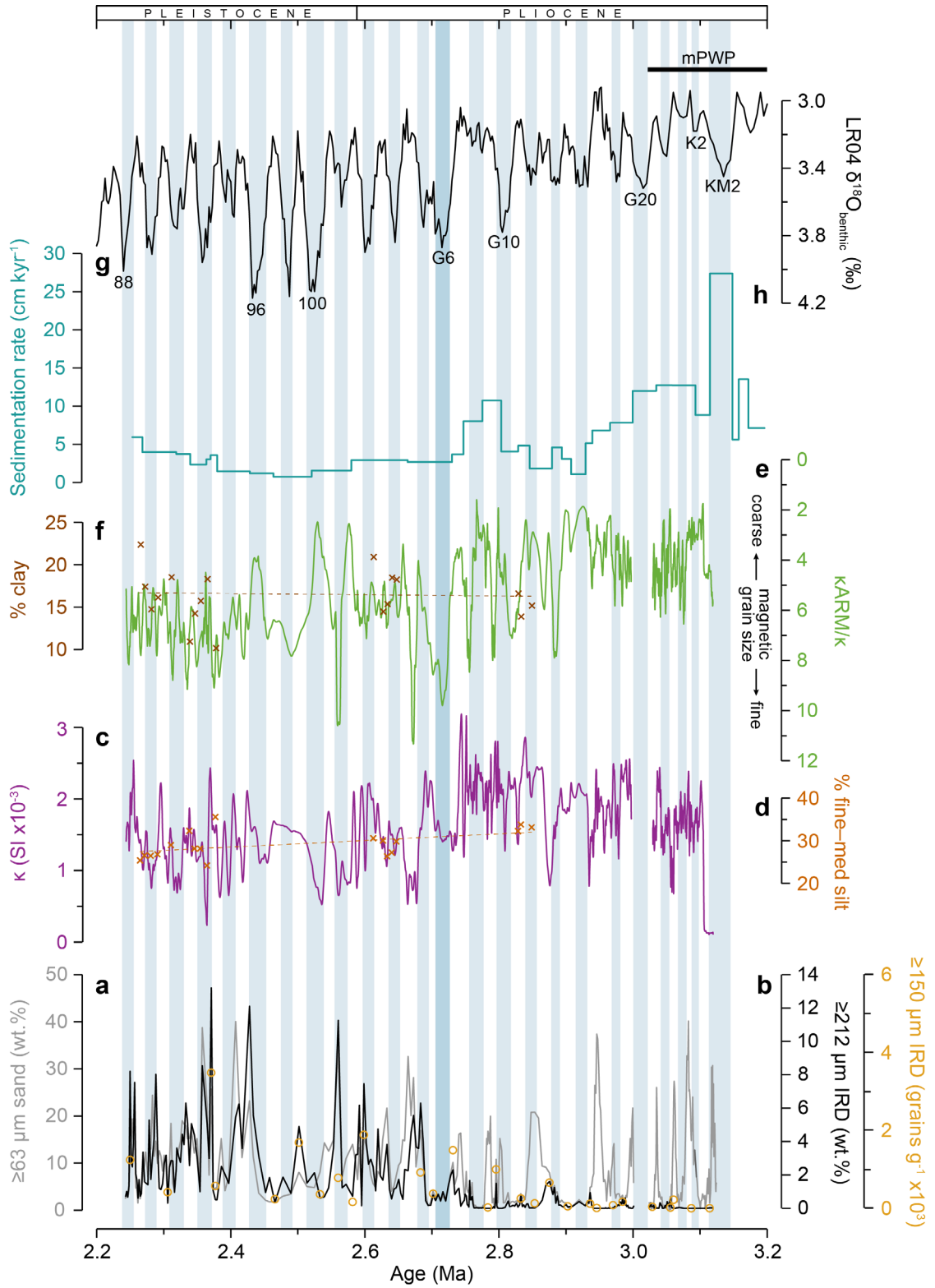

Figure 4.10 Site U1307 palaeoclimate records: (**a**) wt.% ≥63 µm terrigenous sediment, (**b**) wt.% ≥212 µm IRD and grains ≥150 µm,IRD g^{-1}, (**c**) magnetic susceptibility (κ), (**d**) % fine–medium silt (10–32 µm), (**e**) κ_{ARM}/κ, (**f**) % clay (<3 µm) and (**g**) sedimentation rate. The LR04 benthic $\delta^{18}O$ stack is shown in (**h**) for reference (Lisiecki and Raymo, 2005). Numbers in (h) are Marine Isotope Stages, with the duration of the mid-Piacenzian warm period (mPWP; Dolan *et al.*, 2011) also indicated. Vertical blue bars highlight cold stages. See Table 4.3 for values given in (d) and (f).

The bulk magnetic nature of Eirik Drift sediments can be influenced by changes both in sediment source (Stoner *et al.,* 1995; Hatfield *et al.*, 2016) and potentially

sediment texture (Hatfield *et al*., 2013; 2017). The sensitivity of the U1307 magnetic records to both these processes can be established by comparing their relationships to terrigenous grain-size data (Hatfield *et al*., 2016; 2017), and the relationships of κ and κ_{ARM}/κ with percent clay, very fine/fine–medium/medium–coarse silt, and sand in U1307 sediments are shown in Figure 4.11. Terrestrial sources (Hatfield *et al*., 2017) and sediments from Eirik Drift Site MD99-2227 (Hatfield *et al*., 2016) suggest that the magnetic susceptibility of the clay-size fraction is several times lower than the silt-size fractions, and as a result the clay fraction likely exerts restricted influence on bulk κ values (e.g., Hatfield *et al.*, 2019). Relatively low variability in % clay data (Fig. 4.10f) and the little to no correlation between % clay and κ (r = -0.125; Fig. 4.11a) suggests that any increase in magnetically weak clay-size fractions is unlikely to have driven the secular fining signal seen in the magnetic records between ~2.9 and 2.7 Ma from U1307. Of the three silt size fractions, % fine–medium silt (10–32 μm) has the strongest relationship with bulk magnetic properties, and this size fraction has recently been found to exert a strong influence on bulk magnetic susceptibility records (Hatfield *et al.*, 2019). The relatively strong positive correlation that we observe between % fine–medium silt and bulk κ (r = 0.733; Fig. 4.11c) is most likely attributable to the enrichment of ferrimagnetic grains in this terrigenous grain-size fraction (Hatfield *et al*., 2013; 2017).

Bulk Mrs/Ms (ratio of remanent saturation moment (Mrs) to saturation moment (Ms)) values from sediments deposited at Site U1307 during the Plio-Pleistocene are generally ~0.1–0.2 (Kawamura *et al*., 2012; Mazaud *et al*., 2015), which implies a relatively restricted coarse PSD-size range of ferrimagnetic grains when viewed on a Day plot (Day *et al*., 1977) (Fig. 4.4). Particle-size-specific studies of terrestrial sources relevant for Eirik Drift provenance (outside of

Heinrich event intervals) show that only silts and sands from Greenland (and not the Cenozoic volcanics of Iceland or of eastern Greenland) can yield Mrs/Ms values <~0.15 (Hatfield *et al*., 2017). Higher fine–medium silt abundance and bulk κ are most strongly associated with lower κ_{ARM}/κ values (r = 0.441; Fig. 4.11h) and thus a coarser magnetic grain-size assemblage, which is consistent with increased sourcing of silt from Greenlandic terranes relative to Cenozoic volcanic contributions (Hatfield *et al*., 2016; 2017). This relationship between bulk magnetic parameters and % silt has previously been observed at Eirik Drift Site MD99-2227, where it has been shown that increases in bulk κ, % silt and coarser magnetic grain-sizes reflect increased export of glaciofluvial silt from Greenland (Hatfield *et al*., 2016; 2017).

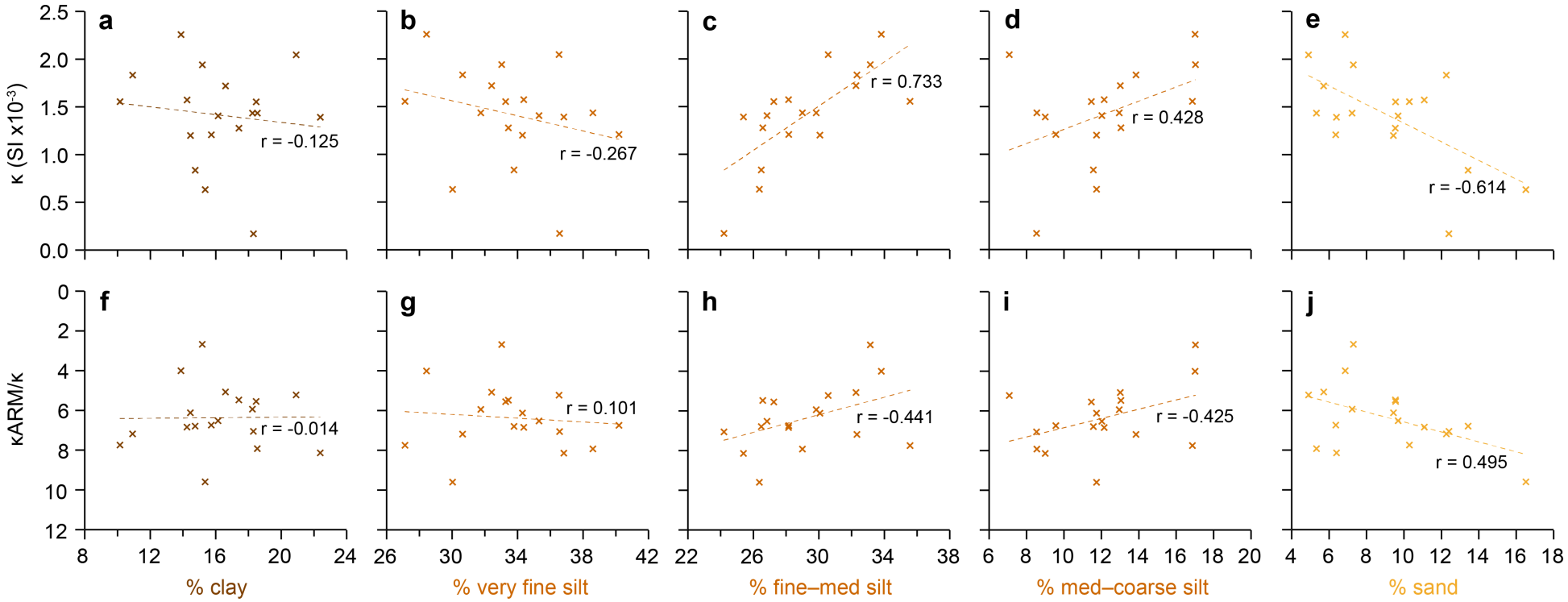

Figure 4.11 Cross-plots of (**a–e**) bulk magnetic susceptibility (κ) and (**f–j**) magnetic grain size (κ_{ARM}/κ; note reversed axis since higher values = coarser magnetic grains) with physical grain size percentage abundance for clay (<3 μm), very fine silt (3–10 μm), fine–medium silt (10–32 μm), medium–coarse silt (32–63 μm) and sand (>63 μm) fractions (following Hatfield *et al.*, 2019) derived from discrete sample analyses (n = 18). See Appendix A Table S4 for full data.

4.3.3 Changes in bottom-current strength recorded at Site U1307 during iNHG

Using what we know about the magnetic properties of Greenlandic vs. Icelandic sediments transported to Eirik Drift, the long-term decrease in average ferrimagnetic grain size and sedimentation rates observed at Site U1307 between ~2.9 and 2.7 Ma (Fig. 4.10) likely reflects a secular decrease in the abundance of silt of Greenlandic origin transported to the site. This interpretation is supported by the discrete grain-size measurements, which show a long-term reduction of ~5% fine–medium silt between 2.85 and 2.25 Ma (Fig. 4.10d). Since we might logically expect a greater influx of Greenland-derived material following the onset of significant NHG ~2.7 Ma, as indicated by the IRD records (Fig. 4.10b), the changes I observe in the magnetics and grain-size records, and the contemporaneous long-term decrease in sedimentation rate, are most likely explained by a shift in the position of the WBUC and delivery of terrigenous sediments to a different area of the drift.

Additional support that the strength of bottom currents bathing the study site changed significantly during iNHG may be found in the record of wt.% ≥63 μm sand (Fig. 4.10a). Peaks in the abundance of well-sorted fine sand, which prior to ~2.7 Ma occur in Site U1307 sediments deposited during interglacials (Fig. 4.10a), may reflect increased export of glaciofluvial sediment from Greenland to Eirik Drift, most strongly during warm stages. This change also appears to be reflected in the grain-size distribution for each selected glacial cycle over iNHG (Fig. 4.12). Two grain-size modes appear to dominate the bulk sediment deposited at U1307 throughout the study period, ~28 μm (medium silt) and ~5.5 μm (very fine silt), with a less significant ~75 μm (fine sand) mode present in the post-2.7 Ma samples (Fig. 4.12). While medium silt was the more dominant mode during both glacial and interglacial conditions of the MIS G12

(~2.83 Ma) cycle (Fig. 4.12d), as iNHG progressed the very fine silt mode became more dominant, particularly during glacial conditions (Figs. 4.12b-c). By MIS 88 (~2.3 Ma), very fine silt was the dominant grain-size deposited at U1307 during all cycle conditions (Fig. 4.12a). Hence, despite an increase in coarse lithic delivery to Eirik Drift by icebergs over iNHG, the average grain-size of U1307 sediments decreased. I therefore propose that prior to ~2.9 Ma, the core flow of the WBUC occupied a depth that permitted the delivery of relatively high abundances of Greenland-derived silt and fine sand to Site U1307 during both warm (predominantly) and cold stages on orbital timescales – so the site was then characterised by a bottom-current-dominated depositional setting – and that between ~2.9 and 2.7 Ma the volume of Greenland-derived silt delivered to Site U1307 decreased, and a glacial IRD-depositional-dominated setting subsequently ensued.

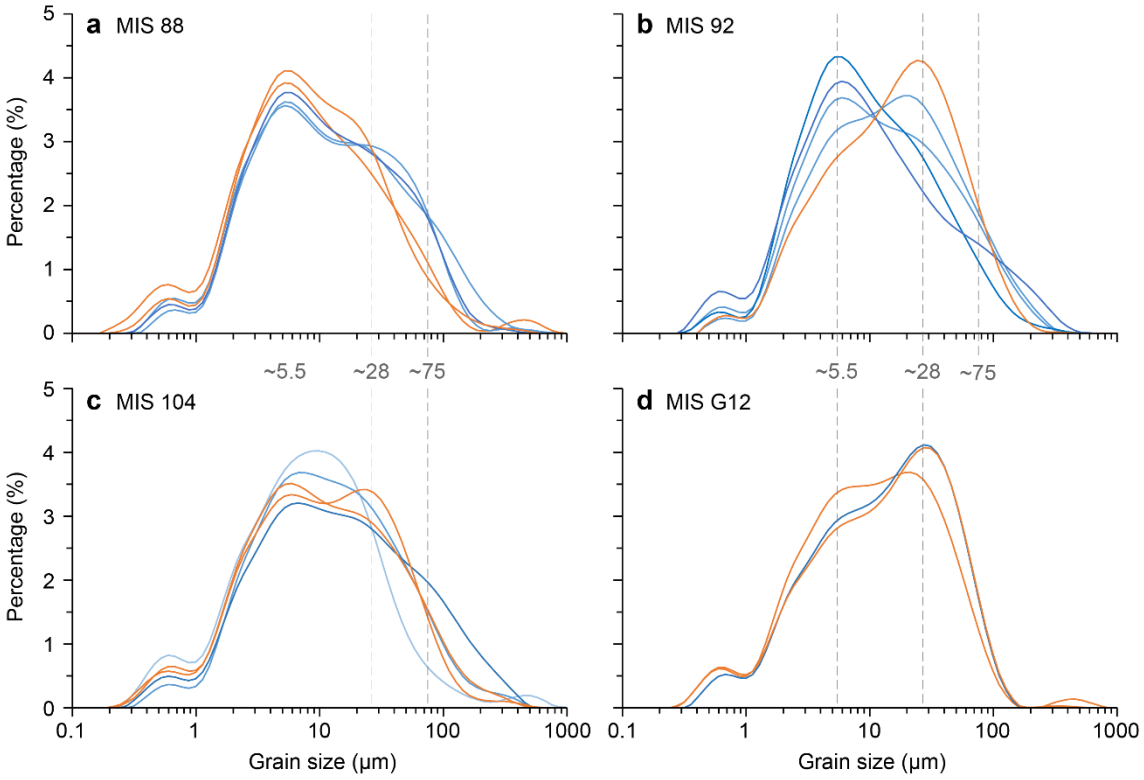

Figure 4.12 Grain-size distribution curves for selected glacial cycles over iNHG: (**a**) Marine Isotope Stage (MIS) 88, ~2.3 Ma; (**b**) MIS 92, ~2.36 Ma; (**c**) MIS 104, ~2.6 Ma; and (**d**) MIS G12, ~2.83 Ma. Orange, dark blue and light blue curves represent interglacial, glacial and deglacial conditions, respectively. Note logarithmic scale of x-axis. See Appendix A Table S4 for full data.

Based on the findings of studies that used depth transects of Eirik Drift sediments to infer changes in WBUC vigour during the late Pleistocene (Hillaire-Marcel *et al.*, 1994; Channell *et al*., 2014; Mazaud *et al*., 2012, 2015), the decreases in sedimentation rate and magnetic grain-size at U1307 during iNHG reported here may show that WBUC vigour increased and that its core flow deepened relative to the study site between ~2.9 and 2.7 Ma. A large deepening of the core flow of the WBUC by ~2.7 Ma is not consistent, however, with changes in sedimentation rates reported for Hole 646B on Eirik Drift at ~3450 m water depth, which also appear to have decreased across ~2.7 Ma (Appendix A Fig. S7b; Wolf and Thiede, 1991). Moreover, a spin-up in the WBUC at this time is also inconsistent with an interpretation based on seismic reflection data that bottom currents not only shallowed, but weakened over Eirik Drift at this time (Müller-Michaelis and Uenzelmann-Neben, 2014), and the observation that iNHG was associated with Last Glacial Maximum-like reductions in the volume of the NADW-overturning cell during cold stages from ~2.7 Ma (Lang *et al*., 2016).

The only mechanism currently proposed that could explain any ‘spin-up’ in the WBUC at this time is the hypothesised late-stage closure history of the Central American Seaway (CAS; e.g., Bartoli *et al*., 2005; Sarnthein et al., 2009). A previous attempt to link phases of CAS closure with the onset of coarse lithic deposition at Site U1307 (Sarnthein *et al*., 2009; based on their ‘Age Model 2’) is now refuted by the new high-fidelity age model and high-resolution IRD record presented in this chapter, which changes the authors’ proposed temporal relationship between the two. By contrast, if WBUC vigour actually decreased at this time, this would be more consistent with forcing by sea-ice expansion and increased glacial meltwater input in the Arctic and Nordic Seas, which could have weakened the WBUC by lowering the salinity and density of the water masses

that contribute to its formation (Raymo *et al.*, 2004). Any reduction in WBUC vigour during iNHG could also be explained by increased activity of the Iceland Hotspot, which is believed to have uplifted the GSR from ~2.7 Ma to restrict Nordic Seas overflows from this time (e.g., Wright and Miller, 1996; Parnell-Turner *et al.*, 2015). Regardless, the new records from Site U1307 provide the first direct geological evidence that the behaviour of the WBUC changed with the expansion of large Northern Hemisphere ice-sheets during the late Pliocene. Ultimately, however, our understanding of whether WBUC vigour increased or decreased during iNHG, and of the potential mechanism(s) and climatological consequences involved, can only be improved by future observations from precisely-dated continuous Pliocene sequences recovered from a depth and spatial transect of drilling sites on Eirik Drift.

4.3.4 Southern GrIS evolution recorded at Site U1307 during iNHG

The general absence of IRD deposition on Eirik Drift (this study and Site 646; Wolf and Thiede, 1991; Appendix A Fig. S7) and the Iceland Plateau (Site 907; Jansen *et al.*, 2000) during the latter half of the mPWP (~3.12–3.03 Ma; Fig. 4.13a and b) suggests that iceberg-calving margins were restricted in northeastern, eastern and southern Greenland during this time. Numerical model simulations indicate that continental ice on Greenland may have been mainly restricted to the southern and eastern highlands during the mPWP (e.g., Dolan *et al.*, 2011). The absence of persistent coarse IRD deposition at U1307, yet relatively coarse magnetic grain-sizes (low κ_{ARM}/κ and Mrs/Ms values <0.12; Appendix A Fig. S4b; Kawamura *et al.*, 2012) and high κ, prior to ~2.7 Ma (Fig. 4.10c and e) suggests that glaciofluvial silt-producing icecaps existed at least inland on southern Greenland prior to the onset of significant Northern Hemisphere glaciation,

including perhaps during the mPWP. The enhanced orbital-scale variability in magnetic grain-size from ~2.9 Ma (Fig. 4.10e) may also reflect an increase in glacial-interglacial dynamism of previously predominantly inland ice-sheet growth and decay in this region of Greenland.

The Site U1307 ≥125 μm grains per gram record lacks orbital resolution, but it highlights that IRD inputs to the site may have become significantly elevated from ~3 Ma, at least during cold stages (Fig. 4.13a). The history of ice-rafting inferred from this record is arguably similar to that recorded at Site 907 based on the ≥125 μm grain-size fraction of IRD (Jansen *et al*., 2000), which suggests that IRD deposition on the Iceland Plateau was also persistently elevated from ~3 Ma (Fig. 4.13b). If correct, this interpretation of these geological data is supported by the finding, based on numerical ice-sheet models, that the mountainous regions of eastern and southern Greenland represent key nucleation points for the Pliocene GrIS (Dolan *et al*., 2011). Arguably, however, a different story can be drawn from both the coarser IRD ≥150 μm grains per gram and wt.% ≥212 μm records from U1307, which appear to show that the first sustained episode of significant ice-rafting from southern Greenland may not have begun until 2.72 Ma, during MIS G6 (compare yellow and black data in Fig. 4.10b). The timing of the onset of continuous major ice-rafting to Eirik Drift during iNHG may therefore actually be most comparable to the history of IRD deposition on the Vøring Plateau in the Nordic Seas, and in the subpolar northeast North Atlantic (e.g., as recorded at ODP Site 644, DSDP Site 611, ODP Site 984, and IODP Site U1308; Fig. 4.1; Jansen and Sjøholm, 1991; Bailey *et al*., 2010; Bailey *et al*., 2013; Bartoli *et al*., 2005). Consequently, the onset of persistent IRD deposition on Eirik Drift ~2.7 Ma may well post-date the first sustained elevation in ice-rafting on orbital

timescales to the more northerly Iceland Plateau (at Site 907), at the cessation of the mPWP ~3 Ma, by ~300 kyr (Fig. 4.13; also see Appendix A Section G).

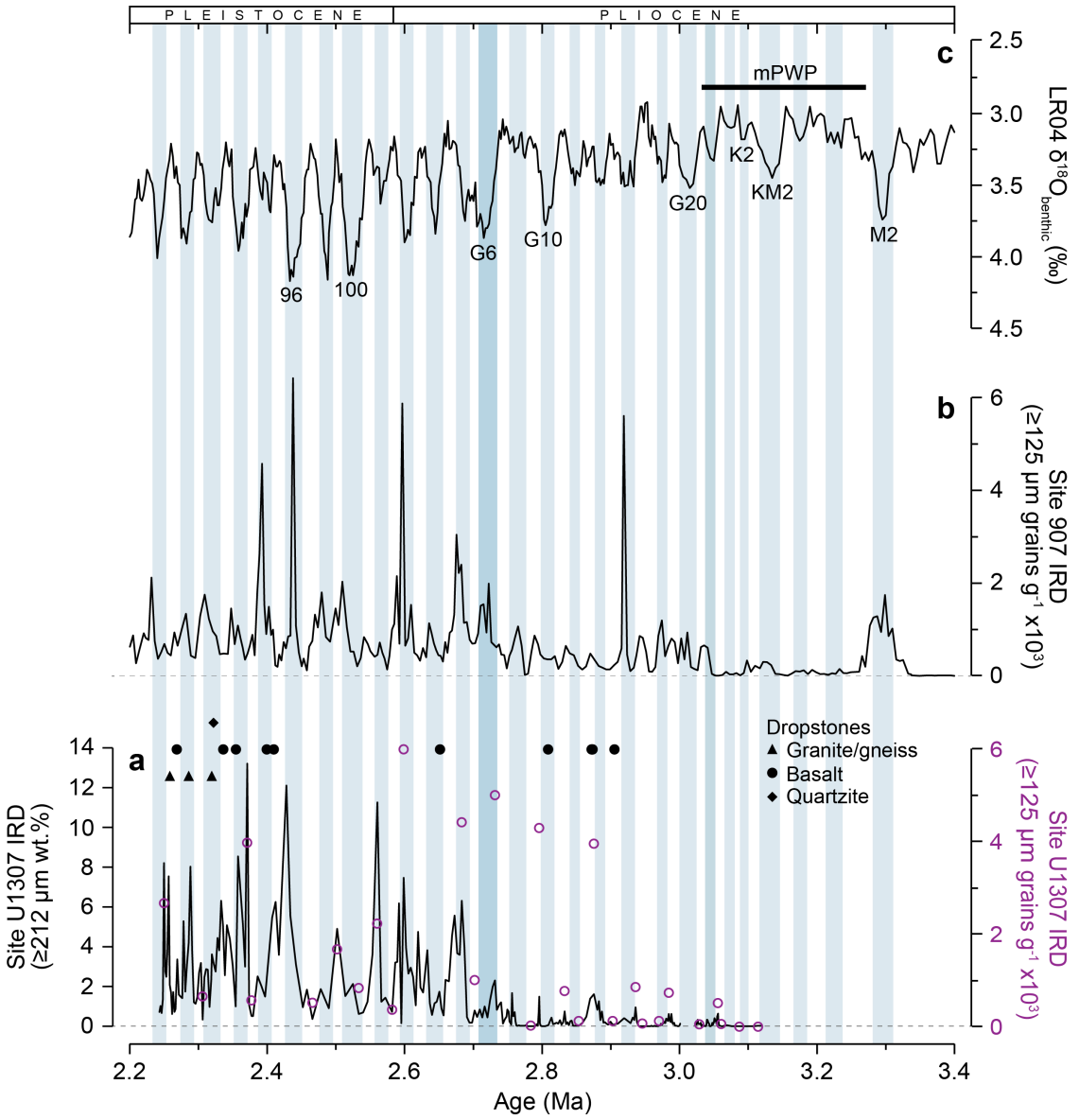

Figure 4.13 Records of IRD abundance from (**a**) IODP Site U1307 (this study; black record wt.% ≥212 µm, purple circles grains ≥150 µm g^{-1}) with shipboard-determined occurrences of dropstones (Expedition 303 Scientists, 2006a), and (**b**) ODP Site 907 (Jansen *et al*., 2000). The LR04 benthic $\delta^{18}O$ stack is shown in (**c**) for reference (Lisiecki and Raymo, 2005). Numbers in (c) are Marine Isotope Stages, with the duration of the mid-Piacenzian warm period (mPWP; Dolan *et al*., 2011) also indicated. Vertical blue bars highlight cold stages.

Any potential delay in the onset of abundant IRD deposition on Eirik Drift relative to the Iceland Plateau cannot be readily explained by iceberg survivability. This is because the EGC was likely a feature of Nordic Seas surface circulation for the past ~4.5 Myr (e.g., De Schepper *et al*., 2015), and iceberg trajectory modelling

for the warm late Pliocene shows that abundant icebergs only reach the surface waters above Eirik Drift when southern Greenland iceberg-calving sources exist (Smith *et al*., 2018; their Fig. 4). Instead, it would hint at a regionally diachronous GrIS maturation during iNHG. The implication being, while at least outlet glaciers extended to the coast in northeastern and eastern Greenland following the cessation of the mPWP ~3 Ma, persistent iceberg-calving margins may not have been established in southern Greenland during cold stages until ~2.7 Ma, when the Fennoscandian and Barents ice-sheets also expanded to their iceberg-calving margins (Jansen and Sjøholm, 1991; Knies *et al*., 2014) and glacial expansion occurred at least inland on Arctic Canada (Lang *et al*., 2014; Bolton *et al*., 2018). This southward expansion may also be echoed in the shipboard-derived dropstone record at U1307 (Fig. 4.13a; Expedition 303 Scientists, 2006a). Although providing a much less temporally-resolved picture, the dominance of dropstones of basaltic lithology in the U1307 stratigraphy prior to ~2.4 Ma contrasts with a mixed suite of basaltic, granitic/gneissic and sandstone dropstones from ~2.4 Ma – consistent with the development of more extensive iceberg-calving sources on Greenland's southern Precambrian basement terranes during iNHG.

The apparent difference in timing of the onset of sustained IRD inputs to U1307 during iNHG that can be determined from the three different grain-size fractions that I examined for evidence of iceberg-rafting highlights the importance of choosing the most appropriate grain-size in sedimentological analysis of IRD. Both the wt.% ≥212 μm and grains ≥150 μm g^{-1} IRD records can be used to infer an almost complete absence of IRD deposition on Eirik Drift during warm periods prior to 2.72 Ma. The earlier onset of elevated glacial IRD inputs at U1307 that I infer from the ≥125 μm terrigenous grain-size fraction may be a product of sea-

ice rafted sand and/or of the coarsest fine sand also transported to the site by stronger bottom-currents prior to ~2.7 Ma, complicating the ability to use this grain-size fraction on Eirik Drift as a proxy for iceberg-rafting. Future investigation using, e.g., grain-size end-member mixing may help to determine whether or not the histories of the onset of significant iceberg-rafting to U1307 and 907 were temporally offset during iNHG. Regardless, using the improved RPI-based age model for U1307, the available IRD data indicate that extensive iceberg-calving margins definitely existed in both eastern and southern Greenland from 2.72 Ma (Fig. 4.13a and b).

Of additional note is the relatively low abundance of IRD deposited at both Sites U1307 and 907 during MIS 100 and 98, 2.52–2.48 Ma (Fig. 4.13), two prominent glacials in the global $\delta^{18}O$ record (Lisiecki and Raymo, 2005) that are recognised as major ice-rafting events to the central North Atlantic (e.g., Jansen and Sjøholm, 1991; Bailey *et al*., 2012, 2013). Sedimentation rates at U1307 are their lowest during this interval, which, while likely primarily attributable to a reduction in the amount of sediment delivered to the site by the WBUC, may also reflect a lack of significant IRD deposition at this time. The strong agreement with the Site 907 record suggests this may be a Greenland-wide signal, which I speculate may have been the result of one of two scenarios: 1) MIS 100–98 may not have resulted in especially pronounced glacial expansions on the Greenland landmass itself, so iceberg-calving margins may have been reduced at this time relative to during, e.g., MIS 96 (Fig. 4.13); or 2) expanded sea-ice around the Greenland landmass during these particularly globally cold glacials may have 'locked in' calved icebergs (as observed during the present day in Antarctica; Lichey and Hallmer, 2001; see also Chapter 5), reducing the number reaching the surrounding open ocean. Both of these interpretations appear to be in line

with provenance analysis of IRD deposited at Site 611 during the full glacial conditions of MIS 100 (Fig. 4.1) that suggests Greenland was not the dominant source of IRD to the central North Atlantic at this time, with more significant contributions from North America and other regions (Bailey *et al*., 2012).

4.4 Conclusions

The history of southern Greenland glaciation during the late Pliocene and earliest Pleistocene intensification of Northern Hemisphere glaciation (iNHG) is poorly constrained. New sedimentological and palaeomagnetic datasets from Site U1307 on Eirik Drift – which receives ice-rafted debris from icebergs transported in the East Greenland Current, and glaciofluvial silt and fine sand via the deep Western Boundary Undercurrent (WBUC) – reveal for the first time that while continental ice existed inland on southern Greenland prior to the onset of significant Northern Hemisphere glaciation, with occasional iceberg-calving margins during cold intervals from the end of the mid-Piacenzian warm period, extensive iceberg-calving margins were only likely a persistent feature in this region from 2.72 Ma. The new datasets also highlight for the first time that the depth of the core flow of the WBUC changed relative to the study site during iNHG. This finding underscores the need to redrill the Plio-Quaternary Eirik Drift to obtain a depth transect of drill sites. Only by doing so can we understand the importance of these observations on the WBUC for changes in Atlantic Meridional Overturning Circulation during iNHG, and the role the oceans may have played in driving glaciation at this time.

Chapter 5

Geochemical evidence that ice existed inland on southern Greenland during the mid-Piacenzian warm period

This chapter is a draft of **Blake-Mizen**, K., Carlson, A.E., Hatfield, R.G., Walczak, M., Bailey, I. Geochemical evidence that ice existed inland on southern Greenland during the mid-Piacenzian warm period. *Geology, in prep*. I performed the X-ray fluorescence data collection and interpreted the data. Anders Carlson carried out principal component analysis, and along with Robert Hatfield and Mo Walczak helped to advise my interpretations of the data.

5.1 Introduction

The Greenland Ice Sheet (GrIS) plays an important role in both regional and global climate change, since variability in its net mass balance is in a tightly-linked interplay with sea-level, sea-ice extent, albedo, atmospheric and oceanic circulation and marine primary productivity (e.g., de Vernal and Hillaire-Marcel, 2000; Box *et al*., 2012; Hawkings *et al*., 2014; Raymo *et al*., 2018). Modern observations (e.g., Willerslev *et al*., 2007; Bevis *et al*., 2019) and late Pleistocene studies (e.g., de Vernal and Hillaire-Marcel, 2008; Reyes *et al*., 2014; Hatfield et al. 2016; 2017) highlight that GrIS mass balance is particularly sensitive to even modest increases in global temperature relative to the present day, an important consideration given that the GrIS holds the equivalent to ~7 metres of eustatic sea-level rise in its current state (Meehl *et al*., 2007). Yet, substantial gaps remain in our understanding of its behaviour during deeper time, especially during the last great climate transition in Earth history: the late Pliocene and early Pleistocene intensification of Northern Hemisphere glaciation (iNHG), ~3.6–2.4 Ma (Mudelsee and Raymo, 2005), when Earth transitioned from the warmer-than-present climate of the early Pliocene to the largely colder-than-present bipolar glacial world of the Quaternary.

The majority of our existing understanding of GrIS evolution prior to the Last Glacial Maximum comes from marine core records of ice-rafted debris (IRD) – clay- to boulder-sized terrigenous material eroded by and incorporated into glaciers on land and calved off in icebergs, which gradually melt and deposit the IRD on the seabed (e.g., Andrews, 2000; Jansen *et al*., 2000; Kleiven *et al*., 2002; Thiede *et al*., 2011; Bailey *et al*., 2013). The spatial distribution of IRD deposition in the Greenland-proximal marine realm, for example on the Iceland Plateau (Jansen *et al*., 2000), in the Irminger Basin (St John and Krissek, 2002) and on

Eirik Drift (Blake-Mizen *et al*., 2019; see also Chapter 4) (Fig. 5.1), indicates that while iceberg-calving outlet glaciers likely occupied (north)eastern Greenland during cold stages from ~3 Ma, persistent and extensive iceberg-calving margins were not established in southern Greenland until ~2.72 Ma, during Marine Isotope Stage (MIS) G6. It is thought, however, that the GrIS may have not survived intervals of interglacial warmth until from ~2.5 Ma (Vanneste *et al*., 1995; Lawrence *et al*., 2009; Willeit *et al*., 2015). Our understanding of GrIS extent prior to MIS G6 is less clear; numerical model-based simulations indicate that Greenland may have been only partially ice-covered during cold stages prior to ~2.7 Ma, and partially to fully deglaciated during intervals of peak interglacial warmth (Willeit *et al*., 2015), including during the mid-Piacenzian warm period (mPWP; ~3.264–3.025 Ma; Dolan *et al*., 2011, 2015).

The mPWP is considered a potential analogue to future equilibrium climate (Burke *et al*., 2018), characterised by atmospheric CO_2 levels >400 ppmv and global temperatures elevated by 2–3 °C relative to today (e.g., Raymo *et al*., 1996; Bachem *et al*., 2017). Numerical climate models simulate variable GrIS extents for the mPWP, ranging from reduced but persistent ice caps in the mountainous regions of eastern and southern Greenland (e.g., Lunt *et al*., 2010; Dolan *et al*., 2011, 2015), to just ~7% of modern GrIS extents surviving in the eastern mountains (Solgaard *et al*., 2011). In addition, estimates of mPWP sea-level rise range widely from ~10 to 30 metres above present, with the upper-bound assuming complete GrIS deglaciation at this time (e.g., Raymo *et al*., 2018). Greenland-proximal IRD records indicate minimal iceberg-calving from the GrIS during the mPWP (e.g., Wolf and Thiede, 1991; Jansen *et al*., 2000; St John and Krissek, 2002; Blake-Mizen *et al*., 2019), but this suggests only a lack of iceberg-calving margins, and does not allow conclusions to be drawn regarding

the extent of inland ice at this time. In addition, results from state-of-the-art coupled ice-sheet-ocean model experiments suggest that the future response of Greenland to global warming may depend heavily on the extent of sea-ice reduction in the Northern Hemisphere (Koenig *et al*., 2014). Documenting GrIS variability and its temporal relationship to Northern Hemisphere sea-ice evolution is therefore required to improve our understanding of its likely response to continued anthropogenic global warming.

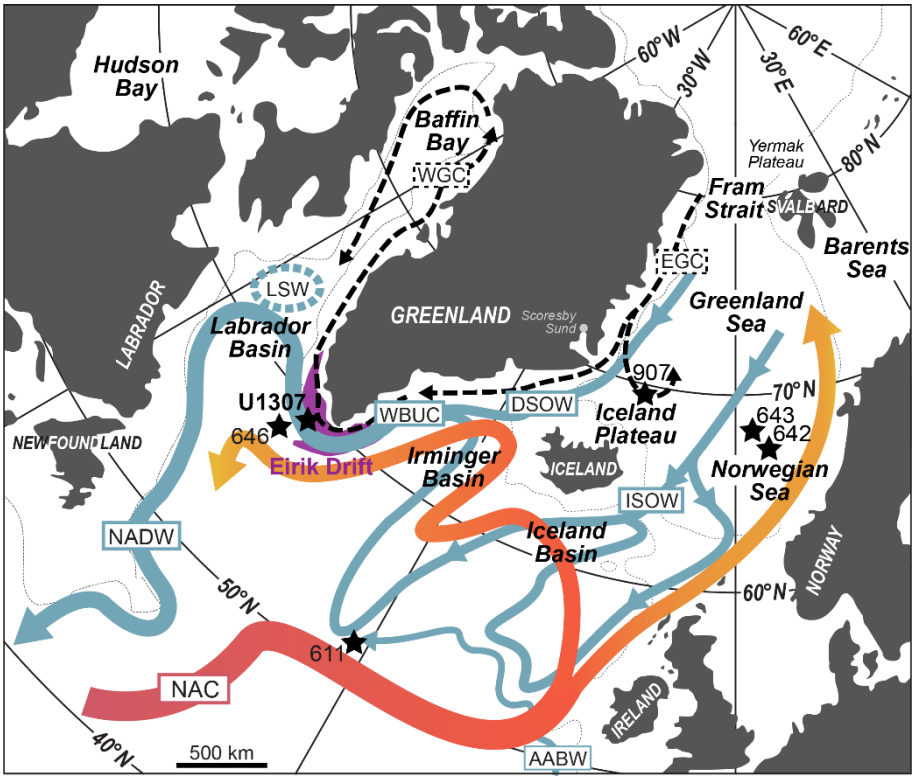

Figure 5.1 Map of Greenland and surrounding landmasses and ocean basins, showing the location of IODP Site U1307 (the focus of this thesis) on Eirik Drift (purple area), the position of North Atlantic ODP/DSDP/IODP drill sites mentioned in the text, and their relationships to the paths of key modern cold deep (blue), warm surface (red-yellow gradient) and surface iceberg-transporting (dashed black) ocean currents relevant to this study. EGC = East Greenland Current, WGC = West Greenland Current, NAC = North Atlantic Current, ISOW = Iceland-Scotland Overflow Water, DSOW = Denmark Strait Overflow Water, AABW = Antarctic Bottom Water, WBUC = Western Boundary Undercurrent, LSW = Labrador Sea Water, NADW = North Atlantic Deep Water. Also labelled are key localities mentioned in the text. The 1000 m isobath is given by thin dotted lines.

Eirik Drift, an elongate contourite drift deposit situated just offshore southern Greenland (Fig. 5.1), contains an expanded sedimentary record through the Plio-

Pleistocene influenced by detrital sedimentation transported by the Western Boundary Undercurrent (WBUC) – a deep current composed of Nordic Seas overflow waters that transports continental material from a range of circum-Arctic sources, including subglacially-eroded southern Greenland Precambrian-age felsic bedrock clay- and silt-size grains, and volcanic detritus from outcrops of the Tertiary-age North Atlantic Igneous Province (NAIP) on East Greenland and Iceland (Carlson *et al*., 2008; Hatfield *et al*., 2016) – as well as IRD from icebergs calved from outlet glaciers on the (south)eastern coasts and transported southward in the overlying East Greenland Current (EGC; Fig. 5.1) (Bigg *et al*., 1998; Hunter *et al*., 2007). Prior to ~2.72 Ma, when evidence of significant IRD deposition in Eirik Drift is largely absent (Blake-Mizen *et al*., 2019; see also Chapter 4), elevated inputs of southern Greenland-sourced glaciofluvial sediments to the region can therefore be used to track the existence of inland ice-caps.

The concentrations of elements K, Ti and Fe (e.g., Carlson *et al*., 2008), as well as the ratio of K to Ti (a proxy for felsic versus basaltic crystalline sediment input; Richter *et al*., 2006; Hodell *et al*., 2010; Grützner and Higgins, 2010) in marine sediments have been used successfully to track the delivery of subglacially-eroded sediment to Eirik Drift and other North Atlantic sediment drifts (Gardar and Faeroe) formed by the Nordic Seas overflows during the late Pleistocene. Here I report new high-resolution X-ray fluorescence (XRF) core-scanning geochemical data spanning ~3.2–2.2 Ma from Integrated Ocean Drilling Program (IODP) Site U1307 on Eirik Drift (Fig. 5.1) to document inland GrIS history. This study benefits from a highly-resolved relative paleointensity (RPI)-based age model (Blake-Mizen *et al*., 2019; see also Chapter 4), enabling the timing of variability in these data to be precisely-dated. Using principal component

analysis of key elements K, Ti, Fe, Si, Sr and Ca, as well as the ratio K/Ti, I demonstrate that indicators of southern Greenland-sourced glaciofluvial sediment input support the continuous presence of ice on southern Greenland since ~3.2 Ma, highlighting the probability that the upper-end estimates for mPWP GrIS loss and associated sea-level rise are too high; and that biogenic productivity in the surface ocean above Site U1307 significantly decreased at the onset of elevated and persistent ice-rafting to the site at MIS G6, ~2.72 Ma, indicating a dramatic cooling of the surface ocean at this time with the expansion of local ice-sheets.

5.2 Study Site and Methods

5.2.1 Study site and sampling

IODP Site U1307 is located on the northern flank of Eirik Drift (Fig. 5.1; 58°30.3'N, 46°24.0'W), at 2575 m water depth. Two holes were drilled at Site U1307 (U1307A and U1307B) during IODP Expedition 303 in 2004, which together recovered a ~175 m composite Plio-Pleistocene section (Expedition 303 Scientists, 2006). I sampled the Site U1307 cores at the MARUM IODP Core Repository in Bremen, Germany, between ~117 and 175 revised metres composite depth (rmcd; sampling was guided initially by the shipboard splice, which was revised following high-resolution magnetic susceptibility analysis; see Chapter 4). I sampled 38 u-channels (typically 2 × 2 × 150 cm^3 continuous samples; Weeks *et al*., 1993) between ~113 and 148 metres below seafloor (mbsf) in U1307A, and between ~110 and 136 mbsf in U1307B (see Chapter 3 for the full description of the sampling method), to capture a near-continuous record of drift sedimentation over iNHG. Based on a newly-resolved orbital-resolution relative paleointensity (RPI)-based age model for U1307 spanning

~3.2 to 2.2 Ma (Blake-Mizen *et al*., 2019; see also Chapter 4 for the full description of how the age model was generated), the average sedimentation rate over the study interval was ~6 cm kyr^{-1}. This rate is highly variable, however; as much as ~10–12 cm kyr^{-1} in the deeper (>3 Ma) part of the record, falling to as low as ~1 cm kyr^{-1} at ~2.5 Ma (Blake-Mizen *et al*., 2019; see also Chapter 4).

5.2.2 Methods

I scanned each of the 38 Site U1307 u-channels at 1 mm (approximately decadal) resolution with a 5-second count time using Oregon State University's ITRAX XRF core scanner, in September–October 2015. XRF scanning was performed with a tube voltage of 45 kV and an X-ray current of 40 mA in order to obtain statistically-significant counts of the key elements Si, K, Ca, Ti, Fe and Sr. Prior to scanning, I carefully smoothed each u-channel surface (across-channel) in order to remove any surficial residue and minimise any small cracks resulting from the core drying in storage, then covered them with 12 μm transparent polypropylene thin-film to minimise desiccation and maximise transmittance for all measured elements (e.g., Richter *et al*., 2006). In order to objectively detect geochemical signatures related to glaciofluvial terrigenous sediment discharge from Greenland's southern terranes (e.g., Carlson *et al*., 2008; Hodell *et al*., 2008; Channell *et al*., 2012; Reyes *et al*., 2014), I normalised the Si, K, Ti, Fe and Sr measurements for Ca-dilution by dividing their values by the inverse linear relationship between each element and Ca (see Appendix D) to reduce the effect of variations in biogenic and detrital carbonate downcore (e.g., Carlson *et al*., 2008), and Anders Carlson applied principal component (PC) analysis to the dataset of all six elements (as per the method of Mix *et al*., 1986 and Carlson *et al*., 2008).

Due to the moderate to high levels of bioturbation evident in U1307 cores (see Chapter 3; also Expedition 303 Scientists, 2006a), it is unlikely that decadal-scale resolution is preserved reliably. In addition, the persistence of small cracks and/or a slightly bumpy u-channel sample surface, as well as changes in sediment texture downcore due to variable contents of IRD, have the capacity to affect data quality; incoming X-ray radiation can be deflected by uneven surface topography (Voglis and Rindby, 1995) and shielded from reaching smaller clasts by larger grains (e.g., Finkelshtein and Brjansky, 2009). Taking these factors affecting the realistic resolution of these XRF-scanning data into account, all records are hence presented here as a 50-point (5 cm) smoothed average.

5.3 Results

The raw trends for each measured element are given in Figure 5.2. Significant glacial-interglacial variability (MIS interpretations based on the published age model for U1307; Blake-Mizen *et al*., 2019; see also Chapter 4) characterises each elemental raw count record, with K, Si and Sr counts generally higher during glacial periods, and vice versa for Ti, Fe and Ca (Fig. 5.2). Terrestrial elements Ti and Fe secularly increase during the study interval; K slightly decreases overall, but does show an upward trend between ~2.7 and 2.45 Ma, with the baseline only decreasing after ~2.4 Ma. Biogenic elements Ca and Sr both decrease over the study interval. In general, the Ti and Fe records show the best agreement throughout the study interval (compare Figs. 5.2c and d), as do K and Si (compare Figs. 5.2a and b), indicating that these pairs of elements share a similar source.

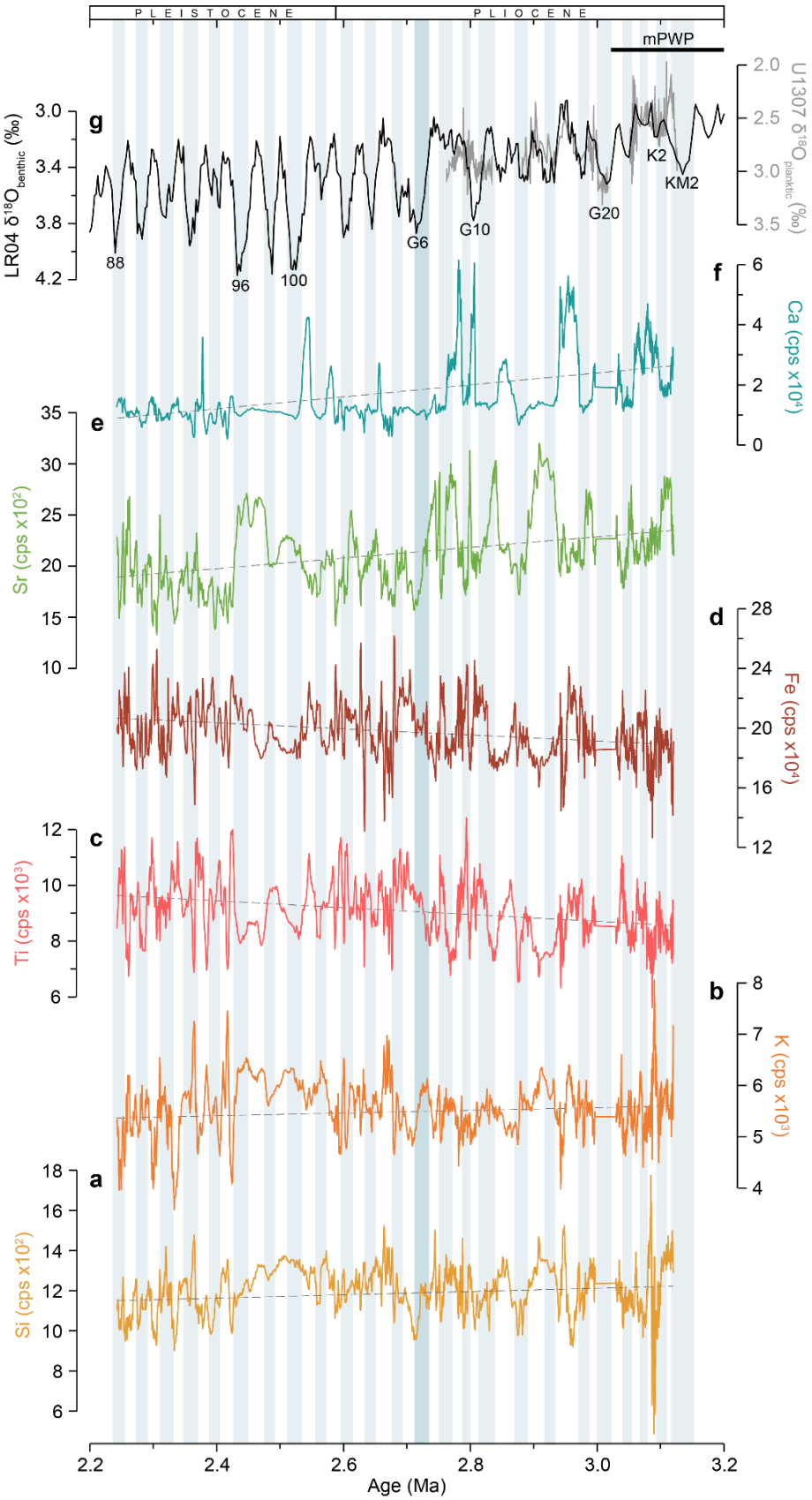

Figure 5.2 Site U1307 raw XRF data (in counts per second, cps, following Ca-correction): (**a**) silica (Si), (**b**) potassium (K), (**c**) titanium (Ti), (**d**) iron (Fe), (**e**) strontium (Sr) and (**f**) calcium (Ca) (plotted as 50-point moving averages; see Appendix D for full data). The LR04 benthic $\delta^{18}O$ stack (black record; Lisiecki and Raymo, 2005), overlain by available U1307 planktic $\delta^{18}O$ data (Sarnthein *et al.*, 2009), is also shown in (**g**) for reference. Numbers in (g) are Marine Isotope Stages, with the duration of the mid-Piacenzian warm period (mPWP; Dolan *et al.*, 2011) also indicated. Vertical blue bars highlight cold stages.

Bivariate plots for each terrestrial element, including Si, are given in Figure 5.3. The different colours highlight that the relationship of each element to another changes over the study interval with the onset of significant ice-rafting to Site U1307 at MIS G6, ~2.7 Ma (Blake-Mizen *et al*., 2019; see also Chapter 4). In agreement with the trends noted in the raw data (Fig. 5.2), Ti and Fe (Fig. 5.3f), and K and Si (Fig. 5.3a) are the elements most strongly associated throughout the whole study interval. Prior to the onset of significant ice-rafting to the site in the interval ~3.2 to 2.7 Ma, Ti and Fe show the strongest association (r = 0.733; Fig. 5.3f), suggesting they shared a very similar source during this time. In the following interval ~2.7 to 2.2 Ma, this relationship is weaker (r = 0.427; Fig. 5.3f), suggesting the source of either or both elements changed or diversified. The opposite is true for K and Si; they show relatively weak association during ~3.2 to 2.7 Ma (r = 0.228; Fig. 5.3a), but their much stronger correspondence ~2.7 to 2.2 Ma (r = 0.7; Fig. 5.3a) indicates their sources converged with the development of extensive iceberg-calving margins at MIS G6. The relationship of K to both Fe and Ti changes completely between the two intervals; during ~3.2 to 2.7 Ma they weakly correspond (r = 0.213; Fig. 5.3b; and r = 0.139; Fig. 5.3e) suggesting they shared some sources at this time, but as southern Greenland glaciation intensified they diverged, showing a stronger negative correlation in the interval ~2.7 to 2.2 Ma (r = -0.335; Fig. 5.3b; and r = -0.443; Fig. 5.3e). Si is weakly to moderately negatively correlated to both Ti and Fe (the latter more so) throughout the entire study interval (Fig. 5.3c and d), suggesting generally different sources for these elements.

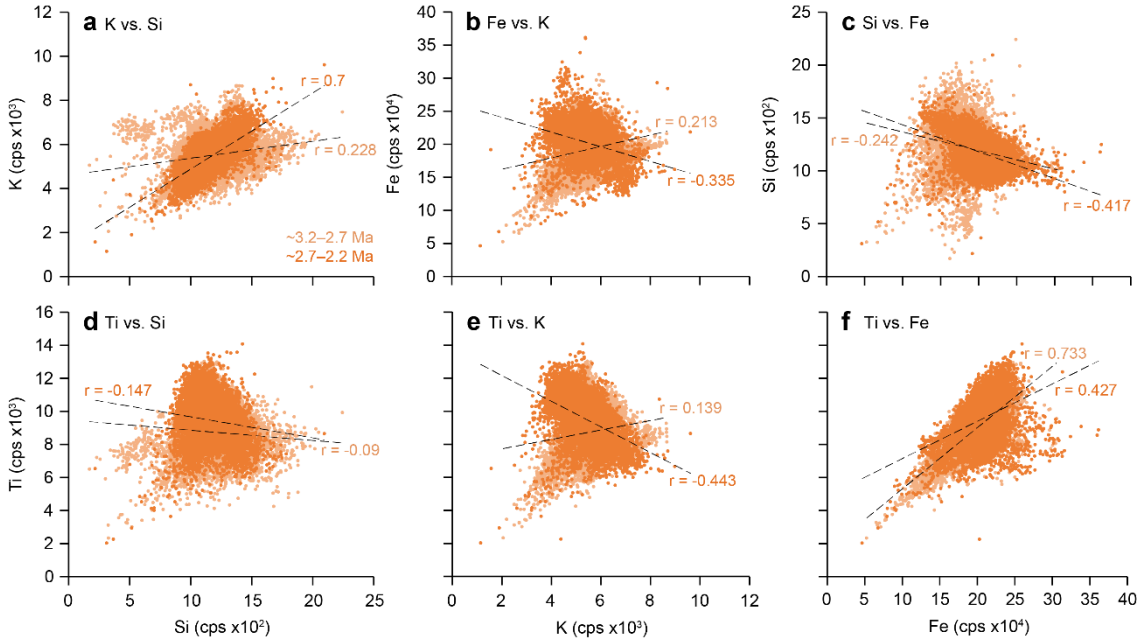

Figure 5.3 Cross-plots of key elements K, Ti, Fe and Si measured by XRF for this study (following Ca-correction). Data is colour-coded for the intervals ~3.2–2.7 Ma (light orange; n = 25,787) and ~2.7–2.2 Ma (dark orange; n = 11,315). The trend lines for each element pair during both intervals are labelled with the r value of correlation, also colour-coded to correspond to each interval.

Relative changes in Ca versus Fe (the ratio Ca/Fe) are widely understood to accurately track glacial-interglacial variability in the North Atlantic, with higher values characterising interglacials (e.g., Richter *et al*., 2006; Dickson *et al*., 2010) due to the greater productivity of calcifying marine organisms (primarily foraminifera) under more favourable interglacial conditions, and their decline and dilution by terrigenous inputs during glacials (e.g., Balsam and McCoy, 1987; Richter *et al*., 2006). Previously published records of Site U1307 coarse (≥212 μm) IRD (tracking (de)glacial iceberg-calving from southeastern Greenland) and fine (≥63 μm) well-sorted sand (tracking interglacial WBUC-sourced sediment input prior to ~2.72 Ma, and (de)glacial IRD input from ~2.72 Ma; Blake-Mizen *et al*., 2019; see also Chapter 4) are given in Figure 5.4 alongside the new record of Ca/Fe. The good correspondence of highs in Ca/Fe with ≥63 μm sand pre-2.72 Ma, and lows with ≥212 μm IRD throughout the study interval, are in good agreement with the inferred climatic relationships (compare Fig. 5.4a to b), with the shapes of Ca/Fe cycles comparable to those in the LR04 $\delta^{18}O$ stack (compare

Fig. 5.4b to c). Prior to the onset of significant ice-rafting ~2.72 Ma, Ca/Fe ratios were relatively variable with highest values characterising interglacials; at ~2.72 Ma, however, Ca/Fe values fell significantly as ≥212 µm IRD inputs significantly increased, recovering only slightly during some interglacials. The interpretation of the biogenic nature of the Ca component is supported by my observations of the discrete samples used to generate the IRD and sand wt.% records (see Chapter 4 and Appendix B); high abundances of foraminifera occur typically in samples characterised by little to no coarse IRD and abundant fine, well-sorted sand. The strong similarity of the Ca/Fe record to the Ca raw count record (Fig. 5.4f) suggests variability in this ratio is primarily controlled by the variability in Ca.

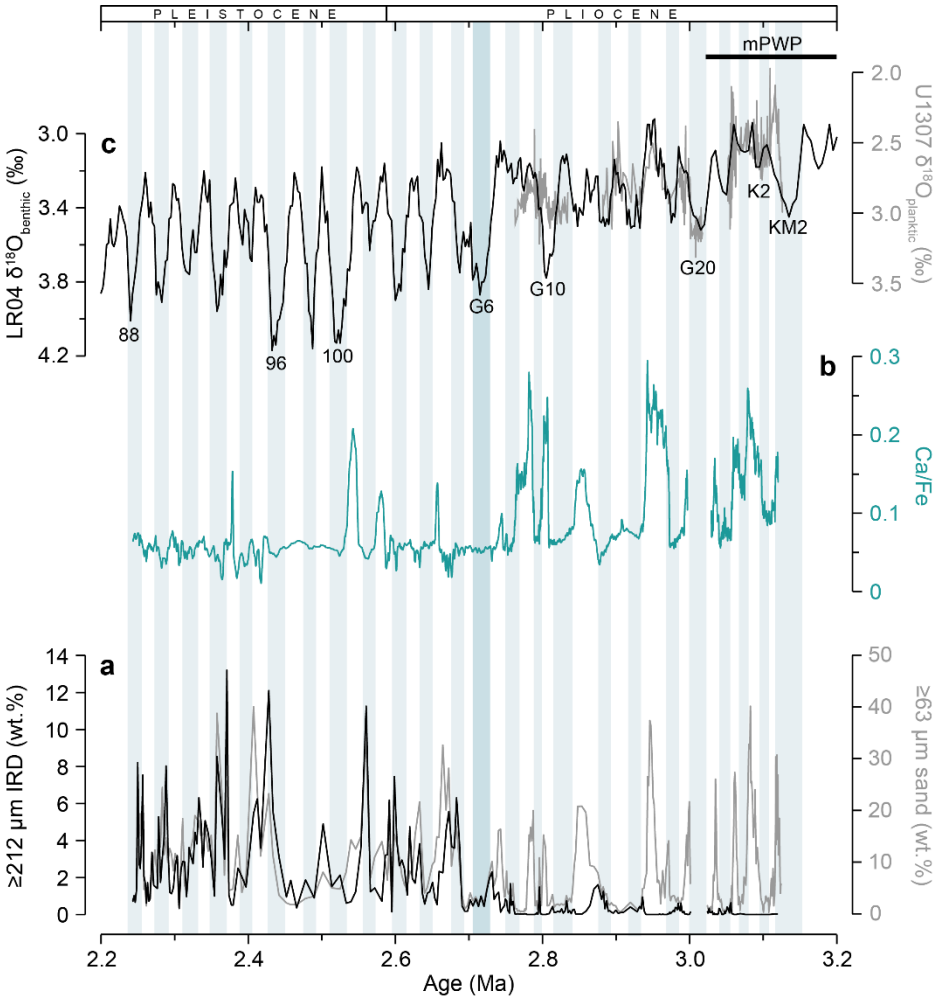

Figure 5.4 Site U1307 (**a**) wt.% ≥212 µm IRD and wt.% ≥63 µm terrigenous sand (see Chapter 4; Blake-Mizen *et al*., 2019), (**b**) the ratio of Ca to Fe (Ca/Fe), and (**c**) planktic $\delta^{18}O$ (Sarnthein *et al*., 2009). The LR04 benthic $\delta^{18}O$ stack is also shown in (c) for reference (Lisiecki and Raymo, 2005). Numbers in (c) are Marine Isotope Stages, with the duration of the mid-Piacenzian warm period (mPWP; Dolan *et al*., 2011) also indicated. Vertical blue bars highlight cold stages.

A dataset such as this – with several variables changing over time as a result of a combination of climatic and environmental processes – benefits from statistical separation of the main trends in the data using principal component (PC) analysis, which can give information on which variables are most closely associated and how the processes jointly affecting them change through time. The results of the PC analysis are given in Table 5.1. The first three principal components account for 87% of the variance in the dataset, while the remaining three each explain <10% of the remaining variance. I therefore choose to focus only on the first three for clarity of interpretation. PC1 (~55% of the variance) has strong loadings with Sr and Ca and a moderate loading with Si, and is moderately opposed by terrestrial elements Ti and Fe (Table 5.1). In this Greenland-proximal setting, Si has both a terrigenous (felsic rocks) and a marine productivity (siliceous tests) component (e.g., Finkenbinder *et al*., 2015), whereas Ca and Sr both primarily reflect marine carbonate productivity (calcareous tests; e.g., Graham *et al*., 1982). The relationship between Ca and Sr (shown in Appendix D Fig. D.1), although strongly positive overall (r = 0.8), is not entirely linear. This suggests some Ca in the U1307 record is of a detrital source (e.g., small regions of Phanerozoic platform carbonates exposed in the region of Scoresby Sund; Fig. 5.1; Escher and Watt, 1976). Despite this, given its association with Sr (strongest) and Si in this component, I interpret PC1 to reflect marine productivity in surface waters. PC2 (~22% of the variance) has strong loadings with K and Si and moderate opposition by Ca (Table 5.1). Since K and Si occur together in high proportions in felsic rocks (e.g., granite), and show strong positive correlation following the onset of significant ice-rafting at MIS G6 (Fig. 5.3a), I hence interpret PC2 to reflect changes in felsic crystalline input (Carlson *et al*., 2008; Finkenbinder *et al*., 2015). PC3 (~10% of the variance) has strong loadings with

Si and Ti, and is strongly opposed by K (Table 5.1). This is less straightforward to interpret, but based upon the longevity of quartz in ocean sediments due to its high resistance to both mechanical and chemical weathering (e.g., Leinen *et al*., 1986) and the felsic vs. mafic interpretation of K vs. Ti, I tentatively suggest PC3 to reflect a bottom-current derived quartz and basalt component, with quartz derived from continental sources in the Arctic region (e.g., Leinen *et al*., 1986) and basalt derived from the NAIP (e.g., Carlson *et al*., 2008; Grützner and Higgins, 2010).

Table 5.1 Principal components (PC) of the Site U1307 XRF elemental dataset with percentage of dataset variance given in brackets, and individual loading coefficients for each element.

Element	PC1 (55%)	PC2 (22%)	PC3 (10%)	PC4 (8%)	PC5 (3%)	PC6 (2%)
Si	0.2557	0.5982	0.6581	-0.3152	0.1325	-0.1635
K	-0.0396	0.7755	-0.4959	0.3470	-0.1727	-0.0297
Ca	0.4698	-0.1907	0.1544	0.6100	-0.0813	-0.5835
Ti	-0.4496	0.0296	0.5401	0.4749	-0.4168	0.3258
Fe	-0.4980	0.0568	0.0671	0.2848	0.7858	-0.2135
Sr	0.5121	0.0174	0.0308	0.3186	0.3935	0.6930

Time-series of the three main principal components and the ratios K/Ti and Ca/Sr are presented in Figure 5.5. PC1, the marine productivity component, shows strong glacial-interglacial variability throughout the first half of the study interval, elevated during the mPWP and interglacial periods (Fig. 5.5c). After ~2.7 Ma, variability significantly reduced to almost consistently negative values. PC2 and K/Ti, the felsic input proxies, are both generally elevated during (de)glacial intervals containing coarse IRD throughout the study interval; this pattern is particularly pronounced after ~2.7 Ma, when IRD inputs significantly increased (Fig. 5.5a-c). This appears to confirm a southern Greenland felsic source for the ice-rafted material. PC3 is less variable than the first two components, but is

generally elevated during interglacials throughout the study interval (Fig. 5.5d) and visibly varies opposite to PC2 and K/Ti, which supports a current-derived interpretation for PC3. This is further backed up by the presence of abundant fine, well-sorted quartz-rich sand during interglacials prior to ~2.7 Ma at U1307 (grey record in Fig. 5.5a), indicative of enhanced bottom-current transport (Blake-Mizen *et al*., 2019; see also Chapter 4). PC3 underwent a slight kick-up at ~2.9 Ma, with muted variability between ~2.85–2.45 Ma relative to the rest of the record (Fig. 5.5d).

The Ca/Sr ratio of Eirik Drift sediments has been used successfully to track Heinrich events (large armadas of icebergs entering the North Atlantic at times of glacial termination; Heinrich, 1988) and meltwater discharge events sourced from the North American Laurentide Ice Sheet (LIS) in the region of Hudson Bay (Fig. 5.1) during the late Pleistocene, due to the characteristic dolomite and carbonate geology of the Hudson Bay region (Carlson *et al*., 2008; Hodell *et al*., 2008; Nicholl *et al*., 2012). The provenance of IRD deposited in the subpolar North Atlantic during iNHG suggests iceberg-calving margins did not develop on North America during cold stages until MIS G2, ~2.64 Ma (Bailey *et al*., 2013), so we may not expect to see significant peaks in Ca/Sr during (de)glacials at U1307 until this time. The record of U1307 Ca/Sr during ~3.2–2.2 Ma (Fig. 5.5f) displays strong glacial-interglacial variability, with higher values (~20 to 30) generally occurring during interglacials. Even after MIS G2, peaks in Ca/Sr do not commonly correspond to (de)glacial intervals, excepting perhaps for relatively minor increases (~10) during the deglacials of MIS 104 and 96 (Fig. 5.5f). Similarities of Ca/Sr to the raw Ca record (Fig. 5.2f), as well as Ca/Fe (Fig. 5.4b), suggest that this ratio is again mainly driven by the large variability in Ca, and so may not be a faithful representation of detrital carbonate concentration.

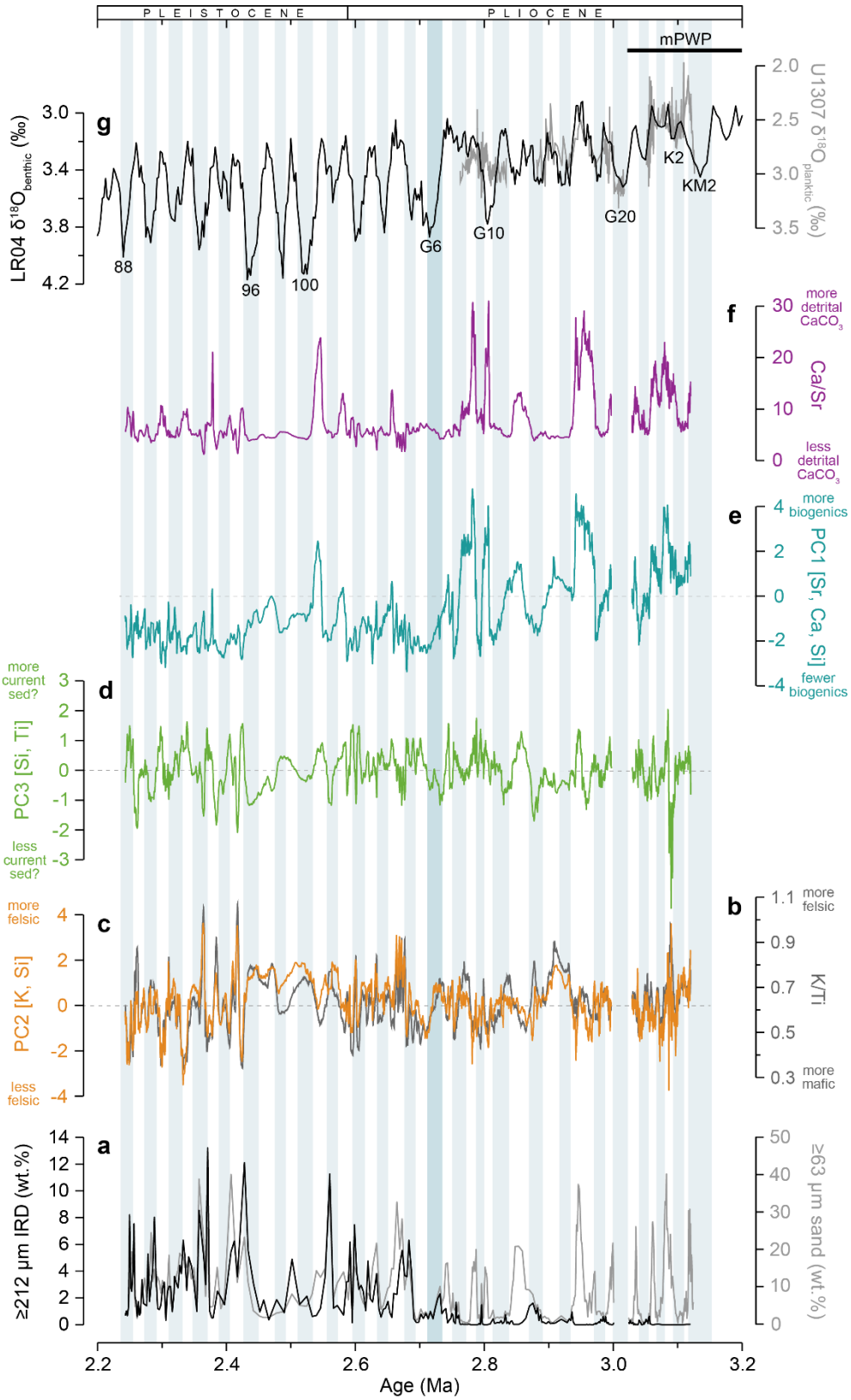

Figure 5.5 Site U1307 sedimentological and geochemical records: (**a**) wt.% ≥212 µm IRD and wt.% ≥63 µm terrigenous sand (see Chapter 4; Blake-Mizen *et al*., 2019), (**b**) XRF ratio of K to Ti (K/Ti), (**c**) principal component (PC)2, (**d**) PC1 and (**e**) PC3 of the XRF elemental dataset, (**f**) XRF ratio of Ca to Sr (Ca/Sr) and (**g**) $\delta^{18}O$ (grey = Sarnthein *et al*., 2009; black = Lisiecki and Raymo, 2005). Records (b), (c), (d), (e) and (f) are plotted as 50-point moving averages of the full datasets, available in Appendix D. Numbers in (g) are Marine Isotope Stages, with the duration of the mid-Piacenzian warm period (mPWP; Dolan *et al*., 2011) also indicated. Vertical blue bars highlight cold stages. See also Table 5.1 for relative variance of each PC and their individual element loading coefficients.

5.4 Discussion

The pattern of variability in the Site U1307 Ca/Sr record (Fig. 5.5f) indicates a generally greater supply of detrital carbonate material during interglacials, especially prior to ~2.7 Ma (likely transported by bottom-currents from local sources, e.g., Proterozoic platform sediments exposed in the East Greenland Caledonides; Escher and Watt, 1979). Only minor increases in Ca/Sr during deglacials following MIS 104 and 96 suggests IRD deposited throughout the iNHG interval at Site U1307 was dominated by local sources, as is the case during the modern (e.g., White *et al*., 2016), despite an increase in LIS-sourced glacial IRD to the subpolar North Atlantic at this time (Bailey *et al*., 2013). In addition, the largest increases in Site U1307 Ca/Sr during the study interval, with values on the order of ~25 to 30 (Fig. 5.5f), are well below those recorded on Eirik Drift for during Heinrich events in the late Pleistocene (~150–240; Hodell *et al*., 2008), and for the LIS outwash event during the early Last Interglacial (~100; Nicholl *et al*., 2012). In addition, as previously noted due to similarities with the raw Ca record (Fig. 5.2f), the pattern of variability in this record is likely primarily driven by variations in biogenic Ca. I am therefore confident that no late Pleistocene-scale LIS glacials, terminations or outwash events are recorded at Site U1307 during ~3.2–2.2 Ma, which continues to support a late Pleistocene onset for Hudson Strait Heinrich events in the North Atlantic (Hodell *et al*., 2008).

PC3, the potential bottom-current sediment supply proxy, underwent a significant decrease at the MIS K2 deglacial (Fig. 5.5d); it is perhaps beyond the scope of this study to speculate on a cause, especially since PC3 only accounts for ~10% of the dataset variance, but core descriptions and photographs do not indicate an unusual event occurred at this depth (Expedition 303 Scientists, 2006). The slight increase in PC3 at ~2.9 Ma (Fig. 5.5d) may reflect intensified

glaciation of (north)eastern Greenland from ~3 Ma as indicated in the IRD record from ODP Site 907 (Fig. 5.1; Jansen *et al*., 2000), and hence a relatively greater basaltic content of glaciofluvial sediments transported to Eirik Drift, particularly during interglacials. A coeval decrease in K/Ti values ~2.9 to 2.8 Ma (Fig. 5.5b) may support this inference. The lack of a secular trend in PC3 suggests a relatively consistent supply of these elements to Eirik Drift over iNHG, and may also be a result of the overall lack of correspondence between Si and Ti during the study interval, especially after ~2.7 Ma (Fig. 5.3d). It is hence not simple to interpret this record as a tracer of relative WBUC-derived sediment supply; proximal southern Greenland sources for Si and Ti (e.g., Escher and Watt, 1976) also likely contributed a significant proportion of the glacial ice-rafted component deposited as iNHG progressed, as the sources of these elements also further diverged. I speculate that this may explain the muted glacial-interglacial variability in PC3 during ~2.85–2.45 Ma (Fig. 5.5d).

Both of the felsic input proxies PC2 and K/Ti were elevated at Site U1307 during the deglacials of MIS KM2 (~3.12 Ma) and K2 (~3.09 Ma) (Fig. 5.5b-c), which I interpret to reflect significant glaciofluvial runoff from southern Greenland at these times. Despite a lack of coarse IRD deposition recorded during these mPWP glacials, indicating no iceberg-calving margins were present in southern Greenland at this time, elevated deglacial glaciofluvial inputs strongly suggest the presence of actively-eroding inland ice on southern Greenland during the coldest stages of the mPWP. This finding appears to be consistent with models that suggest the GrIS was restricted but still present as reduced ice-caps occupying the highlands of southern and eastern Greenland during the mPWP (Dolan *et al*., 2011, 2015), and supports the same inference recently drawn from Site U1307 environmental magnetic records (Blake-Mizen *et al*., 2019; see also Chapter 4).

I hence propose that the new XRF data refutes predictions for complete GrIS deglaciation during the mPWP, ruling out the upper-end estimate of ~30 m eustatic sea-level rise proposed for this time (e.g., Raymo *et al*., 2018). The K/Ti ratio also indicates felsic input increased (relative to basaltic sources) between ~2.7–2.4 Ma (Fig. 5.5b), supporting expansion of southern GrIS iceberg-calving margins over iNHG as interpreted from the Site U1307 coarse IRD record (Fig. 5.5a; Blake-Mizen *et al*., 2019; see also Chapter 4). Following interpretation of changes in Site U1307 environmental magnetics, physical grain-size and sedimentation rate between ~2.9 and 2.5 Ma that suggest a reduction in WBUC-transported southern Greenland-sourced glaciofluvial silt over iNHG (Blake-Mizen *et al*., 2019; see also Chapter 4), these new XRF data demonstrate that the geochemical signature of Eirik Drift sediments still became relatively more dominated by felsic inputs from a progressively more glaciated southern Greenland, supporting an overall decrease in WBUC-driven sediment supply at this time.

The records of PC1 and Ca/Fe suggest high marine productivity in surface waters overlying U1307 during warm intervals, including the mPWP, prior to ~2.7 Ma (Figs. 5.4b, 5.5e). At the onset of significant ice-rafting to Eirik Drift, a sharp and maintained reduction in carbonate productivity took place, with only minor recovery during some interglacials post-2.7 Ma (Figs. 5.4, 5.5). This interpretation is strengthened by the loss of foraminifera abundances at Site U1307 over iNHG (Blake-Mizen *et al*., 2019; see also Chapter 4 and Appendix B). Other sites in the (sub)polar North Atlantic and Nordic Seas show a similar pattern for carbonate productivity; at nearby Eirik Drift ODP Site 646 (Fig. 5.1), carbonate accumulation periodically increased prior to ~2.6 Ma before dropping to low levels for the remainder of the iNHG interval, coeval with almost no carbonate deposition at

Norwegian Sea ODP Sites 642 and 643 (Fig. 5.1) between ~2.6–1.2 Ma (Bohrmann *et al*., 1990). Further south at central North Atlantic Deep Sea Drilling Project (DSDP) Site 611 (Fig. 5.1), abundances of foraminifera dropped sharply at MIS 100, ~2.53 Ma, coeval with the onset of significant IRD inputs to this site (Bailey *et al*., 2012).

The only moderate loading of Si with PC1 (Table 5.1) may reflect the fact silicifying (opal) organisms, primarily diatoms, were more commonly present in high abundances during (de)glacial intervals associated with coarse IRD deposition, and did not undergo a similarly significant reduction over iNHG (see Appendix B). In the modern northern North Atlantic, the highest opal production is restricted close to the Greenland continent due to seasonal cover of the path of the EGC by pack-ice, where diatoms thrive in ice-edge blooms (e.g., Wilson *et al*., 1986; Bohrmann *et al*., 1990). The EGC hence also marks the boundary of the Polar Front (PF) – an atmospheric and oceanic boundary separating cold productive Polar waters to the north from warmer sub-Arctic waters to the south – in the vicinity of Greenland, which in the present day sits close to the latitude of Eirik Drift at ~59 °N (e.g., Ruddiman *et al*., 1977; Dickson *et al*., 1988; McManus *et al*., 1994). High glacial-interglacial variability of biogenic opal production between ~4–2 Ma at Site 646 is interpreted to reflect the development of seasonal pack-ice along the EGC at this time, and orbital-scale latitudinal PF shifts controlling the extent of this sea-ice cover of waters overlying Eirik Drift (Bohrmann *et al*., 1990). This interpretation is supported by recent work demonstrating extended sea-ice presence over the Yermak Plateau and south of Iceland from as early as ~4 Ma (Clotten *et al*., 2019). I hence propose that as iNHG progressed, the PF shifted southward relative to Site U1307 and numbers of foraminifera preserved at the site decreased, owing both to dilution of biogenic

material by terrigenous inputs and to a reduction in foraminiferal productivity associated with reduced surface-ocean light and/or salinity by expanded pack-ice cover (Bailey *et al*., 2012), conditions that remained favourable for diatom productivity throughout the study interval. I also speculate that this inferred expanded sea-ice coverage of waters overlying Site U1307 may have resulted in anomalously reduced IRD deposition at the site during particularly cold glacials MIS 100 and 98 (~2.5 Ma; Fig. 5.5a; see also Chapter 4), as it would have restricted the movement of calved icebergs along the pack-ice-covered EGC at this time.

The work presented here has potentially important implications for changes in Atlantic Meridional Overturning Circulation (AMOC) during iNHG, the oceanic 'conveyor belt' distributing heat and salinity between the high and low latitudes that amplifies glacial-interglacial cycles via ocean-atmosphere feedbacks (e.g., Hunter *et al*., 2007; Thornalley *et al*., 2009). The effect of salinity dominates over temperature in controlling vertical ocean structure in cold subpolar regions like the Nordic Seas (Sigman *et al*., 2004), a region crucial for deep-water formation (Dickson *et al*., 1988; Böhm *et al*., 2015). In the modern, relatively dense, warm, salty surface waters entering the Nordic Seas via the northward-flowing North Atlantic Current (NAC) interact with the subpolar surface ocean and are converted into colder, fresher deep water in the abyss (e.g., Bohrmann *et al*., 1990; Thornalley *et al*., 2009), and then are exported southward over the Greenland-Scotland Ridge as overflow waters which coalesce in the WBUC in the vicinity of Eirik Drift (Fig. 5.1; Hunter *et al*., 2007; Stanford *et al*., 2011). After entraining additional deep waters in the Labrador Sea, this water mass flows southward in the deep North Atlantic as North Atlantic Deep Water (NADW; Fig. 5.1), the northern component of AMOC (e.g., Hunter *et al*., 2007;

Stanford *et al*., 2011). Recent observations suggest that this conversion process taking place in the Nordic Seas is what primarily controls AMOC variability (Lozier *et al*., 2019), with surface-ocean stratification and reduced convective overturning in this region linked to lowered salinity and hence density of NADW (Dickson *et al*., 1988). Expanded sea-ice in the EGC during iNHG is therefore likely to have weakened both NAC influence in the northern North Atlantic, thermally isolating the Greenland landmass and acting as a positive feedback to further cooling and ice-sheet growth (e.g., Lawrence *et al*., 2009; Clotten *et al*., 2019), and the efficiency of NADW formation due to the resultant enhanced stratification of Nordic Seas surface waters (e.g., Hunter *et al*., 2007; Bell *et al*., 2015). These findings are consistent with the recent suggestion that the WBUC may have slowed and shoaled over Eirik Drift during iNHG (Blake-Mizen *et al*., 2019; see also Chapter 4), and that reductions in NADW export during iNHG led to observed incursions of southern-sourced water into the deep North Atlantic during glacials from ~2.7 Ma (Lang *et al*., 2016).

5.5 Conclusions

The spatial maturation of the Greenland Ice Sheet (GrIS) during the Plio-Pleistocene intensification of Northern Hemisphere glaciation (iNHG) – particularly during the mid-Piacenzian warm period (mPWP), a potential analogue for future equilibrium climate – is not currently well-understood. I carried out principal component analysis on a dataset of six key elements Si, K, Ca, Sr, Ti and Fe, measured by X-ray fluorescence analysis of sediments spanning ~3.2 to 2.2 Ma from IODP Site U1307 on Eirik Drift, south of Greenland. Using the ratio K/Ti (indicating relative contributions from felsic vs. basaltic sources) and the felsic input principal component, I infer the persistence of significant inland ice on

southern Greenland during the coldest stages of the mPWP, rendering the upper estimates of eustatic sea-level rise for this time unlikely. As iNHG progressed, increases in the felsic indicators accompanied by contemporaneous decreases in Ca/Fe (a proxy for biogenic versus terrigenous sedimentation) and the marine productivity principal component track the co-evolution of southern GrIS iceberg-calving margins and the southward expansion of sea-ice over Eirik Drift ~2.7 Ma. I propose that this would have acted as a positive feedback to further cooling and ice-sheet growth on Greenland via thermal isolation and surface-ocean stratification, with potentially important implications for Atlantic Meridional Overturning Circulation via reduced NADW production.

Chapter 6

Tracking the provenance of Greenland-sourced ice-rafted debris deposited on Eirik Drift during the Plio-Pleistocene intensification of Northern Hemisphere glaciation

This chapter is a draft of **Blake-Mizen**, K., Lawrence, K.T., Bailey, I. Tracking the lead-isotope and petrographic provenance of Greenland-sourced ice-rafted debris deposited on Eirik Drift during the Plio-Pleistocene intensification of Northern Hemisphere glaciation. *Earth and Planetary Science Letters, in prep.* I performed the Pb-isotope and SEM QEMSCAN® data collection and interpreted the data. Ian Bailey helped to generate the Pb-isotope data, and Gavyn Rollinson and Joe Pickles assisted with SEM QEMSCAN® data processing.

6.1 Introduction

The Greenland Ice Sheet (GrIS) represents the last major surviving stronghold of glaciation in the Northern Hemisphere, and in its current state holds the equivalent to ~7 metres of eustatic sea-level rise (Meehl *et al*., 2007). While ephemeral glaciers are thought to have been a feature of the landmass since at least the late Eocene, with its first ice-shelf glaciations occurring possibly as early as the Miocene (Larsen *et al*., 1994), multiple lines of evidence (e.g., Jansen *et al*., 2000; Thiede *et al*., 2011; Bierman *et al*., 2016; Blake-Mizen *et al*., 2019) indicate that a major ice-sheet with extensive iceberg-calving margins was not a persistent feature on Greenland until during the intensification of Northern Hemisphere glaciation (iNHG), ~3.6–2.4 Ma (Mudelsee and Raymo, 2005); the transition from the warmer-than-present climate of the late Pliocene to the overall colder-than-present climate of the earliest Pleistocene.

Ice-rafted debris (IRD) – clay- to boulder-sized terrigenous material glacially eroded on land and transported offshore in calved icebergs – deposited in the Greenland-proximal marine realm is dominantly sourced from local iceberg-calving locations on this landmass in the present day (e.g., Bigg *et al*., 1996; Linthout *et al*., 2000; Andrews *et al*., 2010; White *et al*., 2016; Smith *et al*., 2018). A recent comparison of high-resolution records of IRD deposition offshore of eastern and southern Greenland indicates that persistent iceberg-calving GrIS margins were established in (north)eastern Greenland ~300 kyr earlier than in southern Greenland during iNHG (~3 Ma vs. 2.72 Ma; Blake-Mizen *et al*., 2019; see also Chapter 4). This inferred history is consistent with what is known about the trajectories of icebergs calved from these regions in the modern and Holocene (e.g., Bigg *et al*., 1996; White *et al*., 2016; Wagner *et al*., 2017). A scenario whereby extensive continental-ice first persisted in (north)eastern

Greenland and finally in southern Greenland during iNHG also makes sense in context with a variety of late Pleistocene, modern and model studies that suggest the southern GrIS is particularly sensitive to warming of only a few degrees Celsius relative to the present (e.g., Cuffey and Marshall, 2000; Willerslev *et al*., 2007; de Vernal and Hillaire-Marcel, 2008; Reyes *et al*., 2014; Bevis *et al*., 2018). Yet, validation of this theory requires a detailed understanding of the source-specific provenance of IRD deposited proximal to Greenland during iNHG. Pinpointing the long-term evolution of specific glacier systems identified as being at risk from ongoing climate change is crucial if we are to better understand their likely response to the magnitude of warming predicted for the next century, and enable numerical models to reliably simulate climatically-driven changes in ice-sheet extent (e.g., Lunt *et al*., 2008b; Dolan *et al*., 2011, 2015; IPCC, 2014).

One tool that has proven useful for tracking the provenance of IRD is the Pb-isotope composition of individual ice-rafted feldspars. This method has been used successfully, for example, to infer the contribution from glacial erosion of tectonic terranes on Greenland, Scandinavia and North America to IRD deposition in the subpolar North Atlantic during the Last Glacial Maximum (LGM; Gwiazda *et al*., 1996; Hemming *et al*., 1998) and iNHG (Bailey *et al*., 2012, 2013). Owing to a recent significant advance in our understanding of the Pb-isotope composition of feldspars eroded by individual glacier systems on Greenland, the geographical origin of IRD deposited in the Greenland-proximal marine realm can now be resolved with greater fidelity (White *et al*., 2016). While this new highly geographically-resolved source dataset has been successfully used to track Holocene to modern-day iceberg-calving sources to Greenland-proximal sites (White *et al*., 2016), it has yet to be applied to reconstructing GrIS iceberg-calving sources during the geological past.

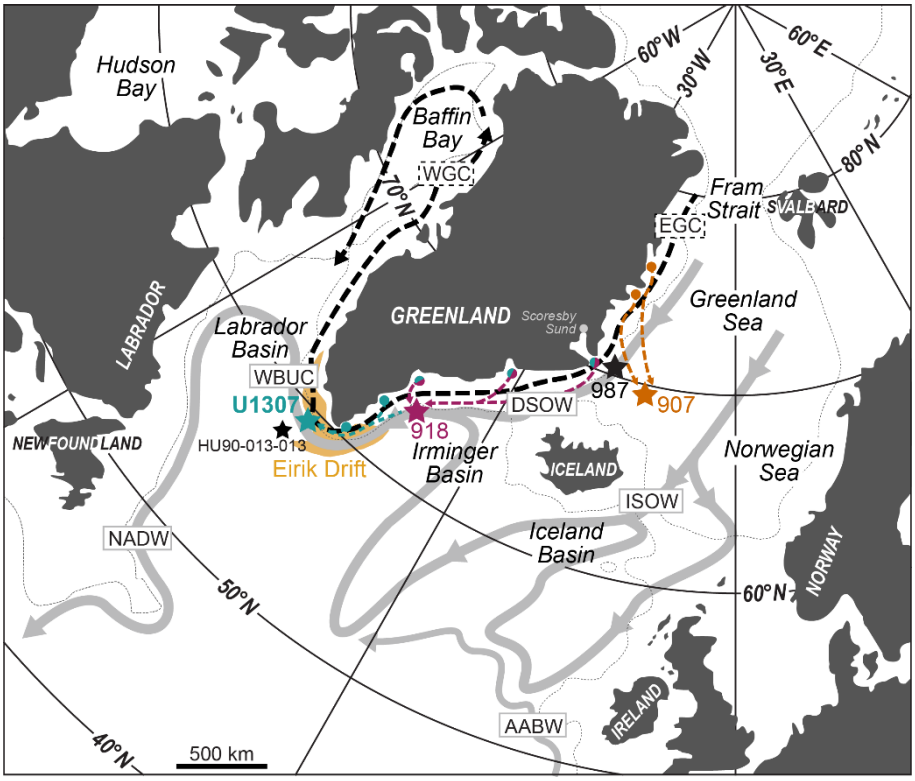

Figure 6.1 Map of Greenland and surrounding landmasses and ocean basins, showing the location of IODP Site U1307 on Eirik Drift and its relationships to the paths of key modern deep (solid grey) and surface (dashed black) ocean currents relevant to this study. The main sources of ice-rafted debris to Site U1307 and ODP Sites 907 and 918 are schematically represented by colour-coded dashed arrows (based on iceberg trajectory simulations for the Last Glacial Maximum by Bigg *et al*., 1996 and for the modern by Wagner *et al*., 2017, and lead-isotope provenance of core-top feldspars by White *et al*., 2016). EGC = East Greenland Current, WGC = West Greenland Current, ISOW = Iceland-Scotland Overflow Water, DSOW = Denmark-Scotland Overflow Water, AABW = Antarctic Bottom Water, WBUC = Western Boundary Undercurrent, NADW = North Atlantic Deep Water. The 1000 m isobath is given by thin dotted lines.

In this chapter, I apply the Pb-isotope provenance technique to sand-sized ice-rafted feldspars deposited between ~3.1 and 2.3 Ma during iNHG at Integrated Ocean Drilling Program (IODP) Site U1307 on Eirik Drift, just offshore southern Greenland (Fig. 6.1). Eirik Drift, an elongate contourite drift deposit, contains an expanded sedimentary record through the Plio-Pleistocene and is influenced by both iceberg-rafted and bottom-current-transported detrital sedimentation (Hunter *et al*., 2007). Eirik Drift is ideally-placed to monitor eastern and southern GrIS history, since the modern (core-top) Pb-isotope distribution of ice-rafted feldspars at Site HU90-013-013 (Fig. 6.1; White *et al*., 2016) demonstrate that

Eirik Drift receives IRD both from local southern sources, and transported southward in the overlying East Greenland Current (EGC) from eastern Greenland sources upstream (Fig. 6.1). Despite the fact that Eirik Drift sediments have greatly increased our understanding of southern GrIS history during the late Pleistocene (e.g., Colville *et al*., 2011; Reyes *et al*., 2014; Hatfield *et al*., 2013, 2017), its spatial maturation over the iNHG interval is still poorly understood.

To compliment inferences from my Pb-isotope analyses, I employ a multi-proxy approach by assessing the petrography of larger dropstones – using light microscopy of thin-sections – and bulk sand samples – using Quantitative Evaluation of Minerals by SCANning Electron Microscopy (QEMSCAN®) – deposited at U1307 over iNHG, and compare the results to those of Greenland geological surveys (e.g., Escher and Watt, 1979; Gilotti and Ravna, 2002; Kalsbeek *et al*., 2008; Gilotti *et al*., 2008). QEMSCAN® is a rapid and automated method of mineralogical analysis via scanning electron microscope (SEM), replacing time-consuming and potentially inaccurate manual point-counts and enabling the modal mineralogy and mineral associations representative of the dominant parent geologies to be easily recognised (e.g., Pirrie *et al*., 2013). The combined results of these analyses demonstrate that Eirik Drift received IRD from a modern-like range of iceberg-calving sources by ~2.4 Ma, and are consistent with the gradual establishment of extensive southern GrIS iceberg-calving margins as iNHG progressed.

6.2 Background

6.2.1 Overview of Greenland geology and modern iceberg-calving sources

The Greenland landmass comprises some of the oldest rocks on Earth, and together with North America and Northern Europe was originally part of a single

ancient North Atlantic craton that has since fragmented (Escher and Watt, 1976). The crystalline Precambrian shield of southern Greenland is divided into three distinct terranes (from north to south): the Nagssugtoqidian Mobile Belt (NMB), the Archaean Block (AB) and the Ketilidian Mobile Belt (KMB) (Fig. 6.2a; Hansen and Friderichsen, 1989). The intercalated orthogneisses (mainly granodioritic) and paragneisses comprising the AB terrane yield the oldest Archaean ages (~3.1–2.6 Ga), with even older gneisses (~3.9–3.8 Ga) occurring in the Isua supracrustal belt and locally around Nuuk (Henriksen *et al*., 2009). Along with large anorthosite units, gabbros, norites and quartz monzonites also occurring in the AB, these Archaean gneisses have remained relatively unaffected by any major subsequent metamorphic or tectonic events (Escher and Watt, 1976).

In the southern NMB, AB gneisses are reworked with quartzites and layers of supracrustal rock (andesine basics, norites, (grano)diorites, granites and gabbros) in the region of Tasiilaq (Fig. 6.2a), dated to the early Proterozoic (~1.9–1.7 Ga), which displays strong deformation with a pronounced regional fabric parallel to the NMB-AB boundary (Escher and Watt, 1976; Connelly and Thrane, 2005). In the northwestern NMB around the region of Disko Bugt (Fig. 6.2a), the Rinkian fold belt is a distinct succession of Paleoproterozoic (~1.87–1.65 Ga) supracrustal rocks (quartzites and metasediments) intercalated with reworked Archaean gneiss (Escher and Watt, 1976; Connelly and Thrane, 2005).

The KMB defines the southernmost tip of the Precambrian shield, with a central ‘early granite’ (~1.85–1.83 Ga) complex (characteristic light-coloured leucogranites, (grano)diorites) and an intricately folded zone of granites, feldspathoid gneisses and metasediments intruded by many large ‘late granite’ (~1.81–1.74 Ga) batholiths (granodiorite to adamellite in composition with more K-feldspar than usual) and the characteristic Rapaviki granite (classified as

quartz monzonite containing large K-feldspars) (Escher and Watt, 1976; Henriksen *et al*., 2009).

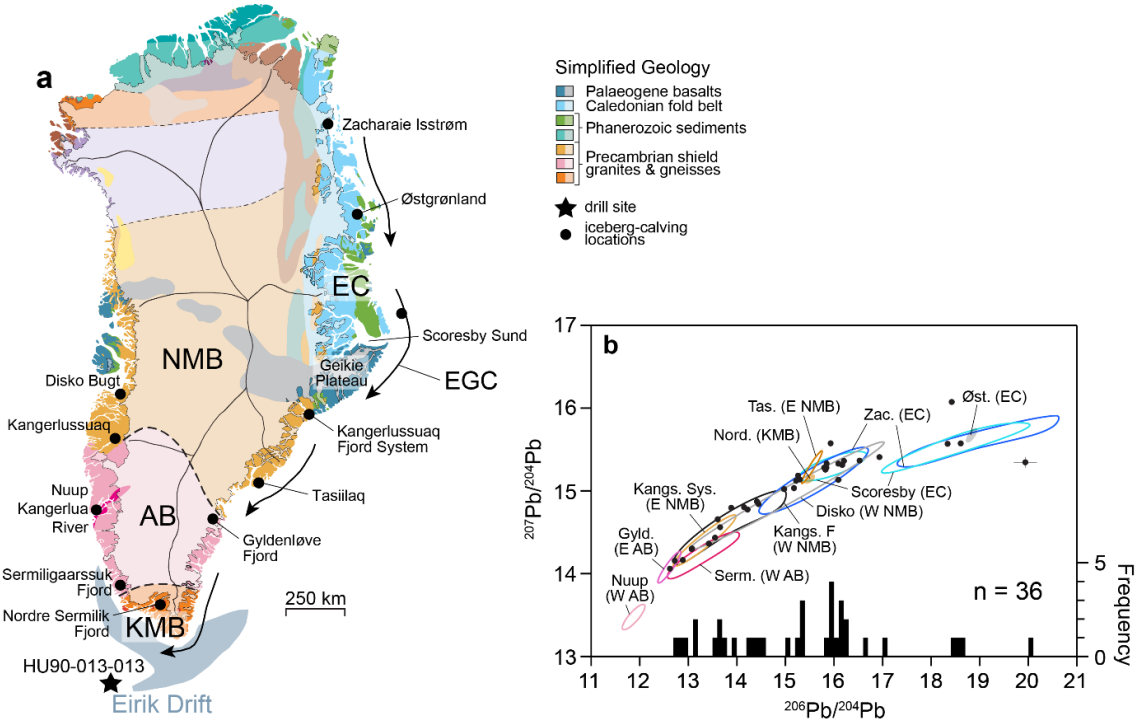

Figure 6.2 (**a**) Geological map of Greenland with interpretation of sub-ice bedrock modified from White *et al*. (2016; their Fig. 1). Ice-free geology at the coast is illustrated by darker-coloured shading. KMB = Ketilidian Mobile Belt, AB = Archaean Block, NMB = Nagssugtoqidian Mobile Belt, EC = East Caledonides. Also labelled is the position of Site HU90-013-013 on Eirik Drift, as well as major glacier/fjord systems and ice sheet divides (black lines) (Weidick, 1995). Black arrows denote the flow path of the modern East Greenland Current (EGC). (**b**) The Pb-isotope composition ($^{206}Pb/^{204}Pb$ vs. $^{207}Pb/^{204}Pb$) of individual sand-sized (>150 µm), ice-rafted feldspars from Site HU90-013-013 deposited during the modern (core-top sediment). Histograms of $^{206}Pb/^{204}Pb$ are also shown for reference. Crosses centred on individual data represent their respective 2σ uncertainties in Pb–Pb space; where no cross is evident, uncertainties are smaller than the width of symbol used. See White *et al*. (2016; their Fig. 2) for data used to define the 'source bubbles' shown for each major glacier/fjord system labelled in (a). Øst. = Østgrønland, Zac. = Zachariae Isstrøm, Scoresby = Scoresby Sund Fan (offshore Scoresby Sund), Disko = Disko Bay, Tas. = Tasiilaq, Serm = Sermiligaarssuk Fjord, Gyld. = Gyldenløve Fjord, Nuup = Nuup Kangerlua River, Kangs. Sys. = Kangerlussuaq Fjord System, Kangs. F = Kangerlussuaq Fjord, Nord. = Nordre Sermilik Fjord Narssarsuaq.

Eastern Greenland forms part of a major lower Paleozoic (~410–390 Ma) Caledonian orogenic fold belt (the East Caledonides, EC) outcropping north of Scoresby Sund (Fig. 6.2a), which comprises thrust sheets of Neoproterozoic to Silurian metasediments and extensive areas of Paleoproterozoic gneisses containing high-pressure eclogites with abundant garnet phenocrysts (Escher and Watt, 1976; Gilotti, 1993; Higgins *et al*., 2004; Cao *et al*., 2018). In the area

of Scoresby Sund (Fig. 6.2a), the Caledonian 'granites' (~466–425 Ma) comprise mafic (i.e., low-silica) granitoid (granodiorite, diorite, quartz monzonite and syenite) and leucogranite plutons (Kalsbeek *et al*., 2008; Gilotti *et al*., 2008). Separating these Caledonian rocks from NMB rocks outcropping in the region of the Kangerlussuaq Fjord System is a succession of tholeiitic flood basalts and alkaline basalts of the Geikie Plateau (Fig. 6.2), representing Paleogene magmatism associated with the emplacement of the North Atlantic Igneous Province (NAIP; Gilotti and Ravna, 2002; Storey *et al*., 2007). The flood basalts are cross-cut with numerous dolerite dykes containing abundant epidote and chlorite (Rose and Bird, 1994).

The main rock types characterising each Greenlandic terrane and their mineralogical compositions, used to assess likely provenance, are given in Table 6.1. For the purposes of this work the Paleogene volcanic rocks of the Geikie Plateau are grouped with rocks of the EC terrane.

Table 6.1 Characteristic rock types of each Greenland geochemical/tectonic terrane and their mineralogical constituents (approximately in order of descending concentration), based on Greenland geological surveys and standard geological definitions.

Terrane	Key Rock Types	Key Mineral Constituents
EC	Eclogite[a,b,e,j]	Garnet, pyroxene
	Tholeiitic/alkaline basalts[a,d]	Alkali feldspar, plagioclase, pyroxene, olivine
	Dolerite dykes[a,c]	Plagioclase, pyroxene, olivine, epidote, chlorite
	Mafic granitoids[a,g,h]	Alkali feldspar, plagioclase, quartz, hornblende, biotite, muscovite, pyroxene
NMB	Gneiss[a,f]	Plagioclase, quartz, alkali feldspar, minor hornblende and biotite
	Granite[a]	Quartz, plagioclase, alkali feldspar, quartz, muscovite, hornblende, biotite
	(Grano)diorite[a]	Plagioclase, quartz, alkali feldspar
	Gabbro[a]	Plagioclase, hornblende, biotite, pyroxene
	Andesine basics[a]	Plagioclase, pyroxene, hornblende
	Quartzite[a]	Quartz, muscovite
AB	Gneiss[a,i]	Plagioclase, quartz, alkali feldspar, muscovite, minor biotite
	Anorthosite[a]	Plagioclase, biotite, hornblende

	Gabbro[a]	Plagioclase, hornblende, biotite, pyroxene
	Norite[a]	Plagioclase, minor pyroxene
	Quartz monzonite[a]	Plagioclase, alkali feldspar, quartz, hornblende, muscovite, biotite
	Granodiorite[a]	Plagioclase, quartz, alkali feldspar
KMB	Feldspathoid gneiss[a,i]	Plagioclase, quartz, alkali feldspar, hornblende, muscovite, biotite
	Leucogranite[a,i]	Plagioclase, quartz, alkali feldspar
	Granodiorite[a]	Plagioclase, quartz, alkali feldspar
	Quartz monzonite[a]	Alkali feldspar, plagioclase, quartz, muscovite, biotite, hornblende, pyroxene

KMB = Ketilidian Mobile Belt, AB = Archaean Block, NMB = Nagssugtoqidian Mobile Belt, EC = East Caledonides (see Fig. 6.2a)
[a]Escher and Watt, 1976; [b]Gilotti, 1993; [c]Rose and Bird, 1994; [d]Gilotti and Ravna, 2002; [e]Higgins *et al*., 2004; [f]Connelly and Thrane, 2005; [g]Kalsbeek *et al*., 2008; [h]Gilotti *et al*., 2008;[i]Henriksen *et al*., 2009; [j]Cao *et al*., 2018

The most notable inter-terrane differences exist between the EC and the southern Precambrian terranes, defined by the presence or absence of felsic (i.e., quartz-rich) rocks and mineral associations (e.g., Andrews *et al*., 2010). The rocks comprising the EC terrane, including the Paleogene flood basalts, are largely quartz-free with overall mafic associations (e.g., plagioclase with pyroxene, olivine, hornblende and biotite; e.g., Andrews *et al*., 2010) with distinct accessory minerals garnet and epidote (e.g, Rose and Bird, 1994; Higgins *et al*., 2004; Cao *et al*., 2018). The southern Precambrian terranes are characterised by generally more felsic rock types with higher quartz content such as granite, gneiss and granodiorite with felsic mineral associations (plagioclase with alkali feldspar, quartz, muscovite and hornblende), although silica-poor rocks such as gabbro, anorthosite and norite are also present (Escher and Watt, 1976; Andrews *et al*., 2010). Principle component analysis of the mineralogy of the coarse sand fraction deposited offshore eastern Greenland between the Scoresby Sund Fan and Kangerlussuaq Trough during the Holocene, measured by X-ray diffraction (Andrews *et al*., 2010), highlights the importance of quartz and pyroxene as compositional end-members distinguishing felsic and mafic sources,

respectively. For the purposes of this work, IRD originating from eastern Greenland is generalised as relatively more mafic, and from southern Greenland relatively more felsic.

At present, iceberg-calving sources focussed in Disko Bugt (western NMB) and Scoresby Sund (eastern NMB) (Fig. 6.2a) contribute to ~13% of the total Greenland iceberg flux each year (Dowdeswell *et al*., 1993; Rignot and Kangaratnam, 2006). The Geikie Plateau (Fig. 6.2a) also has a high concentration of outlet glaciers, and along with the multiple tidewater glaciers of the Kangerlussuaq Fjord System (eastern NMB; Fig. 6.2a) is responsible for the majority of IRD flux to the Kangerlussuaq trough just offshore eastern Greenland (Nuttall, 1993; Rignot and Kangaratnam, 2006; Andrews *et al*., 2014b). Important modern AB iceberg-calving sources are located at outlet glaciers near Nuuk (Nuup Kangerlua River) and in Sermiligaarssuk Fjord (Fig. 6.2a; Weidick and Bennike, 2007).

6.2.2 Pb-isotope signatures of modern-day GrIS iceberg-calving sources

The relative ages of each terrane, as listed above from approximately oldest to youngest, are reflected in the Pb-isotope ratios of feldspars eroded in the catchment area of individual glacier systems, which were sampled from sandurs and fjord sands close to their termini and analysed to characterise the Pb-isotope signature of each catchment area (White *et al*., 2016). Feldspars originating from the oldest Archaean regions yielding the lowest (least radiogenic) values in Pb-isotope space and those from the relatively young Caledonides yielding the highest (most radiogenic) values (Fig. 6.2b; White *et al*., 2016; see their Fig. 3 for data used to define each of the ‘source bubbles’). Feldspars sourced from Scoresby Sund (EC) (sampled from the Scoresby Sund Fan, just offshore to the

east; Fig. 6.2a; White *et al*., 2016) tend to plot in a linear, positive array with $^{206}Pb/^{204}Pb$ ratios between ~17 and 19, with a separate tighter subset between $^{206}Pb/^{204}Pb$ ~14.5 and 15.5 (Fig. 6.2b). This is likely due to the fact feldspars eroded in the catchment of outlet glaciers in the region of Scoresby Sund and transported to the fan offshore reflect the Pb-isotope composition of both the NMB and EC terranes occupied by the catchment area (Fig. 6.2a; White *et al*., 2016). Feldspars sourced from further north in the EC near Østgrønland and Zachariae Isstrøm follow a similar distribution, although the latter can have a larger spread with the most radiogenic values between $^{206}Pb/^{204}Pb$ ~17 and 21 (Fig. 6.2b). To the south on the eastern NMB, feldspars from the Kangerlussuaq Fjord System occupy a narrowly-defined linear array between $^{206}Pb/^{204}Pb$ ~13 and 15, whereas those from Tasiilaq form a distinct tightly-defined, relatively steep positive array between $^{206}Pb/^{204}Pb$ ~15.5 and 16 (Fig. 6.2b). The lower end of the Tasiilaq field overlaps with that of the Nordre Sermilik Fjord on the KMB, where the feldspars plot in a tight grouping with $^{206}Pb/^{204}Pb$ ~15.5 (Fig. 6.2b). With the least radiogenic values of all, feldspars from the Nuup Kangerlua River near Nuuk on the western AB plot in a relatively tight array between $^{206}Pb/^{204}Pb$ ~11.5 and 12.5, distinct from all other source fields (Fig. 6.2b). Feldspars from Gyldenløve Fjord on the eastern AB form a distinct narrow positive linear array with $^{206}Pb/^{204}Pb$ between ~12 and 13, and those from Sermilikgaarssuk Fjord on the western AB also form a well-defined linear array between $^{206}Pb/^{204}Pb$ ~12.5 and 14, overlapping slightly with the Kangerlussuaq Fjord System (Fig. 6.2b).

6.2.3 Current understanding of Plio-Pleistocene GrIS history

Due to the removal of terrestrial evidence for past glaciation on Greenland by the most recent glacial expansions, the majority of our understanding of GrIS history

prior to the Late Quaternary comes from records of IRD deposited in the Greenland-proximal marine realm (e.g., Thiede *et al*., 2011). The most continuous of these records spanning the iNHG interval come from Ocean Drilling Program (ODP) Site 907 on the Iceland Plateau off eastern Greenland (Shipboard Scientific Party, 1996; Jansen *et al*., 2000), ODP Site 918 in the Irminger Basin off southeast Greenland (Shipboard Scientific Party, 1994; St John and Krissek, 2002), and Integrated Ocean Drilling Program (IODP) Site U1307 on Eirik Drift (Expedition 303 Scientists, 2006; Blake-Mizen *et al*., 2019; see also Chapter 4) (Fig. 6.1). According to iceberg-trajectory modelling (Bigg *et al*., 1996; Wagner *et al*., 2017) and Pb-isotope analysis of core-top (Holocene to modern) ice-rafted feldspars (White *et al*., 2016), IRD deposited at Eirik Drift Site HU90-013-013 (Fig. 6.2a) in the present day is mainly sourced from Gyldenløve Fjord (eastern AB) and potential KMB sources that are yet to be fully-characterised, as well as from the Kangerlussuaq Fjord System (eastern NMB) and Scoresby Sund further north on the EC (Fig. 6.2b; White *et al*., 2016). Site 907 IRD in the present day is most likely to be sourced from northeast Greenland iceberg-calving sources (primarily Zachariae Isstrøm; White *et al*., 2016), and IRD to Site 918 is dominated by eastern NMB (primarily the Kangerlussuaq Fjord System, also potentially Tasiilaq) and EC (Scoresby Sund) sources (White *et al*., 2016) (Fig. 6.1).

A short-lived period of IRD deposition is recorded at Sites 907 and 918 during the particularly cold late Pliocene glacial Marine Isotope Stage (MIS) M2, ~3.3 Ma (Jansen *et al*., 2000; St John and Krissek, 2002), indicating expansion of GrIS iceberg-calving margins in at least northeastern and eastern Greenland at this time (the Site U1307 record does not quite extend back to MIS M2). Only very limited amounts of IRD are recorded at all sites during the mid-Piacenzian

warm period (mPWP), ~3.264–3.025 Ma (Dolan *et al*., 2011), widely considered an analogue to near-future climate (Burke *et al*., 2018) with atmospheric CO_2 concentrations >400 parts per million and global temperatures elevated by ~2–3 °C relative to today (e.g., Dowsett *et al*., 2010; Martínez-Botí *et al*., 2015; Bachem *et al*., 2017; Raymo *et al*., 2018), suggesting only sporadic (de)glacial ice-rafting from isolated glaciers took place during the coldest intervals of this period (Jansen *et al*., 2000; St John and Krissek, 2002; Blake-Mizen *et al*., 2019; see also Chapter 4).

IRD deposition at Site 907 became moderately elevated during cold stages from ~3 Ma at the cessation of the mPWP (Jansen *et al*., 2000), indicating glacial iceberg-calving margins were re-established in some parts of northeastern Greenland at this time. At all sites, IRD deposition became significantly and consistently elevated on orbital timescales from MIS G6, ~2.72 Ma (Jansen *et al*., 2000; St John and Krissek, 2002; Blake-Mizen *et al*., 2019), thought to reflect the expansion of persistent GrIS iceberg-calving margins on eastern and southern Greenland at this time. Eight ice-rafted dropstones identified as six basalt and two granite clasts ranging from 3 to 21 mm in diameter recorded shipboard during drilling of Site U1307 (Expedition 303 Scientists, 2006) provide an initial, very low-resolution picture of a provenance transition from basaltic- (eastern Greenland) to granitic- (southern Greenland) dominated IRD deposition over iNHG, supported by the inferred ~300 kyr later onset of widespread iceberg-calving margins in southern Greenland compared to in eastern Greenland (Blake-Mizen *et al*., 2019; see also Chapter 4).

While past fluxes of IRD deposition at each of these sites coupled with knowledge of where detritus-laden icebergs reaching them are sourced from in the modern enables us to hypothesise about past GrIS extents in this way, only

by analysing the provenance of this palaeo-IRD can we draw reliable conclusions about the evolution of GrIS iceberg-calving sources over time. Since the East Greenland Current has likely been a feature of Nordic Seas surface circulation for at least the past ~4.5 Myr (De Schepper *et al*., 2015), we can assume that iceberg trajectories are unlikely to have changed a great deal during this time; however, this should not be taken for granted. The level of source-specific detail now achieved for Holocene ice-rafting to the Greenland-proximal marine realm has yet to be applied further back in time, and so Site U1307 sediments represent a unique opportunity to track the evolution of a whole range of key eastern and southern Greenland iceberg-rafting sources over iNHG.

6.3 Study Site and Methods

6.3.1 Study site and age model

IODP Site U1307 is located on the northern flank of Eirik Drift (Fig. 6.1; 58°30.3'N, 46°24.0'W, at 2575 m water depth. Two holes were drilled at Site U1307 (U1307A and U1307B) during IODP Expedition 303 in 2004, which together recovered a ~175 m composite Plio-Pleistocene section (Expedition 303 Scientists, 2006), that has been recently updated using new high-resolution magnetic susceptibility data (Blake-Mizen *et al*., 2019; see also Chapter 4). A newly-resolved orbital-resolution relative palaeointensity (RPI)-based age model for the iNHG interval of this cored section illustrates that the oldest sediments recovered from Site U1307 are ~3.2 Ma, and that average sedimentation rates over the study interval (~3.2–2.2 Ma) were ~6 cm kyr^{-1} (Blake-Mizen *et al*., 2019; see also Chapter 4).

6.3.2 Sampling

Using the published Site U1307 IRD record (Blake-Mizen *et al*., 2019) as a guide, a subset of the discrete ≥63 μm samples already processed for IRD abundance analysis (see Chapter 4) were selected to analyse the provenance of ice-rafted inputs, during a range of climatic conditions where possible – early glacial (EG), full glacial (FG), deglacial (DG) and interglacial (IG) – over multiple glacial cycles before, during and after the onset of significant ice-rafting to Site U1307 at MIS G6, ~2.7 Ma (Fig. 6.3; Blake-Mizen *et al*., 2019). According to the Site U1307 RPI-based age model, the samples taken target MIS K2, G18, G12, G8, G6, 102, 96 and 92 (Fig. 6.3). These particular glacial cycles and the spread of samples as shown in Figure 6.3 were selected in order to: 1) obtain a picture of the active iceberg-rafting sources to Site U1307 prior to the development of extensive iceberg-calving margins in southern Greenland, and ascertain whether there were any significant contributions from southern sources prior to MIS G6; 2) study the changing provenance of IRD to Site U1307 during the intensification of ice-rafting from the southern terranes at MIS G6; and 3) to ascertain when a modern-like range of iceberg-calving sources were represented at Site U1307 after the onset of major ice-rafting to the site. I analysed a total of 33 bulk sand samples for their mineralogy with QEMSCAN® (Table 6.3), and picked feldspars from 11 samples for Pb-isotope analysis (Table 6.4).

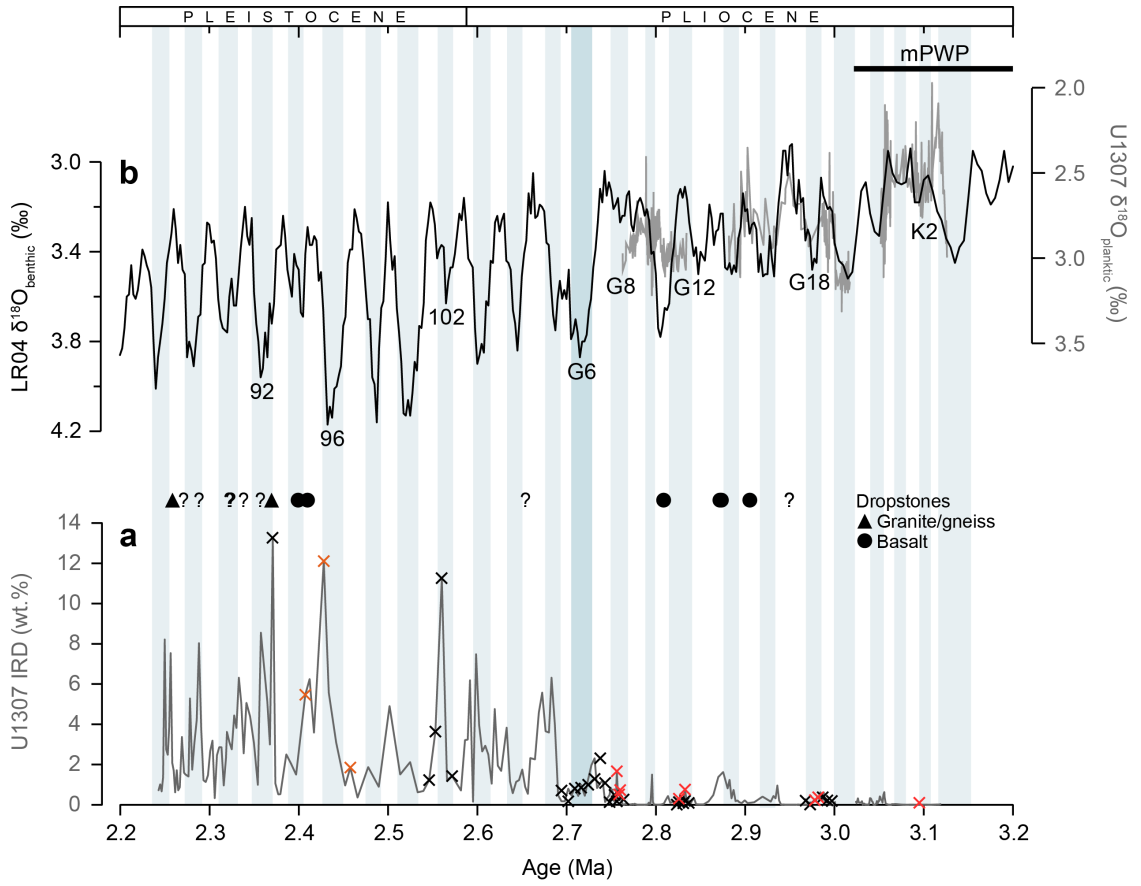

Figure 6.3 Sampling strategy for Site U1307 ice-rafted debris (IRD) provenance analysis. (**a**) Weight percent (wt.%) coarse (≥212 μm) IRD deposited at Site U1307 between ~3.1–2.2 Ma (grey line; Blake-Mizen *et al*., 2019; see also Chapter 4), with orange crosses = samples selected for Pb-isotope analysis, red crosses = samples selected for both Pb-isotope and QEMSCAN analysis, black crosses = samples selected for QEMSCAN analysis. Also indicated are larger (>3 mm) dropstones recovered shipboard (circles = basalt, triangles = granite) and during discrete sampling for this work (question marks). The LR04 benthic $\delta^{18}O$ stack is shown in (**b**) for reference (Lisiecki and Raymo, 2005), with available U1307 planktic $\delta^{18}O$ data superimposed (grey line; Sarnthein *et al*., 2009). Numbers in (b) are Marine Isotope Stages, with the duration of the mid-Piacenzian warm period (mPWP; Dolan *et al*., 2011) also indicated. Vertical blue bars highlight cold stages.

6.3.3 Dropstone petrography

During discrete sampling at MARUM, I encountered eight dropstones of varying lithology (Table 6.2), additional to the eight already noted shipboard. I studied each newly-sampled dropstone in hand-specimen, then petrographic 30 μm-thick thin-sections were prepared by Stephen Pendray in the Rock Preparation Lab at Camborne School of Mines, University of Exeter Penryn Campus. I then studied each thin-section under both plane and crossed polars with a Nikon Eclipse E600 POL polarising petrographic microscope to determine their petrography. I took

representative photomicrographs of each thin-section using a Nikon Digital Sight DS-5M camera mounted onto the microscope.

Table 6.2 List of Site U1307 dropstone occurrences sampled for petrographic analysis and basic hand-specimen descriptions.

Hole	Sample ID	Depth		Age (ka)	Size (mm)	Hand specimen colour
		mbsf	rmcd			
U1307B	13H 2 119–120 cm	111.99	118.51	2269	28	Dark green
U1307B	13H 3 38–39 cm	112.68	119.20	2286	26	Light/mid-grey
U1307A	14H 1 22–23 cm	115.52	120.53	2319	24	Mid-grey
U1307B	13H 4 30–31 cm	114.10	120.62	2322	22	Light grey
U1307B	13H 4 83–84 cm	114.63	121.15	2336	21	Dark grey
U1307A	14H 3 124–129 cm	116.63	121.64	2355	36	Dark grey
U1307A	14H 7 64–65 cm	121.94	126.95	2652	33	Dark grey
U1307A	16H 6 82–85 cm	134.02	139.80	2947	39	Light/mid grey

mbsf = metres below seafloor; rmcd = revised metres composite depth (see Chapter 4; Blake-Mizen *et al*., 2019).

6.3.4 QEMSCAN® quantitative mineralogy

QEMSCAN® is an automated method of mineralogical analysis, consisting of a software package that operates a SEM to rapidly gather and process high-resolution, quantitative mineral data from solid inorganic samples (e.g., Gottlieb *et al*., 2000; Pirrie *et al*., 2004; Pirrie and Rollinson, 2011). Due to its ability to rapidly quantify and produce false-colour images of whole-rock and particulate mineralogy, it has many uses including evaluation of ore grade and processing efficiency in the mining industry (e.g., Pirrie *et al*., 2004; Andersen *et al*., 2009; Pirrie and Rollinson, 2011), crime scene soil provenance in forensic geoscience (e.g. Pirrie *et al*., 2004, 2013), provenance of ancient ceramics in archaeology (e.g., Knappett *et al*., 2011), and soil contamination in environmental monitoring (e.g., Camm *et al*., 2004). QEMSCAN® has very rarely been utilised in studies of IRD, however; one study employed the method to quantify the mineralogy of bulk ice-rafted sand (63–2000 μm) sampled offshore at ODP Site 696 in the Southern

Ocean, close to the Weddell Sea off West Antarctica (Carter *et al*., 2017), but these data were not used to assess the provenance of the IRD.

QEMSCAN® may prove to be an extremely useful, cost- and time-effective tool to rapidly quantify IRD mineralogy using a defined set of rules that easily recognises the presence of particular minerals, and associations of minerals in composite (or polyminerallic) grains composed of more than one distinct mineral, relevant to any given study area. This sort of information is typically collected through time-consuming manual point-counts under light microscope, with high potential for human error. The provenance of the IRD can then be estimated by comparing the mineralogical assemblage and associations of minerals to the geology of potential source terranes, which is most usefully and easily applied where suspected source regions are geochemically distinct (e.g., felsic vs. basaltic).

To investigate the range of IRD mineralogical provenance deposited at Eirik Drift during iNHG, I measured a total of 33 bulk Site U1307 sand (63–1000 μm) samples deposited during Marine Isotope Stage (MIS) G18, G12, G8, G6, 102 and 92 for their bulk mineralogy and mineralogical associations (Table 6.3). Where possible, I sampled a range of conditions over each cycle including early glacial (EG), full glacial (FG), deglacial (DG) and interglacial (IG). I first reduced each bulk sand sample to a suitable representative sample size (a few thousand grains) using a microsplitter, then each sample was mixed with clear epoxy resin in 30 mm-diameter moulds by Stephen Pendray in the Rock Preparation Lab at Camborne School of Mines, University of Exeter Penryn Campus. The sample blocks were placed into a pressure vessel overnight to ensure no bubbles remained in the resin, also allowing the grains to settle naturally to ensure random orientation, then cured in an oven overnight and polished to expose each grain

centre for analysis. Procedures for avoiding cross-contamination of samples, such as clear labelling and tool and workspace cleaning between handling of each sample, were followed throughout the preparation process. I then carbon-coated each sample block to inhibit the build-up of electric charge during analysis (Reed, 2005).

Table 6.3 Sampling guide for discrete Site U1307 bulk sand (63–200 µm) samples analysed for their mineralogy by QEMSCAN® in this study.

Hole	Sample ID	Depth		Age (ka)	MIS
		mbsf	rmcd		
U1307A	14H 2 25–27 cm	114.15	122.06	2371	92 (FG)
U1307A	14H 3 103–105 cm	116.43	124.34	2546	102 (DG)
U1307A	14H 3 114–116 cm	116.54	124.45	2553	102 (DG)
U1307A	14H 3 125–127 cm	116.65	124.56	2560	102 (FG)
U1307A	14H 3 143–145 cm	116.83	124.74	2572	102 (EG)
U1307A	14H 4 10–12 cm	117.00	124.91	2582	102 (IG)
U1307A	14H 6 31–33 cm	120.21	128.12	2694	G6 (IG)
U1307A	14H 6 51–53 cm	120.41	128.32	2702	G6 (IG)
U1307A	14H 6 71–73 cm	120.61	128.52	2709	G6 (DG)
U1307A	14H 6 90–92 cm	120.80	128.71	2716	G6 (DG)
U1307A	14H 6 111–113 cm	121.01	128.92	2724	G6 (DG)
U1307A	14H 6 131–133 cm	121.21	129.12	2731	G6 (FG)
U1307A	14H 7 4–6 cm	121.44	129.35	2738	G6 (EG)
U1307A	14H 7 24–26 cm	121.64	129.55	2743	G6 (IG)
U1307A	14H 7 44–46 cm	121.84	129.75	2748	G6 (IG)
U1307B	14H 3 50–52 cm	122.30	130.20	2754	G8 (IG)
U1307B	14H 3 70–72 cm	122.50	130.40	2756	G8 (DG)
U1307B	14H 3 90–92 cm	122.70	130.60	2759	G8 (FG)
U1307B	14H 3 100–102 cm	122.80	130.70	2760	G8 (EG)
U1307A	16H 3 130–132 cm	130.00	135.78	2823	G12 (DG)
U1307A	16H 3 140–142 cm	130.10	135.88	2826	G12 (DG)
U1307A	16H 4 0–2 cm	130.20	135.98	2828	G12 (DG)
U1307A	16H 4 10–12 cm	130.30	136.08	2831	G12 (DG)
U1307A	16H 4 20–22 cm	130.40	136.18	2833	G12 (FG)
U1307A	16H 4 30–32 cm	130.50	136.28	2835	G12 (EG)
U1307A	16H 4 40–42 cm	130.60	136.38	2837	G12 (EG)
U1307B	15H 4 70–72 cm	133.50	141.20	2968	G18 (IG)
U1307B	15H 4 110–112 cm	133.90	141.60	2973	G18 (IG)
U1307B	15H 5 0–2 cm	134.30	142.00	2978	G18 (DG)
U1307B	15H 5 30–32 cm	134.60	142.30	2982	G18 (FG)
U1307B	15H 5 70–72 cm	135.00	142.70	2987	G18 (EG)

U1307B	15H 5 110–112 cm	135.40	143.10	2992	G18 (EG)
U1307B	15H 6 0–2 cm	135.80	143.50	2997	G18 (IG)

EG = early glacial, FG = full glacial, DG = deglacial, IG = interglacial
mbsf = metres below seafloor; rmcd = revised metres composite depth (see Chapter 4; Blake-Mizen *et al*., 2019).

I performed automated mineral quantification on each sample using the SEM and FEI QEMSCAN® software facility installed in the Environment and Sustainability Institute at the University of Exeter Penryn Campus, at high vacuum, an accelerating voltage of 25 kV, and probe current of 10 nA. The Particle Scan mode of analysis was judged to be most appropriate for this sample type, as individual particles are automatically located and surrounding resin ignored to enable the most efficient measurement time per sample. Typically, around 5000–6000 grains were measured in each sample, and raw data processing was performed using the FEI iDiscover v.4.2 software package following measurement. I narrowed down the initial mineral key provided by the software that recognises minerals based on elemental contents derived from X-ray spectra, known as the Species Identification Protocol (SIP), to a customised list of 11 key minerals (quartz, alkali feldspar, plagioclase feldspar, hornblende, muscovite, biotite, pyroxene, chlorite, olivine, epidote and garnet) relevant to this study (see Table 6.1). I applied quality control using boundary phase processing to transitional or anomalous mineral species identified as noisy pixels within or between minerals, which allows them to be reclassified as the surrounding mineral(s). I report the data for samples across each selected glacial as both modal mineralogy (quantifying the proportion of analysed grains/pixels classified as individual minerals, e.g., quartz, or mineral groups, e.g., alkali feldspar) and mineral associations (quantifying the transitions between one mineral/mineral group and another between adjacent measured pixels) (e.g., Pirrie *et al*., 2013).

6.3.5 Pb-Isotope analysis

To improve our understanding of the range of IRD provenance deposited at Eirik Drift during iNHG, I measured 96 sand-sized (>150 μm) ice-rafted feldspars deposited at Site U1307 during iNHG for their Pb-isotope ratios (Table 6.4). I first sieved each selected discrete Site U1307 sand sample at >150 μm, then picked individual feldspars from this fraction and set them onto circular sticky-back 30 mm-diameter mounts in distinct sample groupings. The grain mounts were then placed into 30 mm-diameter moulds and backfilled with clear Pb-free epoxy resin, then placed into a pressure vessel overnight to ensure no bubbles remained in the resin, by Stephen Pendray in the Rock Preparation Lab at Camborne School of Mines, University of Exeter Penryn Campus. The sample blocks were then cured in an oven overnight and polished to expose each grain centre for analysis. Procedures for avoiding cross-contamination of samples were followed throughout the preparation process.

I carried out all feldspar Pb-isotope analyses at the National Oceanography Centre Southampton using a ThermoFinnigan Neptune multicollector inductively-coupled-plasma mass spectrometer (MC-ICP-MS) coupled with a NewWave/ESI UP193fx homogenised ArF excimer laser ablation system, using a 150 μm spot size, a repetition rate of 10 Hz and a power density of ~5.5 J cm^{-2}. Isobaric interference of ^{204}Hg on ^{204}Pb was initially corrected for using “on-peak zeros” collected while the laser was off during the gas blank. Any ^{200}Hg detected during analysis while the laser was on was used to further correct for isobaric interference of ^{204}Hg on ^{204}Pb using the natural $^{204}Hg/^{200}Hg$ ratio (0.2973; Platzner, 1997). The ^{204}Hg intensity was typically small (<0.5 mV) and only ~0.5 % of the measured ^{204}Pb. Instrumental mass bias was corrected for by bracketing groups of six feldspar analyses with analyses of National Institutes

and Standards (NIST) 610 glass (~400 ppm Pb), using the double-spike Pb isotope ratios of Baker *et al*. (2004). NIST 610 was analysed with a 100-μm diameter spot and a repetition rate of 4 Hz, with similar power density as the unknown feldspars. Coeval analysis of NIST 612 (~40 ppm Pb) with the same settings as used for the unknown feldspars were made throughout the duration of the study. These results indicate that the measurements are sufficiently accurate and precise, yielding the following values and uncertainties to 2 standard deviations (σ) (relative to the values of Baker *et al*., 2004 given in brackets): $^{206}Pb/^{204}Pb$ = 17.093 ±0.016 (17.099 ±0.003), $^{207}Pb/^{204}Pb$ = 15.507 ±0.015 (15.516 ±0.002), $^{208}Pb/^{204}Pb$ = 36.989 ±0.045 (37.020 ±0.007), $^{207}Pb/^{206}Pb$ = 0.90722 ±0.0002 (0.90745 ±0.00004), $^{208}Pb/^{206}Pb$ = 2.1640 ±0.0008 (2.1651 ±0.0001).

Comparing the average signal strengths from the analysis of the standards with that of the feldspars allows for an estimation of the concentration of Pb in the unknown feldspars (Tyrell *et al*., 2006). On this basis, the average Pb concentration of the unknown feldspars is estimated to be ~50 ppm. The 2σ reproducibility of NIST 612 over all analytical sessions is taken to reflect external precision at the 95% confidence level. To quantify reproducibility of measurements for the feldspar analyses, the larger of either the external precision given by NIST 612 or the internal measurement uncertainty of 2σ was used.

Table 6.4 Sampling guide for Site U1307 sand-sized (>150 µm) ice-rafted feldspars analysed for Pb-isotopes in this study.

Hole	Sample ID	Depth		Age (ka)	MIS	No. analyses[a]
		mbsf	mcd			
U1307A	14H 2 98–100 cm	114.88	122.79	2407	96 (DG)	10
U1307A	14H 2 128–130 cm	115.18	123.09	2428	96 (FG)	11
U1307A	14H 3 14–16 cm	115.54	123.45	2458	96 (EG)	7
U1307B	14H 3 70–72 cm	122.50	130.40	2756	G8 (IG)	10
U1307B	14H 3 90–92 cm	122.70	130.60	2759	G8 (DG)	12
U1307B	14H 3 100–102 cm	122.80	130.70	2760	G8 (FG)	10
U1307A	16H 3 140–142 cm	130.10	135.88	2826	G12 (DG)	9
U1307A	16H 4 20–22 cm	130.40	136.18	2833	G12 (FG)	14
U1307B	15H 5 0–2 cm	134.30	142.00	2978	G18 (DG)	2
U1307B	15H 5 30–32 cm	134.60	142.30	2982	G18 (FG)	5
U1307A	18H 1 31–33 cm	145.01	155.51	3095	K2 (DG)	6

[a]Total number of analyses = 96
EG = early glacial; FG = full glacial; DG = deglacial; IG = interglacial
mbsf = metres below seafloor; rmcd = revised metres composite depth (see Chapter 4; Blake-Mizen *et al*., 2019).

6.4 Results

6.4.1 Dropstone petrographic provenance

Hand-specimen and thin-section descriptions for each dropstone sampled from U1307 are given in the following pages (in order of oldest to youngest), with petrographic photomicrographs taken in both plane and crossed polars and an assessment of each dropstone's likely classification and provenance.

6.4.1.1 U1307A 16H 6 82–85 cm (~2.95 Ma)

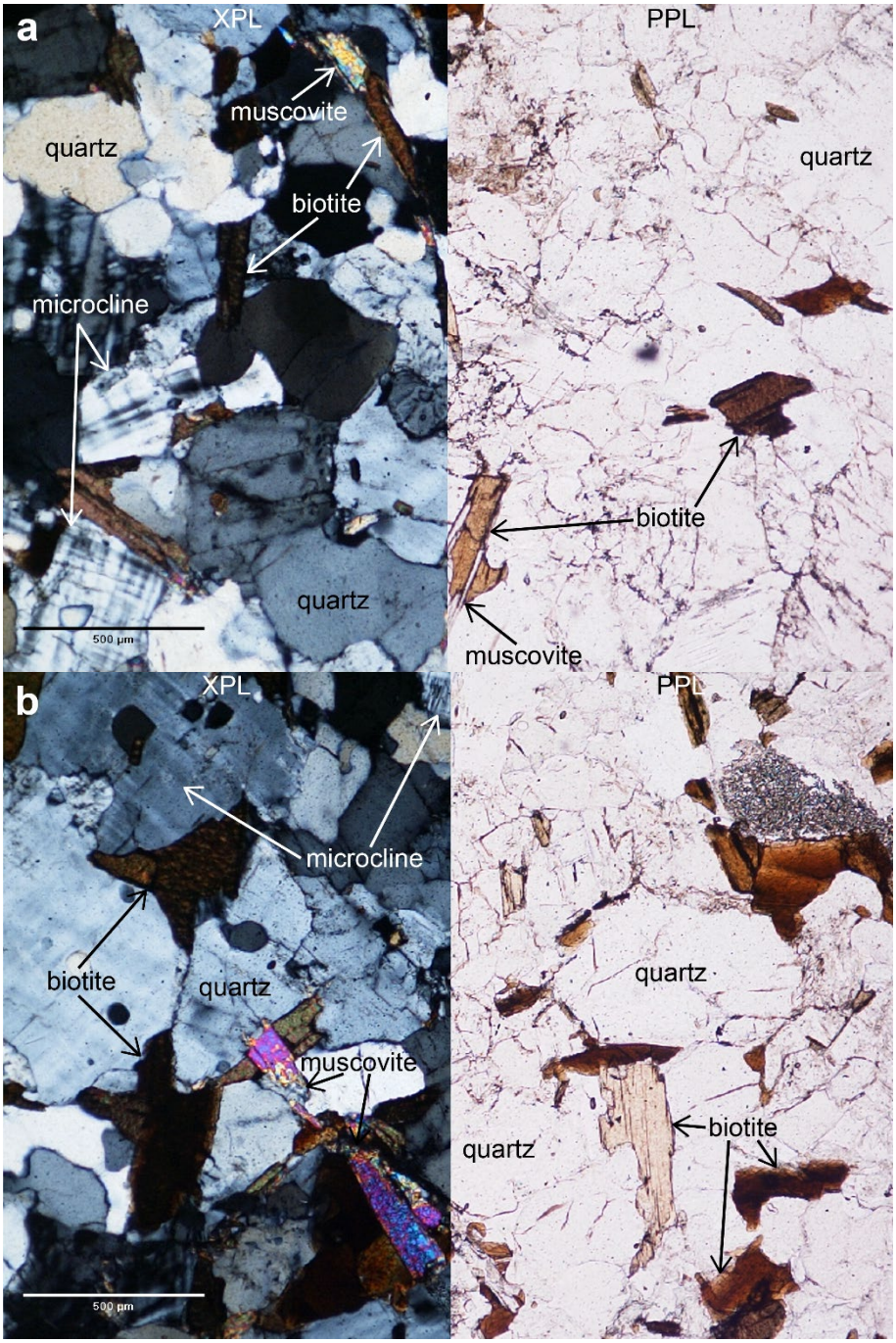

Figure 6.4 Photomicrograph views (**a**) and (**b**) of dropstone specimen U1307A 16H 6 82–85 cm in both plane-and cross-polarised light (XPL and PPL, respectively), with key minerals labelled. Scale bar = 500 µm.

Light grey, medium-grained crystalline hand specimen. In thin section (Fig. 6.4) the specimen is composed mostly of low-relief subhedral quartz (~40%) with some undulose extinction in crossed polars, and feldspar (~40%) with microcline twinning. Biotite exhibiting brown pleiochroism with characteristic cleavage is also

abundant (~15%), as well as muscovite (~5%) with high second-order birefringence. I hence interpret this specimen as a K-feldspar-rich granitoid, perhaps quartz monzonite originating in southern Greenland (Table 6.1).

6.4.1.2 U1307A 14H 7 64–65 cm (~2.65 Ma)

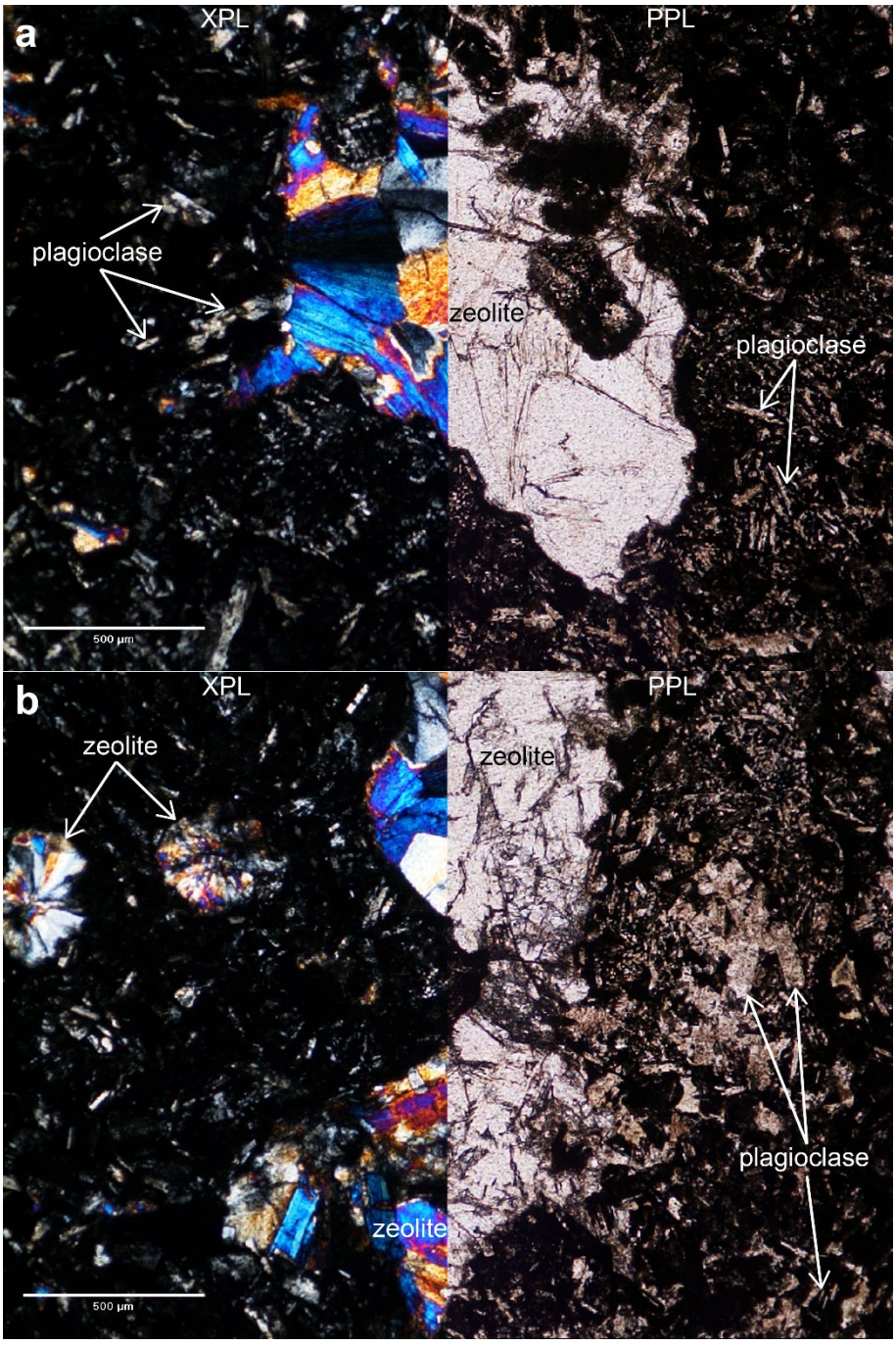

Figure 6.5 Photomicrograph views (**a**) and (**b**) of dropstone specimen U1307A 14H 7 64–65 cm in both plane-and cross-polarised light (XPL and PPL, respectively), with key minerals labelled. Scale bar = 500 µm.

Dark grey, fine-grained hand specimen with amygdaloidal texture. In thin section (Fig. 6.5) the specimen is comprised mostly of a groundmass of pyroxene and olivine (~30–40%) and plagioclase needles (~60–70%) exhibiting characteristic twinning in crossed polars. Abundant amygdales of a secondary high-relief mineral with radial growth pattern and high second-order birefringence, possibly zeolite, commonly infill large irregular and small rounded vesicles. I hence interpret this specimen as a fine-grained basalt with abundant zeolite amygdales, likely originating in the eastern Greenland volcanic province (Table 6.1).

6.4.1.3 U1307A 14H 3 124–129 cm (~2.36 Ma)

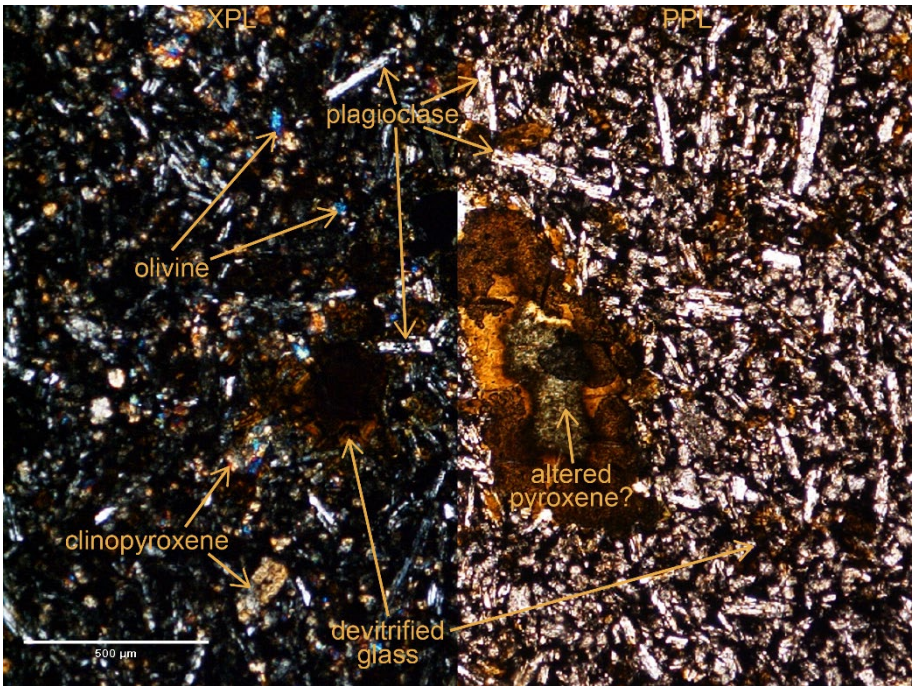

Figure 6.6 Photomicrograph view of dropstone specimen U1307A 14H 3 124–129 cm in both plane-and cross-polarised light (XPL and PPL, respectively), with key minerals and features labelled. Scale bar = 500 µm.

Dark grey, fine-grained hand specimen. In thin-section (Fig. 6.6) the specimen is mostly comprised of a very fine groundmass of pyroxene and olivine (~20–25%) and plagioclase needles (~70%) exhibiting simple twinning in crossed polars. A very altered phenocryst with greenish pleiochroism may be pyroxene. Common small euhedral to subhedral clinopyroxene and olivine (first- and second-order

birefringence, respectively) phenocrysts (~10%). Brown patches of devitrified glass are also present. I hence interpret this specimen as a fine-grained basalt with altered pyroxene phenocrysts, likely originating in the eastern Greenland volcanic province (Table 6.1).

6.4.1.4 U1307B 13H 4 83–84 cm (~2.34 Ma)

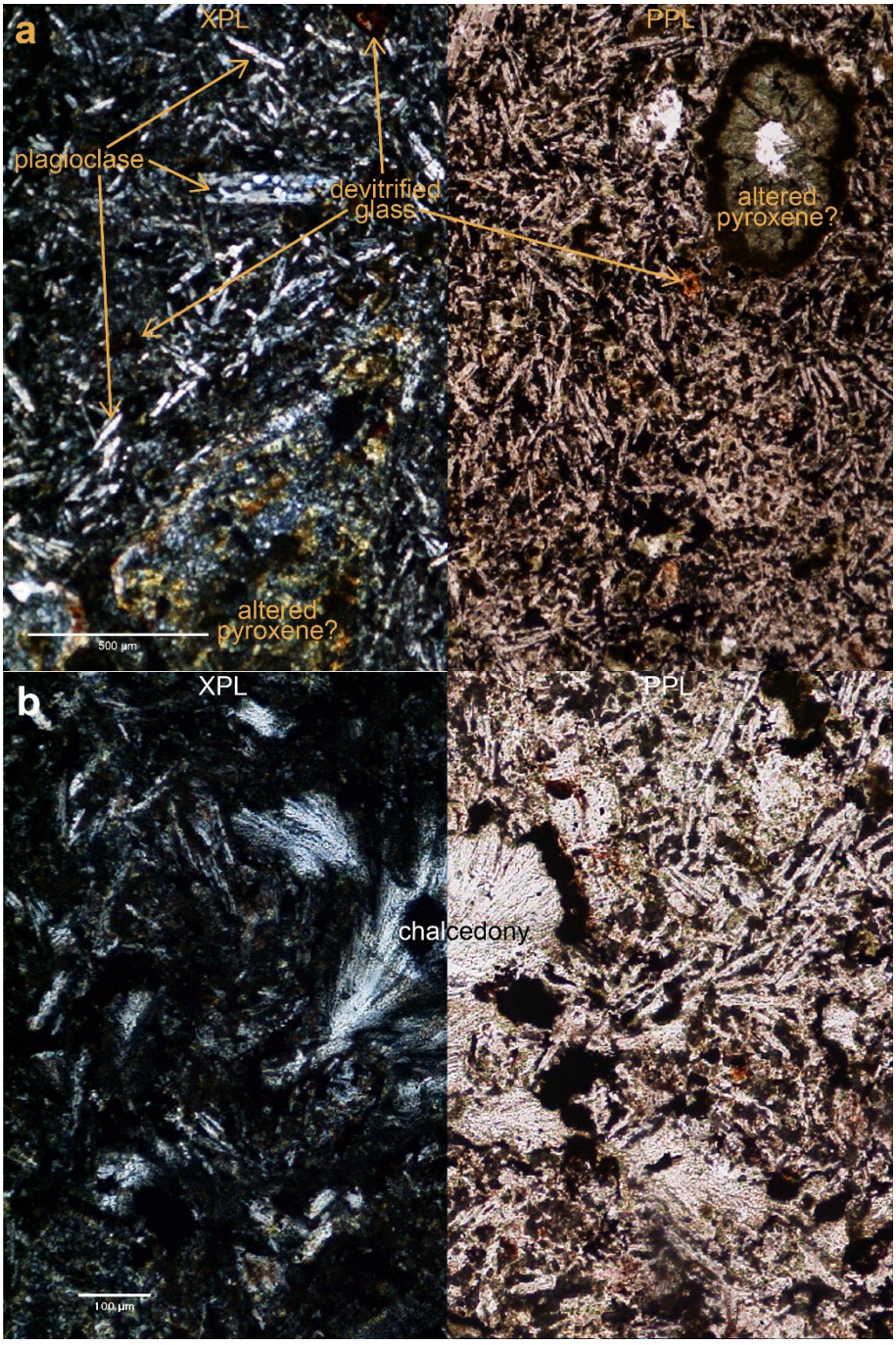

Figure 6.7 Photomicrograph views (**a**) and (**b**; overleaf) of dropstone specimen U1307B 13H 4 83–84 cm in both plane-and cross-polarised light (XPL and PPL, respectively), with key minerals and features labelled. Scale bar in (a) = 500 µm, (b) 100 µm.

Dark grey, fine-grained hand specimen with amygdaloidal texture. The majority of the thin-section (Fig. 6.7) is composed of a very fine groundmass of pyroxene and olivine (~20%) and plagioclase needles (~75%) exhibiting twinning characteristic of albite in crossed polars, with occasional subhedral to anhedral phenocrysts with greenish pleiochroism exhibiting heavy alteration (Fig. 6.7a), interpreted as being originally pyroxene (~5–10%). Brown devitrified glass is also common (Fig. 6.7a). There is also evidence of infilling of former vesicles by a secondary mineral (amygdales), possibly chalcedony due to its quartz-like characteristics and radial growth pattern (Fig. 6.7b). I hence interpret this specimen as a fine-grained basalt with pyroxene phenocrysts and chalcedony amygdales, likely originating in the eastern Greenland volcanic province (Table 6.1).

6.4.1.5 U1307A 14H 1 22–23 cm (~2.32 Ma)

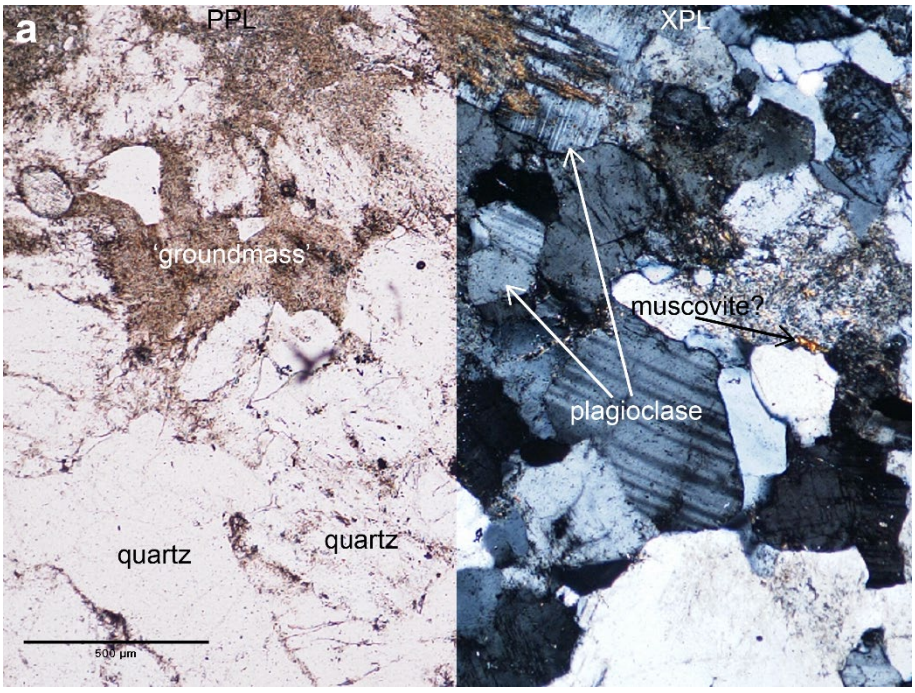

Figure 6.8 Photomicrograph views (**a**) and (**b**; see next page) of dropstone specimen U1307A 14H 1 22–23 cm in both plane-and cross-polarised light (XPL and PPL, respectively), with key minerals and features labelled. Scale bar = 500 µm.

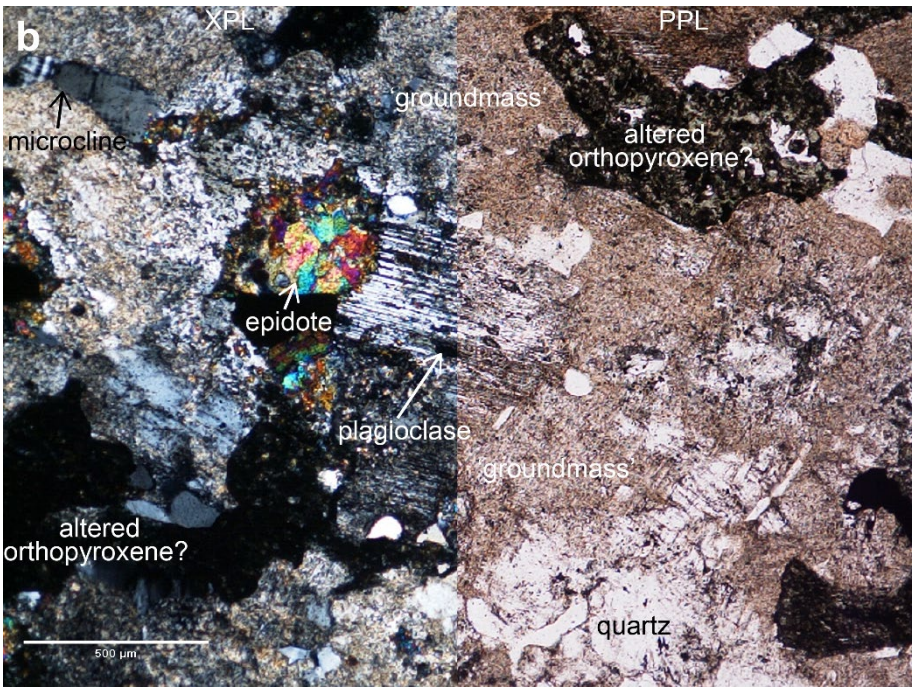

Figure 6.8 (Continued)

Mid-grey, medium-grained hand specimen. In thin-section (Fig. 6.8) the specimen appears very altered but contains recognisable low-relief quartz (~30%) exhibiting undulose extinction, and slightly higher-relief feldspar minerals (~20%) exhibiting cleavage and characteristic plagioclase (albite) twinning in crossed polars, as well as a small amount of microcline. Common minerals with slight yellow pleiochroism and high second-order birefringence with apparent zoning may be epidote (~5%; Fig. 6.8b). A highly altered mineral with slight green pleiochroism and low first-order birefringence may be orthopyroxene (~5%; Fig. 6.8b). Muscovite may also be a minor constituent (Fig. 6.8a). The remainder is a highly altered ‘mulch’ likely comprised of broken-down feldspar (~40%). I hence interpret this specimen as a highly altered mafic granitoid with epidote, likely originating in the EC terrane (Table 6.1).

6.4.1.6 U1307B 13H 4 30–31 cm (~2.32 Ma)

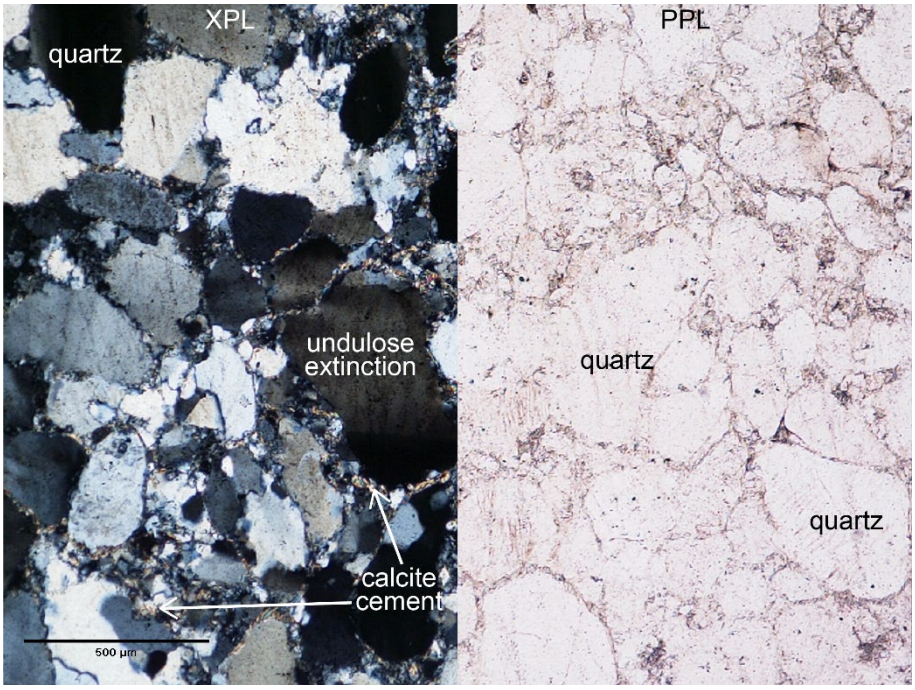

Figure 6.9 Photomicrograph view of dropstone specimen U1307B 13H 4 30–31 cm in both plane- and cross-polarised light (XPL and PPL, respectively), with key minerals and features labelled. Scale bar = 500 µm.

Light grey, medium-grained hand specimen. Very homogeneous in thin-section (Fig. 6.9), vastly composed of sub/anhedral low-relief quartz grains (~90%) in a range of sizes that exhibit normal or sometimes undulose extinction under crossed polars, with some composite grains. Their interlocking nature and undulose extinction is indicative of metamorphism. There also appears to be some high-birefringence calcite cement filling small gaps between the grains. I hence interpret this specimen as a quartzite (originally quartz sandstone), likely originating in the southern NMB terrane (Table 6.1).

6.4.1.7 U1307B 13H 3 38–39 cm (~2.29 Ma)

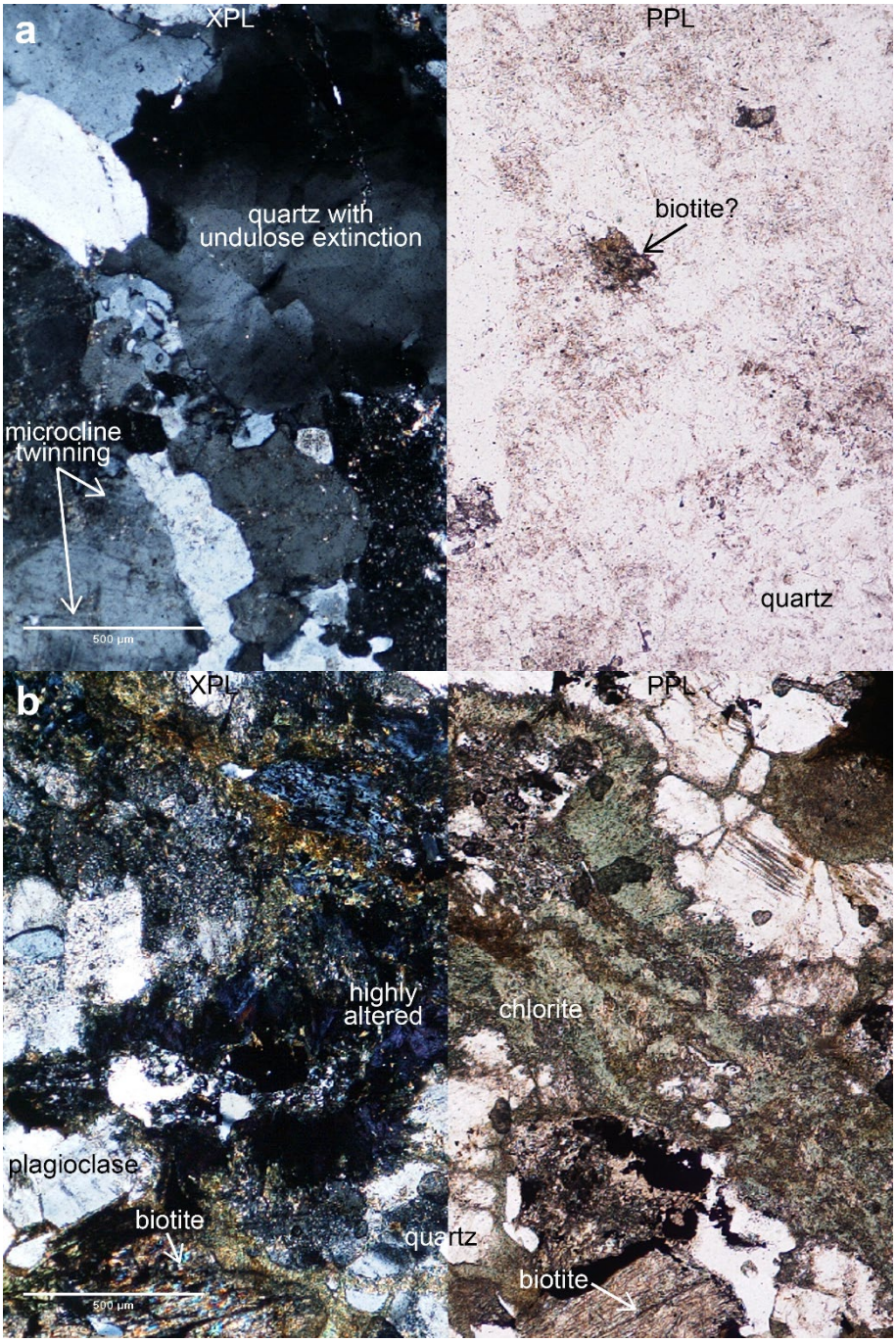

Figure 6.10 Photomicrograph views (**a**) and (**b**) of dropstone specimen U1307B 13H 3 38–39 cm in both plane-and cross-polarised light (XPL and PPL, respectively), with key minerals and features labelled. Scale bar = 500 µm.

Light to mid-grey, medium-grained hand specimen with possible banding. The majority of the thin-section (Fig. 6.10) is composed of sub/anhedral low-relief quartz minerals (~60%), many exhibiting 'wavy' (undulose) extinction under crossed polars (Fig. 6.10a). Also present is feldspar exhibiting cross-hatch

twinning characteristic of microcline under crossed polars, as well as some simple-twinned plagioclase (~20%). Euhedral blades of muscovite also present as a minor constituent. A very distinctive band of brown and light green pleiochroic minerals and anomalous birefringence colours under crossed polars are interpreted as biotite altering to chlorite (Fig. 6.10b). I hence interpret this specimen as an orthogneiss derived from granite, likely originating in the AB terrane (Table 6.1).

6.4.1.8 U1307B 13H 2 119–120 cm (~2.27 Ma)

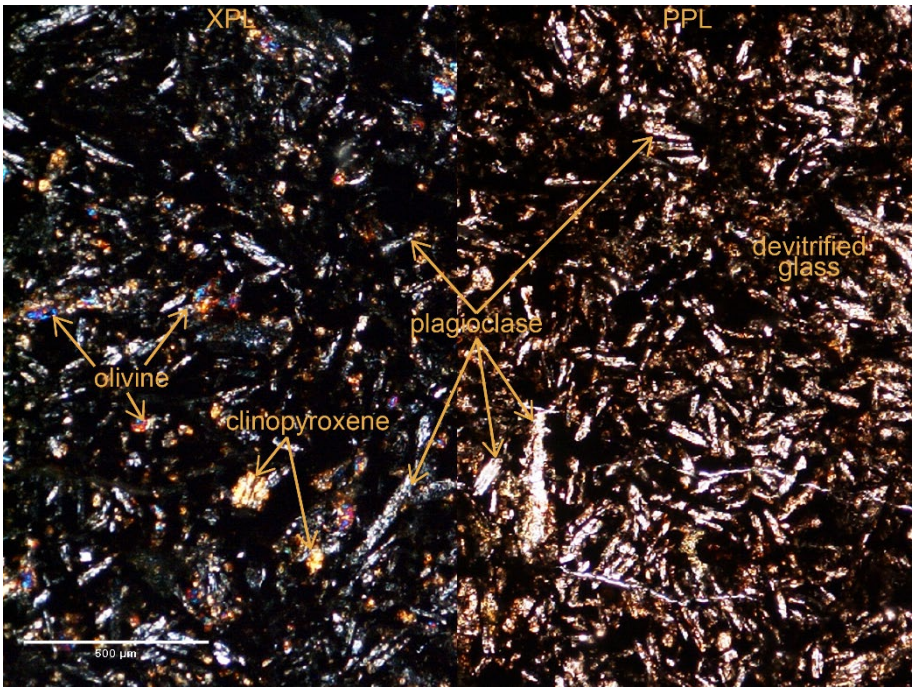

Figure 6.11 Photomicrograph view of dropstone specimen U1307B 13H 2 119–120 cm in both plane-and cross-polarised light (XPL and PPL, respectively), with key minerals and features labelled. Scale bar = 500 µm.

Dark grey-green, fine-grained hand specimen. Majority of thin-section (Fig. 6.11) is composed of a very fine groundmass of pyroxene and olivine (~40%) and plagioclase needles (~50%) with no apparent preferred orientation, exhibiting characteristic simple twinning under crossed polars. Also contains abundant small subhedral phenocrysts (~10%) with relatively high relief, some cracked with second-order birefringence interpreted as olivine, and some exhibiting cleavage

with first-order birefringence, which are likely pyroxenes. Brown devitrified glass is also common. I hence interpret this specimen as a fine-grained basalt, likely originating in the eastern Greenland volcanic province (Table 6.1).

6.4.2 QEMSCAN® quantitative mineralogy of bulk sand

The modal mineralogy of Site U1307 IRD samples analysed with QEMSCAN® is given in Table 6.5 (averaged over each glacial cycle), Figure 6.12 (full glacial samples only) and Figure 6.13 (all samples over each cycle). I have omitted plagioclase feldspar in Figs. 6.12 and 6.13 due to its pervasive presence in all terranes as an intermediate mineral, as are 'Others' and 'Background', and recalculated percentages of the remaining key minerals. Where 'Others' appear to comprise a significant proportion, I studied this fraction for the presence of distinctive minerals or mineral phases, but found it contained merely a higher proportion of transitional mineral phases or pixels classified as 'high BSE', as opposed to being assigned to a specific mineral.

The mineral associations averaged across each cycle are given in Figure 6.14 and Appendix E Tables E.6 to E.11. Taken together with the modal mineralogy (Figs. 6.12 and 6.13), there is a clear overall transition to more felsic mineralogical compositions (i.e., more quartz, fewer mafics) and associations (e.g., plagioclase more strongly with quartz, hornblende more weakly with mafic minerals) of IRD deposited at Site U1307 over the iNHG interval. MIS G18 at the cessation of the mPWP, ~2.98 Ma, is characterised by a mixed suite of mineralogical associations (plagioclase equally with quartz and epidote; hornblende moderately with pyroxene, chlorite and weakly with muscovite; Fig. 6.14f), suggesting small amounts of IRD from both eastern and southern sources were delivered to Site U1307 at this time. There appears to be no clear pattern in

changes in modal mineralogy with glacial cycle conditions over MIS G18 (Fig. F.13e). By MIS G12, ~2.86 Ma, modal mineralogy was relatively more felsic with weaker mafic mineral associations (e.g., plagioclase more weakly with epidote, hornblende more weakly with pyroxene and chlorite; Fig. 6.14e), with a clear pattern over the duration of the cycle to more felsic inputs during full glacial and (especially) deglacial conditions (Figure 6.13d) suggesting relatively greater contributions from southern Greenland at this time.

Table 6.5 Modal mineralogical data (averages, %) for sand-sized (63–1000 μm) sediment from selected glacial Marine Isotope Stages (MIS) over iNHG at Site U1307.*

MIS	92	102	G6	G8	G12	G18
No. analysis points	91755	1449620	1875289	198207	971528	661907
No. particles measured	5442	29569	49793	22732	40221	40744
Plagioclase Feldspar	45.22	33.39	30.55	26.49	35.20	33.97
Quartz	34.55	39.98	38.45	22.31	34.02	30.90
Alkali Feldspar	5.77	12.24	12.34	16.58	12.23	12.35
Hornblende	6.35	4.35	4.82	6.84	1.88	3.79
Garnet	1.28	0.53	0.78	1.94	0.62	0.87
Muscovite	1.14	0.85	0.9	1.14	0.72	1.05
Pyroxene	0.99	1.49	2.23	3.59	1.40	2.22
Epidote	0.76	0.79	1.15	1.77	0.44	0.96
Biotite	0.31	1.55	1.43	2.00	1.26	0.98
Chlorite	0.16	0.58	0.79	0.43	0.38	0.45
Olivine	0.00	0.03	0.04	0.05	0.02	0.04
Others	3.46	4.22	6.53	16.86	11.82	12.43
Background	0.27	0.30	0.61	2.96	1.70	1.97

*Values shown as 0.00 may have the mineral present at an abundance of <0.01%.
See Appendix E Tables E.1 to E.5 for individual sample data for each cycle.

As glacial IRD inputs to Site U1307 began to intensify from MIS G8, ~2.76 Ma, the modal mineralogy appears to have been much more mafic (Fig. 6.12) coupled with overwhelmingly mafic mineral associations (e.g., hornblende very strongly with pyroxene, moderately with chlorite, garnet and epidote; Fig. 6.14d), consistent with typical (north)eastern Greenland parent geologies (e.g., eclogite, tholeiitic basalt, dolerite dykes; Table 6.4). The modal mineralogy also became

more mafic with intensified glacial conditions during MIS G8 (Fig. F.13c), suggesting Site U1307 IRD deposition was dominated by (de)glacial calving from eastern Greenland at this time.

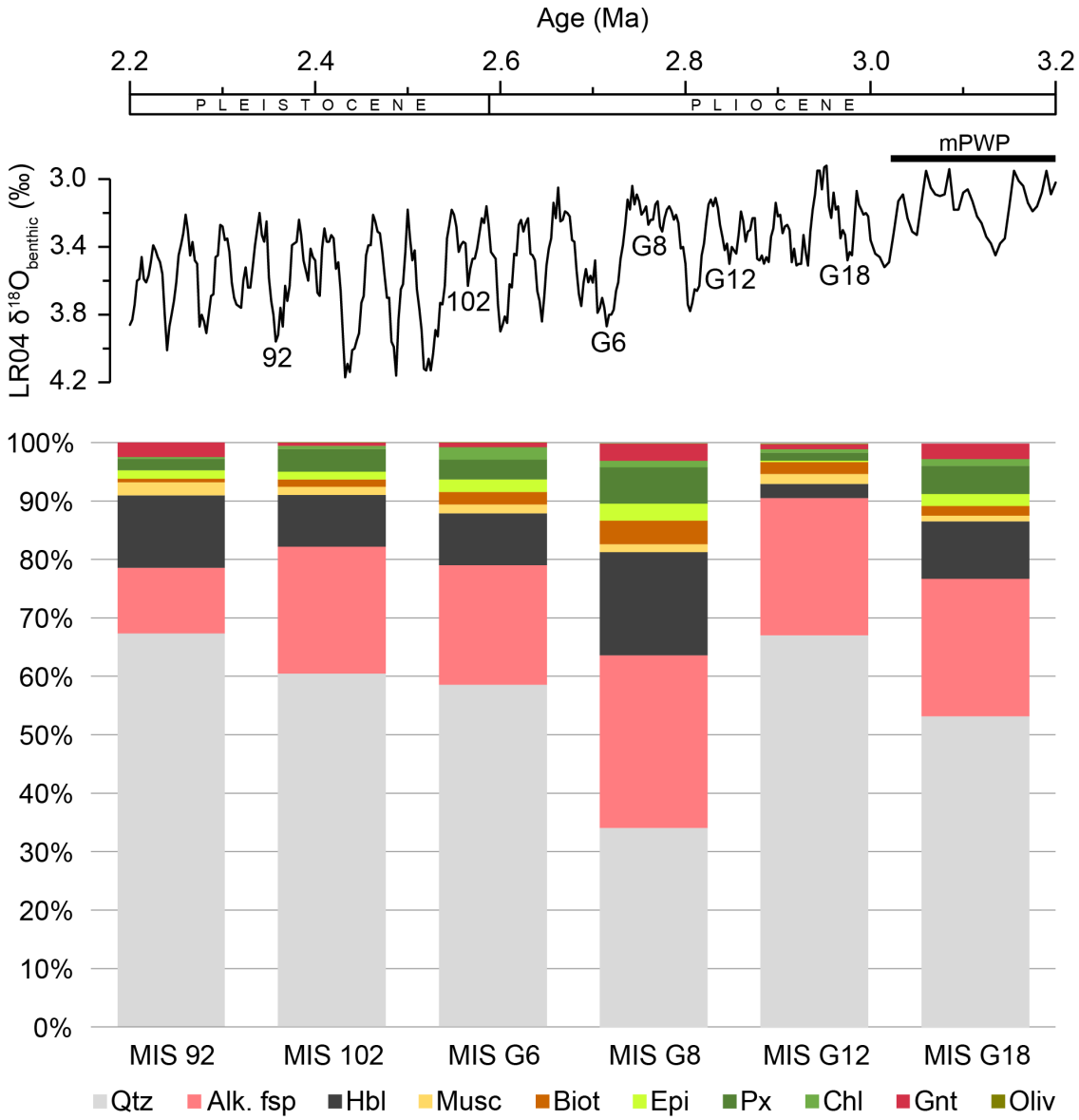

Figure 6.12 Modal mineralogical percentages for sand-sized (63–1000 µm) sediment deposited at Site U1307 during full glacial conditions of Marine Isotope Stage (MIS) 92 (~2.38 Ma), MIS 102 (~2.55 Ma), MIS G6 (~2.72 Ma), MIS G8 (~2.76 Ma), MIS G12 (~2.83 Ma), and MIS G18 (~2.98 Ma). The global benthic $\delta^{18}O$ stack is given at the top for reference (Lisiecki and Raymo, 2005); numbers are Marine Isotope Stages, and the duration of the mid-Piacenzian warm period (mPWP) is also indicated (Dolan *et al.*, 2011). Qtz = quartz, Alk. Fsp = alkali feldspar, Hbl = hornblende, Musc = muscovite, Biot = biotite, Epi = epidote, Px = pyroxene, Chl = chlorite, Gnt = garnet, Oliv = olivine. See Figure 6.13 and Appendix E Tables E.1 to E.5 for individual sample data for each cycle.

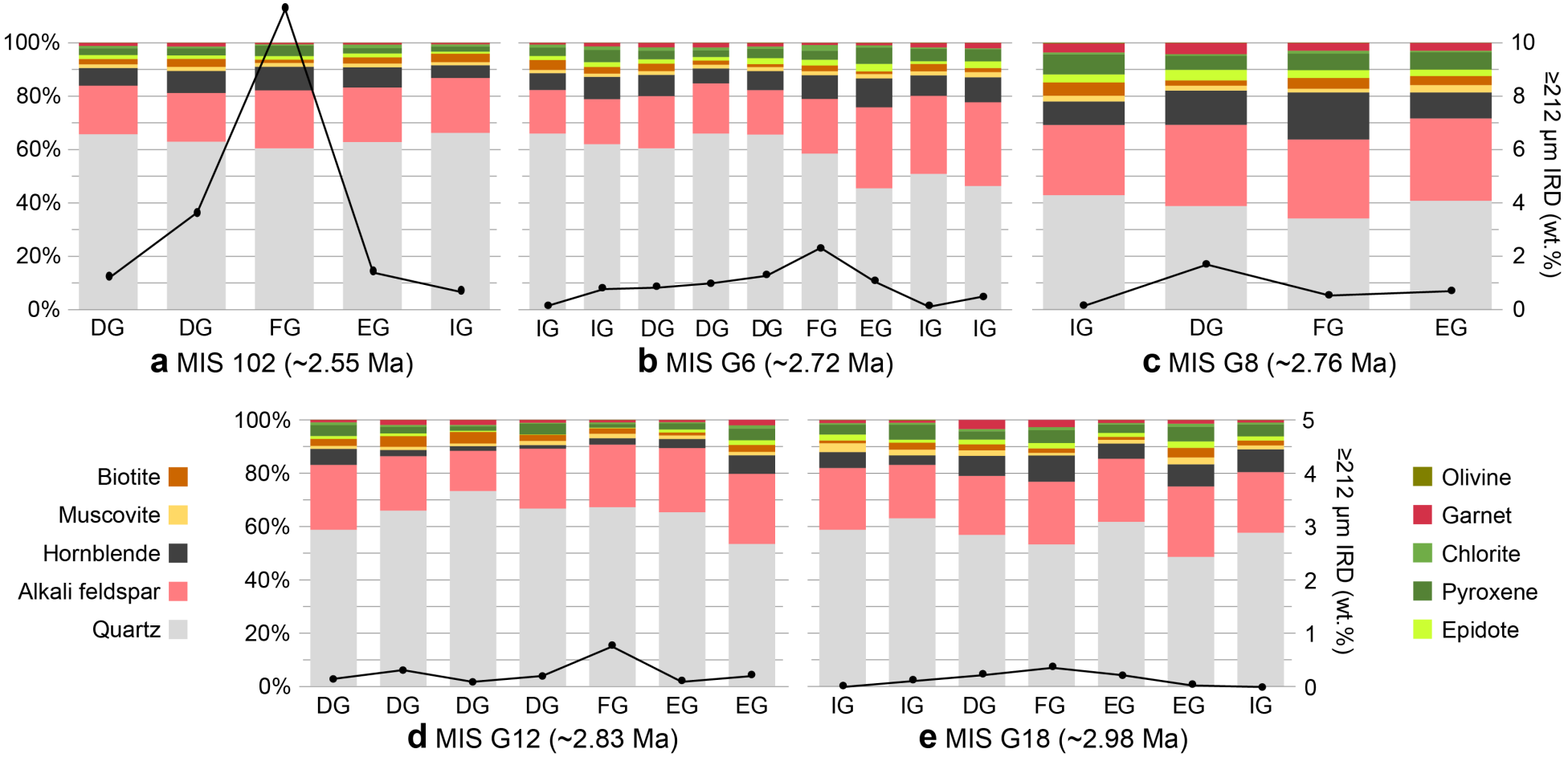

Figure 6.13 Modal mineralogical percentages for sand-sized (63–1000 µm) sediment deposited at Site U1307 over the course of each studied Marine Isotope Stage (MIS) for which samples represent early glacial (EG), full glacial (FG), deglacial (DG) and/or interglacial (IG) conditions: (**a**) MIS 102 (~2.55 Ma); (**b**) MIS G6 (~2.72 Ma); (**c**) MIS G8 (~2.76 Ma); (**d**) MIS G12 (~2.83 Ma); and (**e**) MIS G18 (~2.98 Ma) (see Appendix E for full data). The coarse (≥212 µm) weight percent (wt.%) IRD data for each sample is also shown by the black records superimposed on each cycle's mineralogy (Blake-Mizen *et al*., 2019; see also Chapter 4).

With the onset of persistently elevated IRD deposition at Site U1307 from MIS G6, ~2.72 Ma, to MIS 102, ~2.55 Ma, the modal mineralogy again became increasingly felsic (Fig. 6.12) with greater felsic mineral associations (e.g., plagioclase more with quartz, hornblende less with pyroxene and chlorite; Fig. 6.14c to b) consistent with southern Greenland Precambrian parent geologies (e.g., granite, gneiss, quartz monzonite; Table 6.4). Over the course of the G6 glacial cycle, the modal mineralogy became overall more felsic (Fig. 6.13b), indicating Site U1307 was swamped by IRD from local southern Greenland sources as this cycle progressed. In contrast, despite being more felsic as a whole, IRD deposited during MIS 102 became relatively slightly more mafic during the full glacial and early deglacial (Fig. 6.13a), suggesting eastern Greenland remained an important source of glacial IRD to Site U1307 at this time.

By MIS 92, ~2.37 Ma, the proportion of felsic to mafic mineralogy was the highest of all cycles studied during the iNHG interval (Fig. 6.12), with the strongest felsic mineral associations (e.g., plagioclase with quartz, hornblende with muscovite; Fig. 6.14a). Hornblende's strongest association at this time was still with pyroxene, although both have been noted as occurring in norites of the AB terrane as well as the Rapaviki granite of the KMB (Table 6.4; Escher and Watt, 1976). The proportion of garnet in IRD deposited during MIS 92 (1.28%; Table 6.5) seems anomalously high in context with its overall decrease during the progression of iNHG (Fig. 6.12) and the apparent dominance of proximal southern Greenland IRD inputs at this time. Garnet's strong association during MIS 92 with muscovite, however (see Appendix E Table E.6), raises the tentative interpretation that much of the garnet in this sample may originate from the garnet-mica schists of the Isua supracrustal belt just south of Nuuk in southwestern Greenland (e.g., Higgins, 1990; Rollinson, 2002).

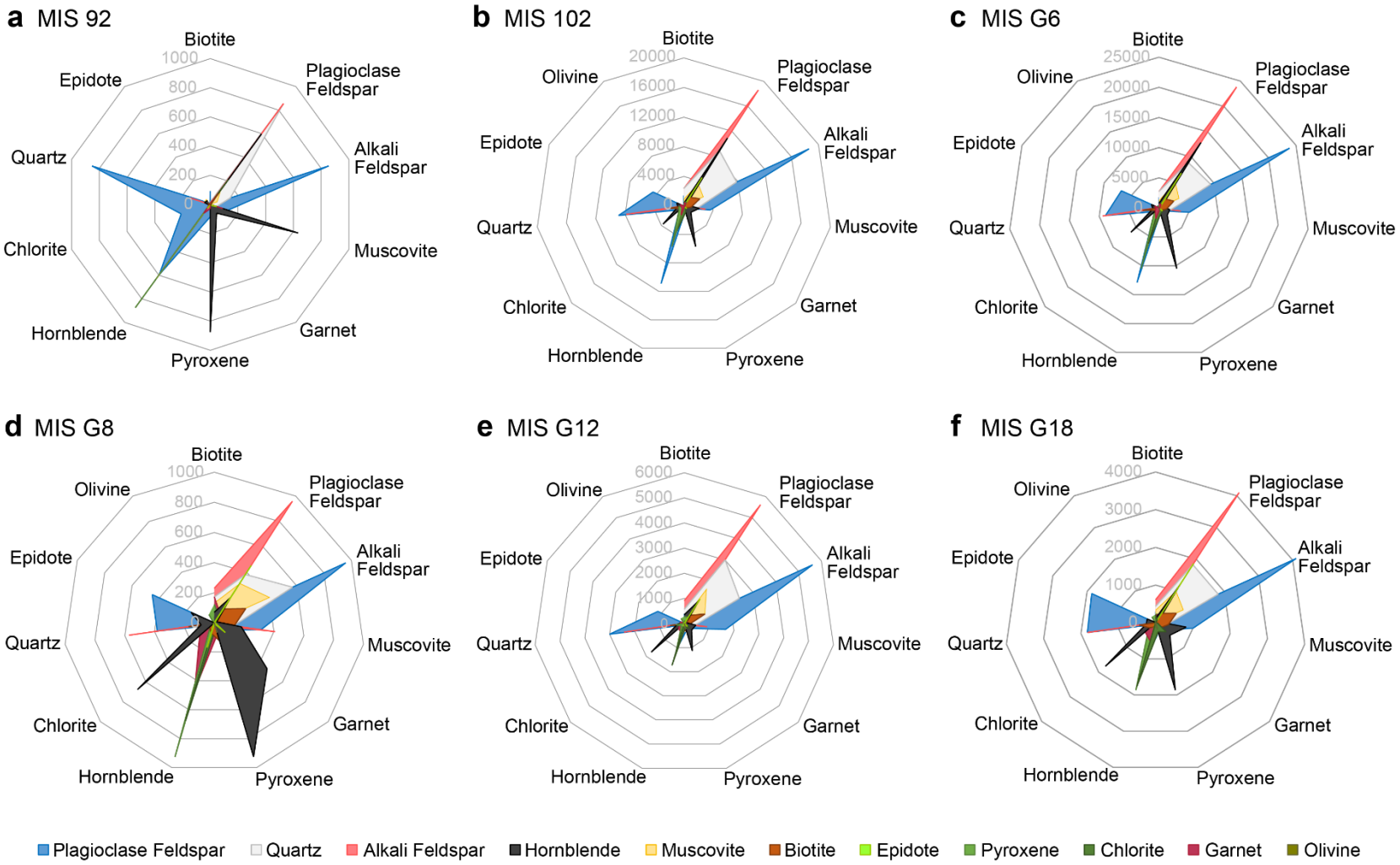

Figure 6.14 Radar plots of mineral associations for sand-sized (63–1000 µm) sediment deposited at Site U1307 during (**a**) Marine Isotope Stage (MIS) 92 (~2.38 Ma); (**b**) MIS 102 (~2.55 Ma); (**c**) MIS G6 (~2.72 Ma); (**d**) MIS G8 (~2.76 Ma); (**e**) MIS G12 (~2.83 Ma); and (**f**) MIS G18 (~2.98 Ma). Axis numbers = number of transitions between each pair of minerals. Colours correspond to reference mineral (see key). See Appendix E Tables E.6 to E.11 for the original data.

6.4.3 Pb-isotope provenance of individual ice-rafted feldspars

The results of Pb-isotope analysis of individual ice-rafted feldspars deposited at Site U1307 between ~3.1 and 2.4 Ma are presented in both $^{206}Pb/^{204}Pb$ vs. $^{207}Pb/^{204}Pb$ (henceforth 206-207) space in Figure 6.15 and $^{206}Pb/^{204}Pb$ vs. $^{208}Pb/^{204}Pb$ (henceforth 206-208) space in Figure 6.16, alongside the core-top (modern) distribution for feldspars deposited at Eirik Drift Site HU90-013-013 (White *et al*., 2016). Histograms of $^{206}Pb/^{204}Pb$ are also given in each panel for reference. I identify the likely source of each feldspar in the following pages by considering its position primarily in 206-207 space, with its position in 206-208 space, Holocene and modern iceberg trajectories (Bigg *et al*., 1996; Wagner *et al*., 2017) and interpretation of Site HU90-013-013 core-top feldspar provenance (White *et al*., 2016) considered for context where ambiguity exists between 206-207 source fields.

The majority of the variance in the Pb-isotope data is in the $^{204}Pb/^{206}Pb$ ratio, as illustrated by the histograms in each panel of Figs. 6.15 and 6.16. As a first-order observation, the selected time windows can be divided based upon the histogram peak distributions. Prior to the onset of significant IRD inputs to Site U1307, during MIS K2 (~3.1 Ma; Fig. 6.15f) and G18 (~2.98 Ma; Fig. 6.15e), data are limited (n = 6 and 7, respectively) due to only very minor amounts of (mostly deglacial) IRD available for analysis (Fig. 6.3); the distribution is too sparse to define a consistent pattern, but still represents important evidence for the key iceberg-calving sources to Eirik Drift during these earlier intervals. As glacial IRD inputs to Site U1307 began to intensify during MIS G12 (~2.83 Ma; Fig. 6.15d) and G8 (~2.76 Ma; Fig. 6.15c), the $^{204}Pb/^{206}Pb$ distributions cluster in a similar manner between ~12.7 and 15.7, and ~18 and 19, with the largest number of analyses in both cases peaking around $^{206}Pb/^{204}Pb$ ~13. Following the onset of

significant ice-rafting to Site U1307, at MIS 96 (~2.42 Ma; Fig. 6.15b), the $^{206}Pb/^{204}Pb$ distribution most closely resembles the modern (core-top) distribution (Fig. 6.15a), both with greatest clustering between $^{206}Pb/^{204}Pb$ ~12.8 and ~16.3 and a concentrated peak around $^{206}Pb/^{204}Pb$ ~16. This initial assessment of the data clearly indicates evolution of major GrIS iceberg-calving sources to Eirik Drift over iNHG, to resemble those active in the modern day.

Of the feldspars sampled from the K2 deglacial, two with $^{206}Pb/^{204}Pb$ >16.5 plot within fields characterising East Caledonide sources (Zachariae Isstrøm and Scoresby Sund), with a third too ambiguously situated in the overlap between Zachariae Isstrøm and Scoresby Sund (EC), Tasiilaq (eastern NMB) and Nordre Sermilik Fjord (KMB) fields to confidently assign a single source. Another appears to plot within the Disko Bay (western NMB) field with $^{206}Pb/^{204}Pb$ 16.9 (Fig. 6.15f). However, iceberg trajectory modelling and the dominantly northward flow of the West Greenland Current (WGC) past this part of the western Greenland coast (Fig. 6.1) suggest icebergs calved from Disko Bay are an unlikely source of IRD to Eirik Drift (Bigg *et al*., 1996; Wagner *et al*., 2017), so this feldspar may represent an EC source not yet characterised. The remaining two K2 deglacial feldspars plot very closely with $^{206}Pb/^{204}Pb$ ~13, most likely representing iceberg-calving from the Kangerlussuaq Fjord System (eastern NMB).

For MIS G18, the two feldspars representing full glacial conditions appear to agree most strongly with a Scoresby Sund (and/or perhaps Zachariae Isstrøm) EC source, suggesting restricted glacial iceberg-calving margins had developed in (north)eastern Greenland by this time (~2.98 Ma). These data appear to be consistent with the ~3 Ma kick-up in glacial IRD recorded at Iceland Plateau Site 907 (Jansen *et al*., 2000). Three feldspars from the G18 deglacial plot in a cluster with $^{206}Pb/^{204}Pb$ ~18.3, likely representing a high rate of calving from the EC,

whereas the other two ($^{206}Pb/^{204}Pb$ ~14.5 and 15.7) do not plot in any source field in 206-207 space (Fig. 6.15e) but are captured by the broad Disko Bugt (western NMB) field in 206-208 space (Fig. 6.16e), indicating they may originate from eastern NMB sources not yet fully-characterised as previously discussed for MIS K2.

The greater amount of feldspar data collected for MIS G12 (~2.83 Ma; n = 22) plot in two clear linear arrays in 206-207 space between $^{206}Pb/^{204}Pb$ ~18 and 19 (EC origin), and $^{206}Pb/^{204}Pb$ ~12.7 to 14 (Fig. 6.15d). Of the full glacial samples, three are consistent with a Scoresby Sund or Zachariae Isstrøm EC source, one appears to have originated from Tasiilaq and two plot within the field for the Kangerlussuaq Fjord System (both eastern NMB). One full glacial feldspar with $^{206}Pb/^{204}Pb$ ~14.9 only plots within the Disko Bugt (western NMB) field in 206-208 space (Fig. 6.16d) and thus is again potentially from an uncharacterised eastern NMB source. The full glacial feldspar with the lowest $^{206}Pb/^{204}Pb$ value of ~12.7 is very likely sourced from Gyldenløve Fjord (eastern AB). The deglacial spread is similar to during the glacial, but mainly concentrated in the EC (n = 4; 29%) and eastern NMB fields (n = 10; 71%, assuming inclusion of two feldspars with $^{206}Pb/^{204}Pb$ ~14.7), particularly the Kangerlussuaq Fjord System, indicating a high rate of calving from these regions at this time.

The greatest number of feldspars was analysed over the MIS G8 cycle (2.76 Ma; n = 34), with the majority (n = 25; 74%) restricted to between $^{206}Pb/^{204}Pb$ ~12.9 and 15.5 (Figs. 6.15c and 6.16c). Feldspars representing full glacial conditions have the broadest distribution, with four (40%) occupying a cluster in the Scoresby Sund field (EC) between $^{206}Pb/^{204}Pb$ ~18.2 and 18.7, and another 4 (40%) with $^{206}Pb/^{204}Pb$ ~14.7 to 16.2 plotting only within the Disko Bugt (western NMB) field in 206-208 space (Fig. 6.16c), likely representing

uncharacterised eastern NMB sources. The remaining two are likely sourced from the Kangerlussuaq Fjord System (eastern NMB) and Gyldenløve Fjord (eastern AB) with $^{206}Pb/^{204}Pb$ ~13.8 and ~12.7, respectively (Fig. 6.15c). Three (21%) of the feldspars deposited during the G8 deglacial plot ambiguously in either the Disko Bugt or Kangerlussuaq Fjord (both western NMB) fields, and so may originate from uncharacterised E NMB sources. Of the other deglacial feldspars, four (30%) are consistent with a Kangerlussuaq Fjord System source, three (21%) may originate from Zachariae Isstrøm, two (15%) appear to be sourced from Scoresby Sund, and one is likely either from Tasiilaq (eastern NMB) or Nordre Sermilik Fjord (KMB). The majority (n = 8; 80%) of feldspars representing interglacial conditions following deglaciation plot in a linear array in 206-207 space between $^{206}Pb/^{204}Pb$ ~13 and 14 (Fig. 6.15c), likely all from the Kangerlussuaq Fjord System (eastern NMB). The remaining two (20%) with $^{206}Pb/^{204}Pb$ ~15.3 and 16.8 again only plot within the Disko Bugt (western NMB) field in 206-208 space, so likely represent uncharacterised eastern NMB sources.

The distribution of feldspars in Pb-isotope space from MIS 96 (~2.4 Ma; n = 28) most closely resembles the modern at Eirik Drift Site HU90-013-013 (compare Figs. 6.15a to b, and 6.16a to b). Feldspars deposited during early glacial conditions plot relatively closely, with the majority (n = 6; 60%) forming a distinctive cluster between $^{206}Pb/^{204}Pb$ ~15.1 and 16.3, which may represent a mixture of Scoresby Sund and Zachariae Isstrøm (EC) sources. Two early glacial feldspars with $^{206}Pb/^{204}Pb$ ~17.2 and 17.4 are also likely Caledonide-sourced, and another two with $^{206}Pb/^{204}Pb$ ~12.9 and 13.7 appear to be sourced from the Kangerlussuaq Fjord System (eastern NMB), but also lie on the border of the Sermiligaarssuk Fjord (western AB) field (Fig. 6.15b). The distribution of feldspar provenance during full glacial conditions is broader, with the majority (n = 8; 73%)

forming two linear arrays between $^{206}Pb/^{204}Pb$ ~14.9 and 16.2, and ~17.9 to 19.8 (Fig. 6.15b). One full glacial feldspar with $^{206}Pb/^{204}Pb$ ~14.3 plots within western NMB fields in 206-207 space (Fig. 6.15b) but may represent an eastern NMB source not yet characterised, and two plot unambiguously in AB fields with $^{206}Pb/^{204}Pb$ ~12.7 (either Gyldenløve or Sermiligaarssuk Fjord; eastern and western AB, respectively) and ~11.7 (Nuup Kangerlua River, W AB). Feldspars representing the deglacial of MIS 96 are relatively restricted again, with two clusters of two with $^{206}Pb/^{204}Pb$ ~16 and 18.4 respectively, two plotting in or very near to the Kangerlussuaq Fjord field (western NMB) with $^{206}Pb/^{204}Pb$ ~13.6 and 14.5, and one with $^{206}Pb/^{204}Pb$ ~13.3 likely sourced from the Kangerlussuaq Fjord System (eastern NMB).

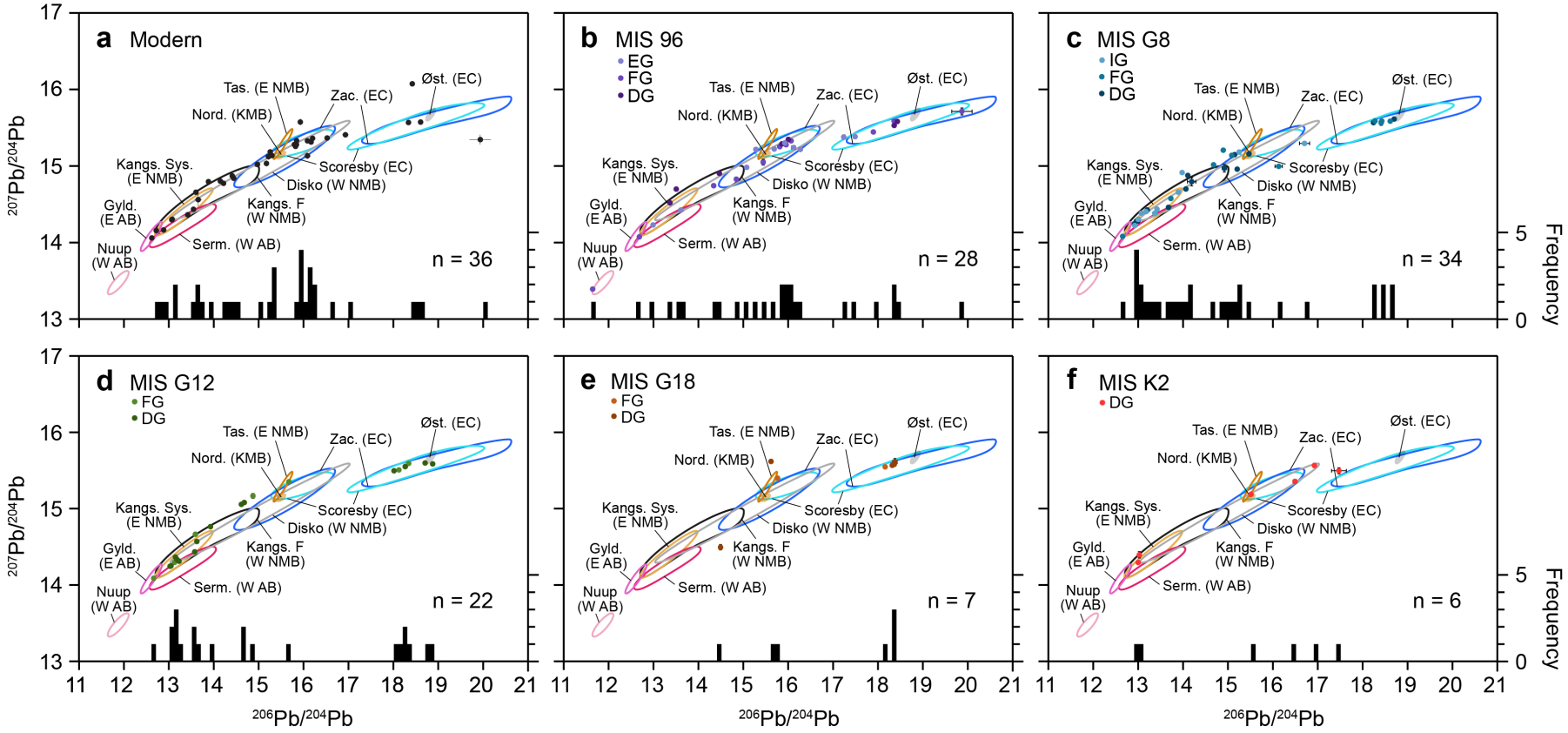

Figure 6.15 The Pb-isotope composition ($^{206}Pb/^{204}Pb$ vs. $^{207}Pb/^{204}Pb$) of individual sand-sized (>150 µm) feldspars deposited at Eirik Drift (**a**) Site HU90-013-013 during the modern (core-top sediment; White *et al.*, 2016), and Site U1307 during early glacial (EG), full glacial (FG), deglacial (DG) and/or interglacial (IG) conditions of (**b**) Marine Isotope Stage (MIS) 96 (~2.42 Ma), (**c**) MIS G8 (~2.76 Ma), (**d**) MIS G12 (~2.83 Ma), (**e**) MIS G18 (~2.98 Ma), and (**f**) MIS KM2 (~3.1 Ma). Histograms of $^{206}Pb/^{204}Pb$ are also shown for reference. Crosses centred on individual data represent their respective 2σ uncertainties in Pb–Pb space. Where no cross is evident, uncertainties are smaller than the width of symbol used. See White *et al.* (2016; their Fig. 3) for data used to define 'source bubbles' shown in all six panels. Øst. = Østgrønland, Zac. = Zachariae Isstrøm, Scoresby = Scoresby Sund Fan, Disko = Disko Bugt, Tas. = Tasiilaq, Serm = Sermiligaarssuk Fjord, Gyld. = Gyldenløve Fjord, Nuup = Nuup Kangerlua River, Kangs. Sys. = Kangerlussuaq Fjord System, Kangs. F = Kangerlussuaq Fjord, Norde. = Nordre Sermilik Fjord Narssarsuaq, Baffin = Northeast Baffin Bay, KMB = Ketilidian Mobile Belt, E/W AB = East/West Archaean Block, E/W NMB = East/West Nagssugtoqidian Mobile Belt, EC = East Caledonides. Data >21 $^{206}Pb/^{204}Pb$ (n = 1) indicative of EC or Scandinavian sources during MIS G12 not shown. See Appendix F for full data.

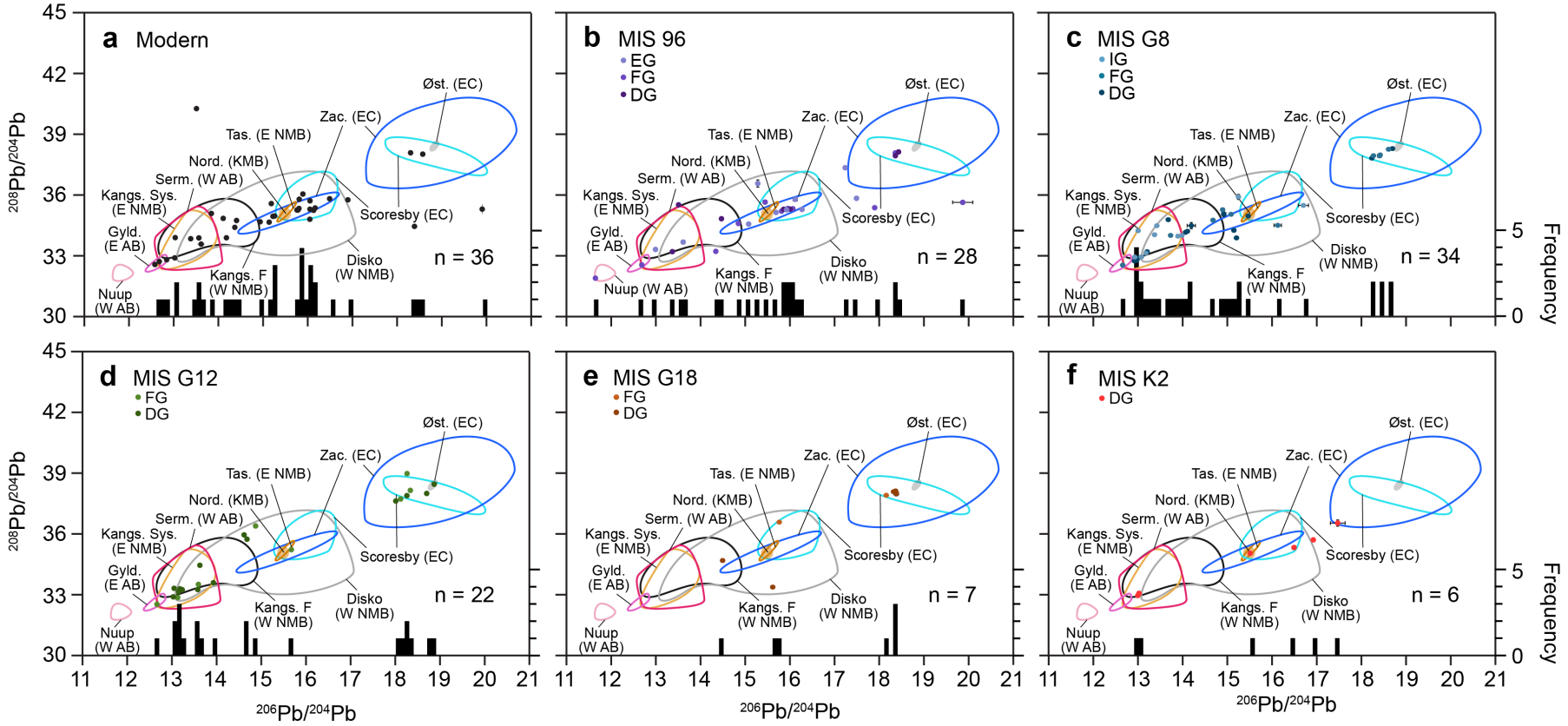

Figure 6.16 The Pb-isotope composition ($^{206}Pb/^{204}Pb$ vs. $^{208}Pb/^{204}Pb$) of individual sand-sized (>150 µm) feldspars deposited at Eirik Drift (**a**) Site HU90-013-013 during the modern (core-top sediment; White et al., 2016), and Site U1307 during early glacial (EG), full glacial (FG), deglacial (DG) and/or interglacial (IG) conditions of (**b**) Marine Isotope Stage (MIS) 96 (~2.42 Ma), (**c**) MIS G8 (~2.76 Ma), (**d**) MIS G12 (~2.83 Ma), (**e**) MIS G18 (~2.98 Ma), and (**f**) MIS KM2 (~3.1 Ma). Histograms of $^{206}Pb/^{204}Pb$ are also shown for reference. Crosses centred on individual data represent their respective 2σ uncertainties in Pb–Pb space. Where no cross is evident, uncertainties are smaller than the width of symbol used. See White *et al*. (2016; their Fig. 3) for data used to define 'source bubbles' shown in all six panels. Øst. = Østgrønland, Zac. = Zachariae Isstrøm, Scoresby = Scoresby Sund Fan, Disko = Disko Bugt, Tas. = Tasiilaq, Serm = Sermiligaarssuk Fjord, Gyld. = Gyldenløve Fjord, Nuup = Nuup Kangerlua River, Kangs. Sys. = Kangerlussuaq Fjord System, Kangs. F = Kangerlussuaq Fjord, Norde. = Nordre Sermilik Fjord Narssarsuaq, Baffin = Northeast Baffin Bay, KMB = Ketilidian Mobile Belt, E/W AB = East/West Archaean Block, E/W NMB = East/West Nagssugtoqidian Mobile Belt, EC = East Caledonides. Data >21 $^{206}Pb/^{204}Pb$ (n = 1) indicative of EC or Scandinavian sources during MIS G12 not shown. See Appendix F for full data.

6.5 Discussion

The new petrographical, mineralogical and geochemical records for Site U1307 IRD provenance presented here, summarised in Figure 6.17, together tell a clear narrative of the gradual establishment of extensive iceberg-calving margins on southern Greenland with the progression of iNHG. At the lowest resolution, the dropstone record suggests ice-rafting was dominated by basaltic eastern Greenland sources prior to ~2.4 Ma, at which point more numerous dropstones of a range of lithologies including granitic, basaltic, mafic granitoid, gneiss and quartzite indicate the apparently relatively abrupt onset of active iceberg-calving from a wide distribution of eastern and southern Greenland sources. More detailed mineralogical and geochemical information about selected time windows over the iNHG interval gleaned from quantitative mineralogy and Pb-isotope analyses improve the resolution of this transition, and enable the most highly geographically- and temporally-resolved reconstruction of southern GrIS evolution over iNHG to date.

6.5.1 Late Pliocene (~3.1 to 2.8 Ma)

Despite very low coarse IRD inputs (<1 wt.%; Fig. 6.17) to Site U1307 during the coldest periods of the mPWP, the Pb-isotope distribution for the MIS K2 deglacial indicates a significant mass of ice must have existed at least inland on (south)eastern Greenland at this time, with isolated but active iceberg-calving focussed in Scoresby Sund (EC) and the Kangerlussuaq Fjord System (eastern NMB) as deglaciation took place. This finding is consistent with Site U1307 magnetic susceptibility and elemental X-ray fluorescence data (see Chapters 4 and 5, respectively) that indicate active glacial erosion must have taken place at least inland on the southern felsic Precambrian terranes during the coldest stages

of the mPWP, and hence also with models that predict the GrIS was restricted but still present as reduced ice-caps occupying the highlands of southern and eastern Greenland at this time (Dolan *et al*., 2011, 2015). These records from Site U1307 constitute convincing evidence that Greenland was not fully deglaciated during the mPWP, as is often assumed in the upper-end estimates for eustatic sea-level rise during this period (~10–30 m above present; Raymo *et al*., 2018).

At the cessation of the mPWP, during MIS G18, both the mineralogy and Pb-isotope provenance of Site U1307 IRD suggest (de)glacial calving was still restricted to Scoresby Sund (EC), and as-yet uncharacterised potential eastern NMB regions (Fig. 6.17). The lack of a trend in mineralogy with changing conditions over the G18 cycle suggests significant glacial calving margins were not established in any particular region at this time, and the small amount of IRD (<1 wt.%; Fig. 6.17) indicates the presence of only isolated glaciers calving at sea-level. This may appear to contradict the onset of elevated glacial IRD delivery to the Iceland Plateau from northeastern Greenland at this time (Jansen *et al*., 2000); due to deflection of iceberg trajectories by surface currents in the northern Greenland Sea (Fig. 6.1; Bigg *et al*., 1996), however, it is possible that significant IRD from northeast Greenland simply would not have reached Eirik Drift at ~3 Ma.

6.5.2 Plio-Pleistocene transition (~2.8 to 2.5 Ma)

Despite IRD input remaining low during MIS G12 (<1 wt.%; Fig. 6.17), its relatively more felsic mineralogy suggests significant glacial expansion was taking place on the southern Precambrian terranes at this time (Fig. 6.17), with the first eastern AB-sourced feldspar measured in this study originating from Gyldenløve Fjord.

MIS G12 may therefore represent the first time restricted glacial iceberg-calving margins developed in this region of southern Greenland. The high concentration of feldspars originating from the Kangerlussuaq Fjord System and Scoresby Sund, however, suggests active GrIS iceberg-calving was still mainly focussed on the EC and eastern NMB at this time. The few feldspars with a Zachariae Isstrøm signature in 206-208 Pb-isotope space (Fig. 6.16d) may be a distal expression of significant northeastern GrIS glacial expansion thought to have taken place from ~3 Ma (Jansen *et al*., 2000; Blake-Mizen *et al*., 2019; see also Chapter 4).

As glacial IRD concentrations began to increase at MIS G8 (1–2 wt.%; Fig. 6.17), the notably more mafic mineralogy and high concentration of feldspars originating from Scoresby Sund, the Kangerlussuaq Fjord System and other possible eastern NMB sources (Fig. 6.17) indicates that (de)glacial calving was overwhelmingly focussed in outlet glaciers fed by catchment areas overlying the Paleogene basalts at this time. Isolated glacial calving appears to have persisted from Gyldenløve Fjord on the eastern AB, however, and the single deglacial feldspar possibly originating from Nordre Sermilik Fjord suggests that inland ice expansion may have been taking place on the southernmost part of the Greenland landmass by ~2.76 Ma. The high concentration of eastern NMB-sourced IRD during the following interglacial also indicates that, by this time, the GrIS was a sufficient size to maintain iceberg-calving margins during warm intervals from regions with a high concentration of outlet glaciers, in particular the Kangerlussuaq Fjord System, which is today an important source of icebergs and IRD to the Greenland-proximal marine realm (Rignot and Kangaratnam, 2006; White *et al*., 2016).

The increasingly felsic mineralogy of IRD deposited with intensification of glacial conditions during MIS G6, at the onset of significant and persistently elevated inputs to Site U1307 (Fig. 6.17), is strong evidence supporting the gradual establishment of more extensive proximal southern GrIS iceberg-calving margins by ~2.72 Ma (Blake-Mizen *et al*., 2019; see also Chapter 4).

6.5.3 Earliest Pleistocene (~2.5 to 2.3 Ma)

By the earliest Pleistocene, during MIS 102, the still-increasing amount and felsic mineralogy of IRD delivered to Site U1307 (Fig. 6.17) suggests southern GrIS iceberg-calving margins were continuing to grow in extent. Since full glacial conditions were characterised by relatively more mafic inputs, however, eastern Greenland may still have hosted the most extensive glacial iceberg-calving margins at this time.

The pattern of IRD Pb-isotope provenance over the MIS 96 cycle suggests iceberg-calving was mainly focussed on the EC during the early stages of glaciation, then iceberg-calving margins expanded southward onto the NMB and AB coasts as the glacial progressed to modern-like extents, with IRD from possibly as far afield as the Nuup Kangerlua River on the western AB reaching Eirik Drift. The cluster (n = 9) of MIS 96 feldspars around $^{206}Pb/^{204}Pb$ ~16, similar to at Site HU90-013-013 during the modern (compare Figs. 6.14a to b and 6.15a to b), may actually have a more proximal southern Greenland origin despite lying within EC source fields. Since this distinctive cluster of ratios is not represented during the late Holocene at Site 918 offshore eastern Greenland, where they should be expected if feldspars with this specific signature originate along the southeastern coast, it has been proposed that this cluster at Site HU90-013-013 represents as-yet uncharacterised local KMB sources (White *et al*., 2016). If this

is also the case during MIS 96 at Site U1307, I speculate that this time (~2.42 Ma) represents the first expansion of GrIS iceberg-calving margins onto the very southern tip of the Greenland landmass, where they persisted throughout early glacial, full glacial and deglacial conditions. The overwhelmingly felsic mineralogy of IRD deposited during MIS 92, ~2.38 Ma, appears to support the establishment of extensive, modern-like iceberg-calving margins on southern Greenland by this time that would have dominated IRD deposition at Site U1307, with mineral associations suggesting significant contributions from the KMB and potentially the western AB.

Holocene and modern-day iceberg-trajectory modelling (e.g., Bigg *et al*., 1996; Wagner *et al*., 2017) suggests that icebergs originating from the western AB should not reach waters overlying Eirik Drift, as their paths are primarily controlled by the velocity of surface currents (Wagner *et al*., 2017), and so according to present-day surface circulation should instead be transported northward from this region by the WGC (Fig. 6.1). The delivery of potentially significant amounts of western AB-sourced IRD to Site U1307 at ~2.4 Ma suggests, therefore, that surface circulation around southern Greenland may have operated differently at that time. The likely expansion of pack-ice covering the East Greenland Current as the GrIS reached its maximum iNHG extents, and hence the speculated southward deflection of the Polar Front at this time (Bohrmann *et al*., 1990; see also Chapter 5), may have enabled icebergs calved from glaciers in the Nuuk region to travel south to waters overlying Eirik Drift. Alternatively, or perhaps jointly, increased offshore wind stress resulting from glacial expansion may have had a significant impact on North Atlantic surface circulation, as inferred for late Pleistocene glacials (Bard and Rickaby, 2009; Sijp and England, 2009) and the LGM (Murati *et al*., 2010). The strength of winds at

the ocean surface has been modelled to affect the trajectories of 'small' (<1.5 km length) icebergs, such that they are deflected in the direction of the prevailing wind (Wagner *et al*., 2017). Hence, it is reasonable to speculate that increased wind stress in a southerly direction with widespread expansion of iceberg-calving margins on Greenland (and North America; Bailey *et al*., 2013) by ~2.4 Ma, coupled with a southward shift of the Polar Front, may have deflected the paths of icebergs calved from southwest Greenland enough to transport IRD to Eirik Drift at this time. Although this may also reduce the doubt of IRD from iceberg-calving sites further north on western Greenland, such as Disko Bay, reaching Eirik Drift, I argue that IRD originating from this region prior to the development of extensive southern iceberg-calving margins (as suggested by a few ambiguously-plotted feldspars during MIS K2, G18, G12 and G8; Figs. 6.15 and 6.16) is still more likely to have been transported northward in the WGC at this time.

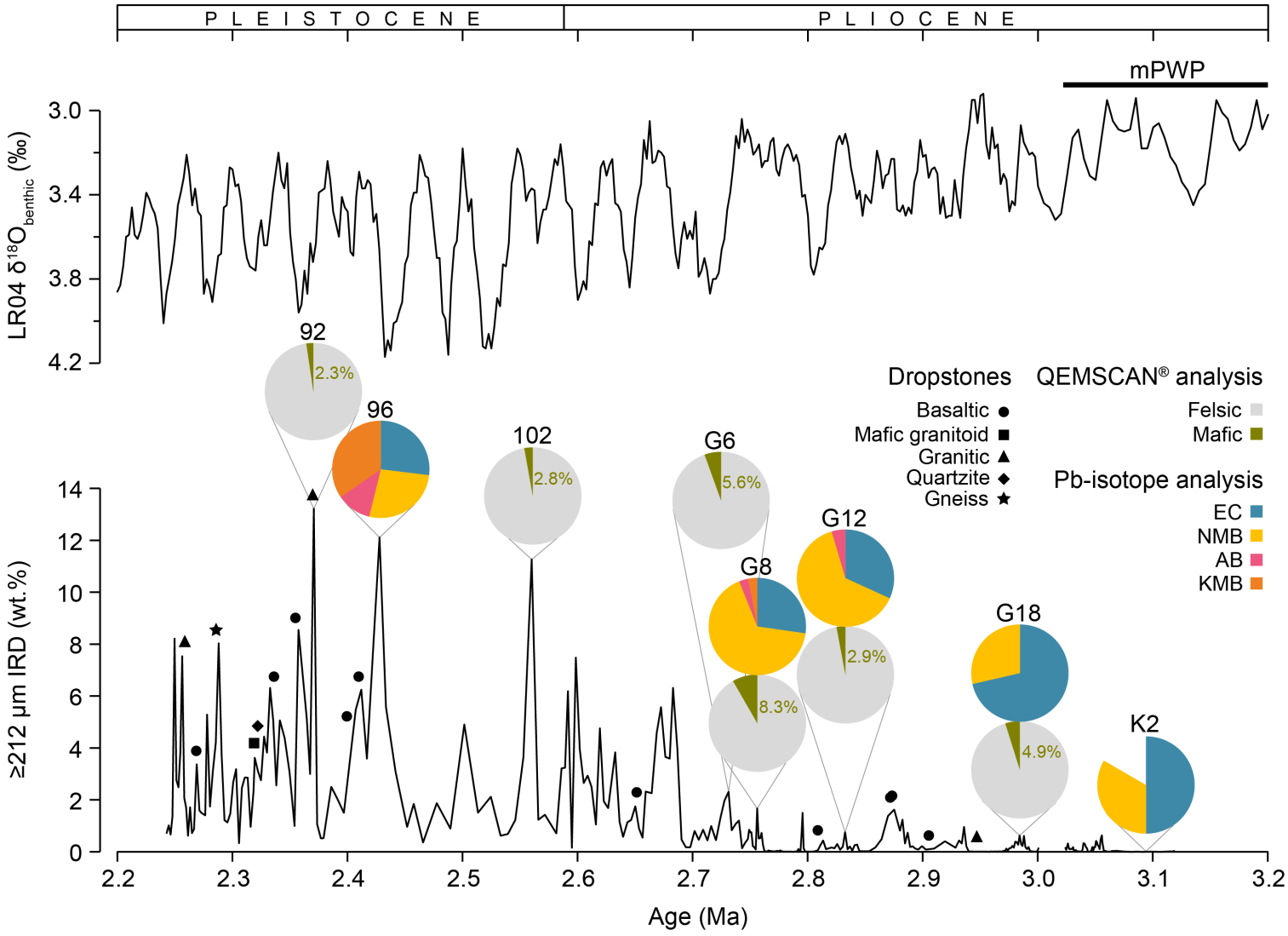

Figure 6.17 Summary figure of dropstone petrography (black symbols), modal mineralogy (felsic vs. basaltic) measured by QEMSCAN® (felsic minerals = quartz, alkali feldspar, muscovite; mafic = pyroxene, olivine; see Fig. 6.12 and Table 6.5) and terrane provenance by Pb-isotope analysis (EC = East Caledonides, NMB = Nagssugtoqidian Mobile Belt, AB = Archaean Block, KMB = Ketilidian Mobile Belt) for select Marine Isotope Stages, annotated onto the coarse (≥212 µm) weight percent (wt.%) IRD record (Blake-Mizen *et al*., 2019; see also Chapter 4). The global benthic $\delta^{18}O$ stack is given at the top for reference (Lisiecki and Raymo, 2005). Note pie-charts are averages of all samples for each cycle; see Appendix E for full data.

6.6 Conclusions

The new suite of multi-proxy provenance data presented here reveals, for the first time, a detailed, terrane-specific history of southern Greenland Ice Sheet (GrIS) extent during the Plio-Pleistocene intensification of Northern Hemisphere glaciation (iNHG). A combination of dropstone petrography, QEMSCAN® quantitative mineralogy of bulk sand and Pb-isotope analysis of individual ice-rafted feldspars deposited at IODP Site U1307 on Eirik Drift between ~3.1 and 2.4 Ma has been successfully used to demonstrate that the southern GrIS reached modern-like extents, with extensive iceberg-calving margins active on all southern Precambrian terranes, during glacials by ~2.4 Ma.

Deglacial calving from isolated glaciers in eastern Greenland during the mid-Piacenzian warm period (mPWP, ~3.264–3.025 Ma), considered an analogue to near-future equilibrium climate state, confirms that reduced ice caps persisted in mountainous regions during warmer-than-present climate conditions, and refutes eustatic sea-level estimates that imply complete GrIS deglaciation took place at this time. Glacial iceberg-calving margins began to expand on southern Greenland following the end of the mPWP, but Site U1307 IRD deposition was dominated by eastern Greenland sources (primarily Scoresby Sund and the Kangerlussuaq Fjord System) until MIS G6, ~2.72 Ma, when IRD inputs to the site became significantly and persistently elevated. By ~2.4 Ma, I infer that GrIS calving margins had expanded onto the southernmost tip of the landmass, and IRD deposition at Site U1307 was dominated by local southern Greenland sources.

Potential IRD contributions from southwest Greenland to Site U1307 at ~2.4 Ma highlight the need to consider different glacial trajectories during historical times when the GrIS was at its largest extent, and clustering of ice-

rafted feldspars in a distinct but ambiguous region of Pb-isotope space at this time makes a clear case for further Pb-isotope characterisation of key southern Greenland iceberg-calving sources, particularly in the southernmost regions. These findings represent a significant improvement in our knowledge of the spatio-temporal evolution of southern Greenland glaciation during iNHG, and provide a more detailed understanding of how important modern-day iceberg-calving sources have responded to both warmer- and colder-than present climate states in the past.

Chapter 7

Key Findings and Research Outlook

This chapter provides a synthesis of all data chapter findings in context with the original literature review, an assessment of the extent to which the research questions have been answered and research aims met, and suggestions for future work to refine and build on the findings of this research.

The research presented in this thesis aims to improve our understanding of the spatio-temporal maturation of the Greenland Ice Sheet (GrIS) during the latest Pliocene and earliest Pleistocene intensification of Northern Hemisphere glaciation (iNHG; ~3.6 to 2.4 Ma), but also to provide new insight on the potential causal mechanisms behind widespread continental-ice expansion on the Northern Hemisphere landmasses at this time. The findings from this research represent a significant improvement to our knowledge of GrIS evolution and contemporaneous changes in the oceanic realm during iNHG.

To refresh, the stated aims of this research were as follows:

A1: To reconstruct southern Greenland Ice Sheet ice-rafting history and spatial extents over the intensification of Northern Hemisphere glaciation interval, including the mid-Piacenzian warm period (mPWP; ~3.264 to 3.025 Ma);

A2: To measure the presence of internal, actively-eroding Greenland ice in the absence of abundant ice-rafted debris during the mPWP;

A3: To elucidate changes, if any, in deep-ocean circulation over the intensification of Northern Hemisphere glaciation.

The key findings from the work undertaken to address the above aims is summarised below, followed by a short discussion of the wider implications of these findings in context with the literature review in Chapter 2.

(**1**) Due to low abundances of benthic foraminifera at high-latitude North Atlantic sites like IODP Site U1307 on Eirik Drift, it is very challenging to generate independent orbital-resolution benthic oxygen isotope ($\delta^{18}O$) stratigraphies to accurately date the cored material. Improvements to the Site U1307 splice using new high (1 cm)-

resolution magnetic susceptibility data, and the construction of a high-fidelity relative palaeointensity (RPI) estimate using the regression of natural remanent magnetisation with anhysteretic remanent magnetisation (NRM/ARM), have enabled the construction of a near-continuous, orbitally-resolved age model via correlation of the RPI to other globally-distributed RPI records from sites that also benefit from strong benthic $\delta^{18}O$ age-control. This new RPI-based age model for Site U1307 is the first of its kind for high-latitude sediments deposited during iNHG, and enables the timing of variability in all records from the site to be accurately and precisely dated, and correlated with high confidence to changes in global climate. As a result, changes in sedimentation rate at Site U1307 are also resolved at a much greater resolution than was possible shipboard. Future work generating RPI-based age models for other sites in the high-latitude North Atlantic will help to better-constrain the timing of similar variability in their sediments, facilitating higher-fidelity correlations to be made between multiple records spanning iNHG.

(**2**) Minimal coarse ice-rafted debris (IRD) deposition sourced from (south)eastern Greenland during deglacial intervals of the mPWP suggests that iceberg-calving was likely restricted to mountain glaciers at this time, but that these were still active as far south as the Kangerlussuaq Fjord System. X-ray fluorescence (XRF) felsic terrigenous input indicators – K/Ti and the felsic terrigenous principal component – demonstrate that southern Greenland glaciofluvial inputs remained elevated during the mPWP, particularly during interglacials, which indicates significant inland ice persisted on southern Greenland during the coldest intervals of the mPWP, and hence that Greenland was not fully deglaciated during this period of warmth analogous to near-future equilibrium climate. More detailed studies using, for example, cosmogenic radioisotopes ^{10}Be and ^{26}Al of sediment deposited at Greenland-proximal

sites with high enough sedimentation rates through the mPWP, may be able to glean more information about the inland spatial history of the GrIS during this time.

(**3**) Abundances of coarse IRD, with more felsic modal mineralogy and mineral associations, became persistently elevated at Site U1307 from Marine Isotope Stage (MIS) G6, ~2.72 Ma, indicating significant expansion of southern GrIS iceberg-calving margins at this time. This is ~300 kyr later than the onset of significant glacial iceberg-rafting from (north)eastern Greenland, as inferred from the IRD record from Site 907 on the Iceland Plateau. A striking increase in mafic mineralogy prior to MIS G6, at MIS G8, ~2.76 Ma, is taken to reflect this earlier establishment of extensive iceberg-calving margins in eastern Greenland relative to in the south. Both proxies for southern Greenland glaciofluvial input from XRF support an increase in the amount of subglacially-eroded, southern Greenland sourced sediment input to Site U1307 at ~2.72 Ma, coeval with increased iceberg-rafting. A slight reduction in these proxies indicating relatively more mafic inputs prior, at ~2.9 Ma, again may reflect the relatively earlier onset of extensive eastern Greenland glaciation. Lead (Pb)-isotope ratios of individual ice-rafted feldspars, accompanied by determinations of provenance from thin-sections of larger dropstones, demonstrate that the GrIS reached modern-like extents with active iceberg-calving margins on all geochemical terranes by MIS 96, ~2.4 Ma. At this point, the proximal Ketilidian Mobile Belt (KMB) at Greenland's southernmost tip may have been an especially important source of IRD to Eirik Drift, and both Pb-isotope ratios and mineralogy suggest potentially significant contributions from southwest Greenland. This work has highlighted the need to further isotopically characterise potentially important source regions for Greenland IRD, particularly on the KMB, and to consider that trajectories of icebergs calved from southwest

Greenland may have been deflected south to reach the region of Eirik Drift at times of maximum ice-sheet configuration.

(**4**) Despite the significant increase in southern Greenland-sourced IRD delivery to Site U1307 over iNHG, multiple other proxies including magnetic susceptibility, magnetic grain-size, physical grain-size and sedimentation rate strongly indicate that bottom-current sedimentation, controlled by the strength and depth of the deep Western Boundary Undercurrent (WBUC) flowing over Eirik Drift, decreased between ~2.9 and 2.7 Ma. We infer that this represents a slow-down of the WBUC at the depth of Site U1307, potentially linked to a reduction in the volume of overflow waters originating in the Nordic Seas that comprise the WBUC in the region of Eirik Drift. Without a depth and spatial transect of drill sites spanning this time interval across the drift, however, we cannot ascertain whether this change at Site U1307 represents a true slow-down, and hence shoaling, of the WBUC, or a deepening and change of course so that it bypassed the study site. Regardless, this work represents the first direct evidence that deep North Atlantic circulation changed with the expansion of iceberg-calving margins on southern Greenland during iNHG.

(**5**) The sharp decline in foraminifera abundance and XRF marine productivity indicators – Ca/Ti and the marine productivity principal component – in Site U1307 sediments at ~2.72 Ma is used to infer the expansion of sea-ice southward over the site, coeval with the expansion of iceberg-calving margins on southern Greenland. A notably low abundance of IRD deposited at Site U1307 during MIS 98 and 100, thought to be particularly cold glacials due to the magnitude of their defining positive $\delta^{18}O$ excursions, may be explained by a covering of the East Greenland Current by a large amount of pack-ice at this time, which may have restricted the transport of IRD-laden icebergs to Site U1307. Further research using, for example, diatom

assemblages and biomarkers from a transect of sites south of Greenland will provide a more detailed picture of the changing extent of sea-ice in this region, and its potential implications, over iNHG.

Wider Implications

The major findings presented in this thesis have wider implications, particularly for the causes of iNHG as outlined in Chapter 2 and ground-truthing of ice-sheet models:

(**a**) The contemporaneous reduction in bottom-current sedimentation and disappearance of planktic foraminifera with greatly expanded southern Greenland iceberg-calving margins recorded at Site U1307 between ~2.9 and 2.7 Ma indicates a close relationship between climate state, Northern Hemisphere continental ice-sheet volume and the vigour of Atlantic Meridional Overturning Circulation (AMOC) existed during the Plio-Pleistocene (e.g., Thornalley *et al*., 2009; Song *et al*., 2017). The inferred southward expansion of sea-ice over Eirik Drift would have likely thermally isolated the Greenland landmass from the warm northward-flowing North Atlantic Current (e.g., Lawrence *et al*., 2009) and contributed to stratification of the high-latitude North Atlantic (e.g., Clotten et al., 2019), which in turn would have prevented reventilation of CO_2 to the atmosphere and reduced vertical mixing (e.g., Sigman *et al*., 2004, 2010). Weakened overturning in the Nordic Seas is likely to have reduced North Atlantic Deep Water (NADW) formation in the region (e.g., Hunter *et al*., 2007; Bell *et al*., 2015), and the reduction in WBUC-delivered glaciofluvial silt observed at Site U1307 may be a direct result of reduced overflow export via the Greenland-Scotland Ridge. All of these factors may therefore have interacted in a closely-linked positive feedback loop to further sequester CO_2, thermally isolate the Northern Hemisphere landmasses and weaken AMOC via reduced deep-water formation,

enabling the build-up of large and persistent Northern Hemisphere continental ice-sheets under favourable orbital conditions by ~2.6 Ma. Such an implication is supported by the identification of incursions of southern-sourced water into the deep North Atlantic at the expense of NADW from ~2.7 Ma (Lang *et al*., 2016), and may also be consistent with modelled increased Iceland mantle plume activity restricting Nordic Seas overflows at this time (e.g., Parnell-Turner *et al*., 2015).

(**b**) Due to the continued presence of minor amounts of deglacial IRD and indicators for inland glaciofluvial erosion through the mPWP at Site U1307, upper-end estimates for eustatic sea-level rise during this time (~30 m above present; Raymo *et al*., 2018) should be considered unlikely, since it is clear the Greenland Ice Sheet persisted as inland ice-caps and mountain glaciers throughout this period of relative warmth. This, along with a detailed history of the evolution of important modern-day southeast Greenland iceberg-calving sources from Pb-isotope IRD provenance during iNHG, may prove to be extremely valuable information to ice-sheet climate modellers as it provides ground-truthed constraints on likely GrIS behaviour under a range of warmer- and colder-than-present climate states.

Bibliography

Adkins, J.F., 2013. The role of deep ocean circulation in setting glacial climates. *Paleoceanography* **28**, 539–561.

Alley, R.B., Andrews, J.T, Brigham-Grette, J., Clarke, G.K.C., Cuffey, K.M., Fitzpatrick, J.J., Funder, S., Marshall, S.J., Miller, G.H., Mitrovica, J.X., Muhs, D.R., Otto-Bleisner, B.L., Polyak, L., White, J.W.C., 2010. History of the Greenland Ice Sheet: Paleoclimatic insights. *Quaternary Science Reviews* **29 (15–16)**, 1728–1756.

Álvarez, M., Pérez, F.F., Bryden, H., A. F. Ríos, 2004. Physical and biogeochemical transports structure in the North Atlantic subpolar gyre. *Journal of Geophysical Research* **109**, C03027, doi:10.1029/2003JC002015.

Anagnostou, E., John, E.H., Edgar, K.M., Foster, G.L., Ridgwell, A., Inglis, G.N., Pancost, R.D., Lunt, D.J., Pearson, P.N., 2016, Changing atmospheric CO_2 concentration was the primary driver of early Cenozoic climate. *Nature* **533**, 380–384.

Andersen, J., Rollinson, G., Snook, B., Herrington, R. & Fairhurst. R., 2009. Use of QEMSCAN for the characterization of Ni-rich and Ni-poor goethite in laterites. *Minerals Engineering* **22**, 1119–1129.

Andrews, J.T., Keigwin, L., Hall, F., Jennings, A.E., 1999. Abrupt deglaciation events and Holocene palaeoceanography from high-resolution cores, Cartwright Saddle, Labrador Shelf, Canada. *Journal of Quaternary Science* **14 (5)**, 383–397.

Andrews, J. T., 2000. Icebergs and iceberg rafted detritus (IRD) in the North Atlantic: facts and assumptions. *Oceanography* **13**, 100–108.

Andrews, J.T., Jennings, A.E., Coleman, G.C., Eberl, D.D., 2010. Holocene variations in mineral and grain-size composition along the East Greenland glaciated margin (ca 67–70°N): Local versus long-distance sediment transport. *Quaternary Science Reviews* **29**, 2619–2632.

Andrews, J.T., Bigg, G.R., Wilton, D.J., 2014a. Holocene ice-rafting and sediment transport from the glaciated margin of East Greenland (67–70°N) to the N Iceland shelves: detecting and modelling changing sediment sources. *Quaternary Science Reviews* **91**, 204–217.

Andrews, J.T., Bigg, G.R., Wilton, D.J., 2014b. Holocene sediment transport from the glaciated margin of East/Northeast Greenland (67-80°N) to the N Iceland shelves: Detecting and modeling changing sediment sources. *Quaternary Science Reviews* **91**, 204–217.

Applegate, P.J., Kirchner, N., Stone, E.J., Keller, K., Greve, R., 2012. An assessment of key model parametric uncertainties in projections of Greenland Ice Sheet behaviour. *The Cryosphere* **6**, 589–606.

Bachem, P.E., Risebrobakken, B., De Schepper, S., McClymont, E.L., 2017. Highly variable Pliocene sea surface conditions in the Norwegian Sea. *Climate of the Past* **13**, 1153–1168.

Badger, M.P.S., Lear, C.H., Pancost, R.D., Foster, G.L., Bailey, T.R., Leng, M.J., Abels, H.A., 2013. CO_2 drawdown following the middle Miocene expansion of the Antarctic Ice Sheet. *Paleoceanography* **28**, 42–53.

Bailey, I., Bolton, C.T., DeConto, R.M., Pollard, D., Schiebel, R., Wilson, P.A., 2010. A low threshold for North Atlantic ice rafting from 'low-slung and slippery' late Pliocene ice sheets. *Paleoceanography* **25**, PA1212, doi:10.1029/2009PA001736.

Bailey, I., Liu, Q., Swann, G.E.A., Jiang, Z., Sun, Y., Zhao, X., Roberts, A.P., 2011. Iron fertilisation and biogeochemical cycles in the sub-Arctic northwest Pacific during the late Pliocene intensification of northern hemisphere glaciation. *Earth and Planetary Science Letters* **307 (3–4)**, 253–265.

Bailey, I., Foster, G.L., Wilson, P.A., Jovane, L., Storey, C.D., Trueman, C.N., Becker, J., 2012. Flux and provenance of ice-rafted debris in the earliest Pleistocene sub-polar North Atlantic Ocean comparable to the last glacial maximum. *Earth and Planetary Science Letters* **341–344**, 222–233.

Bailey, I., Hole, G.M., Foster, G.L., Wilson, P.A., Storey, C.D., Trueman, C.N., Raymo, M.E., 2013. An alternative suggestion for the onset of major northern hemisphere glaciation based on the geochemical provenance of North Atlantic Ocean ice-rafted debris. *Quaternary Science Reviews* **75**, 181–194.

Baker, J., Peate, D., Waight, T., Meyzen, C., 2004. Pb isotopic analysis of standards and samples using a ^{207}Pb–^{204}Pb double spike and thallium to correct for mass bias with a double-focusing MC-ICP-MS. *Chemical Geology* **211 (3–4)**, 275–303.

Balco, G., Rovey, C.W., 2010. Absolute chronology for major Pleistocene advances of the Laurentide Ice Sheet. *Geology* **38 (9)**, 795–798.

Balsam, W.L., McCoy, F.W., 1987. Atlantic sediments: Glacial/interglacial comparisons. *Paleoceanography* **2**, 531–542.

Banerjee, S., King, J.W., Marvin, J., 1981. A rapid method for magnetic granulometry with applications to environmental studies. *Geophysical Research Letters* **8 (4)**, 333–336.

Bard, E., Rickaby, R.E.M., 2009. Migration of the subtropical front as a modulator of glacial climate. *Nature* **460**, 380–383.

Barnola, J.M., Raynaud, D., Korotkevich, Y.S., Lorius, C., 1987. Vostok ice core provides 160,000-year record of atmospheric CO_2. *Nature* **329**, 408–414.

Barreiro, M., Philander, G., Pacanowski, R., Fedorov, A., 2006. Simulations of warm tropical conditions with application to middle Pliocene atmospheres. *Climate Dynamics* **26**, 349–365.

Bart, P.J., 2003. Were West Antarctic Ice Sheet grounding events in the Ross Sea a consequence of East Antarctic Ice Sheet expansion during the middle Miocene? *Earth and Planetary Science Letters* **216**, 93–107.

Bartoli, G., Sarnthein, M., Weinelt, M., Erlenkeuser, H., Garbe-Schönberg, D. and Lea, D.W., 2005. Final closure of Panama and the onset of northern hemisphere glaciation. *Earth and Planetary Science Letters* **237**, 33–44.

Bartoli, G., Hönisch, B., Zeebe, R.E., 2011. Atmospheric CO_2 decline during the Pliocene intensification of Northern Hemisphere glaciations. *Paleoceanography* **26**, PA4213.

Bashirova, L.D., Kandiano, E.S., Sivkov, V.V., Bauch, H.A., 2014. Migrations of the North Atlantic Polar front during the last 300 ka: Evidence from planktic foraminiferal data. *Oceanology* **54 (6)**, 798–807.

Beerling, D.J., Royer, D.L., 2011. Convergent Cenozoic CO_2 history. *Nature Geoscience* **4**, 418–420.

Bell, D.B., Jung, S.J.A., Kroon, D., 2015. The Plio-Pleistocene development of Atlantic deep-water circulation and its influence on climate trends. *Quaternary Science Reviews* **123**, 265–282.

Bennike, O., Björck, S., 2002. Chronology of the last recession of the Greenland Ice Sheet. *Journal of Quaternary Science* **17 (3)**, 211–219.

Bevis, M., Harig, C., Khan, S.A., Brown, A., Simons, F.J., Willis, M., Fettweis, X., van den Broeke, M.R., Madsen, F.B., Kendrick, E., Caccamise II, D.J., van Dam, T., Knudsen, P., Nylen, T., 2019. Accelerating changes in ice mass within Greenland, and the ice sheet's sensitivity to atmospheric forcing. *PNAS* **116 (6)**, 1934–1939.

Bigg, G., Wadley, W.R., Stevens, D.P., Johnson, J.A., 1996. Prediction of iceberg trajectories for the North Atlantic and Arctic oceans. *Geophysical Research Letters* **23**, 3587–3590.

Bigg, G., Wadley, M., Stevens, D., Johnson, J., 1998. Simulations of two last glacial maximum ocean states. *Paleoceanography and Paleoclimatology* **13(4)**, 340–351.

Bierman, P.R., Shakun, J.D., Corbett, L.B., Zimmerman, S.R., Rood, D.H., 2016. A persistent and dynamic East Greenland Ice Sheet over the past 7.5 million years. *Nature* **540**, 256–260.

Billups, K., Ravelo, A.C., Zachos, J.C., 1997. Early Pliocene deep-water circulation: stable isotope evidence for enhanced northern component deep water. In: Shackleton, N.J., Curry, W.B., Richter, C., Bralower, T.J. (eds.), *Proceedings of the Ocean Drilling Program, Scientific Results* **154**, 319–330.

Bilodeau, G., Hillaire-Marcel, C., de Vernal, A., Stoner, J., 1998. Changes in vertical structure of Labrador Sea water masses during the last 25 ka based on oxygen isotopes in planktic and benthic foraminifera. *Geoscience Canada* **23** (Supplement: Quebec 1998 Abstract), 18–19.

Bindoff, N.L., Stott, P.A., AchutaRao, K.M., Allen, M.R., Gillett, N., Gutzler, D., Hansingo, K., Hegerl, G., Hu, Y., Jain, S., Mokhov, I.I., Overland, J., Perlwitz, J., Sebbari, R., Zhang, X., 2013. Detection and Attribution of Climate Change: from Global to Regional. In: Stocker, T.F., Qin, D., Plattner, G.-K., Tignor, M., Allen, S.K., Boschung, J., Nauels, A., Y. Xia, Y., Bex, V., Midgley, P.M. (eds.): *Climate Change 2013: The Physical Science Basis. Contribution of Working Group I to the Fifth Assessment Report of the Intergovernmental Panel on Climate Change.* Cambridge University Press, Cambridge, United Kingdom and New York, NY, USA.

Birchfield, G.E. and Wertman, J., 1983. Topography, albedo-temperature feedback, and climate sensitivity. *Science* **219**, 284–285.

Birkenmajer, K., 1988. Tertiary glacial and interglacial deposits, South Shetland Islands, Antarctica: Geochronology versus biostratigraphy (a progress report). *Bulletin of the Polish Academy of Earth Sciences* **36**, 133–145.

Bjørk, A.A., Kjær, K.H., Korsgaard, N.J., Khan, S.A., Kjeldsen, K.K., Andresen, C.S., Box, J.E., Larsen, N.K., Funder, S., 2012. An aerial view of 80 years of climate-related glacier fluctuations in southeast Greenland. *Nature Geoscience* **5**, 427–432.

Blake-Mizen, K., Hatfield, R.G., Stoner, J.S., Carlson, A.E., Xuan, C., Walczak, M., Lawrence, K.T., Channell, J.E.T., Bailey, I., 2019. Southern Greenland glaciation and Western Boundary Undercurrent evolution recorded on Eirik Drift during the late Pliocene intensification of Northern Hemisphere glaciation. *Quaternary Science Reviews* **209**, 40–51.

Bloemendal, J., King, J.W., Hall, F.R., Doh, S.-J., 1992. Rock magnetism of Late Neogene and Pleistocene deep-sea sediments: Relationship to sediment source, diagenetic processes, and sediment lithology. *Journal of Geophysical Research* **97 (B4)**, 4361–4375.

Böhm, E., Lippold, J., Gutjahr, M., Frank, M., Blaser, P., Antz, B., Fohlmeister, J., Frank, N., Andersen, M.B., Deininger, M., 2015. Strong and deep Atlantic meridional overturning circulation during the last glacial cycle. *Nature* **517**, 73–76.

Bohrmann, G., Henrich, R., Thiede, J., 1990. Miocene to Quaternary Paleoceanography in the Northern North Atlantic: Variability in Carbonate and Biogenic Opal Accumulation. In: Bleil, U., Thiede, J. (eds.), *Geological History of the Polar oceans: Arctic Versus Antarctic.* NATO ASI Series (Series C: Mathematical and Physical Sciences) **308**. Springer, Dordrecht, 647–675.

Bolton, C.T., Wilson, P.A., Bailey, I., Friedrich, O., Beer, C.J., Becker, J., Baranwal, S., Schiebel, R., 2010. Millennial-scale climate variability in the subpolar North Atlantic Ocean during the late Pliocene. *Paleoceanography* **25**, PA4218.

Bolton, C.T., Lawrence, K.T., Gibbs, S.J., Wilson, P.A., Herbert, T.D., 2011. Biotic and geochemical evidence for a global latitudinal shift in ocean biogeochemistry and export productivity during the late Pliocene. *Earth and Planetary Science Letters* **308 (1–2)**, 200–210.

Bond, G., Heinrich, H., Broecker, W., Labeyrie, L., McManus, J., Andrews, J., Huon, S., Janschik, R., Clasen, S., Simet, C., Tedesco, K., Klas, M., Bonani, G., Ivy, S., 1992. Evidence for massive discharges of icebergs into the North Atlantic ocean during the last glacial period. *Nature* **360**, 245–249.

Bond, G., Broecker, W., Johnsen, S., McManus, J., Labeyrie, L., Jouzel, J., Bonani, G., 1993. Correlations between climate records from North Atlantic sediments and Greenland ice. *Nature* **365**, 143–147.

Box, J.E., Fettweis, X., Stroeve, J.C., Tedesco, M., Hall, D.K., Steffen, K., 2012. Greenland ice sheet albedo feedback: thermodynamics and atmospheric drivers. *The Cryosphere* **6**, 821–839.

Brierley, C. M., Fedorov, A. V., Zhonghui L., Herbert, T. D., Lawrence, K. T., LaRiviere, J. P., 2009. Greatly expanded tropical warm pool and weakened Hadley Circulation in the early Pliocene. *Science* **323**, 1714–1718.

Brierley, C.M., Fedorov, A.V., 2010. Relative importance of meridional and zonal sea surface temperature gradients for the onset of the ice ages and Pliocene-Pleistocene climate evolution. *Paleoceanography* **25**, PA2214.

Brigham-Grette, J., Melles, M., Minyuk, P., Andreev, A., Tarasov, P., DeConto, R., Koenig, S., Nowaczyk, N., Wennrich, V., Rosén, P., Haltia, E., Cook, T., Gebhardt, C., Meyer-Jacob, C., Snyder, J., Herzschuh, U., 2013. Pliocene warmth, polar amplification, and stepped Pleistocene cooling recorded in NE Arctic Russia. *Science* **340**, 1421–1427.

Broecker, W.S., 1982. Ocean chemistry during glacial time. *Geochimica et Cosmochimica Acta* **46 (10)**, 1689–1705.

Burke, K.D., Williams, J.W., Chandler, M.A., Haywood, A.M., Lunt, D.J., Otto-Bleisner, B.L., 2018. Pliocene and Eocene provide best analogs for near-future climates. *PNAS* **115 (52)**, 13288–13293.

Camm, G.S., Glass, H.J., Bryce, D.W., Butcher, A.R., 2004. Characterisation of a mining-related arsenic-contaminated site, Cornwall, UK. *Journal of Geochemical Exploration* **82 (1–3)**, 1–15.

Cane, M.A., 1998. A role for the tropical Pacific. *Science* **282**, 59–61.

Cane, M.A., Molnar, P., 2001. Closing of the Indonesian seaway as a precursor to east African aridification around 3–4 million years ago. *Nature* **411**, 157–162.

Cao, W., Gilotti, J.A., Massonne, H.-J., Ferrando, S., Foster, C.T. Jr., 2018. Partial melting due to breakdown of an epidote-group mineral during exhumation of ultrahigh-pressure eclogite: An example from the North-East Greenland Caledonides. Journal of Metamorphic Geology 37 (1), 15–39.

Carlson, A.E., Stoner, J.S., Donnelly, J.P., Hillaire-Marcel, C., 2008. Response of the southern Greenland Ice Sheet during the last two deglaciations. *Geology* **36(5)**, 359–362.

Carlson, A. E., Winsor, K., Ullman, D.J., Brook, E.J., Rood, D.H., Axford, Y., LeGrande, A.N., Anslow, F.S., Sinclair, G., 2014. Earliest Holocene south Greenland ice sheet retreat within its late Holocene extent. *Geophysical Research Letters*, **41(15)**, 5514–5521.

Carter, A., Riley, T.R., Hillenbrand C.D., Rittner M., 2017. Widespread Antarctic glaciation during the Late Eocene. *Earth and Planetary Science Letters* **458**, 49–57.

Cerling, T.E., Harris, J.M., MacFadden, B.J., Leakey, M.G., Quade, J., Eisenmann, V., Ehleringer, 1997. Global vegetation change through the Miocene/Pliocene boundary. *Nature* **389**, 153–158.

Channell, J.E.T., Mazaud, A., Sullivan, P., Turner, S., Raymo, M.E., 2002. Geomagnetic excursions and paleointensities in the 0.9–2.15 Ma interval of the Matuyama chron at ODP Site 983 and 984 (Iceland Basin). *Journal of Geophysical Research*, doi:10.1029/2001JB000491.

Channell, J. E. T., Guyodo, Y., 2004. The Matuyama Chronozone at ODP Site 982 (Rockall Bank): Evidence for Decimeter-Scale Magnetisation Lock-In Depths. In: Channell, J.E.T., Kent, J.V., Lowrie, W. and Meert, J.G. (eds.), *Timescales of the Paleomagnetic Field.* American Geophysical Union, Washington, D. C. doi:10.1029/145GM15.

Channell, J., Wright, J., Mazaud, A., Stoner, J., 2014. Age through tandem correlation of Quaternary relative paleointensity (RPI) and oxygen isotope data at IODP Site U1306 (Eirik Drift, SW Greenland). *Quaternary Science Reviews* **88**, 135–146.

Channell, J., Hodell, D., Curtis, J., 2016. Relative paleointensity (RPI) and oxygen isotope stratigraphy at IODP Site U1308: North Atlantic RPI stack for 1.2–2.2 Ma

(NARPI-2200) and age of the Olduvai Subchron. *Quaternary Science Reviews* **131**, 1–19.

Chen et al., 2016, G^3

Chen, X., Zhang, X., Church, J.A., Watson, C.S., King, M.A., Monselesan, D., Legresy, B., Harig, C., 2017. The increasing rate of global mean sea-level rise during 1993–2014. *Nature Climate Change* **7**, 492–495.

Chiang, J.C.H., Bitz, C.M., 2005. Influence of high latitude ice cover on the marine Intertropical Convergence Zone. *Climate Dynamics* **25 (5)**, 477–496.

Clark, R.A., 1984. Transport through the Cape Farewell Flemish Cap section. *ICES Report* **185**, 120–130.

Clark, P.U., Alley, R.B., Pollard, D., 1999. Northern Hemisphere ice-sheet influences on global climate change. *Science* **286**, 1104–1111.

Clemens, S.C., Murray, D.W., Prell, W.L., 1996. Nonstationary phase of the Plio-Pleistocene Asian monsoon. *Science* **274**, 943–948.

Clementz, M., Bajpai, S., Ravikant, V., Thewissen, J.G.M., Saravanan, N., Singh, I.B., Prasad, V., 2011. Early Eocene warming events and the timing of terrestrial faunal exchange between India and Asia. *Geology* **39**, 15–19.

Clotten, C., Stein, R., Fahl, K., Schreck, M., Risebrobakken, B., De Schepper, S., 2019. On the causes of Arctic sea ice in the warm Early Pliocene. *Scientific Reports* **9**, 989.

Colville, E.J., Carlson, A.E., Beard, B.L., Hatfield, R.G., Stoner, J.S., Reyes, A.V., Ullman, D.J., 2011. Sr-Nd-Pb isotope evidence for ice-sheet presence on southern Greenland during the Last Interglacial. *Science* **333**, 620–623.

Connelly, J.N., Thrane, K., 2005. Rapid determination of Pb isotopes to define Precambrian allochthonous domains: An example from West Greenland. *Geology* **33 (12)**, 953–956.

Contoux, C., Ramstein, G., Jost, A., 2012. Modelling the mid-Pliocene Warm Period climate with the IPSL coupled model and its atmospheric component LMDZ5A. *Geoscientific Model Development* **5**, 903–917.

Cooper A.K., O'Brien, P.E., 2004. Leg 188 synthesis: Transitions in the glacial history of the Prydz Bay region, East Antarctica, from ODP drilling. In: Cooper, A.K., *et al*. (eds.). *Proceedings of the Ocean Drilling Program, Scientific results* **188**, 1–42. College Station, Texas, Ocean Drilling Program.

Coxall, H.K., Wilson, P.A., Pälike, H., Lear, C.H., Backman, J., 2005. Rapid stepwise onset of Antarctic glaciation and deeper calcite compensation in the Pacific Ocean. *Nature* **433**, 53–57.

Coxall, H.K., Huck, C.E., Huber, M., Lear, C.H., Legarda-Lisarri, A., O'Regan, M., Sliwinska, K.K., van de Flierdt, T., de Boer, A.M., Zachos, J.C., Backman, J.,

2018. Export of nutrient rich Northern Component Water preceded early Oligocene Antarctic glaciation. *Nature Geoscience* **11**, 190–196.

Croudace, I.W., Rothwell, R.G., 2015. *Micro-XRF Studies of Sediment Cores.* Springer.

Crundwell, M., Scott, G., Naish,T., Carter, L., 2008. Glacial–interglacial ocean climate variability from planktonic foraminifera during the Mid-Pleistocene transition in the temperate Southwest Pacific, ODP Site 1123. *Palaeogeography, Palaeoclimatology, Palaeoecology* **260 (1–2)**, 202–229.

Cuffey, K.M., Marshall, S.J., 2000. Substantial contribution to sea-level rise during the last interglacial from the Greenland ice sheet. *Nature* **404**, 591–594.

Dalziel, I.W.D., Lawver, L.A., Pearce, J.A., Barker, P.F., Hastie, A.R., Barfod, D.N., Schenke, H.-W., Davis, M.B., 2013. A potential barrier to deep Antarctic circumpolar flow until the late Miocene? *Geology* **41 (9)**, 947–950.

Dansgaard, W., Johnsen, S.J., Clausen, H.B., Dahl-Jensen, D., Gundestrup, N.S., Hammer, C.U., Hvidberg, C.S., Steffensen, J.P., Sveinbjörnsdottir, A.E., Jouzel, J., Bond, G., 1993. Evidence for general instability of past climate from a 250-kyr ice-core record. *Nature* **364**, 218–220.

Darby, D.A., 2003. Sources of sediment found in sea ice from the western Arctic Ocean, new insights into processes of entrainment and drift patterns. *Journal of Geophysical Research: Oceans* **108 (C8)**, doi: 10.1029/2002JC001350.

Davini, P., von Hardenberg, J., Corti, S., 2015. Tropical origin for the impacts of the Atlantic Multidecadal Variability on the Euro-Atlantic climate. *Environmental Research Letters* **10 (9)**, doi:10.1088/1748-9326/10/9/094010.

Day, R., Fuller, M., Schmidt, V.A., 1977. Hysteresis properties of titanomagnetites: Grain-size and compositional dependence. *Physics of the Earth and Planetary Interiors* **13 (4)**, 260–267.

DeConto, R.M., Pollard, D., 2003a. Rapid Cenozoic glaciation of Antarctica induced by declining atmospheric CO_2. *Nature* **421**, 245–249.

DeConto, R.M., Pollard, D., 2003b. A coupled climate–ice sheet modeling approach to the Early Cenozoic history of the Antarctic ice sheet. *Palaeogeography, Palaeoclimatology, Palaeoecology* **198 (1–2)**, 39–52.

DeConto, R., Pollard, D., Harwood, D., 2007. Sea ice feedback and Cenozoic evolution of Antarctic climate and ice sheets. *Paleoceanography* **22 (3)**, PA3214, doi:10.1029/2006PA001350.

DeConto, R.M., Pollard, D., Wilson, P.A., Palike, H., Lear, C.H. and Pagani, M., 2008. Thresholds for Cenozoic bipolar glaciation. *Nature* **455**, 652–656.

De Schepper, S., Head, M.J., Groeneveld, J., 2009. North Atlantic Current variability through marine isotope stage M2 (circa 3.3 Ma) during the mid-Pliocene. *Paleoceanography* **24**, PA4206, doi:10.1029/2008PA001725.

De Schepper, S., Groeneveld, J., Naafs, B.D.A., Van Renterghem, C., Hennissen, J., Head, M.J., Louwye, S. and Fabian, K., 2013. Northern Hemisphere Glaciation during the Globally Warm Early Late Pliocene. *PloS ONE* **8 (12)**, e81508.

De Schepper, S., Schreck, M., Beck, K.M., Matthiessen, J., Fahl, K., Mangerud, G., 2015. Early Pliocene onset of modern Nordic Seas circulation related to ocean gateway changes. *Nature Communications* **6**, doi:10.1038/ncomms9659.

de Vernal, A., Hillaire-Marcel, C., 2000. Sea-ice cover, sea-surface salinity and halo-/thermocline structure of the northwest North Atlantic: modern versus full glacial conditions. *Quaternary Science Reviews* **19 (1–5)**, 65–85.

de Vernal, A., Hillaire-Marcel, C., 2008. Natural variability of Greenland climate, vegetation, and ice volume during the past million years. *Science* **320**, 1622–1625.

Dickson, R.R., Meincke, J., Malmberg, S.-A., Lee, A.J., 1988. The "Great Salinity Anomaly" in the Northern North Atlantic 1968-1982. *Progress in Oceanography* **20**, 103–151.

Dickson, R.R., Brown, J., 1994. The production of North Atlantic Deep Water: sources rates and pathways. *Journal of Geophysical Research* **99 (C6)**, 12319–12341.

Dickson, A.J., Leng, M.J., Maslin, M.A., Röhl, U., 2010. Oceanic, atmospheric and ice-sheet forcing of South East Atlantic Ocean productivity and South African monsoon intensity during MIS-12 to 10. *Quaternary Science Reviews* **29**, 3936–3947.

Ding, Z.L., Derbyshire, E., Yang, S.L., Yu, Z.W., Xiong, S.F., Liu, T.S., 2002. Stacked 2.6-Ma grain size record from the Chinese loess based on five sections and correlation with the deep-sea $\delta^{18}O$ record. *Paleoceanography* **17 (3)**, doi:10.1029/2001PA000725.

Dolan, A.M., Haywood, A.M., Hill, D.J., Dowsett, H.J., Hunter, S.J., Lunt, D.J., Pickering, S.J., 2011. Sensitivity of Pliocene ice sheets to orbital forcing. *Palaeogeography, Palaeoclimatology, Palaeoecology* **309**, 98–110.

Dolan, A.M., Hunter, S.J., Hill, D.J., Haywood, A.M., Koenig, S.J., Otto-Bleisner, B.L., Abe-Ouchi, A., Bragg, F., Chan, W.-L., Chandler, M.A., Contoux, C., Jost, A., Kamae, Y., Lohmann, G., Lunt, D.J., Ramstein, G., Rosenbloom, N.A., Sohl, L., Stepanek, C., Ueda, H., Yan, Q., Zhang, Z., 2015. Using results from the PlioMIP ensemble to investigate the Greenland Ice Sheet during the mid-Pliocene Warm Period. *Climate of the Past* **11**, 403–424.

Dowdeswell, J.A., 1986. The distribution and character of sediments in a tidewater glacier, southern Baffin Island, NWT, Canada. *Arctic and Alpine Research* **18 (1)**, 45–56.

Dowdeswell, J.A., Villinger, H., Whittington, R.J., Marienfeld, P., 1993. Iceberg scouring in Scoresby Sund and on the East Greenland continental shelf. *Marine Geology* **111**, 37–53.

Dowdeswell, J.A., Maslin, M.A., Andrews, J.T., McCave, I.N., 1995. Iceberg production, debris rafting, and the extent and thickness of Heinrich layers (H-1, H-2) in North Atlantic sediments. *Geology* **23 (4)**, 301–304.

Dowsett, H.J., Cronin, T.M., Poore, R.Z., Thompson, R.S., Whatley, R.C., Wood, A.M., 1992. Micropaleontological evidence for increased meridional heat transport in the North Atlantic Ocean during the Pliocene. *Science* **258**, 1133–1135.

Dowsett, H., Robinson, M., Haywood, A.M., Salzmann, U., Hill, D., Sohl, L.E., Chandler, M., Williams, M., Foley, K., Stoll, D.K., 2010. The PRISM3D paleoenvironmental reconstruction. *Stratigraphy* **7(2–3)**, 123–139.

Driscoll, N.W., Haug, G.H., 1998. A short circuit in thermohaline circulation: A cause for Northern Hemisphere glaciation? *Science* **282**, 436–438.

Dunlop, D. J., and Özdemir, Ö., 1997. *Rock Magnetism, Fundamentals and Frontiers.* Cambridge University Press, Cambridge, U. K.. doi: 10.1017/CBO9780511612794.

Dwyer, G.S., Cronin, T.M., Baker, P.A., Raymo, M.E., Buzas, J.S., Corrège, T., 1995. North Atlantic deepwater temperature change during Late Pliocene and Late Quaternary climatic cycles. *Science* **270**, 1347–1351.

Eldevik, T., Nilsen, J.E.Ø., Iovino, D., Olsson, K.A., Sandø, A.B., Drange, H., 2009. Observed sources and variability of Nordic seas overflow. *Nature Geoscience* **2**, 406–410.

Eldrett, J.S., Harding, I.C., Wilson, P.A., Butler, E. and Roberts, A.P., 2007. Continental ice in Greenland during the Eocene and Oligocene. *Nature* **446**, 176–179.

Escher, A., Watt, W.S., 1976. *Geology of Greenland.* The Geological Survey of Greenland, Denmark.

Etourneau, J., Schneider, R., Blanz, T., Martinez, P., 2010. Intensification of the Walker and Hadley atmospheric circulations during the Pliocene–Pleistocene climate transition. *Earth and Planetary Science Letters* **297 (1–2)**, 103–110.

Evans, H. F., Channell, J. E. T., Stoner, J. S., Hillaire-Marcel, C., Wright, J. D., Neitzke, L. C., Mountain, G. S., 2007. Paleointensity-assisted chronostratigraphy of detrital layers on the Eirik Drift (North Atlantic) since marine isotope stage 11. *Geochemistry Geophysics Geosystems* **8 (11)**, doi:10.1029/2007GC001720

Expedition 303 Scientists, 2006a. Site U1307. In: Channell, J.E.T., Kanamatsu, T., Sato, T., Stein, R., Alvarez Zarikian, C.A., Malone, M.J., and the Expedition 303/306 Scientists. *Proceedings of the IODP, 303/306*: College Station TX

(Integrated Ocean Drilling Program Management International, Inc.). doi:10.2204/iodp.proc.303306.107.2006

Expedition 303 Scientists, 2006b. Site U1308. In: Channell, J.E.T., Kanamatsu, T., Sato, T., Stein, R., Alvarez Zarikian, C.A., Malone, M.J., and the Expedition 303/306 Scientists. *Proceedings of the IODP, 303/306*: College Station TX (Integrated Ocean Drilling Program Management International, Inc.). doi:10.2204/iodp.proc.303306.107.2006

Fedorov, A.V., Dekens, P.S., McCarthy, M., Ravelo, A.C., deMenocal, P.B., Barreiro, M., Pacanowski, R.C., Philander, S.G., 2006. The Pliocene paradox (mechanisms for a permanent El Niño). *Science* **312 5779)**, 1485–1489.

Fedorov, A.V., Brierley, C.M., Emanuel, K., 2010. Tropical cyclones and permanent El Niño in the early Pliocene epoch. *Nature* **463**, 1066–1070.

Fedorov, A.V., Brierley, C.M., Lawrence, K.T., Liu, Z., Dekens, P.S., Ravelo, A.C., 2013. Patterns and mechanisms of early Pliocene warmth. *Nature* **496**, 43–49.

Finkelshtein, A., Brjansky, N., 2009. Estimating particle size effects in X-ray fluorescence spectrometry. *Nuclear Instruments and Methods in Physics Research Section B: Beam Interactions with Materials and Atoms* **267 (14)**, 2437–2439

Finkenbinder, M.S., Abbott, M.B., Finney, B.P., Stoner, J.S., Dorfman, J.M., 2015. A multi-proxy reconstruction of environmental change spanning the last 37,000 years from Burial Lake, Arctic Alaska. *Quaternary Science Reviews* **126**, 227–241.

Flatau, M.K., Talley, L., Niiler, P.P., 2003. The North Atlantic oscillation, surface current velocities, and SST changes in the subpolar North Atlantic. *Journal of Climate* **16**, 2355–2369.

Flower, B.P., Kennett, J.P., 1995. Middle Miocene deepwater paleoceanography in the southwest Pacific: Relations with East Antarctic Ice Sheet development. Paleoceanography 10(6), 1095–1112.

Flower, B.P., Oppo, D.W., McManus, J.F., Venz, K.A., Hodell, D.A., Cullen, J.L., 2010. North Atlantic Intermediate to Deep Water circulation and chemical stratification during the past 1 Myr. *Paleoceanography* **15 (4)**, doi: 10.1029/1999PA000430

Foster, G.L., Lunt, D.J., Parrish, R.R., 2010. Mountain uplift and the glaciation of North America – a sensitivity study. *Climate of the Past* **6**, 707–717.

Foster, G.L., Royer, D.L., Lunt, D.J., 2017. Future climate forcing potentially without precedent in the last 420 million years. *Nature Communications* **8**, 14845, doi:10.1038/ncomms14845.

Friedrich, O., Wilson, P.A., Bolton, C.T., Beer, C.J., Schiebel, R., 2013. Late Pliocene to early Pleistocene changes in the North Atlantic Current and suborbital-scale sea-surface temperature variability. *Paleoceanography* **28 (2)**, 274–282.

Fronval, T. and Jansen, E., 1996. Late Neogene paleoclimates and paleoceanography in the Iceland–Norwegian Sea: evidence from the Iceland and Voring Plateaus. In: Thiede, J., Myhre, A. M., Firth, J., V., Johnson, G. L. and Ruddiman, E. F. (eds.): *Proceedings of the Ocean Drilling Program, Scientific Results* **151**, 455–468. Ocean Drilling Program, College Station, TX.

Funder, S., Hjort, C., Landvik, J.Y., Nam, S.-I., Reeh, N., Stein, R., 1998. History of a stable ice margin—East Greenland during the Middle and Upper Pleistocene. *Quaternary Science Reviews* **17 (13)**, 77–123.

Funder, S., Bennike, O., Bocher, J., Israelson, C., Petersen, K.S., Simonarson, L.A., 2001. Late Pliocene Greenland - The Kap Kobenhavn Formation in North Greenland. *Bulletin of the Geological Society of Denmark* **48**, 117–134.

Fyke, J. G., Weaver, A. J., Pollard, D., Eby, M., Carter, L., Mackintosh, A., 2011. A new coupled ice sheet/climate model: description and sensitivity to model physics under Eemian, Last Glacial Maximum, late Holocene and modern climate conditions. *Geoscientific Model Development* **4**, 117–136.

Garzione, C.N., 2008. Surface uplift of Tibet and Cenozoic global cooling. *Geology* **36 (12)**, 1003–1004.

Gilotti, J.A., 1993. Discovery of a medium-temperature eclogite province in the Caledonides of North-East Greenland. *Geology* **21**, 523–526.

Gilotti, J.A., Ravna, E.J.K., 2002. First evidence for ultrahigh-pressure metamorphism in the North- East Greenland Caledonides. *Geology* **30 (6)**, 551–554.

Gilotti, J.A., Jones, K.A., Elvevold, S., 2008. Caledonian metamorphic patterns in Greenland. In: Higgins, A.K., Gilotti, J.A., Smith, M.P. (eds.). *The Greenland Caledonides: Evolution of the Northeast Margin of Laurentia.* Geological Society of America Memoir **202**, 201–225.

Giraudeau, J., Grelaud, M., Solignac, S., Andrews, J.T., Moros, M., Jansen, E., 2010. Millennial-scale variability in Atlantic water advection to the Nordic Seas derived from Holocene coccolith concentration records. *Quaternary Science Reviews* **29 (9–10)**, 1276–1287.

Gogorza, C.S.G., Irurzun, M.A., Chaparro, M.A.E., Lirio, J.M., Nunez, H., Bercoff, P.G., Sinito, A.M., 2006. Relative paleointensity of the geomagnetic field over the last 21,000 years BP from sediment cores, Lake El Trébol (Patagonia, Argentina). Earth Planets Space 58 (10), 1323–1332.**Gottleib**, P., Wilkie, G., Sutherland, D., Ho-tun, E., Suthers, S., Perera, K., Jenkins, B., Spencer, S., Butcher, A., Rayner,

J., 2000. Using Quantitative Electron Microscopy for Process Mineralogy Applications. *JOM* **52 (4)**, 24–25.

Grant, K.M., Rohling, E.J., Bar-Matthews, M., Ayalon, A., Medina-Elizalde, M., Ramsey, B., Satow, C., Roberts, A.P., 2012. Rapid coupling between ice volume and polar temperature over the past 150,000 years. *Nature* **491**, 744–747.

Greenop, R., Foster, G.L., Wilson, P.A., Lear, C.H., 2014. Middle Miocene climate instability associated with high-amplitude CO_2 variability. *Paleoceanography* **29 (9)**, 845–853.

Grobe, H., 1987. A simple method for the determination of ice-rafted debris in sediment cores. *Polarforschung* **57(3)**, 123–126.

Groeneveld, J., Hathorne, E.C., Steinke, S., DeBey, H., Mackensen, A., Tiedemann, R., 2014. Glacial induced closure of the Panamanian Gateway during Marine Isotope Stages (MIS) 95–100 (~2.5Ma). *Earth and Planetary Science Letters* **404**, 296–306.

Grützner, J., Higgins, S.M., 2010. Threshold behavior of millennial scale variability in deep water hydrography inferred from a 1.1 Ma long record of sediment provenance at the southern Gardar Drift. *Paleoceanography and Paleoclimatology* **25 (4)**, doi:10.1029/2009PA001873.

Gu, Y., 2003. Automated Scanning Electron Microscopy Based Mineral Liberation Analysis. An Introduction to JKMRC/FEI Mineral Liberation Analyser. *Journal of Minerals & Materials Characterization & Engineering* **2 (1)**, 33–41.

Gwiazda, R.H., Hemming, S.R., Broecker, W.S., 1996. Tracking the sources of icebergs with lead isotopes: The provenance of ice-rafted debris in Heinrich layer 2. *Paleoceanography* **11 (1)**, 77–93.

Hanna, E., Cappelen, J., Fettweis, X., Huybrechts, P., Luckman, A., Ribergaard, M.H., 2009. Hydrologic response of the Greenland ice sheet: the role of oceanographic warming. *Hydrological Processes* **23 (1)**, 7–30.

Hansen, B.T., Friderichsen, J.D., 1989. The influence of recent lead loss on the interpretation of disturbed U-Pb systems in zircons from igneous rocks in East Greenland. *Lithos* **23 (3)**, 209–223.

Haq, B., Hardenbol, U., Vail, P. R., 1988. Mesozoic and Cenozoic chronostratigraphy and cycles of sea-level change. *Society of Economic Paleontologists and Mineralogists, Special Publication* **42**, 72–108.

Hatfield, R.G., Stoner, J.S., Carlson, A.E., Reyes, A.V., Housen, B.A., 2013. Source as a controlling factor on the quality and interpretation of sediment magnetic records from the northern North Atlantic. *Earth and Planetary Science Letters* **368**, 69–77.

Hatfield, R.G., Reyes, A.V., Stoner, J.S., Carlson, A.E., Beard, B.L., Winsor, K., Welke, B., 2016. Interglacial responses of the southern Greenland ice sheet over the last 430,000 years determined using particle-size specific magnetic and isotopic tracers. *Earth and Planetary Science Letters* **454**, 225–236.

Hatfield, R.G., Stoner, J.S., Reilly, B.T., Tepley F.J., Wheeler, B.H., Housen, B.A., 2017. Grain size dependent magnetic discrimination of Iceland and South Greenland terrestrial sediments in the northern North Atlantic sediment record. *Earth and Planetary Science Letters* **474**, 474–489.

Hatfield, R.G., Wheeler, B.H., Reilly, B., Stoner, J.S., Housen, B., 2019. Particle size specific magnetic properties across the Norwegian-Greenland Seas: Insights into the influence of source and texture on bulk magnetic records. *Geochemistry, Geophysics, Geosystems* (accepted manuscript).

Haug, G.H., Tiedemann, R., 1998. Effect of the formation of the Isthmus of Panama on Atlantic Ocean thermohaline circulation. *Nature* **393**, 673–676.

Haug, G.H., Sigman, D.M., Tiedemann, R., Pedersen, T.F., Sarnthein, M., 1999. Onset of permanent stratification in the subarctic Pacific Ocean. *Nature* **401**, 779–782.

Haug, G.H., Günther., D., Peterson, L.C., Sigman, D.M., Hughen, K.A., Aeschlimann, B., 2003. Climate of the collapse of Maya civilisation. *Science* **299**, 1731–1735.

Hawkings, J.R., Wadham, J.L., Tranter, M., Raiswell, R., Benning, L.G., Statham, P.J., Tedstone, A., Nienow, P., Lee, K., Telling, J., 2014. Ice sheets as a significant source of highly reactive nanoparticulate iron to the oceans. *Nature Communications* **5**, doi: 10.1038/ncomms4929.

Haywood, A.M. and Valdes, P.J., 2004. Modelling Pliocene warmth: contribution of atmosphere, oceans and cryosphere. *Earth and Planetary Science Letters* **218 (3–4)**, 363–377.

Haywood, A.M., Dekens, P., Ravelo, A.C., Williams, M., 2005. Warmer tropics during the mid-Pliocene? Evidence from alkenone paleothermometry and a fully coupled ocean-atmosphere GCM. *Geochemistry, Geophysics, Geosystems* **6(3)**, Q03010, doi:10.1029/2004GC000799.

Haywood, A.M., Valdes, P.J., Peck, V.L., 2007. A permanent El Niño–like state during the Pliocene? *Paleoceanography* **22 (1)**, doi:10.1029/2006PA001323.

Haywood, A.M., Dowsett, H.J., Valdes, P.J., Lunt, D.J., Francis, J.E., Sellwood, B.W., 2009. Introduction: Pliocene climate, processes and problems. *Philosophical Transactions of the Royal Society of London, Series A* **367 (1886)**, 3–17.

Heinrich, H., 1988. Origin and consequences of cyclic ice rafting in the Northeast Atlantic Ocean during the past 130,000 years. *Quaternary Research* **29**, 143–152.

Helland, P.E., Holmes, M.A., 1997. Surface textural analysis of quartz sand grains from ODP Site 918 off the southeast coast of Greenland suggests glaciation of southern Greenland at 11 Ma. *Paleogeography Paleoclimatology Paleoecology* **135 (1–4)**, 109–121.

Hemming, S.R., Broecker, W.S., Sharp, W.D., Bond, G.C., Gwiazda, R.H., McManus, J.F., Klas, M., Hajdas, I., 1998. Provenance of Heinrich layers in core V28-82, northeastern Atlantic: $^{40}Ar/^{39}Ar$ ages of ice-rafted hornblende, Pb isotopes in feldspar grains, and Nd–Sr–Pb isotopes in the fine sediment fraction. *Earth and Planetary Science Letters* **164 (1–2)**, 317–333.

Hemming, S.R., 2004. Heinrich events: Massive late Pleistocene detritus layers of the North Atlantic and their global climate imprint. *Reviews of Geophysics* **42 (1)**, doi:10.1029/2003RG000128.

Hennissen, J.A.I., Head, M.J., De Schepper, S., Groeneveld, J., 2014. Palynological evidence for a southward shift of the North Atlantic Current at ~2.6 Ma during the intensification of late Cenozoic Northern Hemisphere glaciation. *Paleoceanography* **29 (6)**, 564–580.

Henriksen, N., Higgins, A.K., Kalsbeek, F., Pulvertaft, T.C.R., 2009. Greenland from Archaean to Quaternary. *Geological Survey of Denmark and Greenland Bulletin* **18**, 126 pp.

Hepp, D. A., Mörz, T., Grützner, J., 2006. Pliocene glacial cyclicity in a deep-sea sediment drift (Antarctic Peninsula Pacific Margin). *Palaeogeography, Palaeoclimatology, Palaeoecology* **231**, 181-198.

Herbert, T.D., Lawrence, K.T., Tzanova, A., Peterson, L.C., Caballero-Gill, R., Kelly, C.S., 2016. Late Miocene global cooling and the rise of modern ecosystems. *Nature Geoscience* **9**, 843–847.

Higgins, A.K. 1990: Geological map of Greenland, 1:100 000. Descriptive text. Neria 61 V.1 Nord, Midternæs 61 V.2 Nord. 23 pp. Copenhagen: Grønlands Geologiske Undersøgelse.

Higgins, A.K., Elvevold, S., Escher, J.C., Frederiksen, K.S., Gilotti, J.A., Henriksen, N., Jepsen, H.F., Jones, K.A., Kalsbeek, F., Kinny, P.D., Leslie, A.G., Smith, M.P., Thrane, K., Watt, G.R., 2004. The foreland-propagating thrust architecture of the East Greenland Caledonides 72°–75°N. *Journal of the Geological Society* **161**, 1009–1026.

Hill, D.J., Dolan, A.M., Haywood, A.M., Hunter, S.J., Stoll, D.K., 2010. Sensitivity of the Greenland Ice Sheet to Pliocene sea surface temperatures. *Stratigraphy* **7 (2–3)**, 111–121.

Hill, D. J., Bolton, K. P., Haywood, A. M., 2017. Modelled ocean changes at the Plio-Pleistocene transition driven by Antarctic ice advance. *Nature Communications* **8**, 14376.

Hillaire-Marcel, C., de Vernal, A., Bilodeau, G., Wu, G., 1994. Isotope stratigraphy, sedimentation rates, deep circulation, and carbonate events in the Labrador Sea during the last ~ 200 ka. *Canadian Journal of Earth Science* **31 (1)**, 63–89.

Hillaire-Marcel, C., Bilodeau, G., 2000. Instabilities in the Labrador Sea water mass structure during the last climatic cycle. *Canadian Journal of Earth Science* **37 (5)**, 795–809.

Hillenbrand, C. D., Cortese, G., 2006. Polar stratification: A critical view from the Southern Ocean. *Palaeogeography, Palaeoclimatology, Palaeoecology* **242**, 240–252.

Hodell, D.A., Cieleski, P.F., 1990. Southern Ocean Response to the Intensification of Northern Hemisphere Glaciation at 2.4 Ma. In: Bleil U., Thiede J. (eds.). *Geological History of the Polar Oceans: Arctic versus Antarctic.* NATO ASI Series (Series C: Mathematical and Physical Sciences) **308**, 707–728.

Hodell, D.A., Venz-Curtis, K.A., 2006. Late Neogene history of deepwater ventilation in the Southern Ocean. *Geochemistry, Geophysics, Geosystems* **7 (9)**, doi:10.1029/2005GC001211.

Hodell, D.A., Channell, J.E.T., Curtis, J.H., Romero, O.E., Röhl, U., 2008. Onset of "Hudson Strait" Heinrich events in the eastern North Atlantic at the end of the middle Pleistocene transition (~640 ka)? Paleoceanography 23(4), doi:10.1029/2008PA001591.

Hodell, D.A., Venz-Curtis, K.A., 2009. Late Neogene history of deepwater ventilation in the Southern Ocean. *Geochemistry Geophysics Geosystems* **7 (9)**, Q09001.

Hodell, D.A. Evans, H.F., Channell, J.E.T., Curtis, J.H., 2010. Phase relationships of North Atlantic ice-rafted debris and surface-deep climate proxies during the last glacial period. *Quaternary Science Reviews* **29 (27–28)**, 3875–3886.

Hookakker, B.A.A., Chapman, M.R., McCave, N., Hillaire-Marcel, C., Ellison, R.W.E., Hall, I.R., Telford, R.J., 2011. Dynamics of North Atlantic Deep Water masses during the Holocene. *Paleoceanography* **26**, PA4214, doi:10.1029/2011PA002155, 2011

Horikawa, K., Martin, E.E., Basak, C., Onodera, J., Seki, O., Sakamoto, T., Ikehara, M., Sakai, S., Kawamura, K., 2015. Pliocene cooling enhanced by flow of low-salinity Bering Sea water to the Arctic Ocean. *Nature Communications* **6**, 75–87.

Hounslow, M.W., Maher, B.A., 1999. Source of the climate signal recorded by magnetic susceptibility variations in Indian Ocean sediments. *Journal of Geophysical Research: Solid Earth* **104 (B3)**, 5047–5061.

Huber, M., Brinkhuis, H., Stickley, C.E., Döös., K., Sluijs, A., Warnaar, J., Schellenberg, S.A., Williams, G.L., 2004. *Paleoceanography* **19 (4)**, doi:10.1029/2004PA001014.

Hunter, S., Wilkinson, D., Stanford, J., Stow, D., Bacon, S., Akhmetzhanov, A., Kenyon, N., 2007. The Eirik Drift: a long-term barometer of North Atlantic deepwater flux south of Cape Farewell, Greenland. *Geological Society Special Publication* **276 (1)**, 245–263.

Huybers, P., 2006. Early Pleistocene glacial cycles and the integrated summer insolation forcing. *Science* **313**, 508–511.

Huybers, P., 2007. Glacial variability over the last two million years: an extended depth-derived agemodel, continuous obliquity pacing, and the Pleistocene progression. *Quaternary Science Reviews* **26 (1–2)**, 37–55.

Huybers, P., Wunsch, C., 2004. A depth-derived Pleistocene age model: Uncertainty estimates, sedimentation variability, and nonlinear climate change. *Paleoceanography* **19 (1)**, doi:10.1029/2002PA000857.

Imbrie, J., Boyle, E.A., Clemens, S.C., Duffy, A., Howard, W.R., Kukla, G., Kutzbach, J., Martinson, D.G., McIntyre, A., Mix, A.C., Molfino, B., Morley, J.J., Peterson, L.C., Pisias, N.G., Prell, W.L., Raymo, M.E., Shackleton, N.J., Toggweiler, J.R., 1992. On the Structure and Origin of Major Glaciation Cycles 1. Linear Responses to Milankovitch Forcing. *Paleoceanography* **7 (6)**, 701–738.

Imbrie, J., Mix, A.C., Martinson, D.G., 1993. Milankovitch theory viewed from Devils Hole. *Nature* **363**, 531–533.

Jenkins, R., De Vries, J.L., 1970. *Practical X-ray Spectrometry.* Macmillan, London.

IPCC, 2014. *Climate Change 2014: The Physical Science Basis. Contribution of Working Group I to the Fifth Assessment Report of the Intergovernmental Panel on Climate Change.* Stocker, T.F., Qin, D., Plattner, G.-K., Tignor, M., Allen, S.K., Boschung, J., Nauels, A., Xia, Y., Bex, V., Midgley, P.M. (eds.). Cambridge University Press, Cambridge, United Kingdom and New York, NY, USA, 1535 pp.

IPCC, 2018. Summary for Policymakers. In: Masson-Delmotte, V., Zhai, P., Pörtner, H.O., Roberts, D., Skea, J., Shukla, P.R., Pirani, A., Moufouma-Okia, W., Péan, H.O.C., Pidcock, R., Connors, S., Matthews, J.B.R., Chen, Y., Zhou, X., Gomis, M.I., Lonnoy, E., Maycock, T., Tignor, M., Waterfield, T. (eds.). Global warming of 1.5°C. An IPCC Special Report on the impacts of global warming of 1.5°C above pre-industrial levels and related global greenhouse gas emission pathways, in the context of strengthening the global response to the threat of climate change, sustainable development, and efforts to eradicate poverty. World Meteorological Organization, Geneva, Switzerland, 32 pp.

Itambi, A.C., von Dobeneck, T., Mulitza, S., Bickert, T., Heslop, D., 2009. Millennial-scale northwest African droughts related to Heinrich events and Dansgaard-Oeschger cycles: Evidence in marine sediments from offshore Senegal. *Paleoceanography* **24**, PA1205, doi:10.1029/2007PA001570.

Ivany, L.C., Van Simaeys, S., Domack, E.W., Samson, S.D., 2006. Evidence for an earliest Oligocene ice sheet on the Antarctic Peninsula. *Geology* **34(5)**, 377–380.

Jakob, K.A., Bolton, C.T., Wilson, P.A., Bahr, A., Pross, J., Fiebig, J., Kähler, K., Friedrich, O., 2017. Glacial–interglacial changes in equatorial Pacific surface-water structure during the Plio–Pleistocene intensification of Northern Hemisphere Glaciation. *Earth and Planetary Science Letters* **463**, 69–80.

Jakobsson, M., Backman, J., Rudels, B., Nycander, J., Frank, M., Mayer, L., Jokat, W., Sangiorgi, F., O'Regan, M., Brinkhuis, H., King, J., Moran, K., 2007. The early Miocene onset of a ventilated circulation regime in the Arctic Ocean. *Nature* **447**, 986–990.

Jansen, E., Sjøholm, J., 1991. Reconstruction of glaciation over the past 6 Myr from ice-borne deposits in the Norwegian Sea. *Nature* **349**, 600–603.

Jansen, E., Fronval, T., Rack, F., Channell, J.E.T., 2000. Pliocene-Pleistocene ice rafting history and cyclicity in the Nordic Seas during the last 3.5 Myr. *Paleoceanography* **15(6)**, 709–721.

Japsen, P., Chalmers, J.A., 2000. Neogene uplift and tectonics around the North Atlantic: overview. *Global and Planetary Change* **24 (3–4)**, 165–173.

Jiang, D., Wang, H., Ding, Z., Lang, X., Drange, H., 2005. Modeling the middle Pliocene climate with a global atmospheric general circulation model. *Journal of Geophysical Research* **110 (D14)**, D14107.

Kalsbeek, F., Higgins, A.K., Jepsen, H.F., Frei, R., Nutman, A.P., 2008. Granites and granites in the East Greenland Caledonides. In: Higgins, A.K., Gilotti, J.A., Smith, M.P. (eds.). *The Greenland Caledonides: Evolution of the Northeast Margin of Laurentia*. Geological Society of America Memoir **202**, 227–249.

Kaufman, D.S., Ager, T.A., Anderson, N.J., Anderson, P.M., Andrews, J.T., Bartlein, P.J., Brubaker, L.B., Coats, L.L., Cwynar, L.C., Duvall, M.L., Dyke, A.S., Edwards, M.E., Eisner, W.R., Gajewski, K., Geirsdóttir, A., Hu, F.S., Jennings, A.E., Kaplan, M.R., Kerwin, M.W., Lozhkin, A.V., MacDoald, G.M., Miller, G.H., Mock, C.J., Oswald, W.W., Otto-Bleisner, B.L., Porinchu, D.F., Rühland, K., Smol, J.P., Steig, E.J., Wolfe, B.B., 2004. Holocene thermal maximum in the western Arctic (0–180°W). *Quaternary Science Reviews* **23 (5–6)**, 529–560.

Kawamura, N., Ishikawa, N., Torii, M.., 2012. Diagenetic alteration of magnetic minerals in Labrador Sea sediments (IODP Sites U1305, U1306, and U1307). *Geochemistry Geophysics Geosystems* **13 (8)**, doi:10.1029/2012GC004213

Keeling, R.F., Visbeck, M., 2001. On the linkage between Antarctic surface water stratification and global deep-water temperature. *Journal of Climate* **24** 3545–3557.

Keigwin, L., 1982. Isotopic paleoceanography of the Caribbean and East Pacific: role of Panama uplift in Late Neogene time. *Science* **217 (4557)**, 350–353.

Kelley, S.E., Briner, J.P., Young, N.E., Babonis, G.S., Csatho, B., 2012. Maximum late Holocene extent of the western Greenland Ice Sheet during the late 20th century. *Quaternary Science Reviews* **56**, 89–98.

Kennett, J.P., 1977. Cenozoic Evolution of Antarctic Glaciation, the Circum-Antarctic Ocean, and Their Impact on Global Paleoceanography. *Journal of Geophysical Research* **82 (27)**, 3843–3860.

King, J., Banerjee, S., Marvin, J., 1983. A new rock-magnetic approach to selecting sediments for geomagnetic paleointensity studies: Application to paleointensity for the last 4000 years. *Journal of Geophysical Research: Solid Earth* **88 (B7)**, 5911–5921.

Kirschvink, J.L., 1980. The least squares lines and plane analysis of paleomagnetic data. *Geophysical Journal International* **62**, 699–718.

Kissel, C., Laj, C., Labeyrie, L., Dokken, T., Voelker, A., Blamart, D., 1999. Rapid climatic variations during marine isotopic stage 3: magnetic analysis of sediments from Nordic Seas and North Atlantic. *Earth and Planetary Science Letters* **171(3)**, 489–502.

Kissel, C., Laj, C., Mulder, T., Wandres, C., Cremer, M., 2009. The magnetic fraction: A tracer of deep water circulation in the North Atlantic. *Earth and Planetary Science Letters* **288 (3–4)**, 444–454.

Kleiven, H.F., Jansen, E., Fronval, T., Smith, T.M., 2002. Intensification of Northern Hemisphere glaciations in the circum Atlantic region (3.5–2.4 Ma) – ice-rafted detritus evidence. *Palaeogeography, Palaeoclimatology, Palaeoecology* **184**, 213–223.

Kleiven, H.F., Kissel, C., Laj, C., Ninnemann, U.S., Richter, T.O., Cortijo, E., 2007. Reduced North Atlantic Deep Water coeval with the Glacial Lake Agassiz fresh water outburst. *Science* **319**, 60–64.

Klocker, A., Prange, M., Schulz, M., 2005. Testing the influence of the Central American Seaway on orbitally forced Northern Hemisphere glaciation. *Geophysical Research Letters* **32 (3)**, doi:10.1029/2004GL021564.

Knappett, C., Pirrie, D., Power, M.R., Nikolakopoulou, I., Hilditch, J., Rollinson, G.K., 2011. Mineralogical analysis and provenancing of ancient ceramics using automated SEM-EDS analysis (QEMSCAN®): a pilot study on LB I pottery from Akrotiri, Thera. *Journal of Archaeological Science* **38 (2)**, 219–232.

Knies, J., Matthiessen, J., Vogt, C., Stein, R., 2002. Evidence of 'Mid-Pliocene (similar to 3 Ma) global warmth' in the eastern Arctic Ocean and implications for the Svalbard/Barents Sea ice sheet during the late Pliocene and early Pleistocene (similar to 3–1.7 Ma). *Boreas* **31**, 82–93.

Knies, J., Matthiessen, J., Vogt, C., Laberg, J.S., Hjelstuen, B.O., Smelror, M., Larsen, E., Andreassen, K., Eidvin, T., Vorren, T.O., 2009. The Plio-Pleistocene glaciation of the Barents Sea- Svalbard region: a new model based on revised chronostratigraphy. *Quaternary Science Reviews* **28**, 812–829.

Knies, J., Mattingsdal, R., Fabian, K., Grøsfjeld, K., Baranwal, S., Husum, K., De Schepper, S., Vogt, C., Andersen, N., Matthiessen, J., Andreassen, K., Jokat, W., Nam, S.-I., Gaina, C., 2014. Effect of early Pliocene uplift on late Pliocene cooling in the Arctic–Atlantic gateway. *Earth and Planetary Science Letters* **387** 132–144.

Koenig, S.J., DeConto, R.M., Pollard, D., 2014. Impact of reduced Arctic sea ice on Greenland ice sheet variability in a warmer than present climate. *Geophysical Research Letters* **41 (11)**, 3933–3942.

Kopp, R.E., Simons, F.J., Mitrovica, J.X., Maloof, A.C., Oppenheimer, M., 2009. Probabilistic assessment of sea level during the last interglacial stage. *Nature* **462**, 863–867.

Korstgärd, J.A., Nielsen, O.B., 1989. Provenance of Dropstones in Baffin Bay and Labrador Sea, Leg 105. doi: 10.2973/odp.proc.sr.105.200.1989.

Kostov,Y., Armour, K.C., Marshall, J., 2014. Impact of the Atlantic meridional overturning circulation on ocean heat storage and transient climate change. *Geophysical Research Letters* **41 (6)**, 2108–2116.

Kuijpers, A., Troelstra, S.R., Prins, M.A., Linthout, K., Akhmetzhanov, A., Bouryak, S., Bachmann, M.F., Lassen, S., Rasmussen, S., Jensen, J.B., 2003. Late Quaternary sedimentary processes and ocean circulation changes at the Southeast Greenland margin. *Marine Geology* **195**, 109–129.

Kutzbach, J.E., Guetter, P.J., Ruddiman, W.F., Prell, W.L., 1989. Sensitivity of climate to late Cenozoic uplift in southern Asia and the American west: Numerical experiments. *Journal of Geophysical Research: Atmospheres* **94 (D15)**, 18393–18407.

Ladant, J.-B., Donnadieu, Y., Dumas, C., 2014. Links between CO_2, glaciation and water flow: reconciling the Cenozoic history of the Antarctic Circumpolar Current. *Climate of the Past* **10 (6)**, 1957–1966.

Ladant, J.-B., Donnadieu, Y., Bopp, L., Lear, C.H., Wilson, P.A., 2018. Meridional Contrasts in Productivity Changes Driven by the Opening of Drake Passage. *Paleoceanography and Paleoclimatology* **33(3)**, 302–317.

Lang, D., Bailey, I., Wilson, P.A., Beer, C.J., Bolton, C.T., Friedrich, O., Newsam, C., Spencer, M.R., Gutjahr, M., Foster, G.L., Cooper, M.J., Milton, J.A., 2014. The transition on North America from the warm humid Pliocene to the glaciated Quaternary traced by eolian dust deposition at a benchmark North Atlantic Ocean drill site. *Quaternary Science Reviews* **93**, 125–141.

Lang, D.C., Bailey, I., Wilson, P.A., Chalk, T.B., Foster, G.L., Gutjahr, M., 2016. Incursions of southern-sourced water into the deep North Atlantic during late Pliocene glacial intensification. *Nature Geoscience* **9**, 375–379.

Langton, S.J., Rabideaux, N.M., Borrelli, C., Katz, M.E., 2016. Southeastern Atlantic deep-water evolution during the late-middle Eocene to earliest Oligocene (Ocean Drilling Program Site 1263 and Deep Sea Drilling Project Site 366). *Geosphere* **12 (3)**, 1032–1047.

Larsen, H.C., Saunders, A.D., Clift, P.D., Beget, J., Wei, W., Spezzaferri, S., Ali, J., Cambray, H., Demant, A., Fitton, G., Fram, M.S., Fukuma, K., Gieskes, J., Holmes, M.A., Hunt, J., Lacasse, C., Larsen, L.M., Lykke-Andersen, H., Meltser, A., Morrison, M.L, Nemoto, N., Okay, N., Saito, S., Sinton, C., Stax, R., Vallier, T.L., Vandamme, D., Werner, R. (The ODP Leg 152 Scientific Party), 1994. Seven million years of glaciation in Greenland. *Science* **264**, 952–955.

Laskar, J., Joutel, F., Robutel, P., 1993. Stabilization of the Earth's obliquity by the Moon. *Nature* **361**, 615–617.

Lawrence, K.T., Liu, Z., Herbert, T.D., 2006. Evolution of the eastern tropical Pacific through Plio-Pleistocene glaciation. *Science* **312**, 79–83.

Lawrence, K.T., Herbert, T.D., Brown, C.M., Raymo, M.E., Haywood, A.M., 2009. High-amplitude variations in North Atlantic sea surface temperature during the early Pliocene warm period. *Paleoceanography* **24**, PA2218.

Lawrence, K.T., Sigman, D.M., Herbert, T.D., Riihimaki, C.A., Bolton, C.T., Martinez-Garcia, A., Rosell-Mele, A., Haug, G.H., 2013. Time-transgressive North Atlantic productivity changes upon Northern Hemisphere glaciation. *Paleoceanography* **28**, 740–751.

Lear, C.H., Elderfield, H., Wilson, P.A., 2000. Cenozoic deep-sea temperatures and global ice volumes from Mg/Ca in benthic foraminiferal calcite. *Science* **287**, 269–272.

Lear, C.H., Bailey, T.R., Pearson, P.N., Coxall, H.K., Rosenthal, Y., 2008. Cooling and ice growth across the Eocene-Oligocene transition. *Geology* **36 (3)**, 251–254.

Lear, C.H., Lunt, D.J., 2016. How Antarctica got its ice. *Science* **352**, 34–35.

Lecavalier, B.S., Milne, G.N., Simpson, M.J.R., Wake, L., Huybrechts, P., Tarasov, L., Kjeldsen, K.K., Funder, S., Long, A.J., Woodroffe, S., Dyke, A.S., Larsen, N.K.,

2014. A model of Greenland ice sheet deglaciation constrained by observations of relative sea level and ice extent. *Quaternary Science Reviews* **102**, 54–84.

Lee, S.-Y., Poulsen, C.J., 2006. Sea ice control of Plio–Pleistocene tropical Pacific climate evolution. *Earth and Planetary Science Letters* **24 (1–2)**, 253–262.

Leinen, M., Cwienk, D., Heath, G.R., Biscaye, P.E., Kolla, V., Thiede, J., Dauphin, J.P., 1986. Distribution of biogenic silica and quartz in recent deep-sea sediments. *Geology* **14 (3)**, 199–203.

Letréguilly, A., Huybrechts, P., Reeh, N., 1991. Steady-state characteristics of the Greenland ice sheet under different climates. *Journal of Glaciology* **37 (125)**, 149–157.

Levitus, S., Boyer, T.P., 1994. Temperature. *World Ocean Atlas 1994* **4**, NOAA Atlas NESDIS 4, 117 pp.

Lewis, A.R., Marchant, D.R., Ashworth, A.C., Hemming, S.R., Machlus, M.L., 2007. Major middle Miocene global climate change: Evidence from East Antarctica and the Transantarctic Mountains. *Geological Society of America Bulletin* **119 (11–12)**, 1449–1461.

Li, X.S., Berger, A., Loutre, M.F., Maslin, MA., Haug, G.H., Tiedemann, R.,1998. Simulating Late Pliocene northern hemisphere climate with the LLN 2-D Model. *Geophysical Research Letters* **25 (6)**, 915–918.

Lichey, C., Hellmer, H. H., 2001. Modeling giant-iceberg drift under the influence of sea ice in the Weddell Sea, Antarctica. *Journal of Glaciology* **47 (158)**, 452–460.

Liebrand, D., Beddow, H.M., Lourens, L.J., Pälike, H., Raffi, I., Bohaty, S.M., Hilgen, F.J., Saes, M.J.M, Wilson, P.A., van Dijk, A.E., Hodell, Kroon, D., Huck, C.E., Batenburg, S.J., 2016. Cyclostratigraphy and eccentricity tuning of the early Oligocene through early Miocene (30.1–17.1 Ma): Cibicides mundulus stable oxygen and carbon isotope records from Walvis Ridge Site 1264. *Earth and Planetary Science Letters*, **450**, 392–405.

Liebrand, D., de Bakker, A. T. M., Beddow, H. M., Wilson, P. A., Bohaty, S. M., Ruessink, G., Pälike, H., Batenburg, S. J., Hilgen, F. J., Hodell, D. A., Huck, C. E., Kroon, D., Raffi, I., Saes, M. J. M., van Dijk, A. E., Lourens, L. J., 2017. Evolution of the early Antarctic ice ages. *Proceedings of the National Academy of Sciences* **110**, 3867–3872.

Linthout, K., Troelstra S.R., Kuijpers, A., 2000. Provenance of coarse ice-rafted detritus near the SE Greenland margin. *Netherlands Journal of Geosciences* **79**, 109–121.

Lisiecki, L.E., Raymo, M.E., 2005. A Pliocene-Pleistocene stack of 57 globally distributed benthic $\delta^{18}O$ records. *Paleoceanography* **20**, PA1003.

Lisiecki, L.E., Raymo, M.E., 2007. Plio–Pleistocene climate evolution: trends and transitions in glacial cycle dynamics. *Quaternary Science Reviews* **26**, 56–69.

Liu, Z., Pagani, M., Zinniker, D., DeConto, R., Huber, M., Brinkhuis, H., Shah, S.R., Leckie, R.M., Pearson, A., 2009. Global cooling during the Eocene-Oligocene climate transition. *Science* **323**, 1187–1190.

Liu, Q.S., Roberts, A.P., Larrasoana, J.C., Banerjee, S.K., Guyodo, Y., Tauxe, L., Oldfield, F., 2012. Environmental magnetism: Principles and applications. *Reviews of Geophysics* **50**, RG4002, doi:10.1029/2012RG000393.

Loutre, M.F., Berger, A., 1993. Sensibilite des parametres astro-climatiques au cours des 8 derniers millions d'annees. *Scientific Report 1993/4*. Institut d'Astronomie et de Geophysique G. Lemaitre, Universite Catholique de Louvain, Louvain- la-Neuve.

Lozier, M.S., Li, F., Bacon, S., Bahr, F., Bower, A.S., Cunningham, S.A., de Jong, M.F., de Steur, L., DeYoung, B., Fischer, J., Gary, S.F., Greenan, B.J.W., Holliday, N.P., Houk, A., Houpert, L., Inall, M.E., Johns, W.E., Johnson, H.L., Johnson, C., Karstensen, J., Koman, G., Le Bras, I.A., Lin, X., Mackay, N., Marshall, D.P., Mercier, H., Oltmanns, M., Pickart, R.S., Ramsey, A.L., Rayner, D., Straneo, F., Thierry, V., Torres, D.J., Williams, R.G., Wilson, C., Yang, J., Yashayaev, I., Zhao, J., 2019. A sea change in our view of overturning in the subpolar North Atlantic. *Science* **363**, 516–521.

Lunt, D.J., Valdes, P.J., Haywood, A.M., Rutt, I.C., 2008a. Closure of the Panama Seaway during the Plioene: implications for climate and Northern Hemisphere glaciation. *Climate Dynamics* **30**, 1–18.

Lunt, D.J., Foster, G.L., Haywood, A.M., Stone, E.J., 2008b. Late Pliocene Greenland glaciation controlled by a decline in atmospheric CO_2 levels. *Nature* **454**, 1102–1006.

Lunt, D.J., Haywood, A.M., Foster, G.L., Stone, E.J., 2009. The Arctic cryosphere in the Mid-Pliocene and the future. *Philosophical Transactions of the Royal Society London, Series A* **367**, 49–67.

Lunt, D.J., Haywood, A.M., Schmidt, G.A., Salzmann, U. Valdes, P.J., Dowsett, H.J., 2010. Earth system sensitivity inferred from Pliocene modelling and data. *Nature Geoscience* **3 (1)**, 60–64.

MacAyeal, D.R., 1993. Binge/purge oscillations of the Laurentide Ice Sheet as a cause of the North Atlantic's Heinrich events. *Paleoceanography* **8 (6)**, 775–784.

Marcott, S.A., Shakun, J.D., Clark, P.U., Mix, A.C., 2013. A reconstruction of regional and global temperature for the past 11,300 years. *Science* **339**, 1198–1201.

Marlow, J.R., Lange, C.B., Wefer, G., Rosell-Melé, A., 2000. Upwelling intensification as part of the Pliocene-Pleistocene climate transition. *Science* **290**, 2288–2291.

Marshall, S.J., Tarasov, L., Clarke, G.K.C., Peltier W.R., 2000. Glaciological reconstruction of the Laurentide Ice Sheet: physical processes and modelling challenges. *Canadian Journal of Earth Sciences* **37 (5)**, 769–793.

Martínez-Botí, M.A., Marino, G., Foster, G.L., Ziveri, P., Henehan, M.J., Rae, J.W.B., Mortyn, P.G. and Vance, D., 2015. Boron isotope evidence for oceanic carbon dioxide leakage during the last deglaciation. *Nature* **518**, 219–222.

Martinez-Garcia, A., Rodell-Melé, A., Geibert, W., Gersonde, R., Masqué, P., Gaspari, V., Barbante, C., 2009. Links between iron supply, marine productivity, sea surface temperature, and CO2 over the last 1.1 Ma. *Paleoceanography* **24**, doi:10.1029/2008PA001657.

Maslin, M.A., Li, X.S., Loutre, M.-F., Berger, A., 1998. The contribution of orbital forcing to the progressive intensification of Northern Hemisphere glaciation. *Quaternary Science Reviews* **17**, 411–426.

Mazaud, A., Channell, J., Stoner, J., 2012. Relative paleointensity and environmental magnetism since 1.2Ma at IODP site U1305 (Eirik Drift, NW Atlantic). *Earth Planetary Science Letters* **357–358**, 137–144.

Mazaud, A., Channell, J., Stoner, J., 2015. The paleomagnetic record at IODP Site U1307 back to 2.2 Ma (Eirik Drift, off south Greenland). *Earth and Planetary Science Letters* **429**, 82–89.

McKay, R., Naish, T., Carter, L., Riesselman, C., Dunbar, R., Sjunneskog, C., Winter, D., Sangiorgi, F., Warren, C., Pagani, M., Schouten, S., Willmott, V., Levy, R., DeConto, R., Powell, R.D., 2012. Antarctic and Southern Ocean influences on Late Pliocene global cooling. *Proceedings of the National Academy of Sciences* **109 (17)**, 6423–6428.

McManus, J.F., Bond, G.C., Broecker, W.S., Johnsen, S., Labeyrie, L., Higgins, S., 1994. High-resolution climate records from the North Atlantic during the last interglacial. *Nature* **371**, 326–329.

McPhaden, M.J., Zebiak, S.E., Glantz, M.H., 2006. ENSO as an integrating concept in earth science. *Science* **314**, 1740–1745.

Medina-Elizalde, M., Lea, D.W., 2005. The Mid-Pleistocene transition in the tropical Pacific. *Science* **310**, 1009–1012.

Meehl, G.A., Stocker, T.F., Collins, W.D., Friedlingstein, P., Gaye, A.T., Gregory, J.M., Kitoh, A., Knutti, R., Murphy, J.M., Noda, A., Raper, S., Watterson, A.J., Weaver, Z.C., Zhao, C., 2007. Global Climate Projections. In: Solomon, S., Qin, D., Manning, M., Chen, Z., Marquis, M., Averyt, K.B., Tignor, M., Miller, H.L. (eds.). *Climate Change 2007: The Physical Science Basis. Contribution of Working Group I to the Fourth Assessment Report of the Intergovernmental Panel on*

Climate Change. Cambridge University Press, Cambridge, United Kingdom and New York, NY, USA.

Milkankovitch, M.M., 1941. Kanon der Erdbestrahlung und seine Andwendung auf das Eiszeitenproblem. *Royal Serbian Sciences, Special Publication* **132**, *Section of Mathematical and Natural Sciences* **33**, Belgrade, 633 pp. (Canon of Insolation and the Ice Age Problem, English translation by Israel Program for Scientific Translation and published for the U.S. Department of Commerce and the National Science Foundation, Washington, DC, 1969.)

Miller, K.G., Wright, J.D., Fairbanks, R.G., 1991. Unlocking the Ice House: Oligocene-Miocene oxygen isotopes, eustasy, and margin erosion. *Journal of Geophysical Research: Solid Earth* **96 (B4)**, 6829–6848.

Miller, K.G., Kominz, M.A., Browning, J.V., Wright, J.D., Mountain, G.S., Katz, M.E., Sugarman, P.J., Cramer, B.S., Christie-Blick, N., Pekar, S.F., 2005. The Phanerozoic record of global sea-level change. *Science* **310**, 1293–1298.

Miller, K.G., Wright, J.D., Browning, J.V., Kulpecz, A., Kominz, M., Naish, T.R., Cramer, B.S., Rosenthal, Y., Peltier, W.R., Sosdian, S., 2012. High tide of the warm Pliocene: Implications of global sea level for Antarctic deglaciation. *Geology* **40 (5)**, 407–410.

Mix, A.C., Ruddiman, W.F., McIntyre, A., 1986a. Late Quaternary paleoceanography of the tropical Atlantic, 1: Spatial variability of annual mean sea-surface temperatures, 0-20,000 years B.P. *Paleoceanography* **1 (1)**, 43–66.

Mix, A. C., Ruddiman, W.F., McIntyre, A., 1986b. Late Quaternary paleoceanography of the tropical Atlantic, 2: The seasonal cycle of sea surface temperatures, 0-20,000 years B.P. *Paleoceanography* **1 (3)**, 339–353.

Mix, A.C., Pisias, N.G., Rugh, W., Wilson, J., Morey, A., Hagelberg, T.K., 1995. Benthic foraminifer stable isotope record from Site 849 (0–5Ma): local and global climate changes. In: Pisias, N.G., Mayer, L.A., Janecek, T.R., Palmer-Julson, A., van Andel, T.H. (eds). *Proceedings of the Ocean Drilling Program, Scientific Results* **138**, 371–412.

Molnar, P., England, P., 1990. Late Cenozoic uplift of mountain ranges and global climate change: chicken or egg? *Nature* **3 (46)**, 29–34.

Molnar, P., Cane, M.A., 2002. El Niño's tropical climate and teleconnections as a blueprint for pre-Ice Age climates. *Paleoceanography* **17 (2)**, doi: 10.1029/2001PA000663.

Molnar, P., 2008. Closing of the Central American Seaway and the Ice Age: A critical review. *Paleoceanography* **23**, PA2201.

Montes, C., Bayona, G., Cardoa, A., Buchs, D.M., Silva, C.A., Morón, S., Hoyos, N., Ramírez, D.A., Jaramillo, C.A., Valencia, V., 2012. Arc-continent collision and

orocline formation: Closing of the Central American seaway. *Journal of Geophysical Research: Solid Earth* **117 (B4)**, B04105.

Montes, C., Cardona, A., Jaramillo, C., Pardo, A., Silva, J.C., Valencia, V., Ayala, C., Pérez-Angel, L.C., Rodriguez-Parra, L.A., Ramirez, V., Niño, H., 2015. Middle Miocene closure of the Central American seaway. *Science* **348**, 226–229.

Moran, K., Backman, J., Brinkhuis, H., Clemens, S.C., Cronin, T., Dickens, G.R., Eynaud, F., Gattacceca, J., Jakobsson, M., Jordan, R.W., Kaminski, M., King, J., Koç, N., Krylov, A., Martinez, N., Matthiessen, J., McInroy, D., Moore, T.C., Onodera, J., O'Regan, A.M., Pälike, H., Rea, B., Rio, D., Sakamoto, T., Smith, D.C., Stein, R., St. John, K., Suto, I., Suzuki, N., Takahashi, K., Watanabe, M., Yamamoto, M., Farrell, J., Frank, M., Kubik, P., Jokat, W. and Kristoffersen, Y., 2006. The Cenozoic palaeoenvironment of the Arctic Ocean. *Nature* **441**, 601–605.

Mudelsee, M., Raymo, M.E., 2005. Slow dynamics of the Northern Hemisphere glaciation. *Paleoceanography* **20**, PA4022.

Müller-Michaelis, A., Uenzelmann-Neben, G., 2014. Development of the Western Boundary Undercurrent at Eirik Drift related to changing climate since the early Miocene. *Deep Sea Research Part I: Oceanographic Research Papers* **93**, 21–34.

Naafs, B.D.A., Stein, R., Hefter, J., Khélifi, De Schepper, S., Haug, G.H., 2010. Late Pliocene changes in the North Atlantic Current. *Earth and Planetary Science Letters* **298 (34)**, 434–442.

Naafs, B.D.A., Hefter, J., Acton, G., Haug, G.H., Martínez-Garcia, Pancost, R., Stein, R., 2012. Strengthening of North American dust sources during the late Pliocene (2.7 Ma). *Earth and Planetary Science Letters* **317–318**, 8–19.

Naish, T.R., Woolfe, K.J., Barrett, P.J., Wilson, G.S., Atkins, C., Bohaty, S.M., Bücker, C.J., Claps, M., Davey, F.J., Dunbar, G.B., Dunn, A.G., Fielding, C.R., Florindo, F., Hannah, M.J., Harwood, D.M., Henrys, S.A., Krissek, L.A., Lavelle, M., van der Meer, McIntosh, W.C., Niessen, F., Passchier, S., Powell, R.D., Roberts, A.P., Sagnotti, L., Scherer, R.P., Strong, C.P., Talarico, F., Verosub, K.L., Villa, G., Watkins, D.K., Webb, P.-N., Wonik, T., 2001. Orbitally induced oscillations in the East Antarctic ice sheet at the Oligocene/Miocene boundary. *Nature* **413**, 719–723.

Naish, T., Powell, R., Levy, R., Wilson, G., Scherer, R., Talarico, F., Krissek, L., Niessen, F., Pompilio, M., Wilson, T., Carter, L., DeConto, R., Huybers, P., McKay, R., Pollard, D., Ross, J., Winter, D., Barrett, P., Browne, G., Cody, R., Cowan, E., Crampton, J., Dunbar, G., Dunbar, N., Florindo, F., Gebhardt, C., Graham, I., Hannah, M., Hansaraj, D., Harwood, D., Helling, D., Henrys, S., Hinnov, L., Kuhn,

G., Kyle, P., Läufer, A., Maffioli, P., Magens, D., Mandernack, K., McIntosh, W., Millan, C., Morin, R., Ohneiser, C., Paulsen, T., Persico, D., Raine, I., Reed, J., Riesselman, C., Sagnotti, I., Schmitt, D., Sjunneskog, C., Strong, P., Taviani, M., Vogel, S., Wilch, T., Williams, T., 2009. Obliquity-paced Pliocene West Antarctic ice sheet oscillations. *Nature* **458**, 322–328.

Nicholl, J.A.L., Hodell, D.A., Naafs, B.D.A., Hillaire-Marcel, C., Channel, J.E.T., Romero, O.E., 2012. A Laurentide outburst flooding event during the last interglacial period. *Nature Geoscience* **5**, 901–904.

Nuttall, A.-M., 1993. *Glaciological Investigations in East Greenland using Digital LANDSAT imagery*. Cambridge, UK, 107 pp.

Oda, H., Xuan, C., 2014. Deconvolution of continuous paleomagnetic data from pass-through magnetometer: A new algorithm to restore geomagnetic and environmental information based on realistic optimization. *Geochemistry, Geophysics, Geosystems* **15**, 3907–3924.

Ogg, J. G., 2012. Chapter 5 – Geomagnetic Polarity Time Scale, In: Gradstein, F. M., Ogg, J. G., Schmitz, M. D., Ogg, G. M. (eds.). *The Geologic Time Scale*. Elsevier, Boston, 85–113.

Ohno, M., Hayashi, T., Komatsu, F., Murakami, F., Zhao, M., Guyodo, Y., Acton, G., Evans, H., Kanamatsu, T., 2012. A detailed paleomagnetic record between 2.1 and 2.75 Ma at IODP Site U1314 in the North Atlantic: Geomagnetic excursions and the Gauss-Matuyama transition. *Geochemistry Geophysics Geosystems* **13**, Q12Z39.

Otto-Bliesner, B.L., Marshall, S.J., Overpeck, J.T., Miller, G.H., Hu, A., CAPE Last Interglacial Project members, 2006. Simulating Arctic climate Warmth and icefield retreat in the last interglaciation. *Science* **311**, 1751–1753.

Paillard, D., 1998. The timing of Pleistocene glaciations from a simple multiple-state climate model. *Nature* **391**, 378–381.

Pagani, M., Zachos, J.C., Freeman, K.H., Tipple, B., Bohaty, S., 2005. Marked decline in atmospheric carbon dioxide concentrations during the Paleogene. *Science* **309**, 600–603.

Pagani, M., Liu, Z., LaRiviere, J., Ravelo, A.C., 2009. High Earth-system climate sensitivity determined from Pliocene carbon dioxide concentrations. *Nature Geoscience* **3**, 27–30.

Pagani, M., Huber, M., Liu, Z., Bohaty, S.M., Henderiks, J., Sijp, W., Krishnan, S., DeConto, R.M., 2011. The role of carbon dioxide during the onset of Antarctic glaciation. *Science* **334**, 1261–1264.

Pälike, H., Shackleton, N.J., Röhl, U., 2001. Astronomical forcing on late Eocene marine sediments. *Earth and Planetary Science Letters* **193**, 589–602.

Parnell-Turner, R., White, N.J., McCave, I.N., Henstock, T.J., Murton, B., Jones, S.M., 2015. Architecture of North Atlantic contourite drifts modified by transient circulation of the Icelandic mantle plume. *Geochemistry, Geophysics, Geosystems* **16 (10)**, 3414–3435.

Pearson, P.N., Palmer, M.R., 2000. Estimating Paleogene atmospheric pCO_2 using boron isotope analysis of foraminifera. *GFF* **22**, 127–128.

Pearson, P. N., Foster, G. L., and Wade, B. S., 2009. Atmospheric carbon dioxide through the Eocene-Oligocene climate transition. *Nature* **461**, 1110–1113.

Pekar, S.F., Christie-Blick, N., Kominz, M.A., Miller, K.G., 2002. Calibration between eustatic estimates from backstripping and oxygen isotopic records for the Oligocene. *Geology* **30 (10)**, 903–906.

Petit, J.R., Jouzel, J., Raynaud, D., Barkov, N.I., Barnola, J.-M., Basile, I., Bender, M., Chappellaz, J., Davis, M., Delaygue, G., Delmotte, M., Kotlyakov, V.M., Legrand, M., Lipenkov, V.Y., Lorius, C., Pépin, L., Saltzman, E., Stievenard, M., 1999. Climate and atmospheric history of the past 420,000 years from the Vostok ice core, Antarctica. *Nature* **399**, 429–463.

Philander, S.G., Fedorov, A.V., 2003. Role of tropics in changing the response to Milankovich forcing some three million years ago. *Paleoceanography* **18 (2)**, doi:10.1029/2002PA000837.

Pickart, R.S., 1992. Water mass components of the North Atlantic deep western boundary current. *Deep-Sea Research* **39 (9)**, 1553–1572.

Pirrie, D., Butcher, A.R., Power, M.R., Gottlieb, P., Miller, G.L., 2004. Rapid quantitative mineral and phase analysis using automated scanning electron microscopy (QemSCAN); potential applications in forensic geoscience. In: Pye, K., Croft, D.J. (eds.). *Forensic Geoscience: Principles, Techniques and Applications.* Geological Society, London, Special Publications **232**, 123–136.

Pirrie, D., Rollinson, G.K., Power, M.R., Webb, J., 2013. Automated forensic soil mineral analysis; testing the potential of lithotyping. In: Pirrie, D., Ruffell, A., Dawson, L.A. (eds.). *Environmental and Criminal Geoforensics*. Geological Society, London, Special Publications *384*, 47–64.

Pirrie, D., Rollinson, G.K., 2011. Unlocking the applications of automated mineral analysis. *Geology Today* **26 (6)**, 226–235.

Pisias, N.G., Moore Jr., T.C., 1981. The evolution of the Pleistocene climate: a time series approach. *Earth and Planetary Science Letters* **52**, 450–458.

Platzner, I. T., Habfast, K., Walder, A. J., Goetz, A., 1997. *Modern isotope ratio mass spectrometry.* John Wiley & Sons, Chichester, West Sussex, England: 514 p.

Pollard, D., DeConto, R.M., 2009. Modelling West Antarctic ice sheet growth and collapse through the past five million years. *Nature* **458**, 329–332.

Praetorius, S.K., 2018. North Atlantic circulation slows down. *Nature* **556**, 180–181.

Pritchard, H.D., Arthern, R.J., Vaughan, D.G., Edwards, L.A., 2009. Extensive dynamic thinning on the margins of the Greenland and Antarctic ice sheets. *Nature* **461**, 971–975.

Rasmussen, T.L., van Weering, T.C.E., Labeyrie, L., 1997. Climatic instability, ice sheets and ocean dynamics at high northern latitudes during the last glacial period (58-10 KA BP). *Quaternary Science Reviews* **16 (1)**, 71–80.

Ravelo, A.C., Andreasen, D.H., Lyle, M., Lyle, A.O., Wara, M.W., 2004. Regional climate shifts caused by gradual global cooling in the Pliocene epoch. *Nature* **429** 263–267.

Ravelo, A.C., Wara, M.W., 2004. The role of the tropical oceans on global climate during a warm period and a major climate transition. *Oceanography* **17 (3)**, 32–41.

Raymo, M.E., Ruddiman, W.F., Froelich, P.N., 1988. Influence of late Cenozoic mountain building on ocean geochemical cycles. *Geology* **16 (7)**, 649–653.

Raymo, M.E., Ruddiman, W.F., Shackleton, N.J., Oppo, D.W., 1990. Evolution of Atlantic-Pacific $\delta^{13}C$ gradients over the last 2.5 my. *Earth and Planetary Science Letters* **97 (3–4)**, 353–368.

Raymo, M.E., Ruddiman, W.F., 1992. Tectonic forcing of late Cenozoic climate. *Nature* **359**, 117–122.

Raymo, M.E., Grant, B., Horowitz, M., Rau, G.H., 1996. Mid-Pliocene warmth: stronger greenhouse and stronger conveyor. *Marine Micropaleontology* **27**, 313–326.

Raymo, M.E., Kozdon, R., Evans, D., Lisiecki, L., Ford, H.L., 2018. The accuracy of mid-Pliocene δ18O-based ice volume and sea level reconstructions. *Earth-Science Reviews* **177**, 291–302.

Reed, S.J.B., 2005. *Electron Microprobe Analysis and Scanning Electron Microscopy in Geology*. Cambridge University Press, New York, U.S.A.

Reyes, A.V., Carlson, A.E., Beard, B.L., Hatfield, R.G., Stoner, J.S., Winsor, K., Welke, B., Ullman, D.J., 2014. South Greenland ice-sheet collapse during Marine Isotope Stage 11. *Nature* **510**, 525–528.

Richter, T.O., Lassen, S., van Weering, Tj.C.E., de Haas, H., 2001. Magnetic susceptibility patterns and provenance of ice-rafted material at Feni Drift, Rockall Trough: implications for the history of the British–Irish ice sheet. *Marine Geology* **173 (1–4)**, 37–54.

Richter, T.O., van der Gaast, S., Koster, B., Vaars, A., Gieles, R., de Stigter, H.C., de Haas, H., van Weering, T.C.E., 2006. The Avaatech XRF Core Scanner: technical description and applications to NE Atlantic sediments. In: Rothwell, R.G., 2006. *New Techniques in Sediment Core Analysis*. Geological Society, London, Special Publications **267**, 39–50.

Riesselman, C.R., Dunbar, R.B., 2013. Diatom evidence for the onset of Pliocene cooling from AND-1B, McMurdo Sound, Antarctica. *Palaeogeography, Palaeoclimatology, Palaeoecology* **369**, 136–153.

Rignot, E., Kanagaratnam, P., 2006. Changes in the velocity structure of the Greenland ice sheet. *Science* **311**, 986–990.

Roberts, A.P., 2015. Magnetic mineral diagenesis. *Earth-Science Reviews* **151**, 1–47.

Robinson, M.M., 2009. New quantitative evidence of extreme warmth in the Pliocene Arctic. *Stratigraphy* **6 (4)**, 265–275.

Rohling, E.J., Bigg, G.R., 1998. Paleosalinity and 18O: A critical assessment. *Journal of Geophysical Research* **103**, 1307–1318.

Rohling, E.J., Foster, G.L., Grant, K.M., Marino, G., Roberts, A.P., Tamisiea, M.E., Williams, F., 2014. Sea-level and deep-sea-temperature variability over the past 5.3 million years. *Nature* **508**, 477–482.

Rohling, E.J., Hibbert, F.D., Williams, F.H., Grant, K.M., Marino, G., Foster, G.L., Hennekam, R., de Lange, G.J., Roberts, A.P., Yu, J., Webster, J.M., Yokoyama, Y., 2017. Differences between the last two glacial maxima and implications for ice-sheet, $\delta^{18}O$, and sea-level reconstructions. *Quaternary Science Reviews* **176**, 1–28.

Rollinson, H., 2002. The metamorphic history of the Isua Greenstone Belt, West Greenland. *Geological Society, London, Special Publications* **199**, 329–350.

Rose, N.M., Bird, D.K., 1994. Hydrothermally altered dolerite dykes in East Greenland: implications for Ca-metasomatism of basaltic protoliths. *Contributions to Mineralogy and Petrology* **116 (4)**, 420–432.

Rothwell, R.G., Hoogakker, B., Thomson, J., Croudace, I.W., Frenz, M., 2006. Turbidite emplacement on the southern Balearic Abyssal Plain (western Mediterranean Sea) during Marine Isotope Stages 1–3: an application of ITRAX XRF scanning of sediment cores to lithostratigraphic analysis. *Geological Society, London, Special Publications* **267**, 79–98.

Ruddiman, W.F., 1977. Late Quaternary deposition of ice-rafted sand in the subpolar North Atlantic (lat 40° to 65°N). *Geological Society of America Bulletin* **88**, 1813–1827.

Ruddiman, W.F., McIntyre, A., 1977. Late Quaternary surface ocean kinematics and climatic change in the high-latitude North Atlantic. *Journal of Geophysical Research* **82 (27)**, 3877–3887.

Ruddiman, W.F., Raymo, M.E., 1988. Northern Hemisphere climate régimes during the past 3 Ma: possible tectonic connections. *Philosophical Transactions of the Royal Society B: Biological Sciences* **318**, 411–430.

Ruddiman, W.F., Kutzbach, J.E., 1989. Forcing of late Cenozoic northern hemisphere climate by plateau uplift in southern Asia and the American west. *Journal of Geophysical Research: Atmospheres* **94 (D15)**, doi: 10.1029/JD094iD15p18409

Salzmann, U., Haywood, A.M., Lunt, D.J., Valdes, P.J., Hill, D.J., 2008. A new global biome reconstruction and data-model comparison for the Middle Pliocene. *Global Ecology and Biogeography* **17 (3)**, 432–447.

Sarmiento, J.L., Toggweiler, J.R., 1984. A new model for the role of the oceans in determining atmospheric P CO_2. *Nature* **308**, 621–624.

Sarmiento, J.L., Gruber, N., Brzezinski, M.A., Dunne, J.P., 2004. High-latitude controls of thermocline nutrients and low latitude biological productivity. *Nature* **427**, 56–60.

Sarnthein, M., Bartoli, G., Prange, M., Schmittner, A., Schneider, B., Weinelt, M., Andersen, N., Garbe-Schönberg, D., 2009. Mid-Pliocene shifts in ocean overturning circulation and the onset of Quaternary-style climates. *Climate of the Past* **5**, 269–283.

Schaefer, J.M., Finkel, R.C., Balco, G., Alley, R.B., Caffee, M.W., Briner, J.B., Young, N.E., Gow, A.J., Schwartz, R., 2016. Greenland was nearly ice-free for extended periods during the Pleistocene. *Nature* **540**, 252–255.

Scher, H.D., Bohaty, S.M., Zachos, J.C., Delaney, M.L., 2011. Two-stepping into the icehouse: East Antarctic weathering during progressive ice-sheet expansion at the Eocene–Oligocene transition. *Geology* **39 (4)**, 383–386.

Schmitz, W.J. Jr., 1996. On the World Ocean Circulation. Volume 1. Some Global Features / North Atlantic Circulation. *World Ocean Circulation* **1**, Woods Hole Oceanographic Institution, Massachusetts.

Seager, R., Battisti, Yin, J., Gordon, N., Naik, N., Clement, A.C., Cane, M.A., 2002. Is the Gulf Stream responsible for Europe's mild winters? *Quarterly Journal of the Royal Meteorological Society* **128 (586)**, 2563 –2586.

Seki, O., Foster, G.L., Schmidt, D.N., Mackensen, A., Kawamura, K., Pancost, R.D., 2010. Alkenone and boron-based Pliocene *p*CO_2 records. *Earth and Planetary Science Letters* **292** (12) 201–211.

Shackleton, N.J., Backman, J., Zimmerman, H., Kent, D.V., Hall, M.A., Roberts, D.G., Schnitker, D., Baldauf, J.G., Desprairies, A., Homrighausen, R., Huddlestun, P., Keene, J.B., Kaltenback, A.J., Krumsiek, K.A.O., Morton, A.C., Murray, J.W., Westberg-Smith, J., 1984. Oxygen isotope calibration of the onset of ice-rafting and history of glaciation in the North Atlantic region. *Nature* **307** 620–623**.**

Shackleton, N.J., Imbrie, F.R.S. and Pisias, N.G., 1988. The evolution of oceanic oxygen-isotope variability in the North Atlantic over the past three million years.

Philosophical Transactions of the Royal Society of London. Series B, Biological Sciences **318**, 679–688.

Shackleton, N.J., Hall, M.A., Pate, D., 1995. Pliocene stable isotope stratigraphy of Site 846. In: Pisias, N.G., Mayer, L.A., Janecek, T.R., Palmer-Julson, A., van Andel, T.H. (eds.), *Proceedings of the Ocean Drilling Program, Scientific Results* **138**, 337–355.

Shakun, J.D., Clark, P.U., He, F., Marcott, S.A., Mix, A.C., Liu, Z., Otto-Bleisner, B., Schmittner, A., Bard, E., 2012. Global warming preceded by increasing carbon dioxide concentrations during the last deglaciation. *Nature* **484**, 49–54.

Shipboard Scientific Party, 1987. Site 646. In: Srivastava, S.P., Arthur, M., Clement, B., *et al*. (eds.), *Proceedings of the ODP, Initial Reports* **105**: College Station, TX (Ocean Drilling Program), 419–674.

Shipboard Scientific Party, 1994. Site 918. In: Larsen, H.C., Saunders, A.D., Clift, P.D., *et al*. (eds.), *Proceedings of the ODP, Initial Reports* **152**: College Station, TX (Ocean Drilling Program), 177–256.

Shipboard Scientific Party, 1996. Site 907 (revisited). In: Jansen, E., Raymo, M.E., Blum, P., *et al*. (eds.), *Proceedings of the ODP, Initial Reports* **162**: College Station, TX (Ocean Drilling Program), 223–252.

Sigman, D.M., Jaccard, S.L., Haug, G.H., 2004. Polar stratification in a cold climate. *Nature* **428**, 59–63.

Sigman, D.M., Hain, M.P., Haug, G.H., 2010. The polar ocean and glacial cycles in atmospheric CO2 concentration. *Nature* **466**, 47–55.

Sijp, W.P., England, M.H., 2004. Effect of the Drake Passage throughflow on global climate. *Journal of Physical Oceanography*. **34** 1254–1266.

Smith, Y.M., Hill, D.J., Dolan, A.M., Haywood, A.M., Dowsett, H.J., Risebrobakken, B., 2018. Icebergs in the Nordic Seas throughout the Late Pliocene. *Paleoceanography* **33**, 318–335.

Snowball, I., Moros, M., 2003. Saw-tooth pattern of North Atlantic current speed during Dansgaard-Oeschger cycles revealed by the magnetic grain size of Reykjanes Ridge sediments at 59°N. *Paleoceanography* **18 (2)**, 1026, doi:10.1029/2001PA000732.

Solgaard, A.M., Reeh, N., Japsen, P., Nielsen, T., 2011. Snapshots of the Greenland ice sheet configuration in the Pliocene to early Pleistocene. *Journal of Glaciology* **57(205)**, 871–880.

Solignac, S., Seidenkrantz, M.-S., Jessen, C., Kuijpers, A., Gunvald, A.K., Olsen, J., 2011. Late-Holocene sea-surface conditions offshore Newfoundland based on dinoflagellate cysts. *The Holocene* **21 (4)**, 539–552.

Song, Z., Latif, M., Park, W., 2017. Expanding Greenland Ice Sheet Enhances Sensitivity of Plio-Pleistocene Climate to Obliquity Forcing in the Kiel Climate Model. Geophysical Research Letters 44, 9957–9966.

Sosdian, S., Rosenthal, Y., 2009. Deep-sea temperature and ice volume changes across the Pliocene-Pleistocene climate transitions. *Science* **325**, 306–310.

Spielhagen, R.F., Tripati, A., 2009. Evidence from Svalbard for near-freezing temperatures and climate oscillations in the Arctic during the Paleocene and Eocene. *Palaeogeography Palaeoclimatology Palaeoecology* **278**, 48–56.

Srivastava, S. P., Tapscott, C.R., 1986. Plate kinematics of the North Atlantic. In: Vogt, P.R., Tucholke, B.E., (eds.), *The geology of North America, v. M., the western North Atlantic region*. Geological Society of America, p. 379–404.

Srivastava, S.P., Arthur, M.A., 1989. Tectonic evolution of the Labrador Sea and Baffin Bay: constraints imposed by regional geophysics and drilling results from Leg 105. In: Srivastava, S.P., Arthur, M., Clement, B., *et al*. (eds.), *Scientific Results*. Ocean Drilling Program, College Station, pp. 989–1009.

Stephens, B.B., Keeling, R.F., 2000. The influence of Antarctic sea ice on glacial–interglacial CO 2 variations. *Nature* **404**, 171–174.

St John, K.E.K., Krissek, L.A., 2002. The late Miocene to Pleistocene ice-rafting history of Southeast Greenland. *Boreas* **31**, 28–35.

St John, K., 2008. Cenozoic ice-rafting history of the central Arctic Ocean: Terrigenous sands on the Lomonosov Ridge. *Paleoceanography* **23 (1)**, PA1S05.

St John., Passchier, S., Tantillo, B., Darby, D., Kearns, L., 2015. Microfeatures of modern sea-ice-rafted sediment and implications for paleo-sea-ice reconstructions. *Annals of Glaciology* **56 (69)**, 83–93.

Stanford, J.D., Rohling, E.J., Hunter, S.E., Roberts, A.P., Rasmussen, S.O., Bard, E., McManus, J., Fairbanks, R.G., 2006. Timing of meltwater pulse 1a and climate responses to meltwater injections. *Paleoceanography* **21 (4)**, PA4103, doi:10.1029/2006PA001340.

Stanford, J.D., Rohling, E.J., Bacon, S., Roberts, A.P., Grousset, F.E., Bolshaw, M., 2011. A new concept for the paleoceanographic evolution of Heinrich event 1 in the North Atlantic. *Quaternary Science Reviews* **30 (910)**, 1047–1066.

Stein, R., Hefter, J., Grützner, J., Voelker, A., Naafs, B.D.A., 2009. Variability of surface water characteristics and Heinrich-like events in the Pleistocene midlatitude North Atlantic Ocean: Biomarker and XRD records from IODP Site U1313 (MIS 16–9). P*aleoceanography* **24 (2)**, PA2203, doi:10.1029/2008PA001639.

Steinberger, B., Spakman, W., Japsen, P. and Torsvik T.H., 2015. The key role of global solid-Earth processes in preconditioning Greenland's glaciation since the Pliocene. *Terra Nova* **27 (1)**, 1–8.

Stickley, C.E., Brinkhuis, H., Schellenberg, S.A., Sliujs, A., Röhl, U., Fuller, M., Grauert, M., Huber, M., Warnaar, J., Williams, G.L., 2004. Timing and nature of the deepening of the Tasmanian Gateway. *Paleoceanography* **19 (4)**, PA4027, doi:10.1029/2004PA001022.

Stickley, C.E., St John, K., Koç, N., Jordan, R.W., Passchier, S., Pearce, R.B., Kearns, L.E., 2009. Evidence for middle Eocene Arctic sea ice from diatoms and ice-rafted debris. *Nature* **460**, 376–379.

Stone, E.J., Lunt, D.L., Annan, J.D., Hargreaves, J.C., 2013. Quantification of the Greenland ice sheet contribution to Last Interglacial sea level rise. *Climate of the Past* **9**, 621–639.

Stoner, J., Channell, J., Hillaire-Marcel, C., 1995. Magnetic properties of deep-sea sediments off southwest Greenland: Evidence for major differences between the last two deglaciations. *Geology* **23 (3)**, 241.

Storey, M., Duncan, R.A., Tegner, C., 2007. Timing and duration of volcanism in the North Atlantic Igneous Province: Implications for geodynamics and links to the Iceland hotspot. *Chemical Geology* **241 (3–4)**, 264–281.

Tan, N., Ramstein, G., Dumas, C., Contoux, C., Ladant, J.-B., Sepulchre, P., Zhang, Z., De Schepper, S., 2017. Exploring the MIS M2 glaciation occurring during a warm and high atmospheric CO2 Pliocene background climate. Earth and Planetary Science Letters 472, 266–276.

Tan, N., Ladant, J.-B., Ramstein, G., Dumas, C., Bachem, P., Jansen, E., 2018. Dynamic Greenland ice sheet driven by pCO2 variations across the Pliocene Pleistocene transition. *Nature Communications* **9**, 47–55.

Tarasov, L., Peltier, W.R., 2002. Greenland glacial history and local geodynamic consequences. *Geophysical Journal International* **150 (1)**, 198–229.

Theibault, F., Cremer, M., Debrabant, P., Foulon, J., Nielsen, O.B., Zimmerman, H., 1989 In: Srivastava, S.P., Arthur, M., Clement, B., *et al*. (eds.), *Proceedings of the Ocean Drilling Program, Scientific Results* **105**, 83–100.

Thiede, J., Vorren, T.O., 1994. The Arctic Ocean and its geologic record: Research history and perspectives. *Marine Geology* **119 (3–4)**, 179–184.

Thiede, J., Winkler, A., Wolf-Welling, T., Eldholm, O., Myhre, A.M., Karl-Heinz, B., Henrich, R., Stein, R., 1998. Late Cenozoic history of the Polar North Atlantic: results from ocean drilling. Quaternary Science Reviews 17, 185–208.

Thiede, J., Jessen, C., Knutz, P., Kuijpers, A., Mikkelsen, N., Nørgaard-Pedersen, N., Spielhagen, R. F., 2011. Millions of years of Greenland Ice Sheet history recorded in ocean sediments. *Polarforschung* **80 (3)**, 141–159.

Tiedemann, R., 1991. Acht Millionen Jahre Klimageschichte von Nordwest Afrika und Pal~io-Ozeanographie des angren- zenden Atlantiks: Hochaufl6sende Zeitreihen von ODP-Sites 658-661. Thesis. University of Kiel, 127 pp.

Tiedemann, R., Sarnthein, M., Shackleton, N.J., 1994. Astronomic timescale for the Pliocene Atlantic δ18O and dust flux records of Ocean Drilling Program Site 659. *Paleoceanography* **9 (4)**, 619–638.

Toggweiler, J.R., Dixon, K., Broecker, W.S., 1991. The Peru upwelling and the ventilation of the south Pacific thermocline. *Journal of Geophysical Research: Oceans* **96 (C11)**, 20467–20497.

Toggweiler, J.R., 1999. Variation of atmospheric CO_2 by ventilation of the ocean's deepest water. *Paleoceanography* **14 (5)**, 571–588.

Tripati, A.K., Eagle, R.A., Morton, A., Dowdeswell, J.A., Atkinson, K.L., Bahé, Y., Dawber, C.F., Khadun, E., Shaw, R.M.H., Shorttle, O., Thanabalasundaram, l., 2008. Evidence for glaciation in the Northern Hemisphere back to 44 Ma from ice-rafted debris in the Greenland Sea. *Earth and Planetary Science Letters* **265(1–2)**, 112–122.

Tripati, A., Darby, D., 2018. Evidence for ephemeral middle Eocene to early Oligocene Greenland glacial ice and pan-Arctic sea ice. Nature Communications 9, 1038, doi: 10.1038/s41467-018-03180-5.

Tyrell, S., Haughton, P.D.W., Daly, J.S., Kokfelt, T.F., Gagnevin, D., 2006. The use of the common Pb Isotope composition of detrital K-feldspar grains as a provenance tool and its application to Upper Carboniferous paleodrainage, Northern England. Journal of Sedimentary Research 76 (2), 324–345.

Tzedakis, P.C., Crucifix, M., Mitsui, T., Wolff, E.W., 2017. A simple rule to determine which insolation cycles lead to interglacials. *Nature* **542** 427–432.

Valet, J., Meynadier, L., 1993. Geomagnetic field intensity and reversals during the past four million years. *Nature* **366**, 234–238.

Valet, J., Fournier, A., Courtillot, V., Herrero-Bervera, E., 2012. Dynamical similarity of geomagnetic field reversals. *Nature* **490**, 89–93.

Valet, J.-P., Bassinot, F., Bouilloux, A., Bourlès, D., Nomade, S., Guillou, V., Lopes, F., Thouveny, N., Dewilde, F., 2014. Geomagnetic, cosmogenic and climatic changes across the last geomagnetic reversal from Equatorial Indian Ocean sediments. *Earth and Planetary Science Letters* **397**, 67–79.

Valet, J., Meynadier, L., Simon, Q., Thouveny, N., 2016. When and why sediments fail to record the geomagnetic field during polarity reversals. *Earth and Planetary Science Letters* **453**, 96–107.

Vanneste, K., Uenzelmann-Neben, G., Miller, H., 1995. Seismic evidence for long-term history of glaciation on central East Greenland shelf south of Scoresby Sund. *Geo-Marine Letters* **15**, 63–70.

Veersteegh, G.J.M., Brinkhuis, H., Visscher, H., Zonneveld, K.A.F., 1996. The relation between productivity and temperature in the Pliocene North Atlantic at the onset of northern hemisphere glaciation: a palynological study. *Global and Planetary Change* **11 (4)**, 155–165.

Vincent, E., Berger, W.H., 2013. Carbon Dioxide and Polar Cooling in the Miocene: The Monterey Hypothesis. In: Sundquist, E., Broecker, W. (eds.). *The Carbon Cycle and Atmospheric CO_2: Natural Variations Archean to Present.* doi: 10.1029/GM032p0455

Voglis, P., Rindby, A., 1995. Quantitative methods for the application of the scanning X-ray analytical microprobe (SXRAM). *Journal of Trace Microprobe Technology* **13**, 177–193.

Waddell, L.M., Hendy,I.L., Moore, T.C., Lyle, M.W., 2009. Ventilation of the abyssal Southern Ocean during the late Neogene: A new perspective from the Subantarctic Pacific. *Paleoceanography* **24 (3)**, PA3206, doi:10.1029/2008PA001661.

Wagner, T.J.W., Dell, R.W., Eisenman, I., 2017. An analytical model of iceberg drift. *Journal of Physical Oceanography* **47**, 1605–1616.

Walker, J.C.G., Hays, P.B., Kasting, J.F., 1981. A negative feedback mechanism for the long-term stabilization of Earth's surface temperature. *Journal of Geophysical Research: Oceans* **86 (C10)**, 9776–9782.

Wang, C., Zhao, X., Liu, Z., Lippert, P.C., Graham, S.A., Coe, R.S., Yi, H., Zhu, L., Liu, S., Li, Y., 2008. Constraints on the early uplift history of the Tibetan Plateau. *PNAS* **105 (13)**, 4987–4992.

Wara, M.W., Ravelo, A.C., Delaney, M.L., 2005. Permanent El Niño-like conditions during the Pliocene warm period. *Science* **309**, 758–761.

Weeks, R, Laj, C, Endignoux, L., Fuller, M., Roberts, A., Manganne, R., Blanchard, E., Goree, W., 1993. Improvements in long-core measurement techniques: applications in palaeomagnetism and palaeoceanography. *Geophysical Journal International* **114**, 651–662.

Weidick, A., 1995. Satellite Image Atlas of the Glaciers of the World: Greenland. Williams, R. S., Ferrigno, J. (eds.), *U.S. Geological Survey Professional Paper* **1386-C**, 153 pp.

Weidick, A., Bennike, O., 2007. Quaternary glaciation history and glaciology of Jakobshavn Isbræ and the Disko Bugt region, West Greenland: a review. *Geological Survey of Denmark and Greenland Bulletin* **14**, 78 pp.

Willeit, M., Ganopolski, A., Calov, R., Robinson, A., Maslin, M., 2015. The role of CO2 decline for the onset of Northern Hemisphere glaciation. *Quaternary Science Reviews* **119**, 22–34.

White, L., Bailey, I., Foster, G., Allen, G., Kelley, S., Andrews, J., Hogan, K., Dowdeswell, J., Storey, C., 2016. Tracking the provenance of Greenland-sourced, Holocene aged, individual sand-sized ice-rafted debris using the Pb-isotope compositions of feldspars and 40 Ar/ 39 Ar ages of hornblendes. *Earth and Planetary Science Letters* **433**, 192–203.

Willerslev, E., Cappellini, E., Boomsma, W., Nielsen, R., Hebsgaard, M.B., Brand, T.B., Hofreiter, M., Bunce, M., Poinar, H.N., Dahl-Jensen, D., Johnsen, S., Steffensen, J.P., Bennike, O., Schwenninger, J.-L., Nathan, R., Armitage, S., de Hoog, C.-J., Alfimov, V., Christl, M., Beer, J., Muscheler, R., Barker, J., Sharp, M., Penkman, K.E.H., Haile, J., Taberlet, P., Gilbert, M.T.P., Casoli, A., Campani, E., Collins, M.J., 2007. Ancient biomolecules from deep ice cores reveal a forested southern Greenland. *Science* **317**, 111–114.

Wilson, D.L., Smith Jr., W.O., Nelson, D.M., 1986. Phytoplankton bloom dynamics of the western Ross Sea ice edge—I. Primary productivity and species-specific production. Deep Sea Research Part A. *Oceanographic Research Papers* **33** (10), 1375–1387.

Wolf, T.C.W., Thiede, J., 1991. History of terrigenous sedimentation during the past 10 m.y. in the North Atlantic (ODP Legs 104 and 105 and DSDP Leg 81). *Marine Geology* **101(1–4)**, 83–102.

Woodard, S.C., Rosenthal, Y., Miller, K.G., Wright, J.D., Chiu, B.K., Lawrence, K.T., 2014. Antarctic role in Northern Hemisphere glaciation. *Science* **346**, 847–851.

Wright, J.D., 1998. Role of the Greenland-Scotland Ridge in Neogene Climate Changes. In: Crowley, T.J., Burke, K. (eds.), *Tectonic Boundary Conditions for Climate Reconstructions.* Oxford University Press, London, 192 pp.

Wunsch, 2003. The spectral description of climate change including the 100 ky energy. *Climate Dynamics* **20 (4)**, 353–363.

Xuan, C., Channell, J., 2009. UPmag: MATLAB software for viewing and processing u channel or other pass-through paleomagnetic data. *Geochemistry Geophysics Geosystems* **10**, Q10Y07.

Xuan, C., Channell, J.E.T., Hodell, D.A., 2016. Quaternary magnetic and oxygen isotope stratigraphy in diatom-rich sediments of the southern Gardar Drift (IODP Site U1304, North Atlantic). *Quaternary Science Reviews* **142**, 74–89.

Yamazaki, T., Oda, H., 2005. A geomagnetic paleointensity stack between 0.8 and 3.0 Ma from equatorial Pacific sediment cores. *Geochemistry Geophysics Geosystems* **6(11)**, Q11H20.

Zachos, J.C., Breza J.B., Wise, S.W., 1992. Early Oligocene ice-sheet expansion on Antarctica: Stable isotope and sedimentological evidence from Kerguelen Plateau, southern Indian Ocean. *Geology* **20 (6)**, 569–573.

Zachos J.C., Quinn, T.M., Salamy, K.A., 1996. High-resolution (104 years) deep-sea foraminiferal stable isotope records of the Eocene-Oligocene climate transition. *Paleoceanography* **11 (3)**, 251–266.

Zachos, J., Pagani, M., Sloan, L., Thomas, E., Billups, K., 2001a. Trends, rhythms and aberrations in global climate 65 Ma to present. *Science* **292**, 686–693.

Zachos, J.C., Shackleton, N.J., Revenaugh, J.S., Pälike, H., Flower, B.P., 2001b. Climate Response to Orbital Forcing Across the Oligocene-Miocene Boundary. *Science* **292**, 274–278.

Zachos, J.C., Dickens, G.R., Zeebe, R.E., 2008. An early Cenozoic perspective on greenhouse warming and carbon-cycle dynamics. *Nature* **451**, 279–283.

Zhang, Y.G., Ji, J., Balsam, W., Liu, L., Chen, J., 2009. Mid-Pliocene Asian monsoon intensification and the onset of Northern Hemisphere glaciation. *Geology* **37(7)**, 599–602.

Zhang, Y. G., Pagani, M., Liu, Z., Bohaty, S. M., DeConto, R., 2013. A 40-million-year history of atmospheric CO_2. *Philosophical Transactions of the Royal Society A* **371**, 20130096, doi:10.1098/rsta.2013.0096.

Zhang, X., Pease, V., Omma, J., Benedictus, A., 2015. Provenance of Late Carboniferous to Jurassic sandstones for southern Taimyr, Arctic Russia: A comparison of heavy mineral analysis by optical and QEMSCAN methods. *Sedimentary Geology* **329**, 116–176.

Zhisheng, A., Kutzbach, J.E., Prell, W.L., Porter, S.C., 2001. Evolution of Asian monsoons and phased uplift of the Himalaya–Tibetan plateau since Late Miocene times. *Nature* **411**, 62–66.

Appendix A: Manuscript and supplementary for Chapter 4

Southern Greenland glaciation and Western Boundary Undercurrent evolution recorded on Eirik Drift during the late Pliocene intensification of Northern Hemisphere glaciation

Keziah Blake-Mizen[1*], Robert G. Hatfield[2], Joseph S. Stoner[2], Anders E. Carlson[2], Chuang Xuan[3], Maureen Walczak[2], Kira T. Lawrence[4], James E.T. Channell[5], Ian Bailey[1*]

1. Camborne School of Mines & Environment and Sustainability Institute, University of Exeter, Penryn Campus, Treliever Road, Cornwall TR10 9FE, UK

2. College of Earth, Ocean, and Atmospheric Sciences, Oregon State University, Corvallis, Oregon 97331, USA

3. Ocean and Earth Science, National Oceanography Centre Southampton, University of Southampton Waterfront Campus, Southampton SO14 3ZH, UK

4. Department of Geology and Environmental Geosciences, Lafayette College, Easton, Pennsylvania 18042, USA

5. Department of Geological Sciences, University of Florida, Gainesville, FL 32611, USA

*Corresponding Authors: krb210@exeter.ac.uk, I.Bailey@exeter.ac.uk

Abstract: We present new sedimentological and environmental magnetic records spanning ~3.2–2.2 Ma, during the intensification of Northern Hemisphere glaciation, from North Atlantic Integrated Ocean Drilling Program Site U1307 on Eirik Drift. Our new datasets and their high-fidelity age control demonstrate that while inland glaciers – and potentially also at times restricted iceberg-calving margins – have likely existed on southern Greenland since at least ~3.2 Ma, persistent and extensive iceberg-calving

glacial margins were only established in this region at 2.72 Ma, ~300 kyr later than in northeastern and eastern Greenland. Despite a dramatic increase in Greenland-sourced ice-rafted debris deposition on Eirik Drift at this time, contemporaneous changes in the bulk magnetic properties of Site U1307 sediments, and a reduction in sediment accumulation rates, suggest a decrease in the delivery of Greenland-sourced glaciofluvial silt to our study site. We attribute these changes to a shift in depositional regime from bottom-current-dominated to glacial-IRD-dominated between ~2.9 and 2.7 Ma, in response to a change in the depth of the flow path of the Western Boundary Undercurrent relative to our study site.

Key Words: Plio-Pleistocene transition; Northern Hemisphere glaciation; Paleoclimatology; Paleoceanography; Paleomagnetism; Greenland Ice Sheet; North Atlantic; Ice-rafted debris; Relative paleointensity

1 Introduction

While glaciers have existed intermittently on Greenland since at least the late Eocene, with its first ice-shelf glaciations occurring possibly as early as the Miocene (Larsen *et al*., 1994), multiple lines of evidence (e.g., Larsen *et al*., 1994; Jansen *et al*., 2000; Thiede *et al*., 2011; Bierman *et al*., 2016) suggest that a major ice-sheet was not a persistent feature on Greenland until the late Pliocene to earliest Pleistocene intensification of Northern Hemisphere glaciation (iNHG), ~3.6–2.4 Ma (Mudelsee and Raymo, 2005). Our understanding of the spatial history of ice-sheet expansion on Greenland at this time, however, remains uncertain.

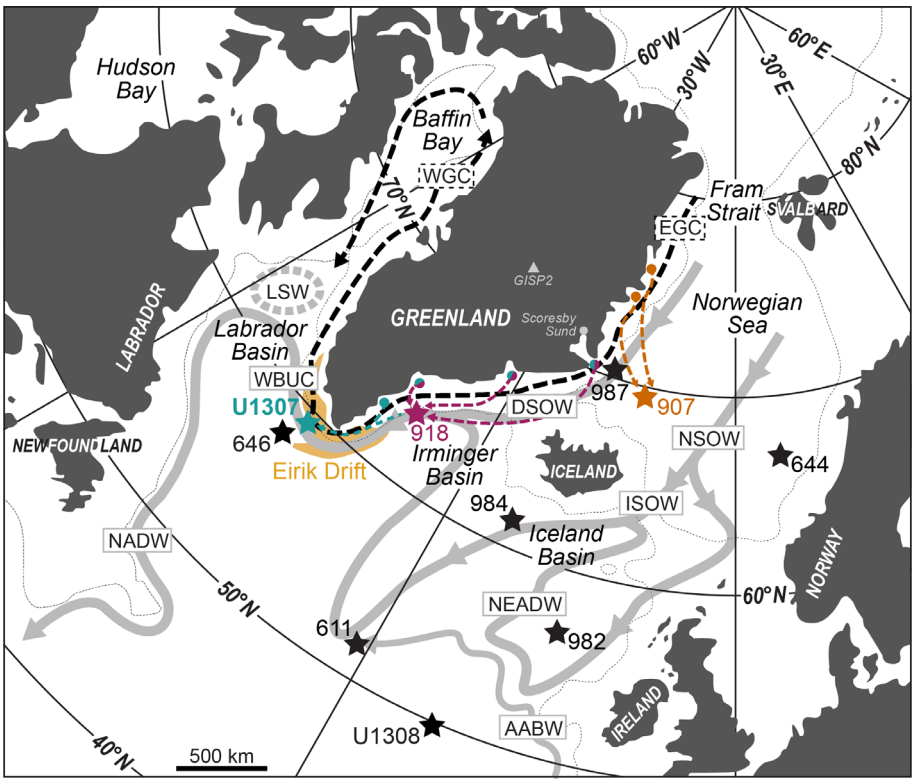

Figure 1 Map of Greenland and surrounding landmasses and ocean basins, showing the location of IODP Site U1307 on Eirik Drift, the position of sites mentioned in this text, and their relationships to the paths of key modern deep (solid grey) and surface (dashed black) ocean currents relevant to this study. ODP Sites 907 and 918, whose ice-rafting records are discussed in the text, are also highlighted, and main sources of ice-rafted debris to these sites and to U1307 are schematically represented by colour-coded arrows (based on iceberg trajectory simulations for the Last Glacial Maximum by Bigg *et al.*, 1998). EGC = East Greenland Current, WGC = West Greenland Current, NSOW = Norwegian Sea Water, ISOW = Iceland-Scotland Overflow Water, DSOW = Denmark-Scotland Overflow Water, NEADW = Northeast Atlantic Deep Water, AABW = Antarctic Bottom Water, WBUC = Western Boundary Undercurrent, LSW = Labrador Sea Water, NADW = North Atlantic Deep Water. The 1000 m isobath is given by thin dotted lines.

Since terrestrial evidence of Greenland glaciation during iNHG is rare (and its temporal interpretation non-unique, e.g., Schaefer *et al.*, 2016) due to its removal by subsequent glacial advances, our understanding of Greenland Ice Sheet (GrIS) evolution during the Plio-Pleistocene mainly relies on Greenland-proximal marine sediment records of ice-rafted debris (IRD; e.g., Jansen *et al.*, 2000; Thiede *et al.*, 2011). Greenland-proximal

IRD deposition is dominated by terrigenous sediment transported mainly by the East Greenland Current (EGC) in icebergs derived from multiple GrIS iceberg-calving sources (Fig. 1; Bigg *et al*., 1998; White *et al*., 2016). Spatial comparisons of orbitally-resolved paleo-records of marine IRD deposition near Greenland can therefore provide important insights into where and when the GrIS extended to the coast during iNHG. For this time period, IRD records are available from sites where ice-rafted sediments were sourced from northeastern (Ocean Drilling Program (ODP) Site 907; Jansen *et al*., 2000), eastern (ODP Site 907; Jansen *et al*., 2000; ODP Sites 914–918; Larsen *et al*., 1994; St John and Krissek, 2002) and southern (ODP Site 646; Wolf and Thiede, 1991) Greenland (Figs. 1 and 2). However, due to low benthic foraminifera abundances, it is not possible to generate independent orbital-resolution benthic $\delta^{18}O$ stratigraphies for any of these Greenland-proximal records spanning iNHG. Poor core recovery has also prevented the construction of detailed paleomagnetic stratigraphies for most of these sites.

The only continuous orbital-resolution Greenland-proximal IRD record with a complete palaeomagnetic reversal stratigraphy for iNHG comes from Site 907 on the Iceland Plateau (Figs. 1 and 2c; Jansen *et al*., 2000). Based on elevated IRD deposition at this site from ~3 Ma (Fig. 2c and d), we can infer that at least isolated iceberg-calving glaciers occupied coastal northeastern and eastern Greenland on orbital timescales following the end of the mid-Piacenzian warm period (mPWP, 3.264–3.025 Ma; Dolan *et al*., 2011) (see iceberg trajectories shown in Fig. 1; Bigg *et al*., 1998). A further and significant increase in IRD deposition at Site 907 from ~2.7 Ma indicates, however, that extensive iceberg-calving margins may not have been established in this region of Greenland until Marine Isotope Stage (MIS) G6, 2.72 Ma (Lisiecki and Raymo, 2005) (Fig. 2c and d). This suggestion is broadly supported by seismic evidence offshore Scoresby Sund that confirms the central-eastern GrIS was only frequently grounded below sea-level from ~2.6 Ma (Vanneste *et al*., 1995), and by a recent study of the

cosmogenic radionuclide (^{10}Be and ^{26}Al) isotope composition of quartz sands from ODP Sites 918 and 987 (Figs. 1 and 2b; Bierman *et al*., 2016) that infers the existence of a large ice-cap on at least eastern Greenland since the onset of the Quaternary. Our ability to improve our understanding of the wider regional history of GrIS growth during this time is hampered, however, by a lack of a well-dated, orbital-resolution continuous IRD record that is well-placed to receive detritus from southeastern and southern Greenland during iNHG.

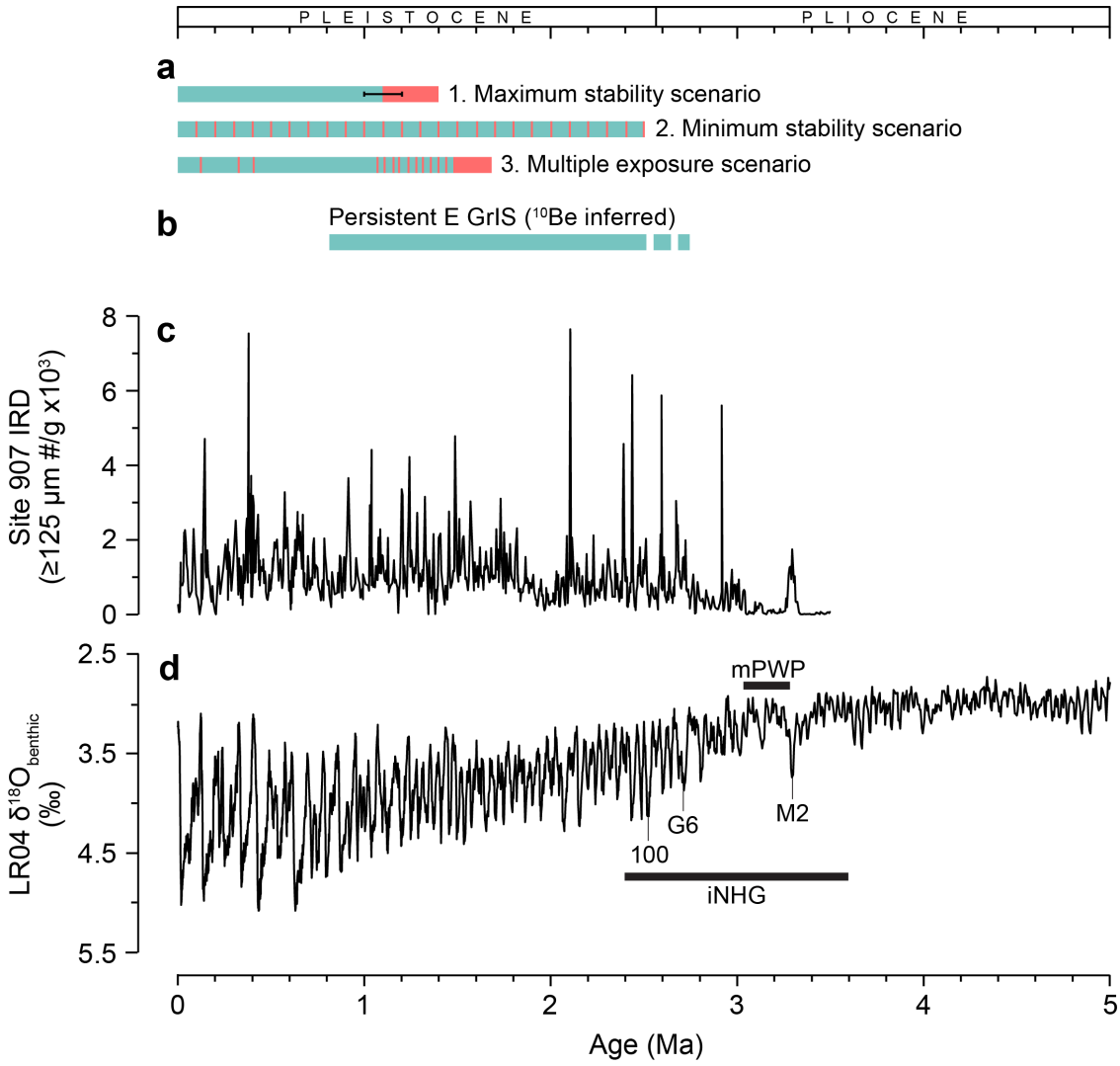

Figure 2 Synthesis of paleoclimatic records relevant to the Plio-Pleistocene history of the Greenland Ice Sheet (GrIS): (**a**) three scenarios for GrIS glaciation consistent with cosmogenic beryllium (^{10}Be) and aluminium (^{26}Al) isotopes in bedrock from the base of the GISP2 ice core (see Fig. 1 for location) (1. Maximum stability scenario = 280 ±30 kyr

ice-free conditions followed by 1.1 Ma continuous ice cover; 2. Minimum stability scenario = ice-free for 8 kyr of each 100-kyr cycle; 3. Multiple exposure scenario = ice-free for several thousand years during numerous major Pleistocene interglacials; Schaefer *et al*., 2016); (**b**) periods of eastern GrIS growth and stability inferred from seismic profiles offshore Scoresby Sund indicating East GrIS frequently grounded below sea-level (Vanneste *et al*., 1995) and from cosmogenic ^{10}Be and ^{26}Al isotopes in marine cores offshore eastern Greenland (Bierman *et al*., 2016); alongside (**c**) Iceland Basin ODP Site 907 IRD flux (Jansen *et al*., 2000); and (**d**) the LR04 $\delta^{18}O_{benthic}$ stack for reference (Lisiecki and Raymo, 2005). Labels in (d) are Marine Isotope Stages, and durations of the intensification of Northern Hemisphere glaciation (iNHG) and the mid-Piacenzian warm period (mPWP; Dolan *et al*., 2011) are also indicated.

Eirik Drift off southern Greenland is ideally located to monitor the history of the southern GrIS because it lies in the path of the EGC, and in the present day receives IRD from a range of eastern and southern Greenland iceberg-calving sources (Bigg *et al*., 1996; White *et al*., 2016). It is also well-positioned to monitor the strength of the Western Boundary Undercurrent (WBUC; Hunter *et al*., 2007), the behaviour of which during iNHG is not fully understood (Hunter *et al*., 2007; Müller-Michaelis and Uenzelmann-Neben, 2014; Parnell-Turner *et al*., 2015). Studies that combine analysis of both the sedimentological character and environmental magnetic signature of Pleistocene sediments from Eirik Drift have proved particularly useful in this regard, because they can be utilised to reconstruct relative changes in bottom-current strength and the provenance of glacially-derived terrigenous sediments from southern Greenland that they entrain (e.g., Evans *et al.*, 2007; Stoner *et al*., 1995; Hatfield *et al*., 2016; 2017; Channell *et al.*, 2014). However, these techniques have yet to be applied to records spanning the iNHG interval.

To further our understanding of GrIS and WBUC behaviour during iNHG, we present high-resolution IRD, paleomagnetic and environmental magnetic records spanning ~3.2 to 2.2 Ma from Integrated Ocean Drilling Program (IODP) Site U1307, situated on Eirik Drift in the northern North Atlantic Ocean (Fig. 1). Our study benefits

from updated chronological control through the generation of a new relative paleointensity (RPI)-based age model – the first of its kind for high-latitude sediments deposited during iNHG. On this high-fidelity age model, our new high-resolution multi-proxy records demonstrate for the first time that glacial maturation of southern Greenland ~2.7 Ma occurred in concert with a change in WBUC behaviour.

2 Study Site and Methods

2.1 Study site and sampling

Eirik Drift is an extensive, elongate contourite drift located just south of Greenland (Fig. 1) that began to form in the Miocene (Hunter *et al*., 2007; Müller-Michaelis and Uenzelmann-Neben, 2014). It lies underneath the path of the EGC, a southward-flowing surface current that transports icebergs calved from outlet glaciers along Greenland's eastern coast. Eirik Drift is also sculpted directly by the vigorous and dynamic deep WBUC, the main axis of which shoals during late Pleistocene glacials (Hillaire-Marcel *et al.*, 1994; Hillaire-Marcel and Bilodeau, 2000; Mazaud *et al*., 2015). The EGC and WBUC constitute major transport pathways for delivering detrital sediments glacially eroded on Greenland to the adjacent marine margins, and ultimately to Eirik Drift (Hunter *et al*., 2007). Icebergs transported along the EGC can contain clay- to boulder-sized IRD from a range of marine-terminating eastern and southern Greenland iceberg-calving sources, which rains out to the seabed as they melt (Fig. 1; White *et al*., 2016). The WBUC can entrain these sediments and mix them with subglacially-eroded southern Greenland Precambrian terrane bedrock clay- and silt-sized grains, as well as volcanic detritus from East Greenland and Iceland (Stoner *et al*., 1995; Carlson *et al*., 2008; Colville *et al*., 2011; Hatfield *et al*., 2016).

IODP Site U1307 is located on the northern flank of Eirik Drift (Fig 1; 58°30.3'N, 46°24.0'W, 2575 m water depth). Two holes were drilled at Site U1307 (U1307A and

U1307B) during IODP Expedition 303 in 2004, which together recovered a ~175 m composite Plio-Pleistocene section (Expedition 303 Scientists, 2006a). To examine the evolution of the southern GrIS and WBUC during iNHG, Site U1307 cores were sampled with u-channels (typically 2 × 2 × 150 cm continuous samples; Weeks *et al*., 1993) and discrete 20 cc scoops at 10 cm intervals at the MARUM IODP Core Repository in Bremen, Germany. Sampling was guided by the shipboard-derived paleomagnetic record and the primary splice (Expedition 303 Scientists, 2006a) between ~113 and 148 metres below seafloor (mbsf) in U1307A, and ~110 and 136 mbsf in U1307B.

2.2 Methods

2.2.1 Paleo- and environmental magnetism

The natural remanent magnetisation (NRM) and anhysteretic remanent magnetisation (ARM) of each u-channel sample were measured at 1-cm intervals using a 2G Enterprises™ model 755-1.65UC superconducting rock magnetometer at the Paleo- and Environmental Magnetism Laboratory at Oregon State University (OSU). NRM was measured following inline stepwise alternating field (AF) demagnetisation at peak AF from 20 to 80 mT. Additional steps up to peak AF of 100 mT were applied to nine u-channels known from shipboard paleomagnetic measurements to contain a polarity reversal (Expedition 303 Scientists, 2006a). Component paleomagnetic directions used to define the characteristic remanent magnetisation (ChRM) directions, and maximum angular deviation (MAD) used to assess the quality of the component magnetisation estimates, were calculated from principal component analysis of 7 equally-spaced demagnetisation steps over 20–50 mT following Kirschvink (1980), using the UPmag software of Xuan and Channell (2009). Guided by the inclination data, declination values were rotated to a mean of 0° (180°) for periods of normal (reversed) polarity on a core-by-core basis.

ARM was acquired inline using a 100 mT peak AF and a 0.05 mT direct current (DC) bias field along each u-channel's long-axis. The ARM was remeasured after each 5–10 mT increment of AF demagnetisation in the 10–60 mT peak field range. Low-field volume-normalised (bulk) magnetic susceptibility (κ) was measured every 1cm for each u-channel at OSU's Marine Geology Repository using a Bartington MS2C 36 mm diameter loop sensor mounted on a software motion-controlled track. ARM and κ both reflect the concentration of ferrimagnetic (titanomagnetite, magnetite) grains in a sample, although ARM is more sensitive to the fine ferrimagnetic fraction (King *et al*., 1983).

The susceptibility of ARM (κ_{ARM}) was determined by normalising ARM by the DC field applied during ARM acquisition. The ratio of κ_{ARM} over the low-field bulk magnetic susceptibility, κ_{ARM}/κ, is commonly used to track variations in ferrimagnetic grain-size. Low (high) κ_{ARM}/κ values imply a coarser (finer) average ferrimagnetic grain-size (King *et al*., 1983; Bloemendal *et al*. 1992), and this parameter has been used in Pleistocene North Atlantic studies to monitor variations in deep-water circulation and inputs of Greenlandic detritus (e.g., Stoner *et al*., 1995; Evans *et al*., 2007; Mazaud *et al*., 2012; Channell *et al*., 2014).

The magnetic signature of Eirik Drift is sensitive to deposition of glaciofluvial silt-size sediments subglacially eroded from Archean and Paleoproterozoic felsic crystalline bedrock by the GrIS, and Cenozoic volcanics from Iceland and eastern Greenland (e.g., Colville *et al*., 2011). These distinct sources can be discriminated using radiogenic (Colville *et al.*, 2011) and magnetic (Hatfield *et al.*, 2013; 2017) properties measured on a particle-size specific basis. Clay-sized terrestrial fractions (defined here as <3 μm) from both Greenland and Iceland are characterised by low concentrations of ferrimagnetic minerals (low κ) and relatively fine ferrimagnetic grain-sizes (high κ_{ARM}/κ). In contrast, silt (and sand) size fractions from both sources have up to an order of magnitude higher magnetic susceptibility (Hatfield *et al.*, 2017), indicating higher

concentrations of ferrimagnetic minerals in the larger size fractions. Silts and sands from Iceland are dominated by magnetically fine-grained titanomagnetite inclusions (yielding higher κ_{ARM}/κ values), which can be discriminated from Greenland-derived silts and sands that are dominated by coarser discrete magnetites (yielding lower κ_{ARM}/κ values) (Hatfield *et al.*, 2013; 2017). While Eirik Drift bulk sediments are an aggregate of magnetically-fine silts and sands from Iceland and magnetically-fine clays that can originate from multiple sources, significant source-driven coarsening of the bulk magnetic grain-size record can only be driven by accumulation of Greenland-derived silt and sand, which can be linked to changes in GrIS dynamics (Colville *et al*., 2011; Hatfield *et al*., 2016).

2.2.2 Shipboard splice revision

To improve the continuity of the iNHG record from Site U1307, we used our new high-resolution u-channel κ data to revise the shipboard splice for our target interval. Our revised splice for ~117–176 revised metres composite depth, rmcd (see Table 1, also Table S1 and Fig. S1 of Supplementary Material) uses, but refines, tie points utilised in the shipboard splice (Expedition 303 Scientists, 2006a; see also Fig. S2 of Supplementary Material).

2.2.3 Relative paleointensity (RPI) based age model

Benthic foraminifera abundances are low in Pliocene-aged Eirik Drift sediments (Expedition 303 Scientists, 2006a). It is therefore difficult to generate a benthic $\delta^{18}O$-based age model for Site U1307, and planktic $\delta^{18}O$-derived records from this region can be influenced by freshwater inputs from ice melt (Hillaire-Marcel *et al.*, 1994). To circumvent these problems, we generated a reversal- and a relative paleointensity (RPI)-based magnetostratigraphy using our u-channel NRM and ARM data. Previous

paleomagnetic studies of Eirik Drift sediments (Stoner *et al*., 1995; Evans *et al*., 2007; Mazaud *et al*., 2012; Channell *et al*., 2014) and of Site U1307 cores in particular (Kawamura *et al*., 2012; Mazaud *et al*., 2015) show that the magnetic assemblage is dominated by (titano)magnetite with a relatively uniform magnetic grain-size in the pseudo-single domain (PSD) range (Fig. S4b), and that RPI is a useful tool to provide chronological control.

Since NRM intensity is sensitive to the strength of Earth's magnetic field upon, or shortly after, sediment deposition, and ferrimagnetic grain concentration, we used ARM to normalise NRM intensity to compensate for variations in magnetic concentration (King *et al*., 1983). RPI was estimated using the slope of NRM and ARM values over the 20–50 mT peak AF demagnetisation interval (Channell *et al*., 2002). To generate a U1307 RPI-based age model, we initially anchored the stratigraphy at the polarity reversal boundaries, then tuned the RPI record within periods of stable polarity to the RPI record from IODP Site U1308 (Channell *et al*., 2016). The Site U1308 RPI record was chosen as a tuning target because it spans the past ~3.15 Ma, has a high-quality magnetic record and orbital-resolution benthic $\delta^{18}O$-based chronology tied to the LR04 stack, and serves as the anchor record for the PISO stack (Channell *et al*., 2009; 2016). To provide a magnetic stratigraphy beyond the u-channelled interval, we constructed inclination and RPI proxy records using lower (5 cm)-resolution shipboard-acquired data for both U1307 (down to the maximum drilled depth) and U1308 (to the end of Hole C) – deriving a RPI estimate from NRM intensity (demagnetised in peak AF of 20 mT) normalised by bulk magnetic susceptibility, κ (see Section B of Supplementary Material and Fig. S3). This estimate of RPI is not as robust as our u-channel-based estimate, partly due to imperfect normalisation of NRM by κ, but its use here is justified by the similarity of this record to our u-channel-derived RPI estimates where overlap exists (Fig. S3). Importantly, it allows

us to extend our observations through the top of the Mammoth subchron (3.207 Ma), which improves our age model validation.

2.2.4 Ice-rafted debris estimates

To examine the history of iceberg-rafting to Site U1307 during iNHG, we generated a record of weight percent (wt.%) IRD for the ≥212 μm size fraction. Each discrete sample was dried in an oven to determine its dry bulk weight, then disaggregated in a Calgon solution and washed over a 63 μm sieve to isolate the sand-sized fraction. The percentage of ice-rafted terrigenous material in the ≥212 μm fraction of each sample (following further sieving) was estimated using a standard method (e.g., St. John and Krissek, 2002). Sand-sized constituents excluded from our definition of 'ice-rafted debris' were volcanic tephra, pyrite, biogenics (mostly diatoms and foraminifers) and burrow casts. Weight percent IRD was then estimated for each sample using the ≥212 μm fraction weight as a percentage of the dry bulk sediment weight. To compare the history of terrigenous sand inputs at Site U1307 to those previously published from Eirik Drift at Ocean Drilling Program (ODP) Site 646 (Fig. 1; Wolf and Thiede, 1991), we also estimated the wt.% of sand-sized terrigenous constituents in the bulk ≥63 μm sand fraction of each of our samples.

The Iceland Plateau Site 907 IRD record is reported in ≥125 μm lithic grains per gram of dry sediment (Jansen *et al*., 2000), whereas our new IRD record from Site U1307 is reported as wt.% ≥212 μm IRD. To help compare our data to those available from Site 907, we generated twenty-eight additional IRD data for Site U1307 for our study interval, expressed as lithic grains (minus fresh volcanic glass and pyrite) ≥125 μm per gram of dry sediment, following Bailey *et al.* (2013). To investigate whether changes in the size fraction used to perform IRD counts have the potential to modify inferences made on the

magnitude of iceberg rafting to our study site, we recounted the same samples after sieving for the ≥150 μm size-fraction.

2.2.5 Grain-size distribution

To evaluate the potential influence of changes in the relative abundance of clay, silt and sand deposited at Site U1307 during iNHG on our bulk magnetic records, we estimated physical grain-size distributions for the terrigenous fraction using discrete 1–2 cm^3 samples for 18 selected points between 136.9 and 118.3 rmcd – an interval containing the largest-amplitude κ and ARM variations in our magnetic records (see Fig. S4a) – using a Malvern Mastersizer 3000 laser diffraction particle size analyser at the University of Exeter's Penryn Campus.

Prior to analysis, organics and biogenics were removed from each sample (see Section E of Supplementary Material). Ten repeat grain-size measurements were made on a well-mixed aliquot of each sample, and this procedure repeated on a separate subsample. The values reported for each sample are an average of all measurements made. Following Hatfield *et al*. (2013; 2017), size fractions are defined here as: clay <3 μm, very fine silt 3–10 μm, fine– medium silt 10–32 μm, medium–coarse silt 32–63 μm, and sand >63 μm.

3. Results and Discussion

3.1 New RPI-based age model for Eirik Drift sediments deposited during iNHG

The results of our nested magnetostratigraphic and RPI-based tuning exercise between Sites U1307 and U1308 are shown in Figure 3 (see also Section C in Supplementary Information). Using the Gauss-Matuyama (G/M) boundary and the top of the Kaena as initial tie-points, the majority of the peaks and troughs in the U1307 and U1308 RPI estimates can be correlated between 3.22 and 2.24 Ma. The mismatch in RPI between

U1307–U1308 during ~3.15–3.10 Ma (Fig. 3b) can be attributed to the low concentration of ferrimagnetic minerals in U1307 sediments deposited during this interval indicated by the magnetic susceptibility low in this site's stratigraphy between 163.4 and 156.4 rmcd (Fig. S4a; Expedition 303 Scientists, 2006a). The match between the two RPI records is achieved using thirty-three tie-points (see Tab. S3 in Supplementary Material) and an assumption of constant sedimentation rate between adjacent tie-points. The regionally-coherent nature of the RPI high captured in our record immediately prior to the G/M boundary, and of the trends in our U1307 record in general, are confirmed by the strong correspondence between our RPI record and that from nearby Gardar Drift Site U1314 between ~2.7 and 2.2 Ma (Fig. S6; Ohno *et al*., 2012). Key similarities also exist between our RPI record and those derived from other globally-distributed sites, including ODP Leg 138 (Valet and Meynadier, 1993) and the equatorial Pacific EPAPIS-3000 stack (Yamazaki and Oda, 2005) (Fig. S6). The limited planktic $\delta^{18}O$ data available for U1307 for this interval (Sarnthein *et al*., 2009) correlate well with the U1308 benthic $\delta^{18}O$ stratigraphy (and with the LR04 stack where U1308 data are absent) on this new age model (Fig. 3c), providing independent confirmation for our RPI tuning.

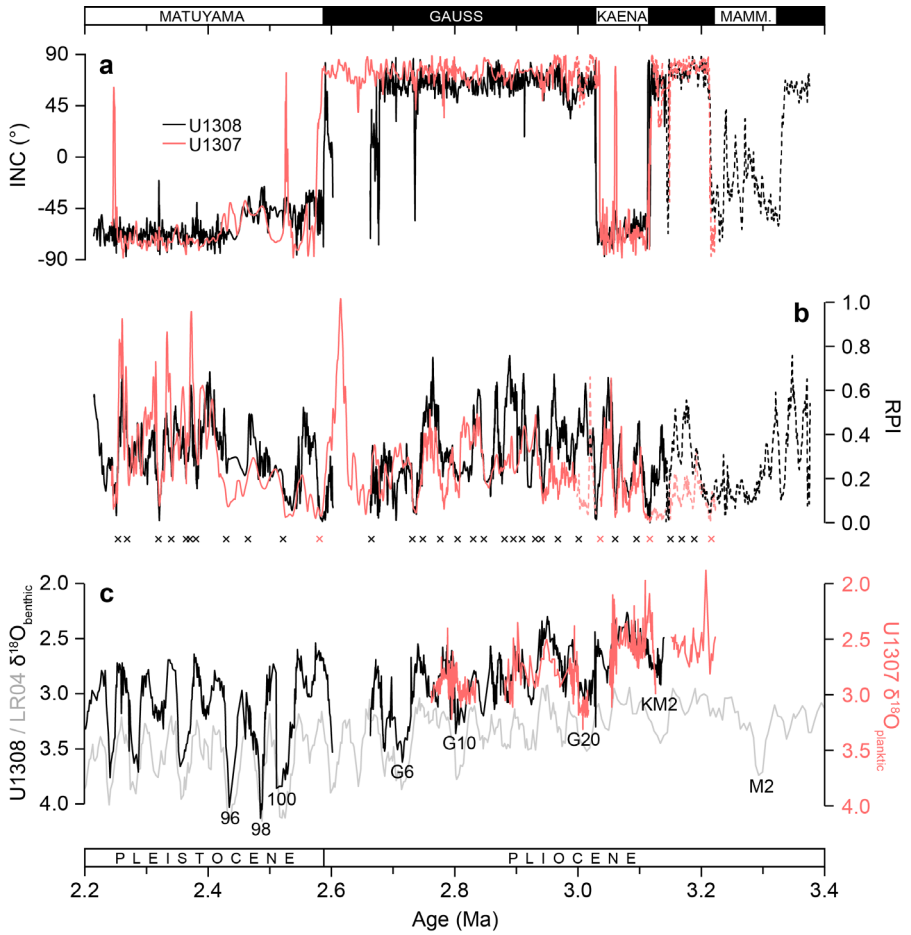

Figure 3 Site U1307 and U1308 records of (**a**) inclination (INC; red = this study; black = Channell *et al*., 2016), (**b**) relative paleointensity (RPI; red = this study; black = Channell *et al*., 2016) and (**c**) $\delta^{18}O$ (red = Sarnthein *et al*., 2009; black = Channell *et al*., 2016; grey = Lisiecki and Raymo, 2005). Solid lines in (a) and (b) show u-channel-derived data. Dashed lines show shipboard-derived split core data (see Section B and Fig. S3 of Supplementary Material). Red/black crosses indicate reversal-/RPI based tie-points, also given in Table S3. Labels in (c) are Marine Isotope Stages. The U1308 reference RPI stratigraphy was 'unhooked' at 197.40 mcd because a hiatus has been identified at this depth spanning MIS G2–104 (~2.65–2.60 Ma; Channell *et al*., 2016).

Based on our new age model, the oldest sediments recovered at Site U1307 are ~3.22 Ma and the oldest observed paleomagnetic reversal is the top of the Mammoth (Fig. 3a; C2An.2r, 3.207 Ma; Ogg, 2012), significantly revising the shipboard-designated age of ~3.58 Ma. This new chronology suggests that the Site U1307 stratigraphy contains a near-complete record of the mPWP between ~175.5 and 146.7 rmcd. We tentatively suggest that the short normal polarity excursion captured near the top of our record (Fig. 3a) is

equivalent to an unnamed event recorded at ODP Site 982 at ~2.24 Ma (Channell and Guyodo, 2004). Other short normal polarity excursions occur at ~2.52 and ~3.06 Ma in our record (Fig. 3a), but to our knowledge excursion events at these times have not been identified elsewhere.

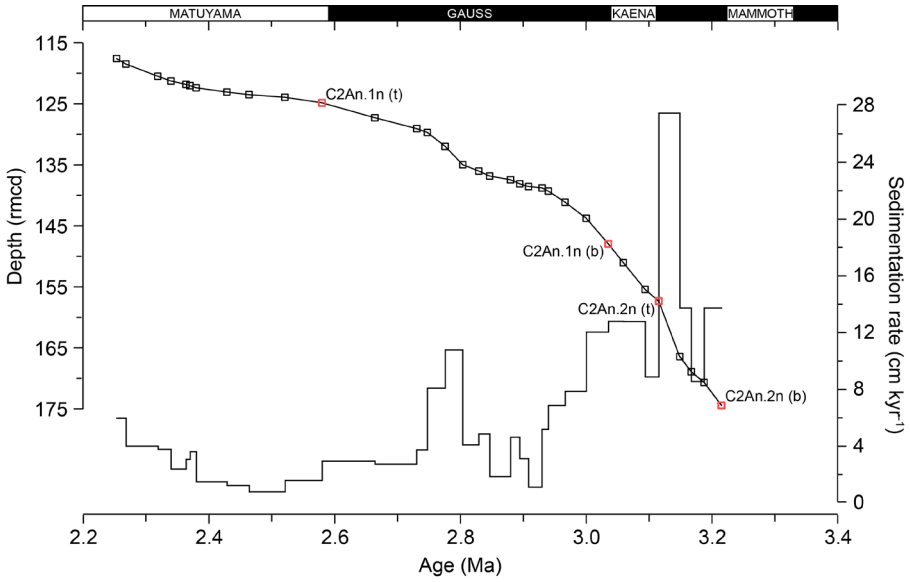

Figure 4 Age-depth relationship for Site U1307 based on tie-points between U1307 and U1308 shown in Fig. 3 (see also Tab. S3 of Supplementary Material), and linear sedimentation rates calculated between each tie-point. Black/red squares indicate relative paleointensity-/reversal-based tie-points used.

Our new age model reveals that between ~3.2 and 2.2 Ma, the average sedimentation rate at Site U1307 was ~6 cm kyr^{-1} (Fig. 4), similar to the average Pleistocene rate of ~5.5 cm kyr^{-1} reported by Mazaud *et al.* (2015). The early part of the record, however, is characterised by much higher and more variable sedimentation rates than this average, which decreased from values of ~10–12 cm kyr^{-1} to ~2–4 cm kyr^{-1} between ~3.0 and 2.7 Ma, reaching a minimum of just ~1 cm kyr^{-1} at ~2.5 Ma before quadrupling between ~2.4 and ~2.2 Ma (Fig. 4). Sedimentation rates estimated for the deeper-water Eirik Drift Site 646 (~3450 m), although highly averaged over our study interval due to limited age control, are broadly consistent with our new highly-resolved

U1307 record and also hint that sedimentation rates likely decreased over a wide range of water depths on Eirik Drift around 2.7 Ma (Fig. S7b; Wolf and Thiede, 1991).

3.2 New records of IRD deposition and environmental magnetism on Eirik Drift during iNHG

Our new late Pliocene to earliest Pleistocene records of coarse (wt.% ≥212 μm and grains ≥150 μm g^{-1}) IRD abundance, wt.% ≥63 μm terrigenous sand, bulk volume-specific magnetic susceptibility (κ) and magnetic grain-size (κ_{ARM}/κ) of Site U1307 sediments deposited between ~3.2 and 2.2 Ma are presented in Figure 5. The coarse IRD deposited at U1307 during our target interval is mainly composed of quartz, feldspar, mica and lithic clasts of granite, gneiss, basalt and troctolite/gabbro, with minor accessory hornblende and epidote. Variability in its abundance follows the same general pattern as that seen in early Pleistocene and other late Pliocene records (IRD elevated periodically on ~41-kyr timescales during cold stages and/or glacial terminations; Fig. 5b). Coarse IRD deposition was mainly absent at U1307 during the mPWP, and IRD is only present in small abundances (~1–2 wt.% ≥212 μm; ~200–1000 grains ≥150 μm g^{-1}) during (de)glacials between ~3 and 2.75 Ma. From MIS G8 onwards, however, coarse IRD inputs were persistently elevated on orbital timescales (with peak abundances during glacials of ~10–14 wt.% ≥212 μm; ~1800–3800 grains ≥150 μm g^{-1}).

The abundance of ≥63 μm sand in U1307 sediments deposited during our study interval also varies most strongly on ~41-kyr timescales, ranging from 0–40 wt.% throughout our study interval (Fig. 5a). In contrast to our coarse wt.% ≥212 μm IRD record, however, ≥63 μm terrigenous sand deposition at Site U1307 is strongly elevated during interglacials prior to ~2.7 Ma that in the vast majority of cases are not associated with coarse IRD deposition (Fig. 5a and b). Sand deposited during these intervals is composed of mostly well-sorted, fine, rounded quartz sand grains, and contains a

significant but variable (~10–70%) biogenic component of both foraminifera and diatom tests. Following the onset of persistently elevated coarse IRD deposition ~2.7 Ma, however, the ≥63 µm terrigenous sand fraction is composed of mostly (sub)angular grains that are heterogeneous in composition with at most a ~20% diatom component, and variations in its abundance closely follow changes in wt.% ≥212 µm IRD.

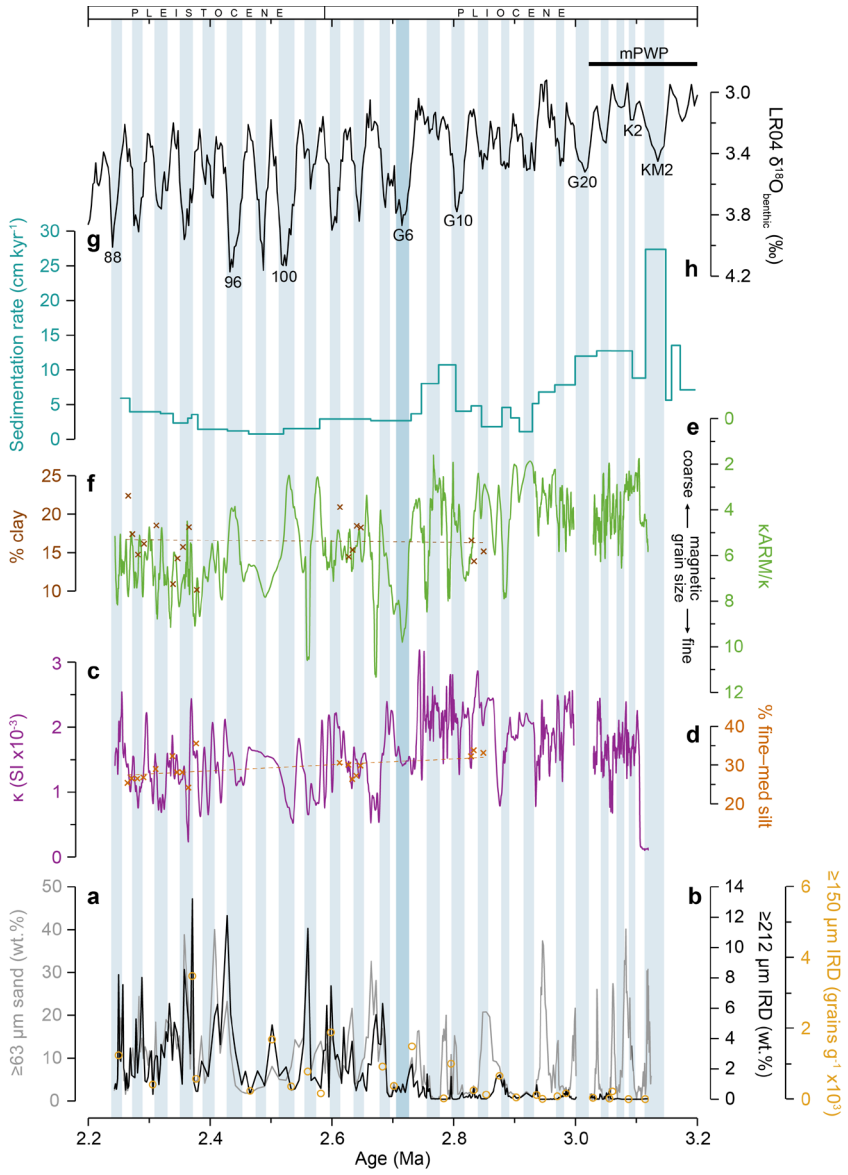

Figure 5. Site U1307 paleoclimate records: (**a**) wt.% ≥63 µm terrigenous sediment, (**b**) wt.% ≥212 µm IRD and grains ≥150 µm,IRD g^{-1} (**c**) magnetic susceptibility (κ), (**d**) % fine–medium silt (10–32 µm), (**e**) κ_{ARM}/κ, (**f**) % clay (<3 µm) and (**g**) sedimentation rate. The LR04 benthic $\delta^{18}O$ stack is shown in (**h**) for reference (Lisiecki and Raymo, 2005). Numbers in (h) are Marine Isotope Stages, with the duration of the mid-Piacenzian warm period (mPWP; Dolan *et al*., 2011) also indicated. Vertical blue bars highlight cold stages. See also Table S3 of Supplementary Material for values given in (d) and (f).

Our environmental magnetic records (κ and κ_{ARM}/κ) exhibit orbital-scale variability throughout most of our study interval, with higher magnetic susceptibility and coarser magnetic grain-size generally characterising (de)glacial intervals containing coarse IRD (compare Fig. 5b to c and e). Site U1307 magnetic susceptibility increased dramatically from near-zero values during the termination of MIS KM2, ~3.1 Ma, and is associated with relatively low κ_{ARM}/κ values. Following the cessation of the mPWP, ~3 Ma, magnetic susceptibility remains high and κ_{ARM}/κ values remain relatively low, but glacial-interglacial variability in these parameters increased between 2.9 and 2.5 Ma, particularly in the κ_{ARM}/κ record. Both records show a marked shift between 2.9 and 2.7 Ma, coincident with the onset of persistently elevated coarse IRD inputs to U1307 – κ decreases and the average magnetic grain-size assemblage fines (higher κ_{ARM}/κ values).

The bulk magnetic nature of Eirik Drift sediments can be influenced by changes both in sediment source (Stoner *et al.,* 1995; Hatfield *et al.*, 2016) and potentially sediment texture (Hatfield *et al*., 2013; 2017). The sensitivity of our magnetic records to both these processes can be established by comparing their relationships to terrigenous grain-size data (Hatfield *et al*., 2016; 2017), and the relationships of κ and κ_{ARM}/κ with percent clay, very fine/fine–medium/medium–coarse silt, and sand in U1307 sediments are shown in Figure 6. Terrestrial sources (Hatfield *et al*., 2017) and sediments from Eirik Drift Site MD99-2227 (Hatfield *et al*., 2016) suggest that the magnetic susceptibility of the clay-size fraction is several times lower than the silt-size fractions, and as a result the clay fraction likely exerts restricted influence on bulk κ values (e.g., Hatfield *et al.*, 2019). Relatively low variability in % clay data (Fig. 5f) and the little to no correlation between % clay and κ ($r = -0.125$; Fig. 6a) suggests that any increase in magnetically weak clay-size fractions is unlikely to have driven the secular fining signal seen in our magnetic records between ~2.9 and 2.7 Ma in U1307. Of the three silt size fractions, % fine–

medium silt (10–32 μm) has the strongest relationship with bulk magnetic properties, and this size fraction has recently been found to have a strong influence on bulk magnetic susceptibility records (Hatfield *et al.*, 2019). The relatively strong positive correlation that we observe between % fine–medium silt and bulk κ (r = 0.733; Fig. 6c) is most likely attributable to the enrichment of ferrimagnetic grains in this terrigenous grain-size fraction (Hatfield *et al*., 2013; 2017).

Bulk Mrs/Ms (ratio of remanent saturation moment (Mrs) to saturation moment (Ms)) values from sediments deposited at Site U1307 during the Plio-Pleistocene are generally ~0.1–0.2 (Kawamura *et al*., 2012; Mazaud *et al*., 2015), which implies a relatively restricted coarse PSD-size range of ferrimagnetic grains when viewed on a Day plot (Day *et al*., 1977) (Fig. S4). Particle-size-specific studies of terrestrial sources relevant for Eirik Drift provenance (outside of Heinrich event intervals) show that only silts and sands from Greenland (and not the Cenozoic volcanics of Iceland or of eastern Greenland) can yield Mrs/Ms values <~0.15 (Hatfield *et al*., 2017). Higher fine–medium silt abundance and bulk κ are most strongly associated with lower κ_{ARM}/κ values (r = 0.441; Fig. 6h) and thus a coarser magnetic grain-size assemblage, which is consistent with increased sourcing of silt from Greenlandic terranes relative to Cenozoic volcanic contributions (Hatfield *et al*., 2016; 2017). This relationship between bulk magnetic parameters and % silt has previously been observed at Eirik Drift Site MD99-2227, where it has been shown that increases in bulk κ, % silt and coarser magnetic grain-sizes reflect increased export of glaciofluvial silt from Greenland (Hatfield *et al*., 2016; 2017).

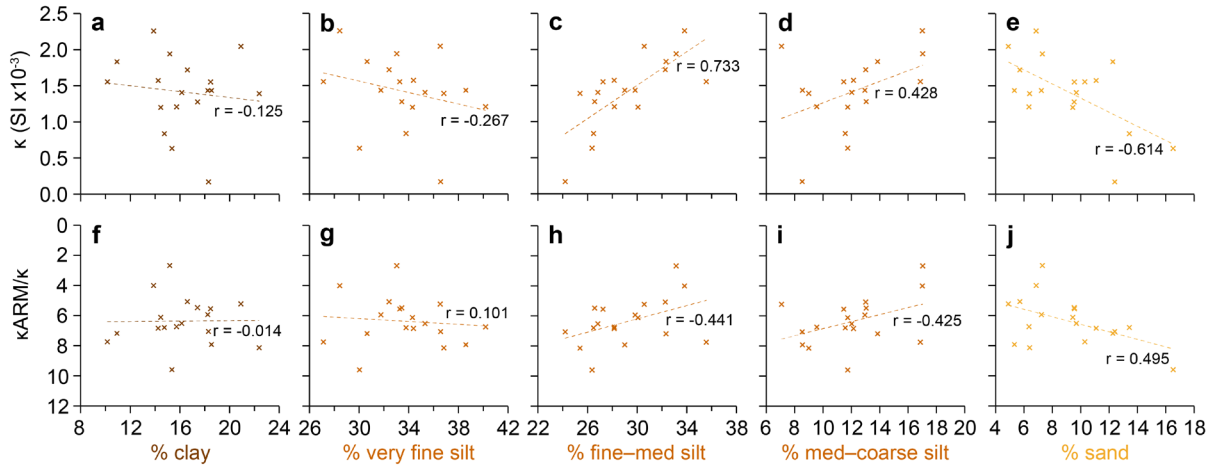

Figure 6 Cross-plots of (**a–e**) bulk magnetic susceptibility (κ) and (**f–j**) magnetic grain-size (κ_{ARM}/κ; note reversed axis since higher values = coarser magnetic grains) with physical grain size percentage abundance for clay (<3 µm), very fine silt (3–10 µm), fine–medium silt (10–32 µm), medium–coarse silt (32–63 µm) and sand (>63 µm) fractions (following Hatfield *et al.*, 2019) derived from discrete sample analyses (n = 18; see also Table S4 of Supplementary Material).

3.3 Changes in bottom-current strength recorded at Site U1307 during iNHG

Using what we know about the magnetic properties of Greenlandic vs. Icelandic sediments transported to Eirik Drift, the long-term decrease in average ferrimagnetic grain-size and sedimentation rates observed at Site U1307 between ~2.9 and 2.7 Ma (Fig. 5) likely reflects a secular decrease in the abundance of silt of Greenlandic origin transported to the site. This interpretation is supported by our discrete grain-size measurements, which show a long-term reduction of ~5% fine–medium silt between 2.85 and 2.25 Ma (Fig. 5d). Since we might logically expect a greater influx of Greenland-derived material following the onset of significant NHG ~2.7 Ma, as indicated by our IRD records (Fig. 5b), the changes we observe in our magnetics records, and the contemporaneous long-term decrease in sedimentation rate, are most likely explained by a shift in the position of the WBUC and delivery of terrigenous sediments to a different area of the drift. Additional support that the strength of bottom currents bathing our study site changed significantly during iNHG may be found in our record of wt.% ≥63 µm sand

(Fig. 5a). Peaks in the abundance of well-sorted fine sand, which prior to ~2.7 Ma occur in Site U1307 sediments deposited during interglacials (Fig. 5a), may reflect increased export of glaciofluvial sediment from Greenland to Eirik Drift, most strongly during warm stages. We therefore propose that prior to ~2.9 Ma, the core flow of the WBUC occupied a depth that permitted the delivery of relatively high abundances of Greenland-derived silt and fine sand to Site U1307 during both warm (predominantly) and cold stages on orbital timescales – so our study site was then characterised by a bottom-current-dominated depositional setting – and that between ~2.9 and 2.7 Ma the volume of Greenland-derived silt delivered to Site U1307 decreased and a glacial IRD-depositional-dominated setting subsequently ensued.

Based on the findings of studies that used depth transects of Eirik Drift sediments to infer changes in WBUC vigour during the late Pleistocene (Hillaire-Marcel *et al.*, 1994; Channell *et al*., 2014; Mazaud *et al*., 2012, 2015), the decreases in sedimentation rate and magnetic grain-size at U1307 during iNHG that we report may show that WBUC vigour increased and that its core flow deepened relative to our study site between ~2.9 and 2.7 Ma. A large deepening of the core flow of the WBUC by ~2.7 Ma is not consistent, however, with changes in sedimentation rates reported for Hole 646B on Eirik Drift at ~3450 m water depth, which also appear to have decreased across ~2.7 Ma (Fig. S7b; Wolf and Thiede, 1991). Moreover, a spin-up in the WBUC at this time is also inconsistent with an interpretation based on seismic reflection data that bottom currents not only shallowed, but weakened over Eirik Drift at this time (Müller-Michaelis and Uenzelmann-Neben, 2014), and the observation that iNHG was associated with Last Glacial Maximum-like reductions in the volume of the NADW-overturning cell during cold stages from ~2.7 Ma (Lang *et al*., 2016).

The only mechanism currently proposed that could explain any ‘spin-up’ in the WBUC at this time is the hypothesised late-stage closure history of the Central American

Seaway (Bartoli *et al*., 2005). By contrast, if WBUC vigour actually decreased at this time, this would be more consistent with forcing by sea-ice expansion and increased glacial meltwater input in the Arctic and Nordic Seas, which could have weakened the WBUC by lowering the salinity and density of the water masses that contribute to its formation (see Raymo *et al.*, 2004). Any reduction in WBUC vigour during iNHG could also be explained by increased activity of the Icelandic Hot Spot, which is believed to have uplifted the GSR from ~2.7 Ma to restrict Nordic Seas overflows from this time (e.g., Wright and Miller, 1996; Parnell-Turner *et al*., 2015). Regardless, our new records provide the first direct geological evidence that the behaviour of the WBUC changed with the expansion of large Northern Hemisphere ice-sheets during the late Pliocene. Ultimately, however, our understanding of whether WBUC vigour increased or decreased during iNHG, and of the potential mechanism(s) and climatological consequences involved, can only be improved by future observations from precisely-dated continuous Pliocene sequences recovered from a depth and spatial transect of drilling sites on Eirik Drift.

3.4 Southern GrIS evolution recorded at Site U1307 during iNHG

The general absence of IRD deposition on Eirik Drift (this study and Site 646; Wolf and Thiede, 1991; Fig. S7) and the Iceland Plateau (Site 907; Jansen *et al.*, 2000) during the latter half of the mPWP (~3.12–3.03 Ma; Fig. 7a and b) suggests that iceberg-calving margins were restricted in northeastern, eastern and southern Greenland during this time. Numerical model simulations indicate that continental ice on Greenland may have been mainly restricted to the southern and eastern highlands during the mPWP (e.g., Dolan *et al*., 2011). The absence of persistent coarse IRD deposition at U1307, yet relatively coarse magnetic grain-sizes (low κ_{ARM}/κ and Mrs/Ms values <0.12; Fig. S4b; Kawamura *et al.*, 2012) and high κ, prior to ~2.7 Ma (Fig. 5c and e) suggests that glaciofluvial silt-

producing icecaps existed at least inland on southern Greenland prior to the onset of significant Northern Hemisphere glaciation, including perhaps during the mPWP. The enhanced orbital-scale variability in magnetic grain-size from ~2.9 Ma (Fig. 5e) may also reflect an increase in glacial-interglacial dynamism of previously predominantly inland ice-sheet growth and decay in this region of Greenland.

Our ≥125 μm grains per gram record lacks orbital resolution, but it highlights that IRD inputs to U1307 may have become significantly elevated from ~3 Ma, at least during cold stages (Fig. 7a). The history of ice-rafting inferred from this record is arguably similar to that recorded at Site 907 based on the ≥125 μm grain-size fraction of IRD (Jansen *et al*., 2000), which suggests that IRD deposition on the Iceland Plateau was also persistently elevated from ~3 Ma (Fig. 7b). If correct, this interpretation of these geological data is supported by the finding, based on numerical ice-sheet models, that the mountainous regions of eastern and southern Greenland represent key nucleation points for the Pliocene GrIS (Dolan *et al*., 2011). Arguably, however, a different story can be drawn from both our coarser IRD ≥150 μm grains per gram and wt.% ≥212 μm records, which appear to show that the first sustained episode of significant IRD deposition at U1307 may not have begun until 2.72 Ma, during MIS G6 (compare yellow and black data in Fig. 5b). The timing of the onset of continuous major ice-rafting to Eirik Drift during iNHG may therefore actually be most comparable to the history of IRD deposition on the Vøring Plateau in the Nordic Seas, and in the subpolar northeast North Atlantic (e.g., as recorded at ODP Site 644, DSDP Site 611, ODP Site 984, and IODP Site U1308; Fig. 1; Jansen and Sjøholm, 1991; Bailey *et al*., 2010; Bailey *et al*., 2013; Bartoli *et al*., 2005). Consequently, the onset of persistent IRD deposition on Eirik Drift ~2.7 Ma may well post-date the first sustained elevation in ice-rafting on orbital timescales to the more northerly Iceland Plateau (at Site 907), at the cessation of the mPWP ~3 Ma, by ~300 kyr (Fig. 7; also see Section G of Supplementary Information).

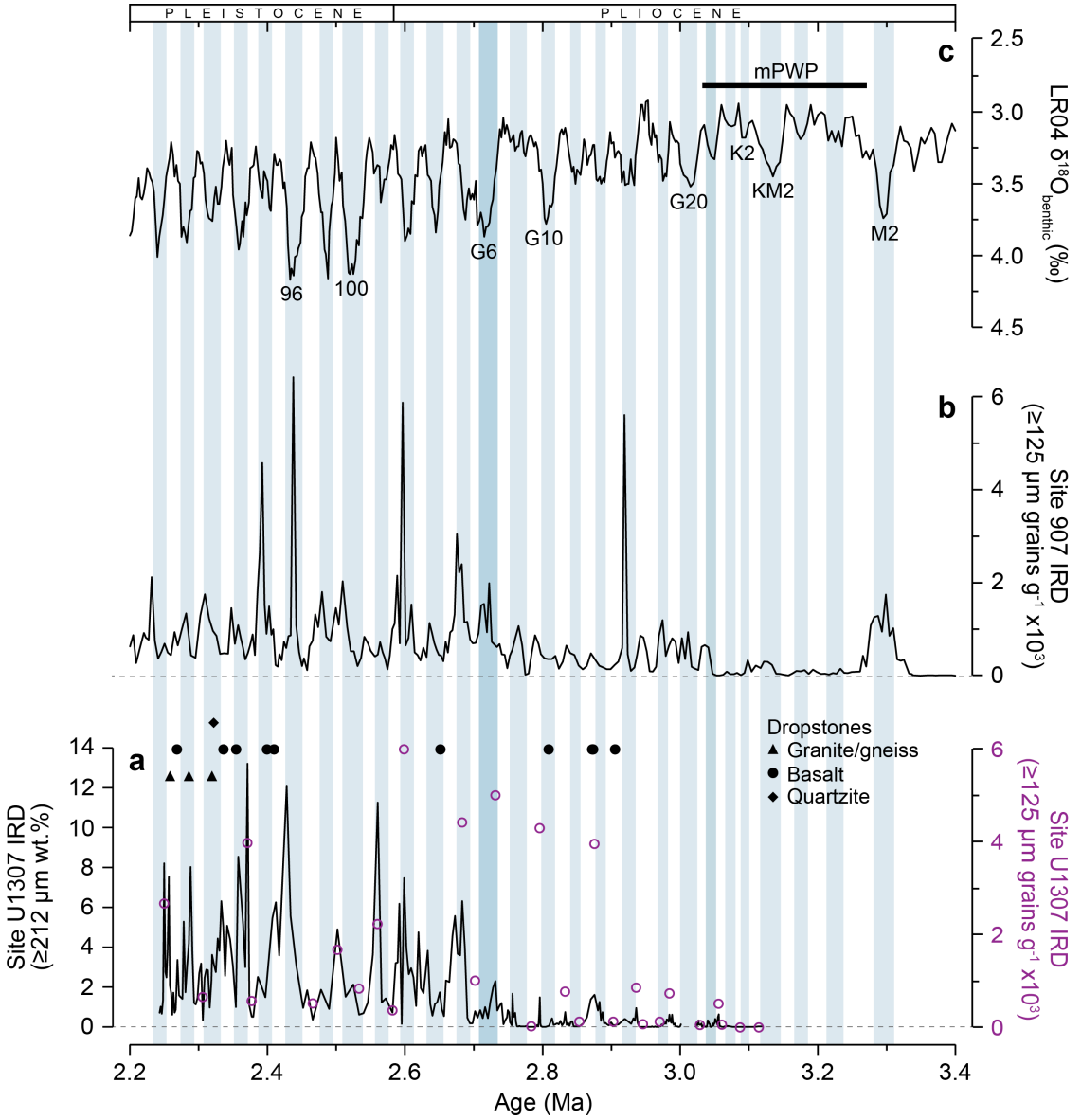

Figure 7. Records of IRD abundance from (**a**) IODP Site U1307 (this study; black record wt.% ≥212 µm, purple circles grains ≥150 µm g^{-1}) with shipboard-determined occurrences of dropstones (Expedition 303 Scientists, 2006a), and (**b**) ODP Site 907 (Jansen *et al*., 2000). The LR04 benthic $\delta^{18}O$ stack is shown in (**c**) for reference (Lisiecki and Raymo, 2005). Numbers in (c) are Marine Isotope Stages, with the duration of the mid-Piacenzian warm period (mPWP; Dolan *et al*., 2011) also indicated. Vertical blue bars highlight cold stages.

Any potential delay in the onset of abundant IRD deposition on Eirik Drift relative to the Iceland Plateau cannot be readily explained by iceberg survivability. This is because the EGC was likely a feature of Nordic Seas surface circulation for the past ~4.5 Myr (e.g.,

De Schepper *et al*., 2015), and iceberg trajectory modelling for the warm late Pliocene shows that abundant icebergs only reach the surface waters above Eirik Drift when southern Greenland iceberg-calving sources exist (Smith *et al*., 2018; their Fig. 4). Instead, it would hint at a regionally diachronous GrIS maturation during iNHG. The implication being, while at least outlet glaciers extended to the coast in northeastern and eastern Greenland following the cessation of the mPWP ~3 Ma, persistent iceberg-calving margins may not have been established in southern Greenland during cold stages until ~2.7 Ma, when the Fennoscandian and Barents ice-sheets also expanded to their iceberg-calving margins (Jansen and Sjøholm, 1991; Knies *et al*., 2014) and glacial expansion occurred at least inland on Arctic Canada (Lang *et al*., 2014; Bolton *et al.*, 2018). This southward expansion may also be echoed in the shipboard-derived dropstone record at U1307 (Fig. 7a; Expedition 303 Scientists, 2006a). Although providing a much less temporally-resolved picture, the dominance of dropstones of basaltic lithology in the U1307 stratigraphy prior to ~2.4 Ma contrasts with a mixed suite of basaltic, granitic/gneissic and sandstone dropstones from ~2.4 Ma – consistent with the development of more extensive iceberg-calving sources on Greenland's southern Precambrian basement terranes during iNHG.

The apparent difference in timing of the onset of sustained IRD inputs to U1307 during iNHG that can be determined from the three different grain-size fractions that we examined for evidence of iceberg-rafting highlights the importance of choosing the most appropriate grain-size in sedimentological analysis of IRD. Our wt.% ≥212 μm and grains ≥150 μm g^{-1} IRD records can both be used to infer an almost complete absence of IRD deposition on Eirik Drift during warm periods prior to 2.72 Ma. The earlier onset of elevated glacial IRD inputs at U1307 that we infer from the ≥125 μm terrigenous grain-size fraction may be a product of sea-ice rafted sand and/or of the coarsest fine sand also transported to our study site by stronger bottom-currents prior to ~2.7 Ma, complicating

our ability to use this grain-size fraction on Eirik Drift as a proxy for iceberg-rafting. Future investigation using, e.g., grain-size end-member mixing may help to determine whether or not the histories of the onset of significant iceberg-rafting to U1307 and 907 were temporally offset during iNHG. Regardless, using our improved RPI-based age model for U1307, the available IRD data indicate that extensive iceberg-calving margins definitely existed in both eastern and southern Greenland from 2.72 Ma (Fig. 7a and b).

4. Conclusions

The history of southern Greenland glaciation during the late Pliocene and earliest Pleistocene intensification of Northern Hemisphere glaciation (iNHG) is poorly constrained. Our new sedimentological and paleomagnetic datasets from Site U1307 on Eirik Drift – which receives ice-rafted debris from icebergs transported in the East Greenland Current, and glaciofluvial silt and fine sand via the deep Western Boundary Undercurrent (WBUC) – reveal for the first time that while continental ice existed inland on southern Greenland prior to the onset of significant Northern Hemisphere glaciation, with occasional iceberg-calving margins during cold intervals from the end of the mid-Piacenzian warm period, extensive iceberg-calving margins were likely only a persistent feature in this region from 2.72 Ma. Our new datasets also highlight for the first time that the depth of the core flow of the WBUC changed relative to our study site during iNHG. This finding underscores the need to redrill the Plio-Quaternary Eirik Drift to obtain a depth transect of drill sites. Only by doing so can we understand the importance of our observations on the WBUC for changes in Atlantic Meridional Overturning Circulation during iNHG, and the role the oceans may have played in driving glaciation at this time.

5. Acknowledgements

This research used marine samples provided by the IODP, which was sponsored by the European Consortium for Ocean Research Drilling (ECORD) and participating countries under management of Joint Oceanographic Institutions, Inc. We thank W. Hale and A. Wuelbers at MARUM Bremen for help with sampling, and M.R. Spencer and P.A. Wilson at the National Oceanography Centre Southampton for their assistance with sample processing. We also thank B.T. Reilly and A. Morey (Ross) at Oregon State University for their help running and processing u-channel paleomagnetic measurements. Gratitude is also given to Aurélie Aubry at Université du Québec à Montréal for discussions about our revised splice and age model. We thank Claude Hillaire-Marcel for editorial handling and two anonymous reviewers for insightful comments that helped to improve this manuscript.

All new data presented here are published on www.pangaea.de (https://doi.org/10.1594/PANGAEA.895029).

This research did not receive any specific grant from funding agencies in the public, commercial, or not-for-profit sectors.

6. References

Bailey, I., Bolton, C.T., DeConto, R.M., Pollard, D., Schiebel, R., Wilson, P.A., 2010. A low threshold for North Atlantic ice rafting from 'low-slung and slippery' late Pliocene ice sheets. Paleoceanography 25, PA1212, doi:10.1029/2009PA001736.

Bailey, I., Hole, G.M., Foster, G.L., Wilson, P.A., Storey, C.D., Trueman, C.N., Raymo, M.E., 2013. An alternative suggestion for the Pliocene onset of major northern hemisphere glaciation based on the geochemical provenance of North Atlantic Ocean ice-rafted debris. Quaternary Sci. Rev. 75, 181–194.

Bartoli, G., Sarnthein, M., Weinelt, M., Erlenkeuser, H., Garbe-Schönberg, D. and Lea, D.W., 2005. Final closure of Panama and the onset of northern hemisphere glaciation. Earth Planet. Sci. Lett. 237, 33–44.

Bierman, P.R., Shakun, J.D., Corbett, L.B., Zimmerman, S.R., Rood, D.H., 2016. A persistent and dynamic East Greenland Ice Sheet over the past 7.5 million years. Nature 540, 256–260.

Bigg, G.M., Wadley, M.R., Stevens, D.P., Johnson, J.A., 1996. Prediction of iceberg trajectories for the North Atlantic and Arctic oceans, Geophys. Res. Lett. 23 (24), 3587–3590.

Bigg, G.M., Wadley, M., Stevens, D., Johnson, J., 1998. Simulations of two last glacial maximum ocean states. Paleoceanography13 (4), 340–351.

Bloemendal, J., King, J.W., Hall, F.R., Doh, S.-J., 1992. Rock magnetism of Late Neogene and Pleistocene deep-sea sediments: Relationship to sediment source, diagenetic processes, and sediment lithology. J. Geophys. Res. 97 (B4), 4361–4375.

Bolton, C.T., Bailey, I., Friedrich, O., Tachikawa, K., de Garidel-Thoron, T., Vidal, L., Sonzogni, C., Marino, G., Rohling, E., Robinson, M., Ermini, M., Inacker, M., Cooper, M., Wilson, P.A., 2018. North Atlantic midlatitude surface-circulation changes through the Plio-Pleistocene intensification of northern hemisphere glaciation. Paleoceanography and Paleoclimatology 33(11), 1186–1205. https://doi.org/10.1029/2018PA003412.

Carlson, A. E., Stoner, J.S., Donnelly, J.P., Hillaire-Marcel, C., 2008. Response of the southern Greenland Ice Sheet during the last two deglaciations. Geology 36 (5), 359–362.

Channell, J.E.T., Mazaud, A., Sullivan, P., Turner, S., Raymo, M.E., 2002. Geomagnetic excursions and paleointensities in the Matuyama chron at Ocean Drilling Program Sites 983 and 984 (Iceland Basin). J. Geophys. Res. 107 (B6), 2114, doi:10.1029/2001JB000491.

Channell, J. E. T., Guyodo, Y., 2004. The Matuyama chronozone at ODP Site 982 (Rockall Bank): Evidence for decimeter-scale magnetisation lock-in depths. In: Channell, J.E.T., Kent, J.V., Lowrie, W. and Meert, J.G. (Eds.), Timescales of the Paleomagnetic Field. American Geophysical Union, Washington, D. C. doi:10.1029/145GM15.

Channell, J., Wright, J., Mazaud, A., Stoner, J., 2014. Age through tandem correlation of Quaternary relative paleointensity (RPI) and oxygen isotope data at IODP Site U1306 (Eirik Drift, SW Greenland). Quaternary Sci. Rev. 88, 135–146.

Channell, J., Hodell, D., Curtis, J., 2016. Relative paleointensity (RPI) and oxygen isotope stratigraphy at IODP Site U1308: North Atlantic RPI stack for 1.2–2.2 Ma (NARPI-2200) and age of the Olduvai Subchron. Quaternary Sci. Rev. 131, 1–19.

Colville, E.J., Carlson, A.E., Beard, B.L., Hatfield, R.G., Stoner, J.S., Reyes, A.V., Ullman, D.J., 2011. Sr-Nd-Pb isotope evidence for ice-sheet presence on southern Greenland during the Last Interglacial. Science 333, 620–623.

Day, R., Fuller, M., Schmidt, V.A., 1977. Hysteresis properties of titanomagnetites: Grain-size and compositional dependence. Phys. Earth Planet. Inter. 13(4), 260–267.De Schepper, S., Schreck, M., Beck, K.M., Matthiessen, J., Fahl, K., Mangerud, G., 2015. Early Pliocene onset of modern Nordic Seas circulation related to ocean gateway changes. Nat. Commun. 6, doi:10.1038/ncomms9659.

Dolan, A.M., Haywood, A.M., Hill, D.J., Dowsett, H.J., Hunter, S.J., Lunt, D.J., Pickering, S.J., 2011. Sensitivity of Pliocene ice sheets to orbital forcing. Paleogeogr. Paleoclimatol. Paleoecol. 309, 98–110.

Expedition 303 Scientists, 2006a. Site U1307. In: Channell, J.E.T., Kanamatsu, T., Sato, T., Stein, R., Alvarez Zarikian, C.A., Malone, M.J., and the Expedition 303/306 Scientists. Proc. IODP, 303/306: College Station TX (Integrated Ocean Drilling Program Management International, Inc.). doi:10.2204/iodp.proc.303306.107.2006

Expedition 303 Scientists, 2006b. Site U1308. In: Channell, J.E.T., Kanamatsu, T., Sato, T., Stein, R., Alvarez Zarikian, C.A., Malone, M.J., and the Expedition 303/306 Scientists. Proc. IODP, 303/306: College Station TX (Integrated Ocean Drilling

Program Management International, Inc.). doi:10.2204/iodp.proc.303306.107.2006
Evans, H. F., Channell, J. E. T., Stoner, J. S., Hillaire-Marcel, C., Wright, J. D., Neitzke, L. C., Mountain, G. S., 2007. Paleointensity-assisted chronostratigraphy of detrital layers on the Eirik Drift (North Atlantic) since marine isotope stage 11. Geochem. Geophys. Geosyst. 8(11). doi:10.1029/2007GC001720
Hatfield, R.G., Stoner, J.S., Carlson, A.E., Reyes, A.V., Housen, B.A., 2013. Source as a controlling factor on the quality and interpretation of sediment magnetic records from the northern North Atlantic. Earth Planet Sci. Lett, 368, pp. 69–77.
Hatfield, R.G., Reyes, A.V., Stoner, J.S., Carlson, A.E., Beard, B.L., Winsor, K., Welke, B., 2016. Interglacial responses of the southern Greenland ice sheet over the last 430,000 years determined using particle-size specific magnetic and isotopic tracers. Earth Planet. Sci. Lett. 454, 225–236.
Hatfield, R.G., Stoner, J.S., Reilly, B.T., Tepley F.J., Wheeler, B.H., Housen, B.A., 2017. Grain size dependent magnetic discrimination of Iceland and South Greenland terrestrial sediments in the northern North Atlantic sediment record. Earth Planet. Sci. Lett 474, 474–489.
Hatfield, R.G., Wheeler, B.H., Reilly, B., Stoner, J.S., Housen, B., 2019. Particle size specific magnetic properties across the Norwegian-Greenland Seas: Insights into the influence of source and texture on bulk magnetic records. Geochem. Geophys. Geosyst. (accepted manuscript).
Hillaire-Marcel, C., de Vernal, A., Bilodeau, G., Wu, G., 1994. Isotope stratigraphy, sedimentation rates, deep circulation, and carbonate events in the Labrador Sea during the last ~ 200 ka. Can. J. Earth Sci. 31 (1), 63–89.
Hillaire-Marcel, C., Bilodeau, G., 2000. Instabilities in the Labrador Sea water mass structure during the last climatic cycle. Can. J. Earth Sci. 37 (5), 795–809.
Hunter, S., Wilkinson, D., Stanford, J., Stow, D., Bacon, S., Akhmetzhanov, A., Kenyon, N., 2007. The Eirik Drift: a long-term barometer of North Atlantic deepwater flux south of Cape Farewell, Greenland. Geol. Soc. Spec. Publ. 276 (1). 245–263.
Jansen, E., Sjøholm, J., 1991. Reconstruction of glaciation over the past 6 Myr from ice-borne deposits in the Norwegian Sea. Nature 349, 600–603.
Jansen, E., Fronval, T., Rack, F., Channell, J.E.T., 2000. Pliocene-Pleistocene ice rafting history and cyclicity in the Nordic Seas during the last 3.5 Myr. Paleoceanography 15 (6), 709–721.
Kawamura, N., Ishikawa, N., Torii, M.., 2012. Diagenetic alteration of magnetic minerals in Labrador Sea sediments (IODP Sites U1305, U1306, and U1307). Geochem. Geophys. Geosyst. 13 (8), doi:10.1029/2012GC004213
King, J., Banerjee, S., Marvin, J., 1983. A new rock-magnetic approach to selecting sediments for geomagnetic paleointensity studies: Application to paleointensity for the last 4000 years. J. Geophys. Res.-Sol. Ea. 88 (B7), 5911–5921.
Kirschvink, J.L., 1980. The least squares lines and plane analysis of paleomagnetic data. Geophys. J. Int. 62, 699–718.
Knies, J., Mattingsdal, R., Fabian, K., Grøsvjeld, K., Baranwal, S., Husum, K., De Schepper, S., Vogt, C., Andersen, N., Matthiessen, J., Andreassen, K., Jokat, W., Nam, S.-I., Gaina, C., 2014. Effect of early Pliocene uplift on late Pliocene cooling in the Arctic–Atlantic gateway. Earth Planet. Sci. Lett. 387, 132–144.
Lang, D.C., Bailey, I., Wilson, P.A., Beer, C.J., Bolton, C.T., Friedrich, O., Newsam, C., Spencer, M.R., Gutjahr, M, Foster, G.L., Cooper, M.J., Milton, J.A., 2014. The transition on North America from the warm humid Pliocene to the glaciated Quaternary traced by eolian dust deposition at a benchmark North Atlantic Ocean drill site. Quaternary Si. Rev. 93, 125–141.

Lang, D.C., Bailey, I., Wilson, P.A., Chalk, T.B., Foster, G.L., Gutjahr, M., 2016. Incursions of southern-sourced water into the deep North Atlantic during late Pliocene glacial intensification. Nat. Geosci. 9(5), 375–379.

Larsen, H.C., Saunders, A.D., Clift, P.D., Beget, J. Wei, W., Spezzaferri, S., 1994. Seven million years of glaciation in Greenland. Science 264, 952–955.

Lisiecki, L., Raymo, M., 2005. A Pliocene-Pleistocene stack of 57 globally distributed benthic $\delta^{18}O$ records. Paleoceanography 20, PA1003.Mazaud, A., Channell, J., Stoner, J., 2012. Relative paleointensity and environmental magnetism since 1.2Ma at IODP site U1305 (Eirik Drift, NW Atlantic). Earth Planet. Sci. Lett. 357-358, 137–144.

Mazaud, A., Channell, J., Stoner, J., 2015. The paleomagnetic record at IODP Site U1307 back to 2.2 Ma (Eirik Drift, off south Greenland). Earth Planet. Sci. Lett. 429, 82–89.

Mudelsee, M., Raymo, M.E., 2005. Slow dynamics of the Northern Hemisphere glaciation. Paleoceanography 20, PA4022, doi:10.1029/2005PA001153.

Müller-Michaelis, A., Uenzelmann-Neben, G., 2014. Development of the Western Boundary Undercurrent at Eirik Drift related to changing climate since the early Miocene. Deep Sea Res. Part I Oceanogr. Res. Pap. 93, 21–34.

Ogg, J. G., 2012. Chapter 5 – Geomagnetic Polarity Time Scale, In: Gradstein, F. M., Ogg, J. G., Schmitz, M. D., Ogg, G. M. (Eds.), The Geologic Time Scale, Elsevier, Boston, 85–113.

Ohno, M., Hayashi, T., Komatsu, F., Murakami, F., Zhao, M., Guyodo, Y., Acton, G., Evans, H., Kanamatsu, T., 2012. A detailed paleomagnetic record between 2.1 and 2.75 Ma at IODP Site U1314 in the North Atlantic: Geomagnetic excursions and the Gauss-Matuyama transition. Geochem. Geophys. Geosyst. 13, Q12Z39.

Parnell-Turner, R., White, N.J., McCave, I.N., Henstock, T.J., Murton, B., Jones, S.M., 2015. Architecture of North Atlantic contourite drifts modified by transient circulation of the Icelandic mantle plume. Geochem. Geophys. Geosyst. 16(10), 3414–3435.

Raymo, M.E., Oppo, D.W., Flower, B.P., Hodell, D.A., McManus, J.F., Venz, K.A., Kleiven, K.F. and McIntyre, K., Stability of North Atlantic water masses in face of pronounced climate variability during the Pleistocene, Paleoceanography 19 (2), 2004, doi:10.1029/2003PA000921.

Sarnthein, M., Bartoli, G., Prange, M., Schmittner, A., Schneider, B., Weinelt, M., Andersen, N., Garbe-Schönberg, D., 2009. Mid-Pliocene shifts in ocean overturning circulation and the onset of Quaternary-style climates. Clim. Past 5, 269–283.

Schaefer, J.M., Finkel, R.C., Balco, G., Alley, R.B., Caffee, M.W., Briner, J.B., Young, N.E., Gow, A.J., Schwartz, R., 2016. Greenland was nearly ice-free for extended periods during the Pleistocene. Nature 540, 252–255.

Shipboard Scientific Party, 1987. Site 646. In: Srivastava, S.P., Arthur, M., Clement, B., et al., Proc. ODP, Init. Repts., 105: College Station, TX (Ocean Drilling Program), 419–674.

Smith, Y.M., Hill, D.J., Dolan, A.M., Haywood, A.M., Dowsett, H.J., Risebrobakken, B., 2018. Icebergs in the Nordic Seas throughout the Late Pliocene. Paleoceanography 33, 318–335.

St John, K.E.K., Krissek, L.A., 2002. The late Miocene to Pleistocene ice-rafting history of southeast Greenland. Boreas 31, 28–35.

Stoner, J., Channell, J., Hillaire-Marcel, C., 1995. Magnetic properties of deep-sea sediments off southwest Greenland: Evidence for major differences between the last two deglaciations. Geology 23 (3), 241.

Thiede, J., Jessen, C., Knutz, P., Kuijpers, A., Mikkelsen, N., Nørgaard-Pedersen, N., Spielhagen, R.F., 2011. Millions of years of Greenland Ice Sheet history recorded in ocean sediments. Polarforschung 80 (3), 141–159.

Valet, J., Meynadier, L., 1993. Geomagnetic field intensity and reversals during the past four million years. Nature 366, 234–238.

Vanneste, K., Uenzelmann-Neben, G., Miller, H., 1995. Seismic evidence for long-term history of glaciation on central East Greenland shelf south of Scoresby Sund. Geo-Mar. Lett. 15, 63–70.

Weeks, R, Laj C, Endignoux L., Fuller, M., Roberts, A., Manganne, R., Blanchard, E., Goree, W., 1993. Improvements in long-core measurement techniques: applications in palaeomagnetism and palaeoceanography. Geophys. J. Int. 114, 651–662.

White, L., Bailey, I., Foster, G., Allen, G., Kelley, S., Andrews, J., Hogan, K., Dowdeswell, J., Storey, C., 2016. Tracking the provenance of Greenland-sourced, Holocene aged, individual sand-sized ice-rafted debris using the Pb-isotope compositions of feldspars and 40 Ar/ 39 Ar ages of hornblendes. Earth Planet. Sci. Lett. 433, 192–203.

Wolf, T.C.W., Thiede, J., 1991. History of terrigenous sedimentation during the past 10 m.y. in the North Atlantic (ODP Legs 104 and 105 and DSDP Leg 81). Mar. Geol. 101 (1–4), 83–102.

Wright, J.D., Miller, K.G., 1996. Control of North Atlantic Deep Water circulation by the Greenland-Scotland Ridge. Paleoceanography 11(2), 157–170.

Xuan, C., Channell, J., 2009. UPmag: MATLAB software for viewing and processing u channel or other pass-through paleomagnetic data. Geochem. Geophys. Geosyst. 10, Q10Y07.

Yamazaki, T., Oda, H., 2005. A geomagnetic paleointensity stack between 0.8 and 3.0 Ma from equatorial Pacific sediment cores. Geochem. Geophys. Geosyst. 6 (11), Q11H20.

Table 1. Site U1307 stratigraphy: comparison of shipboard-derived and revised splice (this study).

Hole-Core	Shipboard splice[a]		Revised splice			Hole-Core	Shipboard splice[a]		Revised splice	
	mbsf	mcd	mbsf	rmcd			mbsf	mcd	mbsf	rmcd
U1307B-13H	116.62	123.15	115.82	122.35	tie	U1307A-14H	115.24	123.15	114.44	122.35
U1307A-14H	120.13	128.04	121.73	129.64	tie	U1307B-14H	120.06	128.04	121.74	129.64
U1307B-14H	-	-	127.22	135.13	tie	U1307A-16H	-	-	129.34	135.13
U1307B-14H	128.40	136.38	-	-	append	U1307B-15H	128.30	136.55	-	-
U1307A-16H	-	-	133.62	139.40	tie	U1307B-15H	-	-	131.70	139.40
U1307B-15H	138.00	146.25	-	-	append	U1307B-16H	137.80	147.12	-	-
U1307B-15H	-	-	138.00	145.70	append*	U1307A-17H	-	-	135.20	145.70
U1307A-17H	-	-	140.93	151.43	tie	U1307B-16H	-	-	139.65	151.43
U1307B-16H	145.25	154.57	145.63	157.41	tie	U1307A-18H	146.18	154.47	146.89	157.41
U1307A-18H	152.93	161.32	152.93	163.44	append	U1307A-19H	153.10	163.71	153.10	165.83
						U1307A-19H	162.81	173.42	162.81	175.54

See Table S1 of Supplementary Material for complete revised splice.

mbsf = metres below seafloor; (r)mcd = (revised) metres composite depth.

[a]Expedition 303 Scientists (2006a).

*See Fig. S2 of Supplementary Material.

A. New splice for Site U1307

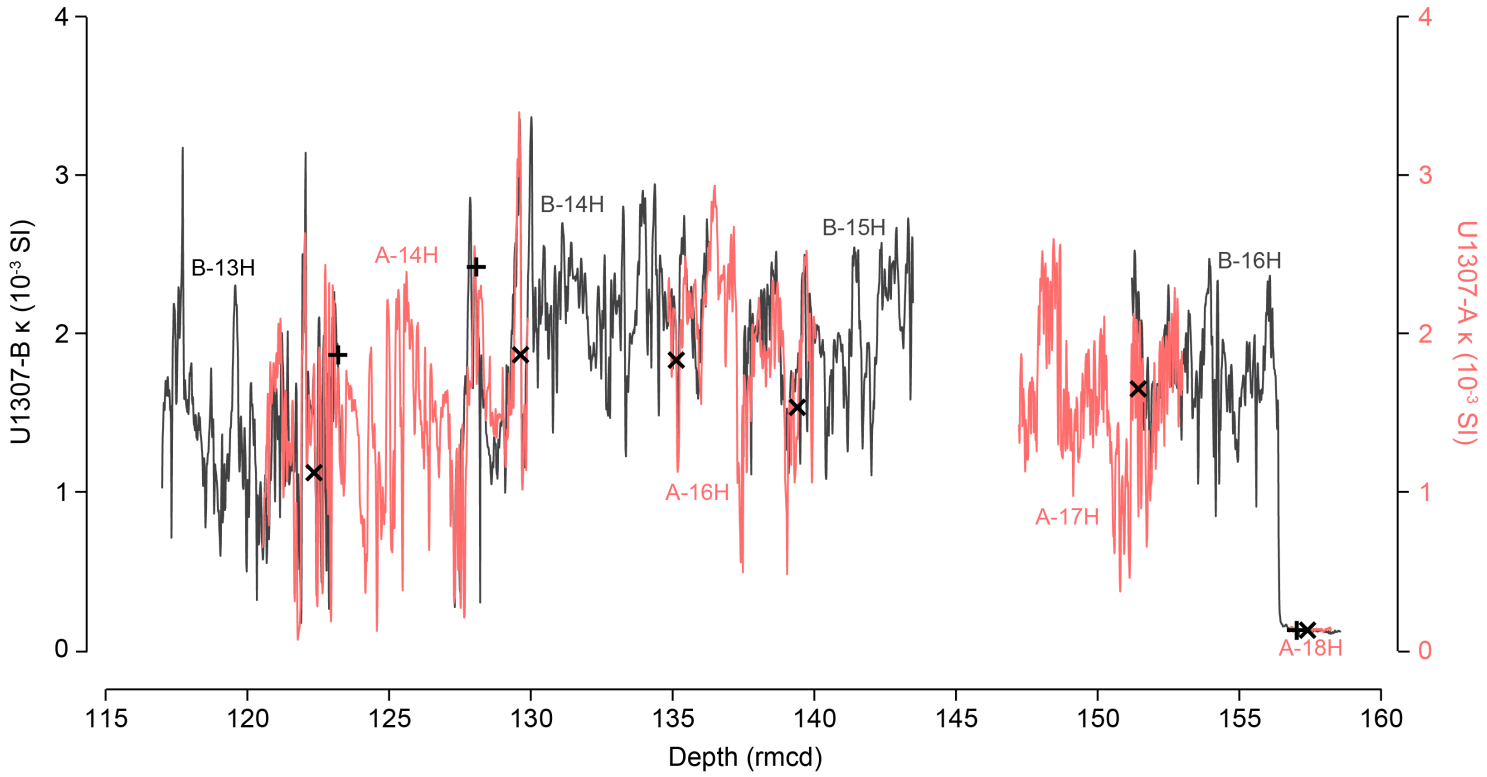

Figure S1. Plot of new high (1 cm)-resolution u-channel-derived magnetic susceptibility (κ) data for IODP Site U1307 Hole A (red) and Hole B (black) between ~117 and 158 revised metres composite depth (rmcd; also see Tab. S1). Newly-determined splice-points denoted by black crosses (×). Original shipboard splice points are indicated by black plus (+) symbols. The data gap between B-15H and A-17H reflects the absence of u-channel κ data for the bottom 223 cm of B-15H and the top 150 cm of A-17H.

Table S1. Revised splice for IODP Site U1307.

	Affine			Splice								
				Start				End				
Core	Top mbsf	Top rmcd	mbsf-rmcd offset	Section	Interval	mbsf	rmcd	Section	Interval	mbsf	rmcd	Relationship
U1307B-1H	0.00	0.00	0.00	1	0.00	0.00	0.00	2	41.70	1.92*	1.92	tie to
U1307A-1H	0.00	0.19	0.19	2	23.10	1.73*	1.92	5	93.10	6.93	7.12	tie to
U1307B-2H	4.80	5.20	0.40	2	41.90	6.72	7.12	5	40.50	11.20	11.60	tie to
U1307A-2H	9.50	9.69	0.19	2	41.10	11.41	11.60	6	51.20	17.51	17.70	tie to
U1307B-3H	14.30	15.60	1.30	2	59.60	16.40	17.70	5	81.90	21.12	22.42	tie to
U1307A-3H	19.00	20.08	1.08	2	84.10	21.34	22.42	6	73.20	27.23	28.31	tie to
U1307B-4H	23.80	26.99	3.19	1	132.00	25.12	28.31	5	88.10	30.68	33.87	tie to
U1307A-4H	28.50	30.54	2.04	3	32.10	31.82*	33.87	6	64.40	36.64	38.68	tie to
U1307B-5H	33.30	37.24	3.94	1	144.00	34.74	38.68	4	63.40	38.43	42.37	tie to
U1307A-5H	38.00	41.05	3.05	1	132.00	39.32	42.37	5	133.70	45.31	48.36	tie to
U1307B-6H	42.80	47.17	4.37	1	118.50	43.99	48.36	7	77.30	52.11	56.48	append
U1307B-7H	52.30	56.67	4.37	1	0.00	52.30	56.67	7	63.30	61.98	66.35	append
U1307B-8H	61.80	66.71	4.91	1	0.00	61.80	66.71	4	18.60	66.49	71.40	tie to
U1307A-8H	62.00	67.13	5.13	3	126.60	66.27	71.40	7	31.30	71.31	76.44	tie to
U1307B-9H	71.30	75.84	4.54	1	60.00	71.90	76.44	7	25.30	80.55	85.09	tie to
U1307A-10H	77.70	84.07	6.37	1	102.00	78.72	85.09	5	95.50	84.66	91.06	tie to
U1307B-10H	80.80	85.56	4.76	4	96.70	86.27	91.03	7	5.20	89.95	94.61	tie to
U1307A-11H	87.20	93.72	6.52	1	88.50	88.09	64.61	4	22.80	91.93	98.45	tie to

U1307B-11H	90.30	95.50	5.20	2	144.50	93.25	98.45	7	110.10*	99.48	104.68	tie to
U1307A-12H	96.70	104.38	7.68	1	30.00	97.00	104.68	3	18.10	99.88	107.56	tie to
U1307B-12H	99.80	106.22	6.42	1	134.00*	101.14	107.56	7	60.60	109.41	115.83	tie to
U1307B-13H	109.30	115.83	6.53	1	0.00	109.30	115.83	5	51.90	115.82	122.35	tie to
U1307A-14H	112.40	120.31	7.91	2	54.30	114.44	122.35	7	33.40	121.73	129.64	tie to
U1307B-14H	118.80	126.70	7.90	2	147.30	121.74	129.64	6	92.40	127.22	135.13	tie to
U1307A-16H	125.70	131.49	5.79	3	64.30	129.34	135.13	6	41.80	133.62	139.40	tie to
U1307B-15H	128.30	136.00	7.70	3	10.30	131.70	139.40	7	70.00	138.00	145.70	append**
U1307A-17H	135.20	145.70	10.50	1	0.00	135.20	145.70	4	124.47	140.93	151.43	tie to
U1307B-16H	137.80	149.58	11.78	2	34.78	139.65	151.43	6	32.58	145.63	157.41	tie to
U1307A-18H	144.70	155.22	10.52	2	66.16	146.89	157.41	6	70.00	152.93	163.44	append
U1307A-19H	153.10	165.83	12.73	1	0.00	153.10	165.83	7	71.00	162.81	175.54	

Portion of shipboard splice revised in this study lies between 115.83–175.54 rmcd. Original splice 0–115.83 rmcd from Expedition 303 Scientists, 2006a.
mbsf = metres below seafloor; rmcd = revised metres composite depth.
*corrected for minor typographical errors present in the splice published in the Site U1307 shipboard report (Expedition 303 Scientists, 2006a).
**see Fig. S2.

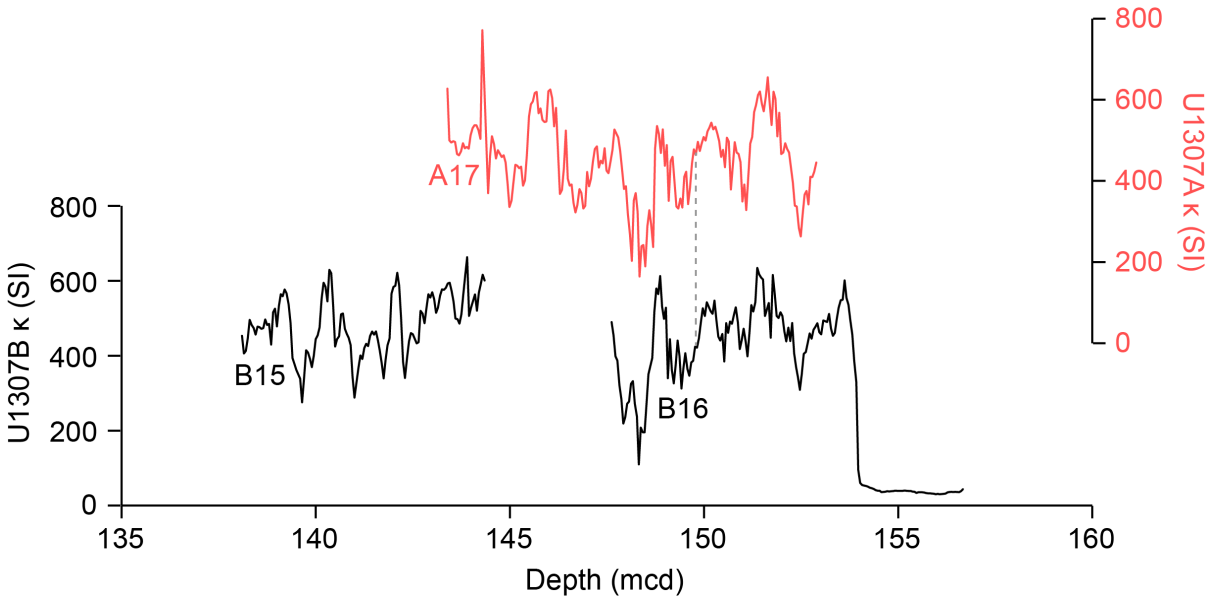

Figure S2. Shipboard magnetic susceptibility core logger (κ) data from Site U1307 on the original shipboard-derived splice metres composite depth (mcd), which appended core B-16H to B-15H to extend the stratigraphy deeper than ~145 mcd (Expedition 303 Scientists, 2006a). Core A-17H was not used in the generation of the original shipboard-derived splice but is included in the revised splice presented here (Tab. S1). Data from A-17H plotted here on mcd relative to its splice tie-point with B-16H in the revised splice presented here (see also Fig. S1 and Tab. S1) justify this decision, since the comparison shown suggests that A-17H captures at least part of the stratigraphy lost from the core gap between B-15H and B-16H. Core A-17H cannot be tied to B-15H. To include this core in our revised splice, we assumed that no stratigraphic gap exists between B-15H and A-17H. While a stratigraphic gap of unknown thickness likely exists between these two cores, our inclination- and RPI-based correlations between Sites U1307 and U1308 (Fig. S3) highlight that this gap is likely to be very small.

B. Extended shipboard-derived NRM/κ record of RPI

The Integrated Ocean Drilling Program (IODP) Site U1308 relative paleointensity (RPI) tuning target for our new IODP Site U1307 record spans 0–3.15 Ma (Channell *et al*., 2016). In order to assign ages to depths in the Site U1307 stratigraphy >3.15 Ma, we extended the u-channel-based inclination (INC) and RPI records (based on natural remanent magnetisation (NRM)/magnetic susceptibility (κ); e.g., Gorgoza *et al*., 2006) for both Site U1307 and U1308 using shipboard data. We did this by appending 5-cm resolution shipboard INC, NRM (10 mT) and κ data from cores U1308C 25H–29H to the base of the Site U1308 splice in Hole C (to extend it from 248 metres composite depth (mcd) to 266.5 mcd; note that Hole A data extends further, but the magnetic signal is not well recorded in the deeper portion; Expedition 303 Scientists, 2006b), and cores U1307A 18H–19H to the base of our revised Site U1307 splice (to extend it from 158 revised metres composite depth (rmcd) to 175.5 rmcd, the maximum drilled depth). Where both types of data were available for a given depth, NRM was normalised by κ to give a 'rough and ready' measure of RPI, which compares favourably with u-channel-derived RPI data from both sites (Fig. S3).

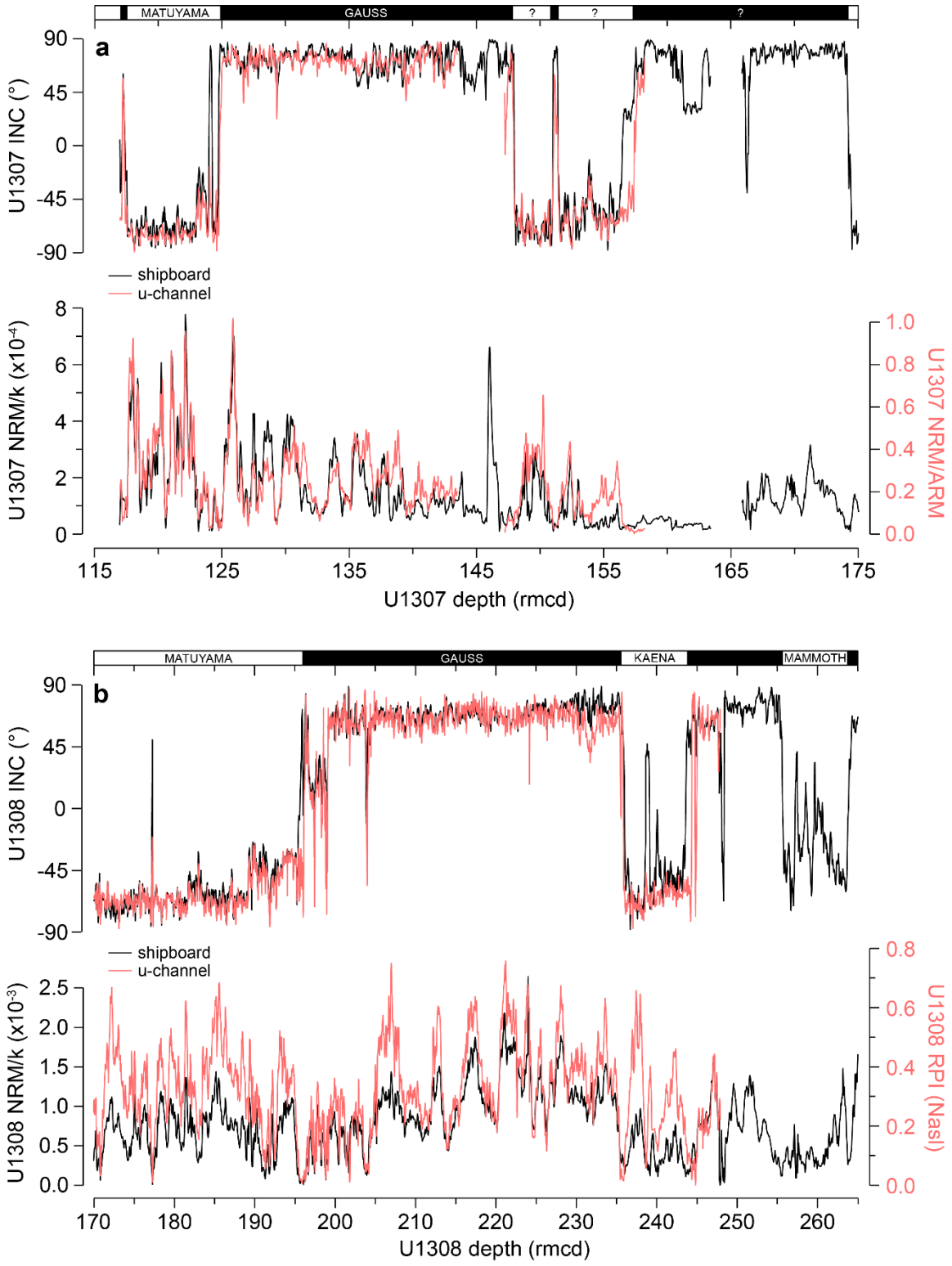

Figure S3. Shipboard- (black lines) and u-channel- (red lines) derived records of inclination (INC) and RPI for IODP Sites (**a**) U1307 and (**b**) U1308. The relationships shown demonstrate that shipboard-derived NRM/κ data >3.15 Ma can be used as a 'rough and ready' RPI record for these sites to help validate the new age model presented in this study for Site U1307.

C. Construction of U1307 RPI-based age model and comparison to other records

To generate reliable RPI estimates, it is generally accepted that variations in magnetic grain size and magnetic concentration should be minimal (less than an order of magnitude in concentration), and that the magnetic mineralogy remains uniform throughout the interval of interest (e.g., Evans *et al*., 2007). For our study interval at Site U1307, κ and ARM vary within an order of magnitude (Fig. S4a). A Day plot (Day *et al*., 1977) of Site U1307 hysteresis ratios (Fig. S4b; Kawamura *et al*., 2012) shows that, for our study interval, ferrimagnetic grain sizes are fairly well-constrained in the coarse PSD range, and are similar to, and overlap with, hysteresis ratios from shallower depths at U1307 (Mazaud *et al*., 2015). This suggests that Site U1307 (titano)magnetites generally fall within the size range considered to be most suitable for RPI determination (King *et al*., 1983). The lack of a clear relationship between NRM/ARM vs. ARM data (Fig. S4c) indicates that NRM/ARM (our RPI estimate) is not dependant on environmental variations in ferrimagnetic concentration, and is thus sensitive to variations in past field intensity.

Component u-channel inclination and declination data for ~117–158 rmcd are given in Figure S5a–b, alongside the MAD values (Fig. S5c). MAD values are generally low (<5°), reflecting a well-defined ChRM magnetisation. However, higher (up to ~45°) values are a feature of polarity reversals and other low intensity intervals, indicating complex or poorly constrained ChRM directions (Fig. S5c). Inclination values for both polarities vary close to the expected value (±72.5°) assuming a geocentric axial dipole field (Fig. S5b). The declination record reveals reversal horizons coeval with the inclination data (Fig. S5a), which can then be correlated to the geomagnetic polarity time scale. Based on these data, we identify the Gauss-Matuyama (G/M) boundary (C2An.1n top) at 125.10 rmcd (~2.581 Ma; Ogg, 2012), the top of the Kaena (C2An.1r) at 147.97 rmcd (~3.032 Ma; Ogg, 2012), and short excursions to normal

polarity within the Matuyama chron at ~117 rmcd and within the Kaena subchron at ~151 rmcd (see Tab. S2).

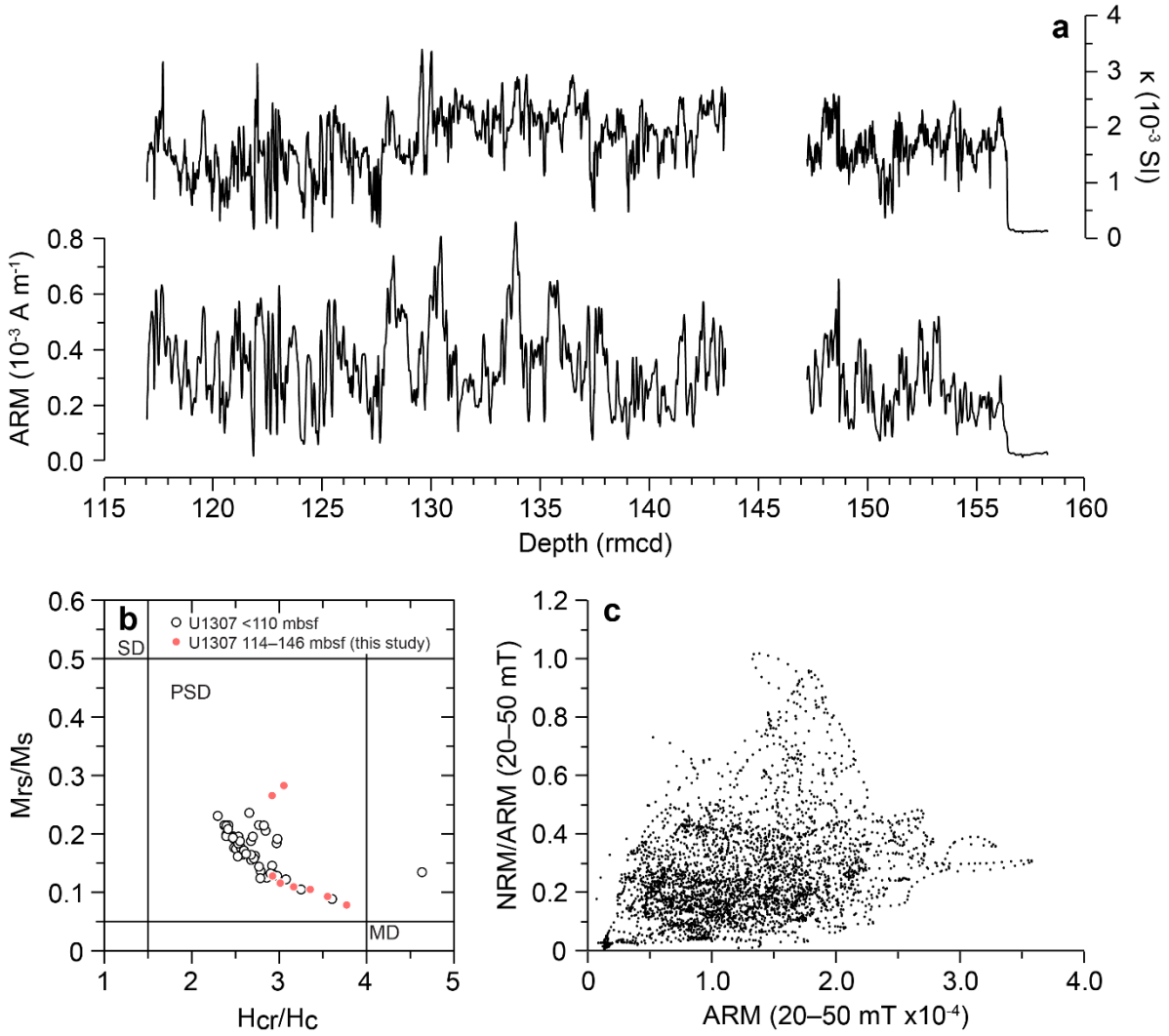

Figure S4. (**a**) Plot of Site U1307 low-field bulk volume magnetic susceptibility (κ) and u-channel-derived anhysteretic remanent magnetisation (ARM before AF demagnetisation) against revised metres composite depth (rmcd); (**b**) hysteresis parameters (Mrs/Ms, ratio of remanent saturation moment Mrs, to saturation moment Ms; against Hcr/Hc, ratio of remanent coercive force, Hcr, to coercive force, Hc) for single U1307 samples showing (titano)magnetite grain size distribution, plotted on a Day *et al.* (1977) diagram (MD = multi-domain grains, PSD = pseudo-single domain, SD = single domain), with samples in our study interval indicated by red points (modified from Kawamura *et al.*, 2012); and (**c**) bivariate plot of natural remanent magnetisation (NRM)/ARM vs ARM for the 20–50 mT peak field interval.

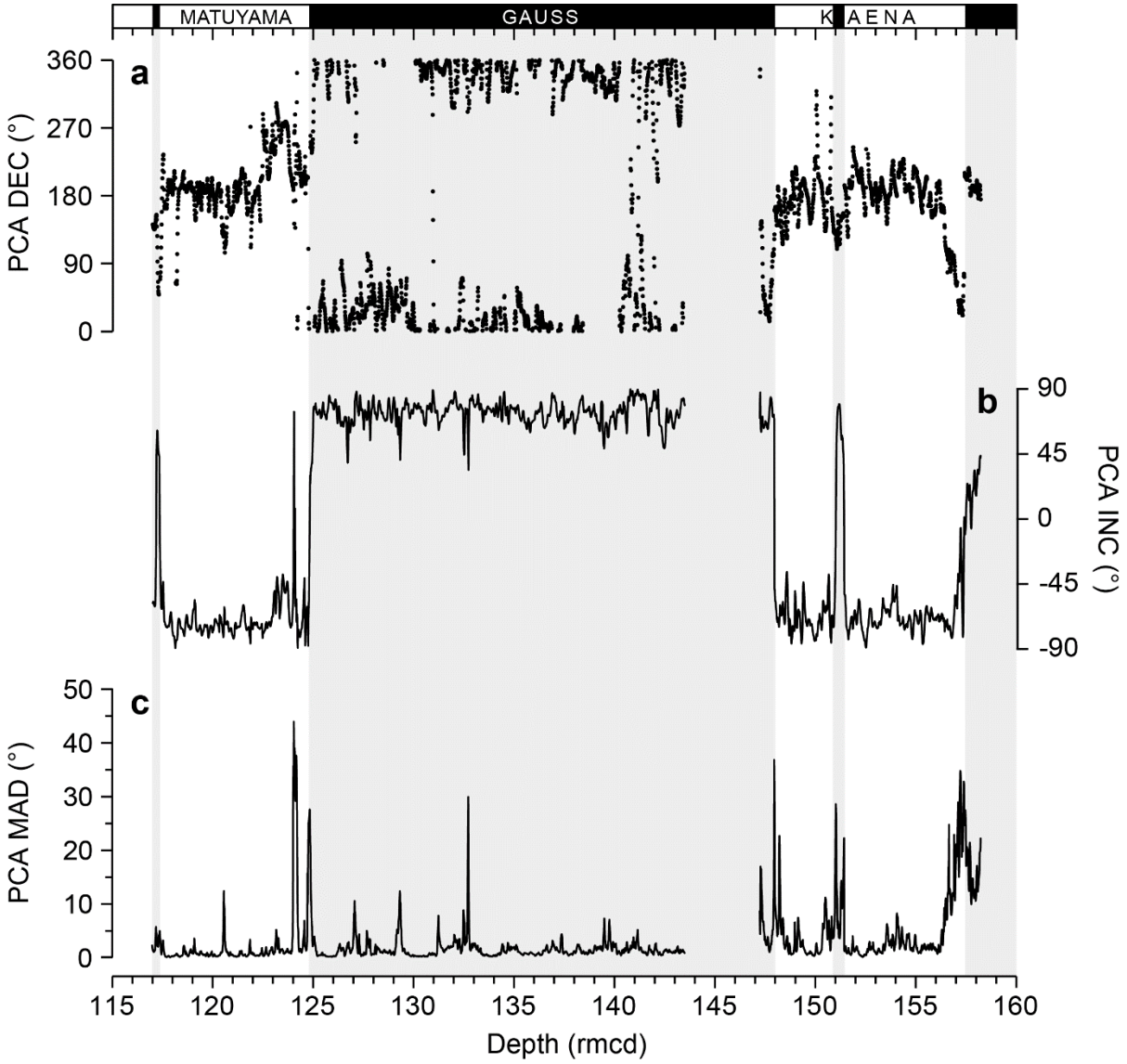

Figure S5. Site U1307 natural remanent magnetisation (NRM) component (**a**) declination, (**b**) inclination and (**c**) maximum angular deviation (MAD) values, calculated for the 20–50 mT peak interval, against revised metres composite depth (rmcd). The absence of data between ~143.5–147.2 rmcd is the result of a sampling gap (the bottom 223 cm of U1307B-15H and the top 150 cm of U1307A-17H could not be u-channelled. Shipboard data do not suggest a reversal occurs during this interval; see Fig. S3). Polarity (normal/reversed) chrons are denoted at the top by black/white horizontal bars/grey vertical bars and labels, based on the age model presented in this study.

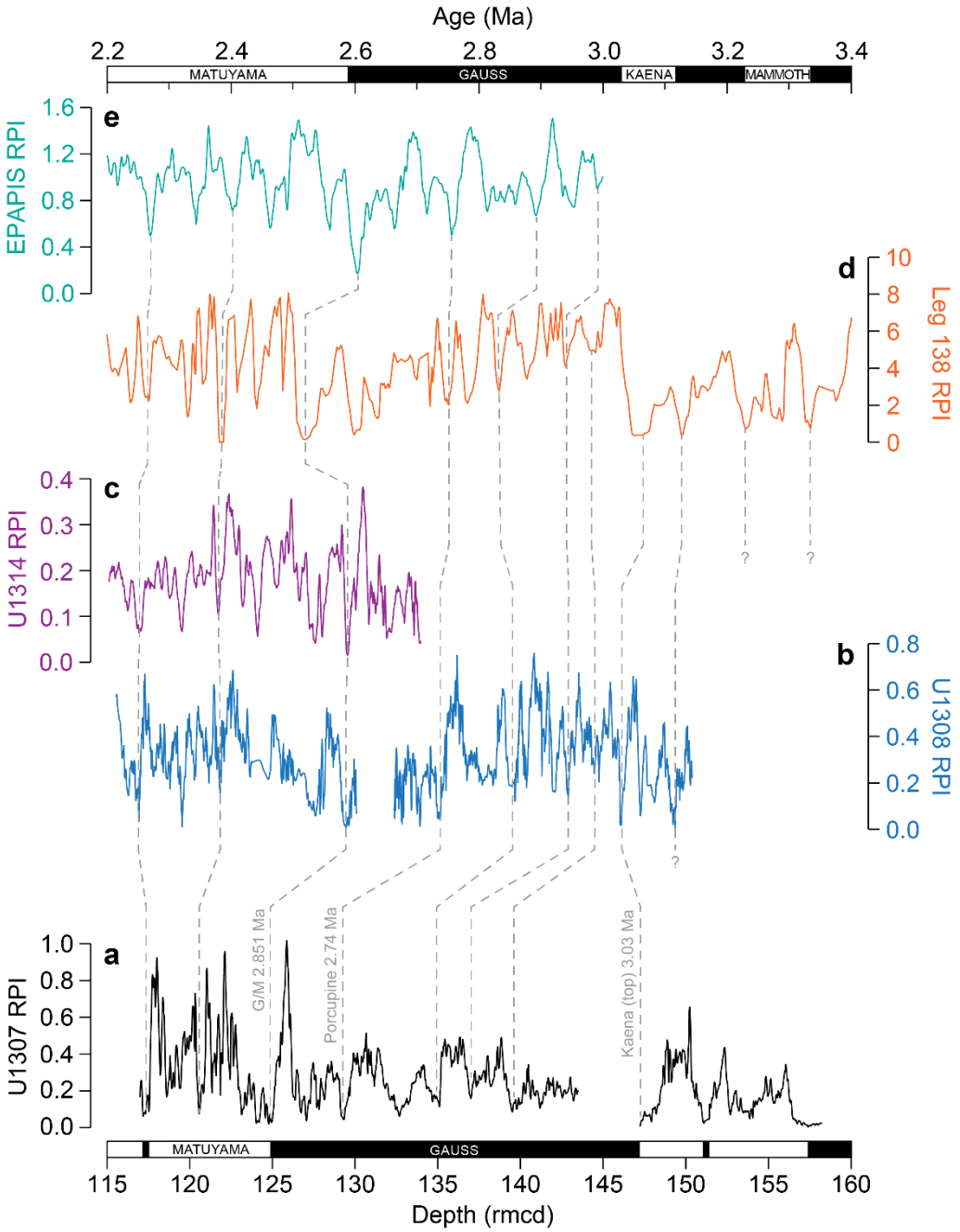

Figure S6. First-order comparison of (**a**) our new RPI record from IODP Site U1307 on revised metres composite depth (rmcd; this study) with other RPI stratigraphies from the North Atlantic ((**b**) Site U1308, Channell *et al*., (2006); (**c**) Site U1314, Ohno *et al*., (2012)) and equatorial Pacific ((**d**) Ocean Drilling Program (ODP) Leg 138, Valet and Meynadier, (1993); (**e**) EPAPIS-3000 stack, Yamazaki and Oda, (2005)) on their respective published age models. This comparison shows that the U1307 RPI stratigraphy records a regionally coherent signal and shares many similarities with records from further afield.

D. Comparison of U1307 and ODP Site 646 sedimentation rate and ≥63 µm sand records

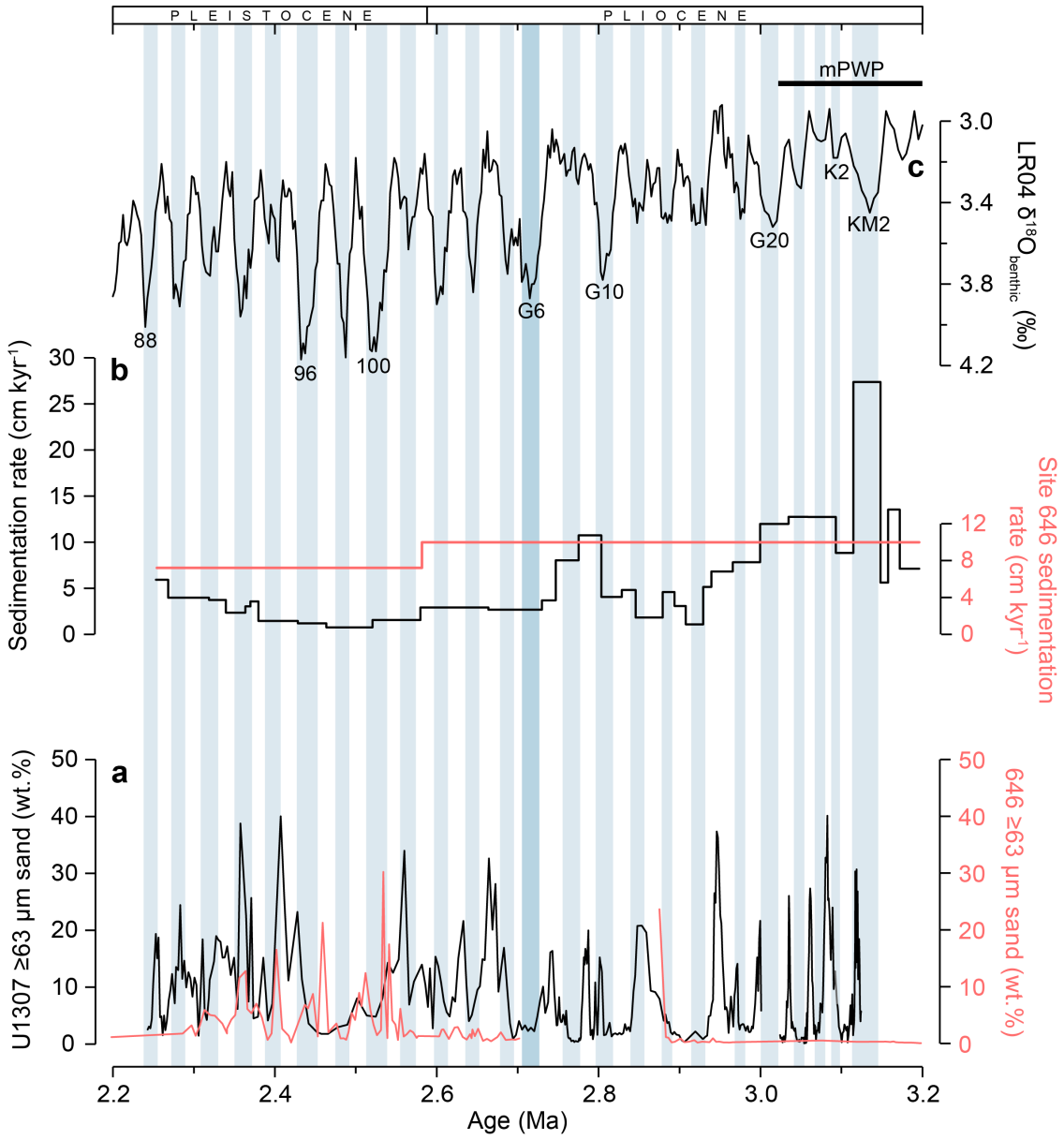

Figure S7. Comparison of Eirik Drift records from IODP Site U1307 and ODP Hole 646B: (**a**) weight percent (wt. %) ≥63 µm terrigenous sand; (**b**) linear sedimentation rates (data from Wolf and Thiede, 1991). The LR04 benthic $\delta^{18}O$ stack (Lisiecki and Raymo, 2005) is also shown in (**c**). Numbers in (c) are Marine Isotope Stages, with the duration of the mid-Piacenzian warm period (mPWP; Dolan *et al*., 2011) also indicated. Vertical blue bars highlight cold stages. The Hole 646B stratigraphy isconstrained by only three palaeomagnetochron reversals spanning ~2.5 Myr (the base of the Jaramillo, 1072 ka; the Gauss/Matuyama, 2581 ka; and the Gauss/Gilbert, 3596 ka). Our ability to compare sand deposition and accumulation rates at U1307 and 646B during our study interval is therefore limited by the absence of a high fidelity $\delta^{18}O$- or relative paleointensity-based age model for the Hole 646B stratigraphy.

E. Method for organic and biogenic matter removal for grain-size analysis

Modified from Povea *et al*. (2015)

1.1 Materials

Total of 18 dried core samples typically ~5 g

10% hydrogen peroxide solution

10% acetic acid solution

1.5 M sodium hydroxide solution

Deionised water

1.2 Step one: Organic matter removal

Dry samples were broken up as finely as possible without influencing grain size and put into 50 mL centrifuge tubes. 40 mL of 10% hydrogen peroxide was added to each sample in the tubes, then these were placed in an oven at 60°C with their lids loosely resting on top to allow safe escape of oxygen gas. The samples were left in the oven for ~48 hours, or until the reaction stopped, after which any remaining liquid was poured off. Deionised water was then added to each sample in the tubes, thoroughly shaken by hand and centrifuged, before the liquid was poured off. The resultant clean samples were then dried in an oven at 60˚C overnight.

1.3 Step two: Biogenic carbonate removal

35 mL of 10% acetic acid was added to each sample in the centrifuge tubes, which were then placed in an end-over-end turner for a few hours (or until fizzing stopped). Next, the liquid was centrifuged off, deionised water was added and thoroughly shaken, and then the samples were centrifuged again. The liquid was then poured off and then the clean samples were dried in an oven at 60˚C overnight.

1.4 Step three: Biogenic silica removal

35 mL of 1.5 M sodium hydroxide added to each sample in the centrifuge tubes, then sonicated in an ultrasonic bath for 5 to 10 minutes. The samples were left in the solution overnight in an oven at 65°C. The next day the tubes were placed in a water bath at 85°C for 2 hours, then the liquid was centrifuged off. Subsequently, 40 mL of 1.5 M sodium hydroxide was added and the samples were placed back in the 85°C water bath for 2 hours. The samples were then left in solution overnight in an oven at 65°C. The next day the liquid was centrifuged off, deionised water added to each sample and shaken thoroughly. They were then centrifuged and the liquid was poured off. This step was repeated two more times, and then the clean samples were dried in an oven at 60˚C overnight.

F. Evaluation of alternative age model for IODP Site U1307

Two alternative age models for the late Pliocene and early Pleistocene portion of the shipboard-derived Site U1307 stratigraphy have previously been proposed by Sarnthein *et al*. (2009), which are based on their interpretation of the shipboard palaeomagnetochron stratigraphy and a discontinuous planktic foraminiferal *Neoglobigerina atlantica* (s) stable oxygen isotope record. The preferred U1307 age model of Sarnthein *et al*. (2009) – 'Age Model 2' – assumes that the lowest-most palaeomagnetochron reversal preserved in the U1307 shipboard INC data is the Gilbert/Gauss reversal ~3.58 Ma, and that the Mammoth reversed subchron (C2An.2r) lies somewhere in the base of A-18H (within a magnetic susceptibility low) and the recovery gap with A-19H. Retuning of our U1307 RPI record to the U1308 stratigraphy guided by Sarnthein *et al*. (2009)'s 'Age Model 2' (Fig. S5) highlights the following deficiencies: (1) U1307-U1308 RPI match is poor below the Kaena (bottom); (2) the alignment of U1307 *N. atlantica* (s) $\delta^{18}O$ and U1308 benthic $\delta^{18}O$ (and the LR04 stack where U1308 $\delta^{18}O$ data are not available) below the Kaena (bottom) is unconvincing; and (3) there is no evidence in the inclination record that the reversed Mammoth subchron lies where assumed by Sarnthein *et al*. (2009). Our new RPI correlation to U1308 illustrates that the basal reversal in U1307 is instead the Mammoth top (~3.22 Ma), reducing the proposed maximum age of sediment recovered at U1307 by ~330 kyr.

The last occurrence (LO) of the dinocyst *Operculodinium eirikianum* identified shipboard in the base of U1307A (Expedition 303 Scientists, 2006a) is dated at ~3.3 Ma, but we argue that it should not be used as an initial tie point in constructing our RPI-based age model for this site: (1) its LO is based on a core catcher sample, so its actual last occurrence could be as much as ~10 m higher in the U1307A stratigraphy than reported; and (2) the ~3.3 Ma age assigned to this dinocyst LO is based on the unspliced stratigraphy from Ocean Drilling Program (ODP) Labrador Sea Site 646 that has poor age control (this site lacks a benthic $\delta^{18}O$-

based age model, and is dated only by a reversal-based magnetostratigraphy that does not resolve the Kaena and Mammoth subchrons; Shipboard Scientific Party, 1987).

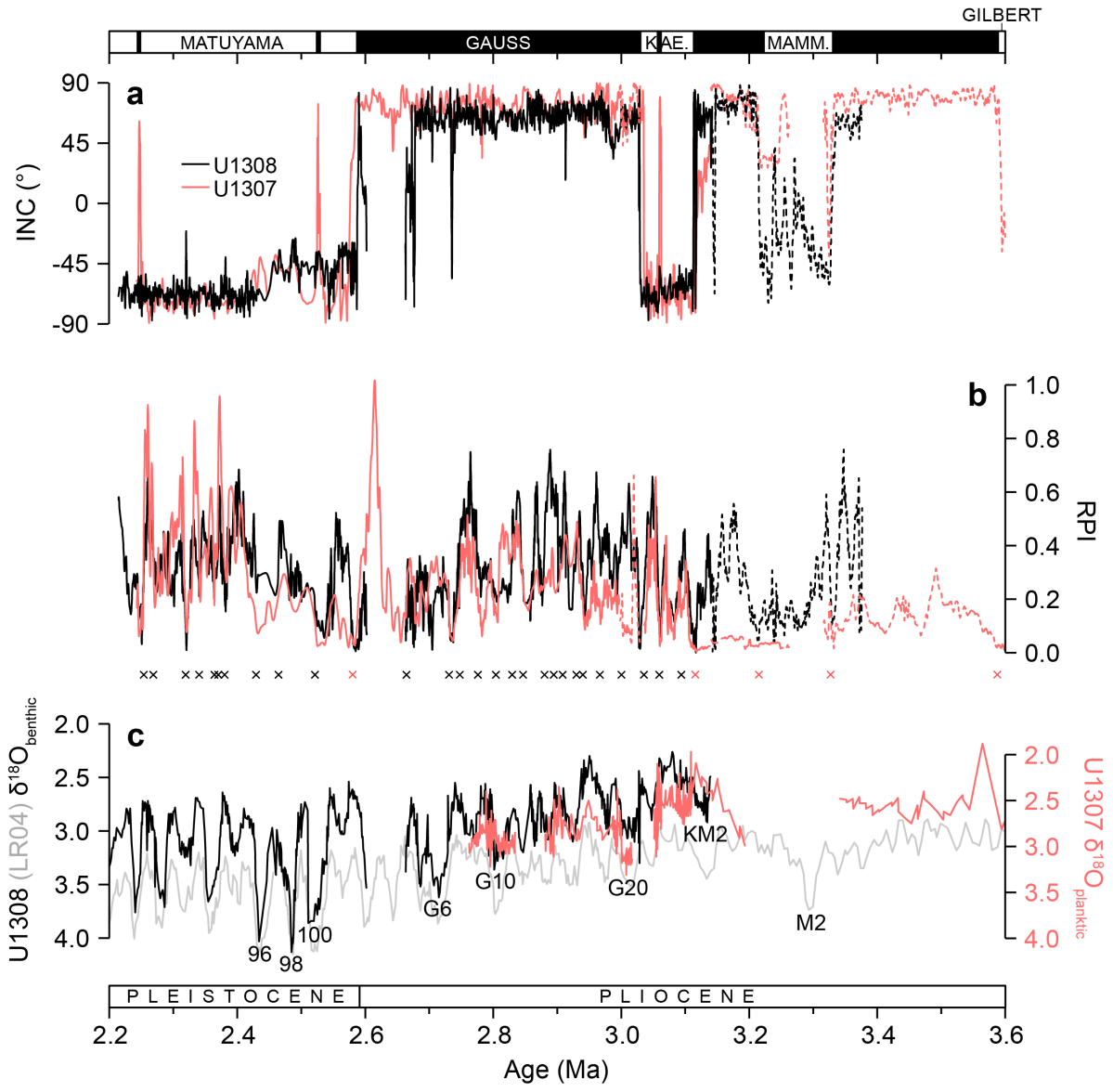

Figure S8. Records of (**a**) inclination (INC; red - this study; black – Channell *et al*., 2016), (**b**) relative paleointensity (RPI; red – this study; black – Channell *et al*., 2016) and (**c**) $\delta^{18}O$ (red – Sarnthein *et al*., 2009; black – Channell *et al*., 2016; grey – Lisiecki and Raymo, 2005). The relationship between the U1307 and U1308 $\delta^{18}O$ datasets shown in (c) is the product of tuning RPIs between U1307 and U1308 based on the 'Age Model 2' scenario for the U1307 stratigraphy proposed by Sarnthein *et al*. (2009). Application of this age model results in a poor fit between the two records prior to 3.1 Ma. Solid lines show u-channel-derived data. Dashed lines show shipboard-derived split core data. Labels in (c) are Marine Isotope Stages. Red/black crosses indicate reversal-/RPI based tie-points.

G. Evaluation of alternative age model for ODP Site 907

Between 3.5–1.0 Ma, the age model for the Iceland Plateau Site 907 IRD record is based on tuning of the 41-kyr component of IRD abundance to orbital parameters within the constraints of the site's paleomagnetic stratigraphy (Jansen *et al*., 2000). An alternative age model for this portion of the Site 907 stratigraphy has been proposed, however, by Lacasse and van den Bogaard (2002), based on laser probe $^{40}Ar/^{39}Ar$ dating of three single-crystal K-feldspar or biotite grains from discrete tephra layers deposited during the intensification of Northern Hemisphere glaciation (iNHG). Based on this alternative age model, the onset of persistently elevated IRD inputs to Site 907 occurred ~2.9 Ma, and not ~3 Ma (Lacasse and van den Bogaard, 2002). This alternative age model is unlikely to represent the best estimate of age-depth relationships in the Site 907 stratigraphy because: (1) it invalidates the reversal-based paleomagnetic stratigraphy for Site 907; (2) it places a large peak in IRD abundance in the Site 907 stratigraphy formerly assigned to MIS M2, ~3.3 Ma, by Jansen *et al*. (2000) at ~3.1 Ma during the mid-Piacenzian warm period, and would represent an ice-rafting event not found in any other IRD record for this time interval from the Nordic Seas and subpolar North Atlantic (e.g., this study; Jansen and Sjöholm, 1991; Kleiven *et al*., 2002; Kneis *et al*., 2014). Regardless, based on either age model, if a temporal offset does exist between the onset of consistently-elevated IRD deposition at Site 907 and at Site U1307 it cannot be attributed to age model uncertainty.

Table S2. Polarity reversals and excursions at Site U1307 determined in this study compared to previously published interpretations.

Hole, core, section, interval (cm)	Depth (rmcd)	Transition interval	Reversal/excursion	Age (ka)	MIS[b]	Shipboard interpretation, age (ka)[d]	Alternative interpretation, age (ka)[e]
U1307B-13H-1 128	117.11	Upper	Unnamed excursion	2236[a]	86	-	-
U1307B-13H-2 11	117.44	Lower					
U1307A-14H-3 143	124.74	Upper	Gauss/Matuyama C2An.1n (t)	2595[b] (2581[c])	103	Gauss/Matuyama C2An.1n (t), 2581	Gauss/Matuyama C2An.1n (t), 2581
U1307A-14H-4 25	125.06	Lower					
U1307A-17H-2 61	147.81	Upper	Kaena top C2An.1n (b)	3029[b] (3032[c])	G21	Kaena top C2An.1n (b), 3040	Kaena top C2An.1n (b), 3040
U1307A-17H-2 97	148.17	Lower					
U1307A-17H-4 70	150.90	Upper	Unnamed excursion (?)	3060	G22	Kaena bottom C2An.2n (t), 3110	-
U1307A-17H-4 147	151.67	Lower				Mammoth top C2An.2n (b), 3220	-
U1307A-18H-2 31	157.06	Upper	Kaena bottom C2An.2n (t)	3116[b] (3110[c])	KM2	Mammoth bottom C2An.3n (t), 3330	Kaena bottom C2An.2n (t), 3110
U1307A-18H-2 82	157.57	Lower					
U1307A-19H-6 60	173.93	Upper	Mammoth top C2An.2n (b)	3207[c]	KM6	Gilbert/Gauss C2An.3n (b), 3580	Gilbert/Gauss C2An.3n (b), 3580
U1307A-19H-6 120	174.53	Lower					

[a]Channell and Guyodo (2004); [b]Channell *et al*. (2016); [c]Ogg *et al*. (2012); [d]Expedition 303 Scientists (2006a); [e]Sarnthein *et al*. (2009).

Table S3. List of revised depth-age tie-points for Site U1307 between 117.63–174.48 rmcd based on our new correlation to the Site U1308 RPI. [a]Channell *et al*. (2016)

Depth (rmcd)	Age (ka)	Type	Chronology	Depth (rmcd)	Age (ka)	Type	Chronology
117.63	2253.84	RPI	IODP U1308[a]	136.86	2846.71	RPI	IODP U1308[a]
118.51	2268.70	RPI	IODP U1308[a]	137.47	2880.09	RPI	IODP U1308[a]
120.52	2319.38	RPI	IODP U1308[a]	138.13	2894.64	RPI	IODP U1308[a]
121.30	2340.27	RPI	IODP U1308[a]	138.56	2908.58	RPI	IODP U1308[a]
121.86	2364.20	RPI	IODP U1308[a]	138.80	2930.08	RPI	IODP U1308[a]
122.05	2370.48	RPI	IODP U1308[a]	139.31	2940.14	RPI	IODP U1308[a]
122.40	2380.28	RPI	IODP U1308[a]	141.12	2966.67	RPI	IODP U1308[a]
123.11	2429.18	RPI	IODP U1308[a]	143.76	3000.41	RPI	IODP U1308[a]
123.53	2464.37	RPI	IODP U1308[a]	147.97	3029	Reversal	Kaena (t)[a]
123.96	2521.41	RPI	IODP U1308[a]	151.01	3059.42	RPI	IODP U1308[a]
124.88	2595	Reversal	Gauss-Matuyama[a]	155.41	3093.99	RPI	IODP U1308[a]
127.32	2664.45	RPI	IODP U1308[a]	157.33	3116	Reversal	Kaena (b)[a]
129.10	2730.77	RPI	IODP U1308[a]	166.48	3149.18	RPI	IODP U1308[a]
129.73	2747.82	RPI	IODP U1308[a]	168.96	3167.34	RPI	IODP U1308[a]
132.00	2776.11	RPI	IODP U1308	170.70	3187.76	RPI	IODP U1308[a]
135.00	2804.08	RPI	IODP U1308[a]	174.48	3207	Reversal	Mammoth (t)[a]
136.03	2829.58	RPI	IODP U1308[a]				

Table S4: Terrigenous grain-size analysis of Site U1307 sediments: sediment size fraction proportion (in %, ±2 standard deviations) measured for each discrete sample* from select glacial cycles during iNHG (~2.8–2.3 Ma).

Sample	Depth (rmcd)	Clay <3 µm	Very fine silt 3–10 µm	Fine-medium silt 10–32 µm	Medium-coarse silt 32–63 µm	Sand >63 µm
MIS 88 (IG)	118.30	22.38 ±7.50	36.82 ±5.69	25.39 ±2.69	9.00 ±0.87	6.40 ±1.35
MIS 88 (IG)	118.63	17.41 ±3.06	33.44 ±2.52	26.57 ±0.88	13.04 ±1.30	9.54 ±2.29
MIS 88 (DG)	119.00	14.74 ±2.99	33.78 ±1.33	26.48 ±0.83	11.57 ±0.87	13.42 ±3.04
MIS 88 (G)	119.40	16.14 ±2.83	35.31 ±1.56	26.83 ±2.67	12.03 ±1.31	9.69 ±0.96
MIS 88 (IG)	120.20	18.54 ±4.00	38.60 ±3.09	28.99 ±3.08	8.55 ±2.27	45.32 ±1.63
MIS 92 (G)	121.24	10.92 ±2.31	30.64 ±4.82	32.32 ±2.36	13.85 ±3.13	12.26 ±2.02
MIS 92 (G)	121.44	14.24 ±3.10	34.37 ±1.63	28.15 ±3.08	12.15 ±1.18	11.09 ±1.00
MIS 92 (IG)	121.64	15.73 ±2.46	40.19 ±0.65	28.16 ±0.88	9.56 ±120	6.35 ±0.67
MIS 92 (G)	121.88	18.30 ±1.04	36.56 ±0.84	24.20 ±0.88	8.54 ±0.78	12.40 ±1.27
MIS 92 (DG)	122.30	10.15 ±1.10	27.12 ±2.55	35.57 ±1.41	16.86 ±2.44	10.29 ±1.60
MIS 104 (IG)	125.82	20.91 ±1.40	36.53 ±1.42	30.57 ±0.57	7.08 ±1.44	4.89 ±1.85
MIS 104 (DG)	126.24	14.45 ±2.17	34.30 ±1.82	30.07 ±2.07	11.74 ±1.38	9.44 ±0.81
MIS 104 (G)	126.42	15.35 ±1.58	30.03 ±1.55	26.36 ±0.87	11.74 ±0.68	16.51 ±1.84
MIS 104 (IG)	126.62	18.47 ±2.97	33.27 ±1.74	27.25 ±0.71	11.46 ±1.19	9.55 ±2.13
MIS 104 (DG)	126.82	18.24 ±4.59	31.75 ±1.69	29.84 ±1.20	12.95 ±0.58	7.23 ±0.92
MIS G12 (IG)	136.00	16.59 ±2.19	32.41 ±0.47	32.27 ±0.30	13.01 ±1.11	5.71 ±1.47
MIS G12 (G)	136.20	13.88 ±1.41	28.43 ±0.99	33.82 ±0.29	17.01 ±0.59	6.86 ±0.97
MIS G12 (IG)	136.90	15.18 ±2.43	33.03 ±2.26	33.14 ±0.84	17.03 ±0.53	7.29 ±0.95

*Ten repeat grain size measurements were made on a well-mixed aliquot of each sample, and this procedure repeated on a separate subsample. Values reported for each sample are an average of all measurements made. MIS = Marine Isotope Stage. IG = interglacial, G = glacial, DG = deglacial

Additional references

Gogorza, C.S.G., Irurzun, M.A., Chaparro, M.A.E., Lirio, J.M., Nunez, H., Bercoff, P.G., Sinito, A.M., 2006. Relative paleointensity of the geomagnetic field over the last 21,000 years BP from sediment cores, Lake El Trébol (Patagonia, Argentina). Earth Planets Space 58 (10), 1323–1332.

Jansen, E., Sjøholm, J., 1991. Reconstruction of glaciation over the past 6 Myr from ice-borne deposits in the Norwegian Sea. Nature 349, 600–603.

Kleiven, H.F., Jansen, E., Fronval, T., Smith, T.M., 2002. Intensification of Northern Hemisphere glaciations in the circum Atlantic region (3.5–2.4 Ma) – ice-rafted detritus evidence. Palaeogeogr. Palaeoclimatol. Palaeoecol. 184, 213–223.

Knies, J., Mattingsdal, R., Fabian, K., Grøsfjeld, K., Baranwal, S., Husum, K., De Schepper, S., Vogt, C., Andersen, N., Matthiessen, J., Andreassen, K., Jokat, W., Nam, S., Gaina, C., 2014. Effect of early Pliocene uplift on late Pliocene cooling in the Arctic–Atlantic gateway. Earth Planet. Sci. Lett. 387, 132–144.

Lacasse, C., van den Bogaard, P., 2002. Enhanced airborne dispersal of silicic tephras during the onset of Northern Hemisphere glaciations, from 6 to 0 Ma records of explosive volcanism and climate change in the subpolar North Atlantic. Geology 30(7), 623–626.

Povea, P., Cacho, I., Moreno, A., Menéndez, M., Méndez, F.J., 2015. A new procedure for the lithic fraction characterization in marine sediments from high productivity areas: Optimization of analytical and statistical procedures. Limnol. Oceanogr.-Meth. 13, 127–137.

Appendix D: XRF data for Chapter 5

D.1 XRF normalisation for Ca-dilution

The five non-Ca elements measured by X-ray fluorescence (XRF), Si, K, Ti, Fe and Sr, were corrected for Ca-dilution prior to further analysis. This was achieved by cross-plotting each element with Ca (see Fig. D.1 overleaf), and the equation of the resultant regression line (in the format y = m*x + c) was used to correct each value for the target element (X) using the corresponding value for Ca in the following equation:

$$\frac{X}{1 + ((m * Ca)/c)}$$

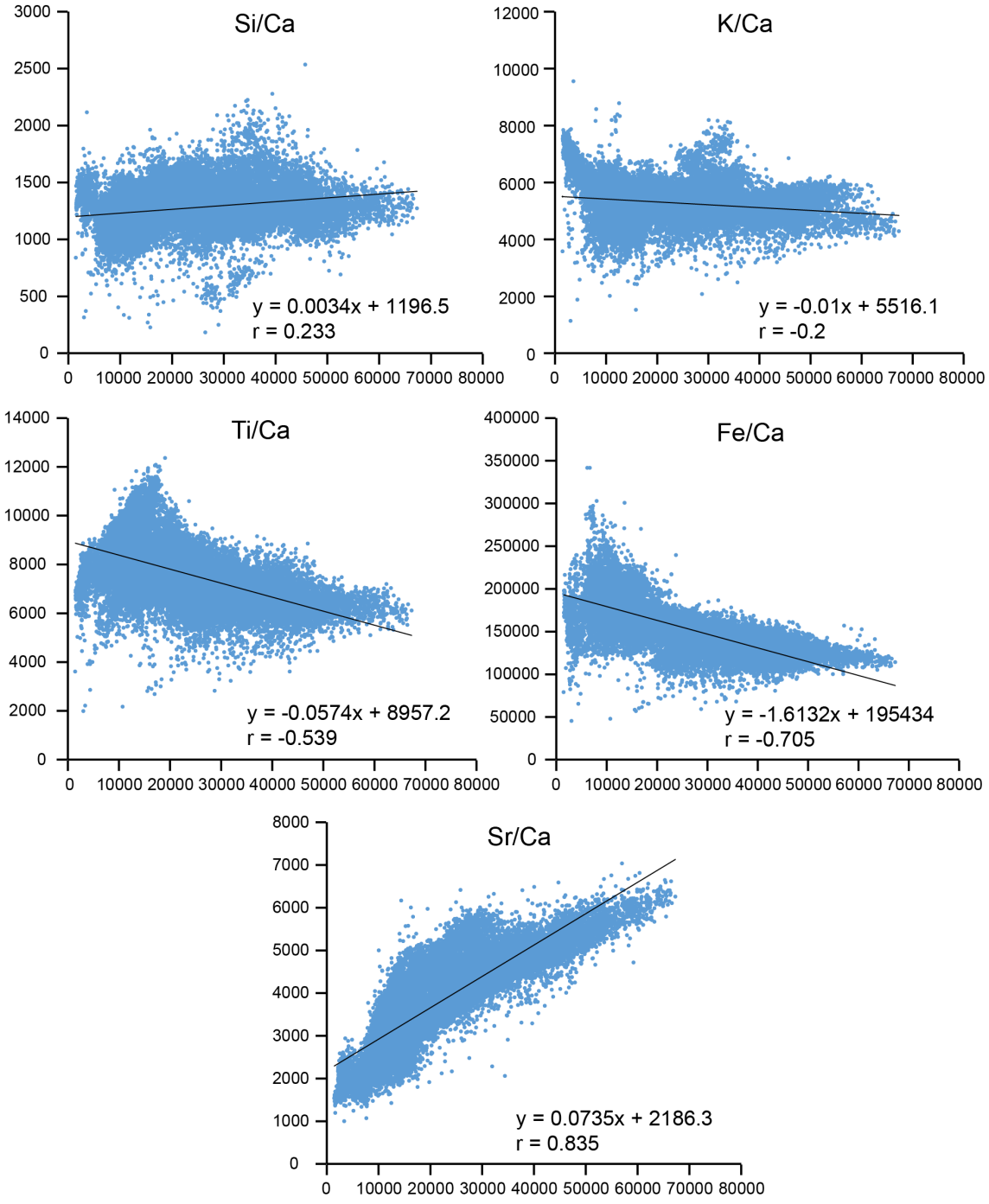

Figure D.1 Cross-plots of selected XRF elements with Ca measured on Site U1307 u-channels. Equation of regression line used to correct each element for Ca-dilution.

Appendix E: Data for Chapter 6

Table E.1 Modal mineralogical data for sand-sized (63–1000 μm) sediment across Marine Isotope Stage (MIS) 102 (~2.55 Ma) at Site U1307.*

MIS 102 samples	1 (DG)	2 (DG)	3 (FG)	4 (EG)	5 (IG)
No. analysis points	346736	242676	159572	391957	308679
No. particles measured	5712	6195	6160	5824	5678
Plagioclase Feldspar	35.01	27.86	38.2	34.15	32.82
Quartz	40.31	41.60	33.94	39.14	42.10
Alkali Feldspar	11.13	12.03	12.19	12.71	13.07
Hornblende	4.08	5.47	4.98	4.71	3.04
Garnet	0.68	0.88	0.32	0.40	0.33
Muscovite	0.82	1.00	0.79	0.90	0.73
Pyroxene	1.57	1.74	2.15	1.23	1.24
Epidote	0.89	0.81	0.75	0.90	0.52
Biotite	1.25	2.01	0.71	1.45	2.00
Chlorite	0.53	0.50	0.31	0.84	0.50
Olivine	0.04	0.03	0.01	0.02	0.03
Others	3.70	6.06	5.64	3.54	3.61
Background	0.24	0.29	0.46	0.33	0.25

*Values shown as 0.00 may have the mineral present at an abundance of <0.01%.
EG = early glacial, FG = full glacial, DG = deglacial, IG = interglacial

Table E.2 Modal mineralogical data for sand-sized (63–1000 μm) sediment across Marine Isotope Stage (MIS) G6 (~2.72 Ma) at Site U1307.*

MIS G6 samples	1 (IG)	2 (IG)	3 (DG)	4 (DG)	5 (FG)	6 (FG)	7 (EG)	8 (IG)	9 (IG)
No. analysis points	4831	6256	5660	3996	5987	6033	5805	5589	5636
No. particles measured	267188	188939	391902	204873	292150	317723	85035	58618	68861
Plagioclase Feldspar	26.50	29.47	30.00	28.80	30.17	33.95	34.86	30.93	36.14
Quartz	44.07	38.97	38.62	42.77	42.85	36.13	24.68	28.73	24.47
Alkali Feldspar	10.90	10.59	12.52	12.19	10.89	12.63	16.43	16.51	16.58
Hornblende	4.21	5.22	5.07	3.62	4.65	5.46	5.86	4.32	4.95
Garnet	0.44	0.82	1.03	1.07	0.84	0.48	0.44	0.94	1.05
Muscovite	0.80	0.78	0.91	0.90	0.98	0.95	0.92	0.86	1.01
Pyroxene	2.10	2.85	2.08	1.65	2.22	2.08	3.31	2.60	2.40
Epidote	1.01	1.58	1.79	0.84	1.46	1.31	1.51	0.55	1.30
Biotite	2.48	1.13	1.02	1.01	0.73	1.34	0.55	1.58	0.82
Chlorite	0.76	0.85	0.81	0.71	0.61	1.33	0.46	0.32	0.20
Olivine	0.01	0.03	0.04	0.04	0.09	0.04	0.07	0.05	0.04
Others	6.74	7.71	6.12	6.39	4.50	4.30	10.92	12.61	11.03
Background	0.34	0.30	0.41	0.33	0.27	0.26	2.50	2.31	2.89

*Values shown as 0.00 may have the mineral present at an abundance of <0.01%.
EG = early glacial, FG = full glacial, DG = deglacial, IG = interglacial

Table E.3 Modal mineralogical data for sand-sized (63–1000 μm) sediment across Marine Isotope Stage (MIS) G8 (~2.76 Ma) at Site U1307.*

MIS G8 samples	1 (DG)	2 (DG)	3 (FG)	4 (EG)
No. analysis points	5761	5633	5443	5895
No. particles measured	52873	59104	41324	44906
Plagioclase Feldspar	26.58	27.63	26.43	24.87
Quartz	23.92	22.33	19.00	23.47
Alkali Feldspar	14.66	17.52	16.42	17.79
Hornblende	4.90	7.39	9.82	5.61
Garnet	1.87	2.44	1.62	1.66
Muscovite	1.19	1.05	0.73	1.57
Pyroxene	4.19	3.03	3.45	3.73
Epidote	1.67	2.25	1.61	1.41
Biotite	2.78	1.16	2.26	1.95
Chlorite	0.42	0.36	0.63	0.35
Olivine	0.13	0.01	0.01	0.03
Others	17.68	14.81	18.01	17.57
Background	2.76	3.53	2.89	2.50

*Values shown as 0.00 may have the mineral present at an abundance of <0.01%.
EG = early glacial, FG = full glacial, DG = deglacial, IG = interglacial

Table E.4 Modal mineralogical data for sand-sized (63–1000 μm) sediment across Marine Isotope Stage (MIS) G12 (~2.83 Ma) at Site U1307.*

MIS G12 samples	1 (DG)	2 (DG)	3 (DG)	4 (DG)	5 (FG)	6 (EG)	7 (EG)
No. analysis points	5805	5691	5333	5489	5916	6351	5636
No. particles measured	171735	136670	59525	64369	228585	239904	70740
Plagioclase Feldspar	35.49	31.22	30.41	30.53	34.54	38.79	38.87
Quartz	30.64	36.15	36.61	35.87	35.42	35.04	27.53
Alkali Feldspar	12.71	11.24	7.54	12.1	12.38	12.97	13.61
Hornblende	3.15	1.27	0.87	0.73	1.27	1.81	3.59
Garnet	0.49	1.02	0.94	0.57	0.47	0.44	1.05
Muscovite	0.58	0.65	0.51	0.82	0.92	0.72	0.67
Pyroxene	2.13	1.33	0.82	2.15	0.71	1.21	2.24
Epidote	0.55	0.56	0.24	0.06	0.12	0.60	0.92
Biotite	1.39	2.20	2.16	1.26	1.06	0.61	1.34
Chlorite	0.56	0.44	0.27	0.22	0.33	0.26	0.66
Olivine	0.01	0.02	0.01	0.02	0.05	0.04	0.00
Others	12.31	13.91	19.62	15.68	12.76	7.51	9.53
Background	2.21	1.61	1.91	1.11	1.46	1.61	1.90

*Values shown as 0.00 may have the mineral present at an abundance of <0.01%.
EG = early glacial, FG = full glacial, DG = deglacial, IG = interglacial

Table E.5 Modal mineralogical data for sand-sized (63–1000 µm) sediment across Marine Isotope Stage (MIS) G18 (~2.98 Ma) at Site U1307.*

MIS G18 samples	1 (IG)	2 (IG)	3 (DG)	4 (FG)	5 (FG)	6 (EG)	7 (IG)
No. analysis points	6122	5279	6058	5882	6091	5585	5727
No. particles measured	112519	74443	105036	96993	124384	50313	98219
Plagioclase Feldspar	32.56	31.92	35.98	36.30	35.12	31.6	32.48
Quartz	30.83	34.11	30.07	27.98	32.71	27.01	32.43
Alkali Feldspar	12.15	10.86	11.72	12.34	12.55	14.7	12.79
Hornblende	3.14	1.92	3.97	5.17	2.98	4.63	4.79
Garnet	0.56	0.42	1.79	1.40	0.57	0.74	0.46
Muscovite	1.73	1.16	1.11	0.52	0.76	1.41	0.83
Pyroxene	1.92	3.02	1.63	2.52	1.67	3.05	2.51
Epidote	1.16	0.60	0.96	1.08	0.78	2.00	0.90
Biotite	0.53	1.42	1.16	0.87	0.59	1.35	1.02
Chlorite	0.35	0.44	0.47	0.61	0.32	0.65	0.42
Olivine	0.05	0.13	0.00	0.00	0.02	0.03	0.06
Others	15.02	14.00	11.14	11.21	11.93	12.81	11.32
Background	2.20	1.39	1.98	2.56	1.61	1.99	1.96

*Values shown as 0.00 may have the mineral present at an abundance of <0.01%.
EG = early glacial, FG = full glacial, DG = deglacial, IG = interglacial

Table E.6 Number of transitions between pairs of key mineral species for sand-sized (63–1000 μm) sediment from MIS 92 (~2.38 Ma) at Site U1307.

MIS 92	Biotite	Plagioclase Feldspar	Alkali Feldspar	Muscovite	Garnet	Pyroxene	Hornblende	Chlorite	Quartz	Epidote
Biotite	0.00	92.00	6.00	0.00	11.00	0.00	0.00	6.00	16.00	0.00
Plagioclase Feldspar	92.00	0.00	855.00	128.00	73.00	85.00	597.00	210.00	853.00	11.00
Alkali Feldspar	6.00	855.00	0.00	51.00	1.00	0.00	0.00	3.00	145.00	0.00
Muscovite	0.00	128.00	51.00	0.00	89.00	0.00	633.00	1.00	46.00	45.00
Garnet	11.00	73.00	1.00	89.00	0.00	28.00	74.00	8.00	0.00	9.00
Pyroxene	0.00	85.00	0.00	0.00	28.00	0.00	875.00	5.00	22.00	1.00
Hornblende	0.00	597.00	0.00	633.00	74.00	875.00	0.00	10.00	41.00	33.00
Chlorite	6.00	210.00	3.00	1.00	8.00	5.00	10.00	0.00	0.00	1.00
Quartz	16.00	853.00	145.00	46.00	0.00	22.00	41.00	0.00	0.00	0.00
Epidote	0.00	11.00	0.00	45.00	9.00	1.00	33.00	1.00	0.00	0.00

Table E.7 Number of transitions between pairs of key mineral species for sand-sized (63–1000 μm) sediment from MIS 102 (~2.55 Ma) at Site U1307.

MIS 102	Biotite	Plagioclase Feldspar	Alkali Feldspar	Muscovite	Garnet	Pyroxene	Hornblende	Chlorite	Quartz	Epidote
Biotite	0.00	1434.00	2373.00	1000.00	389.00	284.00	375.00	447.00	2378.00	17.00
Plagioclase Feldspar	1434.00	0.00	18608.00	3625.00	532.00	702.00	10907.00	790.00	8902.00	4564.00
Alkali Feldspar	2373.00	18608.00	0.00	2951.00	82.00	127.00	351.00	180.00	7834.00	84.00
Muscovite	1000.00	3625.00	2951.00	0.00	200.00	47.00	2122.00	152.00	1867.00	68.00
Garnet	389.00	532.00	82.00	200.00	0.00	159.00	1264.00	318.00	380.00	527.00
Pyroxene	284.00	702.00	127.00	47.00	159.00	0.00	5682.00	878.00	692.00	51.00
Hornblende	375.00	10907.00	351.00	2122.00	1264.00	5682.00	0.00	3709.00	824.00	1044.00
Chlorite	447.00	790.00	180.00	152.00	318.00	878.00	3709.00	0.00	513.00	105.00
Quartz	2378.00	8902.00	7834.00	1867.00	380.00	692.00	824.00	513.00	0.00	126.00
Epidote	17.00	4564.00	84.00	68.00	527.00	51.00	1044.00	105.00	126.00	0.00

Table E.8 Number of transitions between pairs of key mineral species for sand-sized (63–1000 µm) sediment from MIS G6 (~2.72 Ma) at Site U1307.

MIS G6	Biotite	Plagioclase Feldspar	Alkali Feldspar	Muscovite	Garnet	Pyroxene	Hornblende	Chlorite	Quartz	Epidote
Biotite	0.00	1788.00	2708.00	1269.00	612.00	417.00	760.00	614.00	2718.00	29.00
Plagioclase Feldspar	1788.00	0.00	23831.00	5100.00	720.00	894.00	12877.00	949.00	8971.00	6851.00
Alkali Feldspar	2708.00	23831.00	0.00	3703.00	154.00	129.00	450.00	174.00	9443.00	159.00
Muscovite	1269.00	5100.00	3703.00	0.00	265.00	57.00	1822.00	198.00	2021.00	102.00
Garnet	612.00	720.00	154.00	265.00	0.00	319.00	1829.00	793.00	513.00	761.00
Pyroxene	417.00	894.00	129.00	57.00	319.00	0.00	10484.00	1001.00	726.00	109.00
Hornblende	760.00	12877.00	450.00	1822.00	1829.00	10484.00	0.00	6151.00	1009.00	1374.00
Chlorite	614.00	949.00	174.00	198.00	793.00	1001.00	6151.00	0.00	659.00	94.00
Quartz	2718.00	8971.00	9443.00	2021.00	513.00	726.00	1009.00	659.00	0.00	212.00
Epidote	29.00	6851.00	159.00	102.00	761.00	109.00	1374.00	94.00	212.00	0.00

Table E.9 Number of transitions between pairs of key mineral species for sand-sized (63–1000 µm) sediment from MIS G8 (~2.76 Ma) at Site U1307.

MIS G8	Biotite	Plagioclase Feldspar	Alkali Feldspar	Muscovite	Garnet	Pyroxene	Hornblende	Chlorite	Quartz	Epidote
Biotite	0.00	110.00	230.00	134.00	174.00	123.00	71.00	40.00	172.00	3.00
Plagioclase Feldspar	110.00	0.00	959.00	314.00	72.00	56.00	200.00	25.00	382.00	453.00
Alkali Feldspar	230.00	959.00	0.00	408.00	25.00	25.00	18.00	4.00	571.00	3.00
Muscovite	134.00	314.00	408.00	0.00	46.00	6.00	181.00	3.00	130.00	9.00
Garnet	174.00	72.00	25.00	46.00	0.00	76.00	464.00	128.00	64.00	97.00
Pyroxene	123.00	56.00	25.00	6.00	76.00	0.00	926.00	34.00	112.00	6.00
Hornblende	71.00	200.00	18.00	181.00	464.00	926.00	0.00	674.00	88.00	170.00
Chlorite	40.00	25.00	4.00	3.00	128.00	34.00	674.00	0.00	12.00	5.00
Quartz	172.00	382.00	571.00	130.00	64.00	112.00	88.00	12.00	0.00	4.00
Epidote	3.00	453.00	3.00	9.00	97.00	6.00	170.00	5.00	4.00	0.00

Table E.10 Number of transitions between pairs of key mineral species for sand-sized (63–1000 μm) sediment from MIS G12 (~2.83 Ma) at Site U1307.

MIS G6	Biotite	Plagioclase Feldspar	Alkali Feldspar	Muscovite	Garnet	Pyroxene	Hornblende	Chlorite	Quartz	Epidote
Biotite	0.00	385.00	908.00	205.00	212.00	279.00	349.00	87.00	564.00	4.00
Plagioclase Feldspar	385.00	0.00	5616.00	1660.00	291.00	296.00	1072.00	109.00	3008.00	1158.00
Alkali Feldspar	908.00	5616.00	0.00	909.00	75.00	55.00	80.00	7.00	2413.00	12.00
Muscovite	205.00	1660.00	909.00	0.00	82.00	11.00	467.00	45.00	440.00	12.00
Garnet	212.00	291.00	75.00	82.00	0.00	213.00	392.00	305.00	164.00	167.00
Pyroxene	279.00	296.00	55.00	11.00	213.00	0.00	1138.00	155.00	342.00	10.00
Hornblende	349.00	1072.00	80.00	467.00	392.00	1138.00	0.00	1738.00	288.00	117.00
Chlorite	87.00	109.00	7.00	45.00	305.00	155.00	1738.00	0.00	58.00	4.00
Quartz	564.00	3008.00	2413.00	440.00	164.00	342.00	288.00	58.00	0.00	44.00
Epidote	4.00	1158.00	12.00	12.00	167.00	10.00	117.00	4.00	44.00	0.00

Table E.11 Number of transitions between pairs of key mineral species for sand-sized (63–1000 μm) sediment from MIS G18 (~2.98 Ma) at Site U1307.

MIS G8	Biotite	Plagioclase Feldspar	Alkali Feldspar	Muscovite	Garnet	Pyroxene	Hornblende	Chlorite	Quartz	Epidote
Biotite	0.00	295.00	609.00	344.00	192.00	219.00	113.00	209.00	435.00	2.00
Plagioclase Feldspar	295.00	0.00	4104.00	1008.00	298.00	271.00	1189.00	78.00	1831.00	1864.00
Alkali Feldspar	609.00	4104.00	0.00	817.00	55.00	38.00	69.00	13.00	1827.00	9.00
Muscovite	344.00	1008.00	817.00	0.00	74.00	16.00	822.00	51.00	308.00	21.00
Garnet	192.00	298.00	55.00	74.00	0.00	173.00	504.00	369.00	141.00	124.00
Pyroxene	219.00	271.00	38.00	16.00	173.00	0.00	1863.00	245.00	331.00	10.00
Hornblende	113.00	1189.00	69.00	822.00	504.00	1863.00	0.00	1761.00	250.00	243.00
Chlorite	209.00	78.00	13.00	51.00	369.00	245.00	1761.00	0.00	42.00	12.00
Quartz	435.00	1831.00	1827.00	308.00	141.00	331.00	250.00	42.00	0.00	34.00
Epidote	2.00	1864.00	9.00	21.00	124.00	10.00	243.00	12.00	34.00	0.00